

Numerical Prediction of Fracture Toughness of a Reactor Pressure Vessel Steel Based on Experiments Using Sub-Sized Specimens

Zur Erlangung des akademischen Grades eines

Doktors der Ingenieurwissenschaften (Dr.-Ing.)

von der KIT-Fakultät für Maschinenbau des
Karlsruher Instituts für Technologie (KIT)
genehmigte

Dissertation

von

Timo Metzler

geboren am 03.09.1994
in Karlsruhe

Tag der mündlichen Prüfung:	08. April 2025
Hauptreferent:	Prof. Dr.-Ing. Jarir Aktaa
Korreferent:	Prof. Dr. Peter Gumbsch

Kurzfassung

Ein wesentlicher Faktor für den erfolgreichen Übergang zu einer kohlenstoffneutralen Wirtschaft ist der sichere Langzeitbetrieb von Kernreaktoren. Der Reaktordruckbehälter ist ein sicherheitskritischer Teil der meisten derzeit aktiven Reaktoren der zweiten Generation, da er einer kontinuierlichen Neutronenbestrahlung ausgesetzt ist. Daher ist es von entscheidender Bedeutung, die Entwicklung des bruchmechanischen Verhaltens der Strukturstähle unter diesen Bedingungen zu überwachen. Da die Verfügbarkeit von bestrahltem Material stark begrenzt ist, ist es notwendig, Prüfverfahren an kleinen Proben für die bruchmechanische Charakterisierung im Übergangsbereich zu entwickeln. In den vergangenen Jahrzehnten hat sich die miniaturisierte Kompaktzugprobe (MCT) als vielversprechende Geometrie für zukünftige Überwachungsprogramme erwiesen. Allerdings muss die Verwendbarkeit dieser Geometrie noch weiter unter Beweis gestellt werden, da während der Prüfung ein Verlust der Dehnungsbehinderung beobachtet wird. Des Weiteren sind zusätzliche Anstrengungen erforderlich, um die benötigte Materialmenge für die bruchmechanische Charakterisierung zu reduzieren.

Ziel dieser Arbeit ist die Weiterentwicklung eines bestehenden Ansatzes zur Ermittlung der Parameter eines Kohäsivzonenmodells, das in Verbindung mit Finite-Elemente-Modellen der MCT-Probe verwendet werden kann. Mit dem kalibrierten Kohäsivzonenmodell werden Simulationen durchgeführt, um das bruchmechanische Verhalten von ferritischen Stählen im Übergangsbereich vorherzusagen. Statistisch verteilte numerische Bruchzähigkeitswerte werden durch eine zufällige räumliche Verteilung von Kohäsivzonenelementen mit entweder spröden oder duktilen Eigenschaften in der kohäsiven Zone bestimmt. Dabei wird eine numerische Referenztemperatur auf der Grundlage der Norm ASTM E1921 vorhergesagt.

Der experimentell-numerische Ansatz zur Kalibrierung der Modellparameter umfasst die Prüfung von gekerbten Zugproben zur Ermittlung der Kohäsivspannung in Abhängigkeit der Spannungstriaxialität und die Anpassung der Kohäsionsenergie mittels MCT-Versuchen im Übergangsbereich und bei Raumtemperatur. Darüber hinaus werden die MCT-Versuche im Übergangsbereich zur experimentellen Bestimmung der Referenztemperatur genutzt. Umfangreiche fraktografische Analysen werden in Verbindung mit numerischen Simulationen durchgeführt, um Unterschiede im mechanischen und bruchmechanischen Verhalten der MCT-Geometrie und der CT-Geometrien in Standardgröße zu identifizieren. Die Simulationen werden außerdem dazu verwendet, den Verlust des triaxialen Spannungszustands zu bewerten, der bei MCT-Proben mit zunehmender Belastung beobachtet wird.

Mit dem entwickelten Ansatz wird die Referenztemperatur des untersuchten Reaktordruckbehälterstahls genau vorhergesagt. Es wird gezeigt, dass dafür weniger Material erforderlich ist als für eine experimentelle Bestimmung nach der Norm ASTM E1921. Der Ansatz stellt somit einen Schritt zur Reduzierung der Kosten zukünftiger Überwachungsprogramme dar. Die vollständige Beschreibung des statistischen bruchmechanischen Verhaltens von ferritischen Stählen im Übergangsbereich ist das finale Ziel des probabilistischen Ansatzes. Hierfür ist die Einbeziehung von Defektpopulationen (schwächste Glieder) in der kohäsiven Zone erforderlich.

Abstract

An essential factor for the successful transition towards a carbon-neutral economy is the safe long-term operation of nuclear reactors. The reactor pressure vessel is a safety-critical part of most currently active Generation II reactors due to it being subject to continuous neutron irradiation. Therefore, it is crucial to monitor the evolution of the fracture-mechanical behavior of the structural steel under these conditions. Since the availability of irradiated material is severely limited, it is necessary to develop small specimen test techniques for fracture-mechanical characterization within the DBT region. In the past decades, the miniaturized compact tension specimen (MCT) has been shown to be a promising geometry for future surveillance programs. However, further demonstration of the viability of the geometry is required due to the effect of loss of constraint observed during testing. Additional efforts are necessary to further reduce the amount of material required for fracture-mechanical characterization.

The objective of this work is to further develop an existing approach for identifying the parameters of a cohesive zone model to be used in conjunction with finite-element-models of the MCT specimen. Simulations with the calibrated cohesive zone model are performed to predict the fracture-mechanical behavior of ferritic steels within the DBT region. Statistically distributed numerical fracture toughness values are obtained by means of a random spatial distribution of cohesive elements with either brittle or ductile properties throughout the cohesive zone. Thereby, a numerical reference temperature is determined based on the ASTM E1921 standard.

The experimental-numerical approach for calibrating the model parameters includes the testing of notched tensile specimens to identify the cohesive strength depending on the stress triaxiality. Fitting of the cohesive energy is performed by means of MCT tests within the DBT region and at room temperature. In addition, the MCT tests within the transition region are used to determine the reference temperature experimentally. Extensive fractographic analyses are performed in conjunction with numerical simulations to identify differences in the mechanical and fracture-mechanical behavior of the MCT geometry and standard-sized CT geometries. The simulations are further used to assess the loss of constraint observed in MCT specimens with increasing loading.

With the developed approach, the reference temperature of the investigated reactor pressure vessel steel is accurately predicted. It is shown that the method uses less material than is required for an experimental determination following the ASTM E1921 standard. Thus, the approach represents a step towards reducing the cost of future surveillance programs. The complete description of the statistical fracture-mechanical behavior of ferritic steels within the DBT region is the final goal of the probabilistic approach. For this, the inclusion of defect populations (weakest links) in the cohesive zone is required.

Table of contents

Kurzfassung	iii
Abstract	v
Table of contents	vii
List of figures	xi
List of tables	xvii
Abbreviations and notation	xix
1 Introduction	1
1.1 Objective	1
1.2 Structure of this thesis	2
2 State of research	5
2.1 Fracture toughness	5
2.1.1 Energy release rate	6
2.1.2 J-integral	7
2.1.3 Ductile-to-brittle transition in metals	8
2.1.4 Geometric influences on fracture toughness measurements	9
2.2 Experimental fracture toughness determination	11
2.2.1 ASTM E1921 standard for testing in the DBT region	11
2.2.2 ASTM E1820 standard for testing ductile metals	13
2.3 Fracture mechanisms	15
2.3.1 Cleavage fracture	15
2.3.2 Ductile tearing	16
2.4 Cohesive zone model	17
2.4.1 Principle	20
2.4.2 Traction-separation-laws	21
2.4.3 Modifications to the standard CZM	23
2.4.3.1 Triaxiality dependence	23
2.4.3.2 Random spatial distribution of CZM parameters	24
2.4.4 Implementation	25
3 Approach	29
3.1 Deterministic model	29
3.2 Probabilistic model	30
4 Experimental testing and fractography	33
4.1 Material	33
4.1.1 Microstructure	33
4.1.2 Mechanical properties	34
4.2 Tensile testing	36
4.2.1 Experimental setup	36
4.2.2 Specimens	37

4.2.3	Smooth round bar tests	38
4.2.3.1	Direct flow curve determination	38
4.2.3.2	Inverse flow curve determination at intermediate temperatures	43
4.2.4	Notched round bar tests	45
4.3	Fracture mechanics testing.....	47
4.3.1	Experimental setup	47
4.3.2	Specimens	48
4.3.3	Fatigue pre-cracking	48
4.3.4	Front face to load line displacement conversion.....	50
4.3.5	Testing within the DBT region	53
4.3.5.1	Test temperature selection	53
4.3.5.2	Fracture toughness determination	54
4.3.5.3	Master Curve evaluation	55
4.3.5.4	Test temperature recommendations	57
4.3.6	Testing on the upper shelf.....	58
4.3.6.1	Force-displacement curves.....	58
4.3.6.2	Ductile crack extension.....	59
4.3.6.3	J-R curve determination.....	60
4.4	SEM fractography	61
4.4.1	Cleavage initiation sites	61
4.4.1.1	Initiation site locations	62
4.4.1.2	Stress and triaxiality fields near the crack front.....	64
4.4.1.3	Types of initiators	66
4.4.2	Quantitative analysis of the fracture surfaces	69
4.5	Summary of the experiments and fractography	72
5	Cohesive zone parameter identification	75
5.1	Simulation of round bar specimen tests	75
5.1.1	FE-models.....	75
5.1.2	Average true stress – average true strain curves.....	76
5.1.3	Triaxiality-dependent cohesive strength.....	77
5.2	Simulation of the MCT tests	79
5.2.1	FE-models of the MCT geometry	79
5.2.2	Cohesive energy.....	81
5.2.2.1	Criterion for the onset of unstable fracture	82
5.2.2.2	Parameter fitting within the DBT region	83
5.2.2.3	Parameter fitting on the upper shelf.....	86
5.2.3	Summary of the cohesive zone parameter identification	90
6	Simulation of standard-sized CT specimens	93
6.1	FE-models of the standard-sized CT geometries	93
6.2	Numerical results	93
6.2.1	Force-displacement and J-R curves	94
6.2.2	Mechanical fields in front of the crack tip	95
6.2.3	Fracture toughness	103
6.3	Influence of constraint on the numerical fracture toughness	104
6.4	Summary of the standard-sized CT simulations	105

7 Probabilistic CZM approach.....	107
7.1 Mesoscale modeling of the cohesive zone	107
7.2 Probabilistic MCT simulations	109
7.2.1 Initiation of unstable crack growth	109
7.2.2 Influence of ductile cluster location on fracture toughness	112
7.3 Numerical Master Curve prediction.....	113
7.3.1 Variable size of the ductile cohesive element clusters.....	115
7.3.2 Statistical distribution of the numerical fracture toughness.....	117
7.3.3 Material requirement.....	119
7.4 Summary of the probabilistic CZM approach.....	121
8 Discussion.....	123
8.1 Viability of the MCT geometry	123
8.2 Evaluation of the probabilistic CZM approach	124
9 Summary and outlook.....	127
References	131
Appendix	139
A.1 Material block dimensions and cutting plans.....	139
A.2 Specimen geometries and dimensions	141
A.3 Experimental results.....	145
A.4 Fractography results	149
A.5 Numerical results	150
Acknowledgements.....	153
List of publications	155

List of figures

Figure 2.1: Mode I crack loading (a) and center-cracked infinite plate under load (b) adapted from [14].....	6
Figure 2.2: Contour integral to determine J adapted from [27].....	8
Figure 2.3: Ductile-to-brittle transition of fracture toughness of a BCC metal [30]	9
Figure 2.4: Plastic zone size in plane stress and plane strain adapted from [14]	10
Figure 2.5: Master Curve and upper and lower tolerance bounds [10]	13
Figure 2.6: J-R curve for determination of fracture toughness of a ductile material adapted from [41].....	14
Figure 2.7: Classification of cleavage fracture according to the crack path (a) adapted from [46] and SEM micrograph showing transgranular and intergranular cleavage facets in SA-508 Cl.3 (b)	16
Figure 2.8: Cavity formed by coalescence of multiple voids surrounded by cleavage facets in SA-508 Cl.3.....	17
Figure 2.9: Dugdale's model using a constant cohesive traction equal to the materials yield strength (a) and Barenblatt's model using a cohesive traction that depends on the distance from the crack tip (b) adapted from [68]	20
Figure 2.10: Representation of the real ductile fracture process (a) by the CZM (b) adapted from [66].....	21
Figure 2.11: Traction-separation-laws commonly used to simulate fracture of different materials [69,71,73,74].....	22
Figure 2.12: Cohesive elements embedded between continuum elements (a) and normal separation of cohesive elements following external Mode I loading (b) [85].....	26
Figure 2.13: Lower cohesive surface constrained by boundary condition (a) and lower cohesive surface constrained by coupled node displacements (b) [84]	26
Figure 3.1: Overview of the development of the deterministic CZM and its application within this work [86].....	30
Figure 3.2: Overview of the development and application of the probabilistic CZM (adapted from [99])	31
Figure 3.3: Spatial distribution of ductile fracture patches on the fracture surfaces of an MCT specimen that failed by cleavage in the DBT region	32
Figure 4.1: Optical micrographs of the material SA-508 Cl.3 (R-L orientation, mag. 300x (a) and 1000x (b))	34
Figure 4.2: Yield strength and UTS results and exponential fit	35
Figure 4.3: Experimental setup including camera system used for tensile testing	37
Figure 4.4: Representative force-displacement curves for each test temperature obtained from the tensile tests on SRB specimens.....	38
Figure 4.5: Selected images of the contour of specimen SRB13 during testing (a) and corresponding points on the engineering stress - engineering strain curve (b).....	39

Figure 4.6: Diameter of SRB13 along specimen axis at different load levels (a) and reduction of minimum diameter (b) ((b) adapted from [97])	40
Figure 4.7: Fourth order polynomial fit of the specimen radius in the necking region (a) and exponential fit of the curvature radius against engineering strain (b).....	41
Figure 4.8: Average true stress and Bridgman corrected uniaxial true stress for specimen SRB08 tested at -80°C.....	42
Figure 4.9: Plastic flow curves for RT, -60°C and -80°C obtained from the direct determination method (adapted from [99]).....	42
Figure 4.10: Simulated average true stress - average true strain curves at experimental curves at RT, -60 and -80°C.....	42
Figure 4.11: Comparison between numerical and experimental SRB force-displacement curves for all test temperatures	44
Figure 4.12: Plastic flow curves for all test temperatures between RT and -80°C.....	44
Figure 4.13: Force-CHD curves of the 0.1NRB tests (a) and 0.2NRB tests (b) performed at RT, -60, -70 and -80°C.....	45
Figure 4.14: Images of the notches of 0.1NRB01 with a flat notch and 0.1NRB11 with a round notch prior to testing and at the point of fracture (both tested at RT).....	46
Figure 4.15: Average true stress - average true strain curves for the flat-notched (a) and round-notched (b) 0.1NRB specimens and the flat-notched (c) and round-notched (d) 0.2NRB specimens.....	47
Figure 4.16: MCT specimen mounted into the clevises with clip gauge extensometer and thermocouples attached.....	48
Figure 4.17: Resonance testing machine used for fatigue pre-cracking of MCT specimens	49
Figure 4.18: Optical micrograph of the fracture surface of MCT10 tested at -60°C (a) and total crack lengths of all pre-cracked MCT specimens at nine equidistant measurement points along the specimen thickness (b)	50
Figure 4.19: Schematic of the modified MCT geometry showing method of linear interpolation for front face to load line displacement conversion.....	51
Figure 4.20: Simulated conversion factors (solid lines) and constant conversion factors (dotted lines) for different initial crack lengths (a) and KJ curves obtained using the LLD (solid lines) and the converted FFD (dotted lines) (b)	53
Figure 4.21: Simulated and constant conversion factors under the influence of crack growth (a) and J - R curves obtained using the LLD and the converted FFD (b)	53
Figure 4.22: Force-LLD curves from the MCT tests used for the determination of T_0	55
Figure 4.23: Fracture toughness Master Curve for SA-508 Cl.3 established from the uncensored and censored KJc , 1T results obtained from testing MCT specimens between -80 and -45°C	56
Figure 4.24: Force-LLD curves obtained from the tests on MCT specimens at RT	59
Figure 4.25: Fracture surfaces of four MCT specimens tested at RT with final crosshead displacements between 1 and 6 mm.....	60
Figure 4.26: J - R curve for SA-508 Cl.3 at RT obtained by testing MCT specimens.....	61

Figure 4.27: Procedure for locating the cleavage initiation site on the fracture surface of specimen MCT08 tested at -70°C	62
Figure 4.28: Expected location of the initiation site of specimen MCT12 with river lines not pointing towards a particular point or grain boundary	63
Figure 4.29: Locations of the cleavage initiation sites on the fracture surfaces (a) and correlation between KJc , 1T and the distance from the crack front (b)	64
Figure 4.30: Development of the maximum principal stress (a) and triaxiality (b) along the ligament in the center of the specimen with increasing LLD at -60°C	65
Figure 4.31: Development of the maximum principal stress (a) and triaxiality (b) along the thickness direction with increasing LLD at -60°C	65
Figure 4.32: SEM micrographs (mag. 5000x) showing cleavage fracture initiation at particles (a, b) and at grain boundaries (c, d)	67
Figure 4.33: EDX reference spectrum of the steel matrix	68
Figure 4.34: EDX spectrum of the initiating particle found on the fracture surface of MCT08	68
Figure 4.35: Location of the initiating particle on the fracture surface of MCT08	69
Figure 4.36: Determination of the DFR from 15 SEM micrographs (mag. 500x) arranged in a 3x5 pattern in front of the fatigue pre-crack with 16 equidistant data points per micrograph [99]	70
Figure 4.37: SEM micrograph (mag. 2000x) of a fracture surface near the fatigue pre-crack showing the different fracture modes surrounded by cleavage facets (adapted from [99])	70
Figure 4.38: Distribution of the individual fracture modes for specimen MCT12 (adapted from [99])	71
Figure 4.39: Correlation between DFR and test temperature (a) [99] and correlation between DFR and KJc , 1T (b)	72
Figure 4.40: SEM micrograph (mag. 500x) showing the ductile fracture regions on the fracture surface of specimen MCT33 tested at 45°C	72
Figure 5.1: Axisymmetric FE-model of the SRB specimen geometry	76
Figure 5.2: Axisymmetric model of the 0.1NRB geometry with close-up views of the mesh in the vicinity of a flat notch and a round notch	76
Figure 5.3: Numerical average true stress – average true strain curves using both a flat and a round notch geometry and corresponding experimental curves for specimens 0.1NRB10 and 0.1NRB13	77
Figure 5.4: Axial stress and triaxiality at -60°C in the necking region of specimen SRB9 and near the notches of specimens 0.1NRB12 and 0.2NRB12 at the respective fracture points (adapted from [99])	78
Figure 5.5: Linear interpolation of the triaxiality-dependent cohesive strength for RT, -60, -70 and -80°C (adapted from [99])	79
Figure 5.6: Quarter models of the MCT specimen for the crack growth simulations at low temperature and RT (adapted from [99])	81

Figure 5.7: Triangular TSL used for the simulation of unstable fracture at low temperatures (a) and trapezoidal TSL for the simulation of stable crack propagation at RT (b) (adapted from [99]).....	81
Figure 5.8: Crack growth rate against LLD at -60°C using the triaxiality-dependent cohesive strength and a cohesive energy of 2 N/mm.....	83
Figure 5.9: Numerical and experimental force-LLD curves (a-c) and numerical J-R curves (d) for the MCT geometry at -80, -70 and -60°C ((a) adapted from [97], (c) adapted from [99])	85
Figure 5.10: Experimental and simulated force-LLD curves (a) and J-R curves (b) at RT using the interpolated triaxiality-dependent σ_c and Γ_c of 2.25 N/mm.....	86
Figure 5.11: Simulated crack growth rates with and without cohesive strength extrapolation	87
Figure 5.12: Experimental and simulated force-LLD curves (a) and J-R curves (b) at RT using the extrapolated triaxiality-dependent σ_c and Γ_c of 2.25 N/mm (adapted from [99]).....	87
Figure 5.13: Evolution of the shape of the crack front from the MCT tests at RT (top) and corresponding numerical predictions (bottom)	88
Figure 5.14: Experimental and simulated force-LLD curves (a) and J-R curves (b) at RT using the discretization described in this chapter with $\Gamma_c = 2.25$ N/mm and Mahler's discretization with $\Gamma_c = 6$ N/mm	90
Figure 6.1: Quarter model of the 1T CT specimen with the stiff loading pin shown in brown	93
Figure 6.2: Simulated force-LLD and J-R curves from the MCT model (a, b), the 0.5T CT model (c, d) and the 1T CT model (e, f) at -60, -70 and -80°C	95
Figure 6.3: Crack opening stress in the mid thickness (a, b) and along the thickness direction at the x -position of the maximum σ_y (c, d) for $KJ = 35$ MPam.....	96
Figure 6.4: Triaxiality in the mid thickness (a, b) and along the thickness direction at the x -position of the maximum h (c, d) for $KJ = 35$ MPam.....	97
Figure 6.5: Equivalent plastic strain in the mid thickness (a, b) and along the thickness direction at the x -position of the maximum ϵ_p , ϵ_q (c, d) for $KJ = 35$ MPam.....	98
Figure 6.6: Crack opening stress in the mid thickness (a, b) and along the thickness direction at the x -position of the maximum σ_y (c, d) for $KJ = 70$ MPam.....	99
Figure 6.7: Triaxiality in the mid thickness (a, b) and along the thickness direction at the x -position of the maximum h (c, d) for $KJ = 70$ MPam.....	100
Figure 6.8: Equivalent plastic strain in the mid thickness (a, b) and along the thickness direction at the x -position of the maximum ϵ_p , ϵ_q (c, d) for $KJ = 70$ MPam.....	101
Figure 6.9: Simulated plastic zone sizes of the MCT, 0.5T and 1T CT models for $KJ = 70$ MPam at -60°C.....	102
Figure 6.10: Simulated mid thickness plastic zone sizes along the ligament for the MCT, 0.5T and 1T CT geometries at -60°C compared to the analytical plastic zone sizes for plane stress and plane strain	103
Figure 7.1: TSLs for the brittle and ductile cohesive elements	108
Figure 7.2: Probabilistic cohesive zones for -80°C (a) and -45°C (b) with 18x50 μm element cluster size [99]	109

Figure 7.3: Section of the cohesive zone starting from the initial crack tip showing the distribution of ductile and brittle elements (a) and the normal separation (b), crack opening stress (c) and triaxiality (d) at the point of unstable crack initiation.....	110
Figure 7.4: Cohesive stress (a) and separation (b) of a ductile cohesive element and an adjacent brittle element in the initiation region against COD	111
Figure 7.5: Cohesive stress and triaxiality of the ductile element against separation (a) and cohesive stress against separation for both the ductile and brittle element (b)	111
Figure 7.6: Randomly generated cohesive zone of simulation PCZ18_-60_2 with a low number of ductile element clusters near the mid thickness; initiation marked by ellipse	112
Figure 7.7: Correlation of KJc , num and x - (a) and z -coordinates (b) of ductile fracture regions predicted by ten probabilistic simulations at -60°C	113
Figure 7.8: Comparison between the experimental Master Curve (a) and the numerically predicted Master Curve using a constant cluster size of $18 \times 50 \mu\text{m}$ (b) (adapted from [99])	114
Figure 7.9: Cohesive zone with variable size of the element clusters at -60°C	116
Figure 7.10: Master Curve predicted using cohesive element clusters of constant size (a) and Master Curve determined using variable cluster size (b).....	117
Figure 7.11: Histogram of 50 KJc , 1T, num results at -60°C and corresponding three-parameter Weibull PDF with fully fitted parameters [99]	118
Figure 7.12: Cumulative failure probabilities determined experimentally by means of ASTM E1921 and numerically for -60°C (adapted from [99]).....	119
Figure A.1: SA-508 Cl.3 forging dimensions and orientations (dimensions in mm) with location of extracted block in red.....	139
Figure A.2: SA-508 Cl.3 block used for specimen fabrication (dimensions in mm)	139
Figure A.3: Cutting plan for the fabrication of the specimens used for the development of the deterministic CZM	140
Figure A.4: Cutting plan for the fabrication of the specimens used for the development of the probabilistic CZM.....	141
Figure A.5: Smooth round bar specimen geometry	141
Figure A.6: Notched round bar specimen geometry with 0.1 mm notch root radius	142
Figure A.7: Notched round bar specimen geometry with 0.2 mm notch root radius	143
Figure A.8: Miniaturized CT specimen geometry.....	143
Figure A.9: Force-CHD curves obtained from the SRB tests	145
Figure A.10: Uniaxial true stress – true plastic strain curves for all SRB specimens used for the direct flow curve determination	146
Figure A.11: Simulated force-LLD and J-R curves from the 0.5T CT model (a, b) and the 1T CT model (c, d) at -60 , -70 and -80°C using the size-adjusted cohesive energy	151

List of tables

Table 2.1:	Test temperature range dependent weighting factors used to evaluate the data set size criterion [10]	12
Table 4.1:	Chemical composition of the testing material SA-508 Cl.3 (in wt%)	33
Table 4.2:	Mechanical properties of SA-508 Cl.3	35
Table 4.3:	Parameters used for the respective loading steps of the fatigue pre-cracking procedure	49
Table 4.4:	Geometric parameters used for the stationary crack simulations and corresponding conversion factors obtained from Equation (4.11).....	52
Table 4.5:	Average K_{Jc} , 1T and corresponding standard deviation obtained from the valid MCT tests for each test temperature.....	55
Table 4.6:	Contributions of the MCT tests to the data set size criterion in Equation (2.19).....	56
Table 5.1:	Fitting parameters for the linear interpolation of the cohesive strength following Equation (5.1)	79
Table 5.2:	Identified cohesive energy values for -80, -70 and -60°C using the triaxiality-dependent cohesive strength and comparison between the median fracture toughness from the Master Curve and the numerical results from the MCT simulations ...	84
Table 6.1:	Numerical fracture toughness K_{Jc} , num and median fracture toughness from the experimental Master Curve K_{Jc} , MC (size-adjusted for MCT and 0.5T CT)	104
Table 7.1:	DFRs at the temperatures used for the MCT simulations.....	109
Table 7.2:	Location of initiation region and K_{Jc} , num for simulations PCZ18_-60_1 and PCZ18_-60_2.....	112
Table 7.3:	Average and median experimental and numerical fracture toughness values and corresponding standard deviations at each temperature [99].....	115
Table 7.4:	Cohesive element cluster sizes and corresponding ductile fracture area segments with fractions of the total ductile fracture area	116
Table 7.5:	Average and median numerical fracture toughness values and corresponding standard deviations at -60°C using cohesive element clusters of constant and variable size.....	117
Table 7.6:	Parameters of the numerical and experimental three-parameter Weibull distributions and the distribution assumed in the ASTM E1921 standard at -60°C [99].....	118
Table 7.7:	Minimum required number of specimens for calibrating the probabilistic CZM at three temperatures within the DBT region [99]	121
Table A.1:	Measured dimensions of the smooth round bar specimens.....	141
Table A.2:	Measured dimensions of the notched round bar specimens with 0.1 mm notch root radius.....	142
Table A.3:	Measured dimensions of the notched round bar specimens with 0.2 mm notch root radius.....	143
Table A.4:	Measured dimensions of the miniaturized CT specimens	144
Table A.5:	Flow curve data used as material input for the FE-simulations	146

Table A.6: Average true stresses and average true strains at fracture obtained from the SRB tests used for the cohesive strength calibration.....	147
Table A.7: Average true stresses and average true strains at fracture obtained from the 0.1NRB tests used for the cohesive strength calibration.....	147
Table A.8: Average true stresses and average true strains at fracture obtained from the 0.2NRB tests used for the cohesive strength calibration.....	148
Table A.9: Results of the valid MCT tests within the DBT region following ASTM E1921.....	148
Table A.10: Results of the MCT tests on the upper shelf following ASTM E1820	149
Table A.11: Cleavage initiation site locations and numerical maximum principal stress and triaxiality values at the fracture points.....	149
Table A.12: Distribution of the fracture modes on the fracture surfaces of the MCT specimens tested within the DBT region and corresponding ductile fracture ratios	149
Table A.13: Cohesive strength and maximum triaxiality at fracture obtained from the SRB and NRB simulations.....	150
Table A.14: Load line displacement LLD , force F , crack extension Δa and J determined at the point of unstable fracture from the MCT, 0.5T and 1T CT simulations at -60, -70 and -80°C	151
Table A.15: Numerical fracture toughness results from the probabilistic simulations with a constant cluster size of 18x50 μm	151

Abbreviations and notation

Abbreviations

ASME	American Society of Mechanical Engineers
ASTM	American Society for Testing and Materials
CIEMAT	Centre for Energy, Environmental and Technological Research in Spain
CT	Compact tension specimen
CZM	Cohesive zone model
DBT	Ductile-to-brittle transition
DBTT	Ductile-to-brittle transition temperature
EDX	Energy-dispersive X-ray
FE	Finite element
GTN	Gurson-Tvergaard-Needleman
J-R	Crack growth resistance (curve)
MCT	Miniaturized compact tension specimen with a thickness of 4 mm
NPP	Nuclear power plant
NRB	Notched round bar specimen
RA	Reduction of area
RPV	Reactor pressure vessel
RT	Room temperature
SEM	Scanning electron microscopy
SRB	Smooth round bar specimen
SSTT	Small specimen test technique
TSL	Traction-separation-law
UTS	Ultimate tensile strength

Notation

Symbol	Description	Unit
α	Constant depending on specimen type	-
Γ	Integration path	mm
Γ_c	Cohesive energy	N/mm
$\Gamma_{c,adj}$	Size-adjusted cohesive energy	N/mm
$\Gamma_{c,MCT}$	Cohesive energy calibrated for the MCT geometry	N/mm
δ	Separation	mm
δ_1, δ_2	TSL shape parameters	-
δ_c	Critical separation	mm
δ_N	Normal separation	mm
δ_T	Tangential separation	mm
ε_{eng}	Engineering strain	-
$\dot{\varepsilon}_p$	Plastic strain rate tensor	-
$\varepsilon_{p,eq}$	Equivalent plastic strain	-

$\dot{\varepsilon}_{p,eq}$	Equivalent plastic strain rate	1/s
ε_t	True strain	-
$\varepsilon_{t,avg}$	Average true strain	-
Δa	Ductile crack extension	mm
Δa_{max}	Crack extension measurement capacity of a specimen	mm
η	Dimensionless constant	-
ν	Poisson's ratio	-
Π	Elastic strain energy	Nmm
ρ	Curvature radius in the neck of an SRB specimen	mm
σ	Stress	MPa
$\sigma_1, \sigma_2, \sigma_3$	Principal stresses	MPa
σ_c	Cohesive strength	MPa
σ_{ax}	Axial stress	MPa
σ_{eng}	Engineering stress	MPa
σ_{eq}	Von Mises equivalent stress	MPa
σ_h	Hydrostatic stress	MPa
$\sigma_{K_{Jc,1T}}$	Standard deviation of the size-corrected fracture toughness	MPa \sqrt{m}
σ_N	Normal stress	MPa
σ_t	Uniaxial true stress	MPa
$\sigma_{t,avg}$	Average true stress	MPa
σ_{YS}	Yield strength	MPa
$\sigma_{YS,eff}$	Effective yield strength	MPa
τ	Shear stress	MPa
a	Crack length	mm
a_0	Initial crack length	mm
A	Crack area	mm ²
b	Ligament length	Mm
b_0	Initial ligament length	Mm
B	Thickness of fracture mechanics specimen	mm
B_{1T}	25 mm thickness of a standard-sized fracture mechanics specimen	mm
B_{MCT}	4 mm thickness of an MCT specimen	mm
c	Distance between pin holes and front face of a CT specimen	mm
CHD	Crosshead displacement	mm
d_0	Initial diameter of a round bar specimen	mm
d_{min}	Minimum diameter of a round bar specimen	mm
D	Round bar specimen diameter	mm
D_N	Diameter at notch	mm
DFR	Ductile fracture ratio	-
E	Young's modulus	GPa
F	Force	N
FFD	Front face displacement	mm
G	Energy release rate	N/mm
G_I	Mode I energy release rate	N/mm
G_{Ic}	Critical Mode I energy release rate	N/mm
h	Stress triaxiality	-
H	Hight of fracture mechanics specimen	mm
J	J-integral	N/mm
J_{el}	Elastic part of the J-integral	N/mm

J_c	Critical J-integral	N/mm
J_{Ic}	Critical J-integral at the point of crack initiation	N/mm
J_{max}	J-integral measurement capacity of a specimen	N/mm
J_p	Plastic part of the J-integral	N/mm
$J_{p,0}$	Plastic part of the J-integral before correcting for crack growth	N/mm
J_Q	Provisional fracture toughness value at crack initiation	N/mm
K_0	Weibull scale parameter	$MPa\sqrt{m}$
K_I	Mode I stress intensity factor	$MPa\sqrt{m}$
K_{Ic}	Mode I plane strain fracture toughness	$MPa\sqrt{m}$
K_{Jc}	Fracture toughness determined from the J-integral	$MPa\sqrt{m}$
$K_{Jc,1T}$	Fracture toughness size corrected to 25 mm specimen thickness	$MPa\sqrt{m}$
$K_{Jc,med}$	Median fracture toughness	$MPa\sqrt{m}$
$K_{Jc,num}$	Numerical fracture toughness	$MPa\sqrt{m}$
$K_{Jc,num,adj}$	Size-adjusted numerical fracture toughness	$MPa\sqrt{m}$
K_{min}	Lower-bound fracture toughness	$MPa\sqrt{m}$
K_Q	Provisional fracture toughness value	$MPa\sqrt{m}$
L	Round bar specimen length	mm
L_{pix}	Pixel length	μm
LLD	Load line displacement	mm
m	Weibull modulus	-
p_f	Cumulative failure probability from the Weibull distribution	-
r	Round bar specimen radius	mm
r_N	Notch root radius	mm
R	Rotation factor	-
R_p	Plastic zone size	mm
s	Arc length	mm
t	Surface traction vector	MPa
T	Temperature	$^{\circ}C$
T_0	Reference temperature from the Master Curve concept	$^{\circ}C$
$T_{0,num}$	Numerical reference temperature	$^{\circ}C$
\mathbf{u}	Displacement vector	mm
u_1	Displacement in crack growth direction	mm
u_2	Displacement in crack opening direction	mm
U_p	Plastic part of the strain energy	Nmm
w	Elastic strain energy density	N/mm^2
W	Width of fracture mechanics specimen	mm
Y	Geometry factor	-

1 Introduction

Nuclear power plants (NPPs) are an essential factor in achieving the transition towards sustainable energy and a carbon-neutral economy. The success of this transition depends on the long-term operation of existing Generation II reactors and newly built Generation III reactors. The reactor pressure vessel (RPV) contains the reactor core and is an integral part of most currently active nuclear power reactors. It is crucial for nuclear safety as it shields the environment from radiation that results from nuclear fission within the reactor core. The RPV cannot be replaced, and failure of the vessel must be prevented under all circumstances, for example in the event of accidents. Due to their favorable mechanical and physical properties, RPVs are usually made from low-alloy ferritic steels. The main drawback of those materials is that with increasing neutron fluence, their ductile-to-brittle transition temperature (DBTT) is shifted towards higher temperatures. This shift can pose a risk for the safe operation of the reactor due to embrittlement of the RPV. Therefore, periodic testing of the RPV material for its fracture-mechanical behavior to monitor the toughness degradation is mandatory for safe long-term operation [1–3].

This PhD program is part of the FRACTESUS project [4,5], which is aimed at demonstrating and validating the use of small specimens for fracture toughness evaluation of RPV steels in the ductile-to-brittle transition (DBT) region. Small specimen testing has become a necessity to increase the service lifetime of existing Generation II reactors, as the amount of irradiated standard-sized specimens available from surveillance programs is severely limited [6,7]. It is planned to increase the number of available specimens by producing sub-sized specimens from the broken halves of standard-sized Charpy impact and fracture mechanics specimens that have already been tested in monitoring programs. From a manufacturing perspective, eight miniaturized compact tension specimens (MCT; also 0.16T CT) with a thickness of 4 mm can be produced from one broken Charpy specimen [8]. Additional benefits of small specimens are their reduced active mass, which may allow for easier handling, and their reduced volume, increasing the number of specimens that can be irradiated in a reactor at the same time. However, small specimen testing poses challenges related to size-dependent effects that make it impossible to directly compare fracture toughness obtained from miniaturized specimens to standard-sized specimen results [9]. In addition, those effects often lead to an increased number of specimens required for the determination of valid fracture toughness data when applying internationally accepted testing standards such as ASTM E1921 [10]. Therefore, it is of great interest to nuclear regulatory bodies and NPP operators to be able to quantify and predict those size-dependent effects to ultimately reduce the number of specimens required for fracture toughness evaluation.

1.1 Objective

The primary objective of this PhD program is to numerically predict the fracture toughness of an RPV steel in the DBT region using a cohesive zone model (CZM; Section 2.4) based on small specimen test results. Thereby, one goal is to investigate the effects of specimen size on fracture toughness measurements in this temperature region. The parameter identification method by Mahler & Aktaa (2014, 2016) [11,12] is applied and extended to develop a novel probabilistic CZM approach that allows the prediction of the transition behavior of ferritic steels from a limited amount of specimens. In addition to predicting the fracture toughness transition curve, the approach is focused on modeling the statistical

scatter of fracture toughness observed in experiments. The feasibility of the approach is to be measured by the quality of its predictions and the amount of testing material required compared to fracture mechanics testing following the ASTM E1921 standard.

In a first step, fracture mechanics tests on the RPV steel SA-508 Cl.3 are performed using MCT specimens to determine the fracture toughness transition curve (Master Curve) according to ASTM E1921. The viability of small specimen testing is discussed and recommendations for optimal test temperature selection are given. In addition, analyses of the fracture surfaces of the MCT specimens are carried out by means of scanning electron microscopy (SEM) to quantify the amount of slow-stable crack growth prior to unstable fracture and to locate and classify cleavage initiation sites. The initiation site locations are related to numerically determined stress fields to make statements about the influence of geometric effects on cleavage fracture.

A large part of this thesis is the determination and calibration of material parameters to be used as input data for the finite element (FE) simulations. Due to the large inelastic deformations that occur during fracture mechanics testing of ductile materials, an extensive mechanical characterization of the plastic flow behavior of the given RPV steel at multiple temperatures from the lower shelf to the upper shelf is required. Careful calibration of the parameters of the CZM is performed within the DBT region and on the upper shelf to be able to accurately simulate slow-stable crack growth and unstable fracture. The material models are validated using experimental results obtained from small specimens.

The CZM parameters calibrated using small specimens are first applied to standard-sized CT specimen geometries to evaluate the influence of specimen size on the fracture behavior within the DBT region. Subsequently, mesoscale modeling of the cohesive zone based on fractographic analyses of the sub-sized specimens is performed for the probabilistic fracture simulations. An advantage of the probabilistic CZM is that the fracture behavior at any temperature in the lower DBT region can be predicted using only two sets of cohesive zone parameters, one for ductile fracture and one for brittle (unstable) fracture. At temperatures between the calibration points, the ratio of ductile and brittle cohesive zone properties is interpolated. The probabilistic CZM is expected to offer the possibility of detailed numerical characterization of the statistical fracture-mechanical behavior of ferritic steels in the transition region. In the future, the approach may contribute to a reduction of the amount of material used for the evaluation of the fracture toughness Master Curve of RPV steels.

1.2 Structure of this thesis

The current state of research on the fracture mechanics concept of fracture toughness, its experimental determination, and the application of the CZM for the simulation of brittle and ductile fracture is presented in Chapter 2. Furthermore, the mechanisms of cleavage fracture and ductile tearing, as well as their distinctive appearances on fracture surfaces are explained. Special focus is placed on the statistical distribution of fracture toughness within the DBT region.

In Chapter 3, the approach followed in this work for the simulation of fracture toughness using the CZM, based on small specimen tests, is presented. A distinction is made between deterministic modeling, where a single set of cohesive zone parameters is used to simulate fracture, and probabilistic modeling, where the cohesive zone is modeled on the mesoscale using two sets of parameters.

The experimental testing required for the development of the material models for the numerical simulations is described in Chapter 4. From the small specimen fracture mechanics tests within the DBT

region, the Master Curve is evaluated according to ASTM E1921. The viability of small specimen testing is discussed considering the number of specimens required for the determination of a valid reference temperature. In addition, the results of the fractographic analyses of the broken specimens are described and discussed.

Based on the small specimen tests performed in Chapter 4, the identification of the CZM parameters by means of numerical simulations is explained in Chapter 5. The triaxiality-dependent cohesive strength is calibrated from tensile test results, while the cohesive energy is used as a fitting parameter to accurately simulate the MCT tests carried out within the DBT region and on the upper shelf.

In Chapter 6, the generated material models are used to simulate standard-sized CT specimens. The predicted fracture toughness is compared to the small specimen results and the effects of specimen size on the fracture toughness are discussed under consideration of literature data. Thereby, the advantages and limitations of the applied approach are debated.

The application of the probabilistic CZM approach to predict the transition curve of SA-508 C1.3 is described in Chapter 7. The Master Curve concept is applied to the statistically distributed fracture toughness values obtained from the simulations and the resulting reference temperature is compared to the value obtained from experiments. In addition, the scatter of the numerically determined fracture toughness values is compared to the experimental scatter, and measures to increase the predicted scatter are presented.

In Chapter 8, evaluates the results achieved within the framework of this PhD program and the feasibility of the developed probabilistic approach is discussed regarding its potential use within the nuclear energy industry. The thesis is summarized in Chapter 9 and an outlook is given for possible future research activities.

2 State of research

Fracture mechanics is the theoretical basis to describe the mechanical behavior of cracked materials under applied load. To be able to make assumptions about the structural integrity of cracked bodies, fracture-mechanical analyses involve the assessment of the load at the crack tip and subsequent comparison to a characteristic material parameter. The mechanical stress field at the crack tip depends on the applied external load, the geometry of the structure and the size and geometry of the crack. The characteristic material parameter that represents the resistance to crack extension is called fracture toughness [13]. It may be determined by experimental testing of standardized specimens either for materials that fracture under linear-elastic conditions or for fracture processes that are dominated by elasto-plastic material behavior [14]. Several internationally accepted testing standards exist to determine fracture toughness for brittle or ductile materials and, in the case of specific metals, within the DBT region. Within this temperature region in particular, experimental fracture toughness data is subject to statistical scatter and geometric influences that require special consideration when using miniaturized specimens. While there are stochastic models that successfully describe the scatter of fracture toughness, the effect of specimen constraint remains a major focus of international research efforts in this field [15–17].

In addition to experimental testing, several numerical approaches exist to predict fracture toughness based on the finite-element-method. Besides micromechanically motivated approaches such as the GTN model for ductile fracture [18–20], which is based on Gurson’s flow function [21], and the Beremin model for brittle fracture [22], which is based on Weibull statistics, one of the most commonly used approaches is the phenomenological cohesive zone model (CZM). The CZM uses a traction-separation-law (TSL) to relate the stress in front of the crack tip (traction) to the opening of the crack planes (separation). This allows for crack propagation to be simulated in any structure. The CZM has, so far, almost exclusively been used to simulate ductile or brittle fracture in a deterministic way. A CZM that describes the statistical fracture behavior of ferritic steels within the DBT region has yet to be proposed.

In the following sections, the state of research on fracture toughness (Section 2.1), its experimental determination according to international testing standards (Section 2.2), the relevant fracture mechanisms (Section 2.3) and the cohesive zone model (Section 2.4) are described in detail. A particular focus is on the fracture behavior of ferritic steels within the DBT region, including the description of the statistical scatter of fracture toughness observed in experiments.

2.1 Fracture toughness

In 1957, Irwin [23] calculated the Mode I stress field around a crack tip for a linear-elastic material. Mode I fracture, as shown in Figure 2.1 (a), is the crack opening mode where the two crack surfaces move away symmetrically with respect to the undeformed crack plane (xz -plane) [24]. The components of the near-crack stress field for a center-cracked infinite plate are given by

$$\begin{Bmatrix} \sigma_x \\ \sigma_y \\ \tau_{xy} \end{Bmatrix} = \frac{K_I}{\sqrt{2\pi r}} \cos(\varphi/2) \begin{Bmatrix} 1 - \sin(\varphi/2) \sin(3\varphi/2) \\ 1 + \sin(\varphi/2) \sin(3\varphi/2) \\ \sin(\varphi/2) \cos(3\varphi/2) \end{Bmatrix}. \quad (2.1)$$

In the equation, σ denotes the normal stress, τ the shear stress, r is the radial distance from the crack tip and φ is the angle around the crack tip from the xz -plane. In Figure 2.1 (b) the center-cracked infinite plate under load is shown. The amplitude of the crack tip stress field is characterized by the Mode I stress intensity factor K_I , which depends on the geometry of the structure, the crack length and loading. The stress intensity factors for Mode II and Mode III fracture are not discussed here as they are not relevant for this work. From Equation (2.1), K_I can be determined for the center-cracked infinite plate with $\varphi = 0$ [14]:

$$K_I = \lim_{r \rightarrow 0} \sqrt{2\pi r} \sigma_y. \quad (2.2)$$

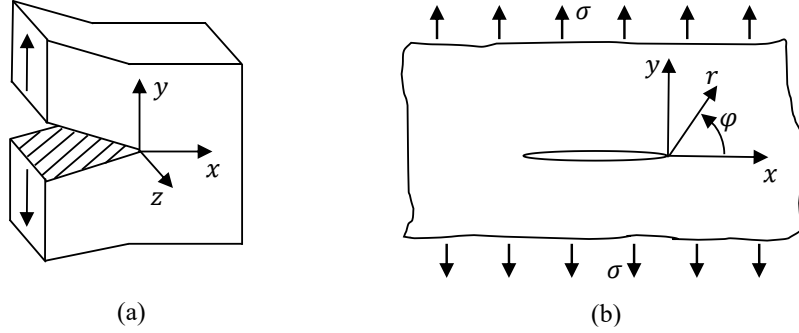


Figure 2.1: Mode I crack loading (a) and center-cracked infinite plate under load (b) adapted from [14]

The expressions in Equation (2.1) hold for any cracked body undergoing Mode I loading. The difference is that the value for K_I changes when other cracked structures than the center-cracked infinite plate are considered [24]. It is therefore necessary to introduce a dimensionless geometry factor Y to the general expression of the stress intensity factor:

$$K_I = \sigma \sqrt{\pi a} Y. \quad (2.3)$$

In case of fracture mechanics specimens, the geometry factor depends on specimen width W and crack length a . Correlations for Y exist for different geometries of fracture mechanics specimens.

From Equation (2.1) it can be deduced that for any given $K_I > 0$, the stress becomes infinite when r approaches zero. Materials react to the high stresses at the crack tip by inelastic deformations and/or debonding. If the size of this plastic zone is small compared to the region dominated by K_I , the state within the plastic zone can indirectly be characterized by the stress intensity factor [14].

Based on the theory that the stress field around a crack tip is only determined by the stress intensity factor, Irwin (1957) [23] proposed a fracture criterion which states that crack growth occurs once K reaches a critical value. The criterion for Mode I fracture is given by

$$K_I = K_{Ic}, \quad (2.4)$$

where K_{Ic} is the critical value of K_I at fracture, called fracture toughness [24]. K_{Ic} is a temperature-dependent material property which defines a material's resistance against crack extension under plane-strain conditions, i.e., for sufficiently thick structures.

2.1.1 Energy release rate

In linear-elastic fracture mechanics an equivalent approach to Irwin's fracture criterion exists, which is based on energetic considerations first proposed by Griffith (1921) [25]. During crack advance, the

elastic strain energy stored within a loaded structure decreases. The released energy is available for the formation of the two fracture surfaces. An energy release rate G can be defined that represents the decrease in elastic strain energy per increase in crack area for a plane problem:

$$G = -\frac{d\Pi}{dA}. \quad (2.5)$$

In this equation, $d\Pi$ is the released elastic strain energy and dA is an infinitesimally small extension of the crack area. For a cracked structure loaded under Mode I conditions, the energy release rate can be expressed in terms of the stress intensity factor:

$$G_I = \frac{(1 - \nu^2)K_I^2}{E}. \quad (2.6)$$

Here, E denotes Young's modulus and ν is Poisson's ratio. A critical energy release rate G_{Ic} can be defined that represents the elastic strain energy required for crack extension:

$$G_I = G_{Ic}. \quad (2.7)$$

Within the framework of linear elastic fracture mechanics, Irwin's K -criterion and Griffith's energy criterion are equivalent and the fracture toughness can be expressed in terms of the critical energy release rate [14]:

$$K_{Ic} = \sqrt{\frac{E G_{Ic}}{(1 - \nu^2)}}. \quad (2.8)$$

2.1.2 J-integral

For ductile materials under sufficiently high loads, the stress field close to the crack tip is no longer dominated by K as the plastic zone is no longer small compared to the dimensions of the crack. Therefore, Irwin's stress intensity factor does not represent the strength of the stress field under large-scale yielding conditions. As many engineering materials show significant inelastic deformation before fracture, a parameter is required that can be used to describe the fracture behavior of ductile materials.

The J-integral is a concept that is equivalent to K and G in linear-elastic fracture mechanics but has the advantage that it can be applied also to inelastic material behavior [14]. In 1968, Rice [26] introduced the J-integral as a contour integral that encloses the crack front to determine an energy quantity that describes the elasto-plastic behavior of ductile materials close to the crack tip. The J-integral

$$J = \int_{\Gamma} \left(w dy - \mathbf{t} \frac{\partial \mathbf{u}}{\partial x} ds \right) \quad (2.9)$$

characterizes the stress field around the crack tip and is therefore equivalent to the energy release rate during crack growth. In Equation (2.9), w denotes the elastic strain energy density, \mathbf{t} is the surface traction vector on the arbitrary volume bounded by Γ , \mathbf{u} is the displacement vector and s is the arc length. The contour integral around a crack tip is shown in Figure 2.2 including the relevant quantities to determine J .

Since the J-integral corresponds to the energy release rate during crack growth in an elastic material, it can be transformed into the stress intensity factor for Mode I loading under plane strain conditions:

$$J = G_I = \frac{(1 - \nu^2)K_I^2}{E}. \quad (2.10)$$

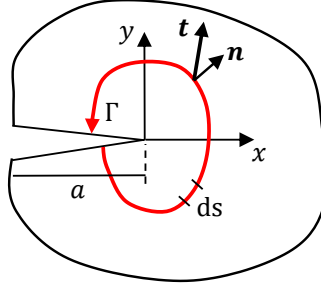


Figure 2.2: Contour integral to determine J adapted from [27]

J can further be applied as a fracture parameter and an equivalent fracture criterion for Mode I,

$$J = J_{Ic} = G_{Ic}, \quad (2.11)$$

can be defined. Therefore, crack propagation initiates once J reaches the critical value J_{Ic} [27].

In an elasto-plastic material, much of the absorbed elastic strain energy is not recovered when the crack grows but is dissipated by plastic deformation. A direct relationship between J , load and crack length is not available. One way to obtain J for an elasto-plastic material is to determine the stresses, strains and displacements numerically along a contour around the crack tip and calculate Equation (2.9) as a line integral. A way to determine J directly from the load-displacement curve of a fracture mechanics test was shown by Rice et al. (1973) [28]. They separated J into an elastic and a plastic part,

$$J = J_{el} + J_p, \quad (2.12)$$

where J_{el} is determined using Equation (2.10) and J_p can be calculated by

$$J_p = \frac{\eta U_p}{Bb}. \quad (2.13)$$

In this equation, U_p is the plastic part of the strain energy absorbed by the specimen, which is equivalent to the plastic part of the area under the load-displacement curve. η is a dimensionless constant, B is the specimen thickness and b is the ligament length [29]. A fracture toughness equivalent to the critical stress intensity factor for elastic materials can then be defined for elasto-plastic materials using the critical J-integral at the onset of unstable fracture:

$$K_{Jc} = \sqrt{\frac{EJ_c}{(1 - \nu^2)}}. \quad (2.14)$$

2.1.3 Ductile-to-brittle transition in metals

The ductile-to-brittle-transition (DBT) refers to the phenomenon where the fracture mode in specific metals changes between slow-stable fracture and fast, unstable fracture depending on environmental conditions such as temperature and neutron irradiation. At low temperatures, the brittle low-energy fracture mode occurs, while at high temperatures the ductile high-energy fracture mode is present. Therefore, metals that exhibit a DBT have a high fracture toughness at temperatures above the ductile-

to-brittle transition temperature (DBTT) and a low fracture toughness below the DBTT. This is shown in Figure 2.3.

Most metals with a face-centered cubic (FCC) lattice structure are intrinsically ductile and do not show transition behavior. In contrast, BCC metals, such as ferritic steels, usually exhibit steep transition behavior with a well-defined DBTT, which is shown schematically in [30]. In those materials, the transition is controlled by the dominance of either cleavage fracture or dislocation nucleation and movement [30]. With increasing temperature, slip systems within the crystalline structure are activated and dislocation movement is facilitated. Energy that would otherwise be available for cleavage fracture is dissipated by plastic deformation. Consequently, the fracture toughness increases with increasing temperature. Exposition to neutron radiation causes the DBTT to be shifted towards higher temperatures due to defects in the lattice structure caused by irradiation. The defects prevent the movement of dislocations and thereby limit the material's ability to plastically deform. This is the main cause for embrittlement of the ferritic steels used for reactor pressure vessels in nuclear power plants [1].

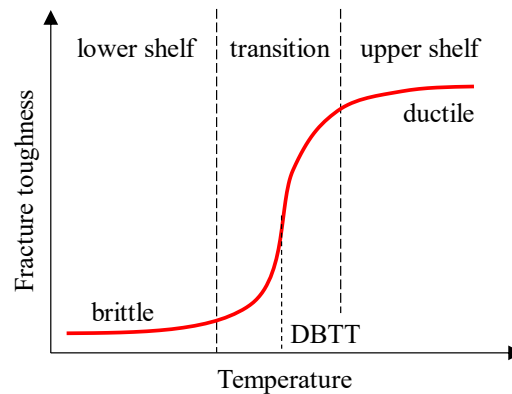


Figure 2.3: Ductile-to-brittle transition of fracture toughness of a BCC metal [30]

Another aspect of the transition behavior of BCC metals is the inherent scatter of fracture toughness within the DBT region. According to the critical tensile stress criterion [31], unstable fracture is assumed to occur when the tensile stress in front of the crack tip enables an existing defect to propagate through the entire structure. Such flaws can be inclusions of brittle particles, voids or grain boundaries among others. Due to the random distribution of critical defects within a material, it was shown that cleavage fracture in ferritic steels is of a statistical nature [32,33]. Therefore, fracture-mechanical investigations within the DBT region require the consideration of the statistical effect on fracture toughness measurements.

2.1.4 Geometric influences on fracture toughness measurements

Fracture toughness is a material property and must therefore be independent of the geometry and size of the structure under consideration. However, as explained in the previous section, it is not possible to obtain a singular value for fracture toughness from fracture mechanics tests in the DBT region due to the statistical nature of cleavage fracture. Likewise, small specimens statistically yield larger fracture toughness values as compared to standard-sized specimens. Following the concept of weakest-link statistics [34,35], cleavage fracture is always initiated at a defect of critical size in front of the crack tip. Since large specimens are thicker than small specimens, the likelihood of encountering a critical defect is higher in large specimens. This size effect on fracture toughness is addressed in the ASTM E1921

standard by introducing a size correction formula when specimens of thickness other than 25 mm are tested.

In addition to the size effect, the effect of constraint is another cause for discrepancies between fracture toughness measurements from specimens of different sizes, geometries and crack lengths. The term “constraint” is used to describe the extent of plastic deformation in front of the crack tip of a structure under load. In that sense, specimens that exhibit limited plastic deformation (small-scale yielding conditions, SSY) are referred to as “high constraint” geometries, while specimens without contained plasticity are “low constraint” geometries [36]. The amount of constraint is strongly correlated to the stress state at the crack tip and, consequently, depends on the stress triaxiality h , which is the ratio between hydrostatic stress σ_h and von Mises equivalent stress σ_{eq} :

$$h = \frac{\sigma_h}{\sigma_{eq}} = \frac{\frac{1}{3}(\sigma_1 + \sigma_2 + \sigma_3)}{\sqrt{\frac{(\sigma_1 - \sigma_2)^2 + (\sigma_2 - \sigma_3)^2 + (\sigma_3 - \sigma_1)^2}{2}}} \quad (2.15)$$

The parameters σ_1 , σ_2 , and σ_3 denote the principal stresses. In Figure 2.4 the plastic zone sizes under plane stress and plane strain conditions for a thick plate are shown schematically. Under plane stress conditions, i.e., at the side surfaces of fracture mechanics specimens, a large plastic zone can develop as the deformation of material points in the out-of-plane direction is not constrained. This results in necking of the specimen ahead of the crack tip. In contrast, the constraint in the center region, where plane strain conditions are prevalent, is high since material points cannot deform out-of-plane under symmetric loading. Therefore, a smaller plastic zone is developed under plane strain conditions and blunting of the crack tip is observed [14]. Since less strain energy is dissipated by plastic deformation in the plane strain region, more energy is available for crack growth. Consequently, less load is required to initiate ductile crack extension and the crack growth rate is increased in plane strain as compared to plane stress. The fracture toughness K_{Ic} is defined for pure plane strain as in this condition, the most conservative value is obtained.

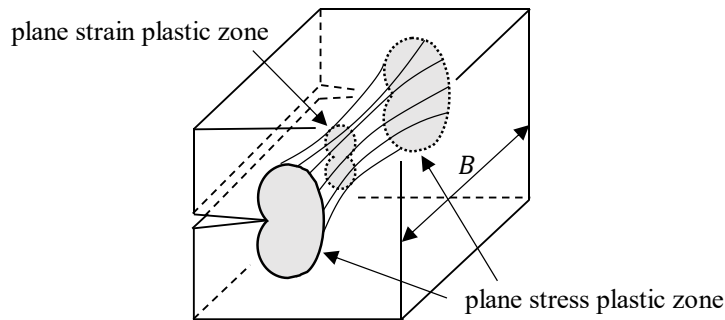


Figure 2.4: Plastic zone size in plane stress and plane strain adapted from [14]

Consequently, different geometries and sizes of fracture mechanics specimens yield different fracture toughness results due to differences in their overall constraint level. Regarding large specimens with a large thickness B , most of the crack front is loaded in plane strain, as opposed to small, thinner specimens, where a significant fraction of the crack front may not be loaded in pure plane strain. The overall constraint level in small specimens is lower and therefore, when plastic deformation is not limited to a small region relative to the crack size, they yield higher fracture toughness values as compared to large specimens. Additionally, the effect of necking at the crack tip, based on the initial thickness, is pronounced in small specimens. This means that with increased plastic deformation, the constraint in small

specimens is reduced even further. This effect is referred to as “loss of constraint” by many authors [29,37–39].

2.2 Experimental fracture toughness determination

There are several internationally accepted and applied standards for fracture toughness determination of metallic materials published by the American Society for Testing and Materials (ASTM) and the International Organization of Standardization (ISO). This work focuses on the standards published by ASTM. Each standard deals with a specific fracture behavior and the corresponding designations are as follows:

- ASTM E399 – Standard Test Method for Linear-Elastic Plane-Strain Fracture Toughness of Metallic Materials [40]
- ASTM E1921 – Standard Test Method for Determination of Reference Temperature, T_0 , for Ferritic Steels in the Transition Range [10]
- ASTM E1820 – Standard Test Method for Measurement of Fracture Toughness [41]

It is expected that the RPV steel examined in this work will show macroscopic plastic deformation before unstable fracture within the considered temperature range. Therefore, the ASTM E399 standard is not described further. As the designation suggests, the ASTM E1921 standard is used to determine fracture toughness within the DBT region by evaluating a reference temperature T_0 . This standard is only applicable to ferritic steels such as RPV steels. The ASTM E1820 standard is applied for fracture toughness determination of ductile metals that exhibit significant plastic deformation before the onset of slow-stable and/or unstable fracture.

2.2.1 ASTM E1921 standard for testing in the DBT region

The ASTM E1921 standard is based on the Master Curve concept developed by Wallin (1991) [42]. It covers the determination of a reference temperature T_0 , which characterizes the fracture toughness of ferritic steels that experience cleavage fracture at elastic or plastic K_{Jc} instabilities. Within the standard, requirements are set on specimen size and total number of tests needed to obtain an acceptable characterization of the fracture toughness transition behavior. The statistical size effect described in Section 2.1.4 is treated using weakest-link theory to a three-parameter Weibull distribution of fracture toughness values,

$$p_f = 1 - \exp\left(-\left(\frac{K_{Jc} - K_{\min}}{K_0 - K_{\min}}\right)^m\right) \quad (2.16)$$

where p_f is the cumulative failure probability, m is the Weibull modulus set to a value of 4, K_0 is the scale parameter and K_{\min} is the lower-bound fracture toughness set to $20 \text{ MPa}\sqrt{\text{m}}$. It is assumed that ferritic steels in the transition range have cumulative failure probability distributions of nearly the same shape, independent of specimen size and temperature.

The standard requires testing of fatigue pre-cracked fracture mechanics specimens, such as compact tension (CT) specimens, in a temperature range with an upper limit on constraint loss and a lower limit above which weakest-link statistics can be applied. K_{Jc} values are calculated from Equation (2.14) after determining the elastic and plastic parts of the J-integral (Equations (2.10) and (2.13)). To ensure high-

constraint conditions along the crack front at fracture, a limit on the K_{Jc} values relative to specimen size is imposed. This upper limit is defined by

$$K_{Jc,limit} = \sqrt{\frac{Eb_0\sigma_{YS}}{30(1-\nu^2)}}, \quad (2.17)$$

where b_0 is the initial length of the ligament in front of the crack tip and σ_{YS} is the material's yield strength at the respective test temperatures. Tests that yield a K_{Jc} value exceeding the $K_{Jc,limit}$ at the respective test temperature are censored, meaning that the K_{Jc} result is replaced by the corresponding $K_{Jc,limit}$. A size correction formula is employed to predict the fracture toughness transition curve and tolerance bounds for 25 mm thick (1T) specimens:

$$K_{Jc,1T} = K_{min} + (K_{Jc} - K_{min}) \left(\frac{B}{B_{1T}} \right)^{\frac{1}{4}}. \quad (2.18)$$

In the equation, $K_{Jc,1T}$ denotes the fracture toughness size-corrected to B_{1T} thickness (25 mm) and K_{Jc} is the fracture toughness measurement obtained from a specimen of thickness B .

From the $K_{Jc,1T}$ data set, a provisional value for the reference temperature T_{0Q} is determined in an iterative calculation, for details of which the reader is referred to the ASTM standard. A lower test temperature limit of 50°C below T_0 is specified in the standard to obtain valid test results. Tests that fall below this limit are removed from the data set and do not contribute to the calculation of the next iteration of T_{0Q} . Additionally, it is assumed in the standard that the accuracy of a K_{Jc} result decreases the further the test temperature lies below T_0 . A weighting system is imposed that specifies the required number of test results according to the criterion

$$\sum_{i=1}^3 r_i n_i \geq 1, \quad (2.19)$$

where r_i is the number of uncensored K_{Jc} values within the i -th temperature range listed in Table 2.1, and n_i is the weighting factor for the tests within the same temperature range [10].

Table 2.1: Test temperature range dependent weighting factors used to evaluate the data set size criterion [10]

$T - T_0$ [°C]	n_i [-]
50 to -14	1/6
-15 to -35	1/7
-36 to -50	1/8

If the number of uncensored $K_{Jc,1T}$ measurements is compliant with the minimum size of the data set specified in Equation (2.19), the provisional T_{0Q} value is replaced with the final reference temperature T_0 . The reference temperature is defined as the temperature where the median fracture toughness is equal to $100 \text{ MPa}\sqrt{\text{m}}$. It is assumed that the shape of the lower transition curve is similar for all ferritic steels. With this assumption, the median fracture toughness $K_{Jc,1T,med}$ can be calculated at any temperature T in the transition region using the empirical formula

$$K_{Jc,1T,med} = 30 + 70 \exp(0.019(T - T_0)) \text{ MPa}\sqrt{\text{m}}. \quad (2.20)$$

The transition curve obtained from Equation (2.20) is shown schematically in Figure 2.5 and referred to as Master Curve. It can be used to quantify a transition temperature shift related to microstructural damage mechanisms such as neutron irradiation. Extensive plastic deformation and ductile crack growth beyond censoring limits may precede cleavage fracture as the upper part of the transition curve is approached. Such test data can be handled using the ASTM E1820 standard [10].

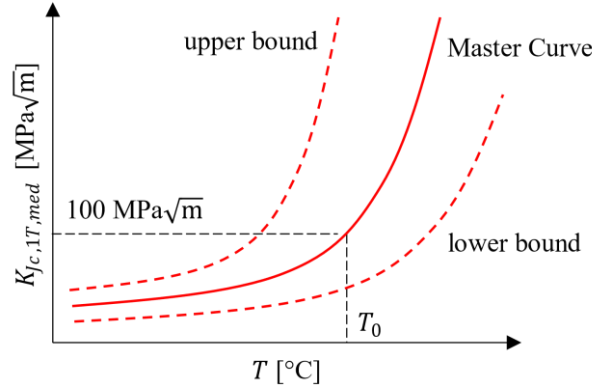


Figure 2.5: Master Curve and upper and lower tolerance bounds [10]

Throughout the past two decades, many authors applied the ASTM E1921 standard to determine the fracture toughness of RPV steels by means of miniaturized fracture mechanics specimens. Sokolov (2017) [9] came to the conclusion that it is possible to obtain a value for T_0 from a relatively small number of sub-sized specimen tests that is in good agreement with the reference temperature obtained from standard-sized specimens. However, he points out that in practice, when the reference temperature is unknown, many more small specimen tests are necessary due to the strict validity requirements of the standard before the final T_0 is determined. In another study, Nanstad and Sokolov (2016) [43] showed that the MCT geometry can be used to obtain a reference temperature within the range of T_0 values determined from various large specimen geometries. In addition, they point out that the scatter of fracture toughness values measured by MCT specimens follows the Weibull distribution, which provides additional validation of this geometry for Master Curve evaluation of RPV steels. Dzuga et al. (2018) [44], Jose et al. (2019) [45] and Lucon et al. (2002) [16] also report good results comparability between miniaturized specimens, including an MCT geometry, and standard-sized specimens tests for the materials investigated. Lucon et al. point out that miniaturized geometries experience significant loss of constraint, which requires testing well below T_0 to obtain enough valid test results. In a 2023 review of MCT testing for fracture characterization of ferritic steels in the DBT region, Sánchez et al. [8] concluded that there is no bias in the reference temperature determined from MCT specimens when compared to larger specimens, but the selection of test temperatures remains a problem due to the reduced measuring capacity of small specimens. This reduced measuring capacity limits the test temperature range where uncensored K_{Jc} results can be obtained. As K_{Jc} values obtained at lower temperatures close to the validity limit contribute less to the data set size requirement specified in the standard, an increasing number of tests is required for the determination of a valid T_0 .

2.2.2 ASTM E1820 standard for testing ductile metals

ASTM E1820 is used to determine fracture toughness of metals that exhibit large-scale yielding and fail by unstable fracture or ductile tearing. Fracture toughness is determined as a point value from tests that are terminated by unstable fracture before ductile tearing is initiated. This case is not explained further

here, as in this work, fracture instability is handled using ASTM E1921. For metals that show stable tearing behavior, a crack resistance curve (J-R curve) is developed from fracture mechanics tests in either a basic procedure or a resistance curve procedure. In the following, only the basic procedure to determine fracture toughness from the J-R curve is described.

The basis procedure requires testing of multiple fatigue pre-cracked fracture mechanics specimens up to different load levels and subsequent unloading. As with ASTM E1921, the J-integral for each test is determined as the sum of an elastic part (Equation (2.10)) and a plastic part (Equation (2.13)) which is obtained from the load-displacement curve. The plastic part J_p is required to be corrected for crack growth using

$$J_p = \frac{J_{p,0}}{1 + \left(\frac{\alpha - 0.5}{\alpha + 0.5} \right) \frac{\Delta a}{b_0}}, \quad (2.21)$$

where $J_{p,0}$ is the plastic part of J before correcting for crack growth, α is a constant depending on specimen type (0.9 for CT specimens) and Δa is the amount of ductile crack extension. The ductile crack extension is the difference between the final physical crack length a_p and the initial crack length a_0 and is determined by analyzing the fracture surface of a specimen using light microscopy or SEM. The crack length is calculated as the average of nine equidistant measurements along the crack front, where the outer two measurements are weighted half the inner measurements. For each test, the crack length corrected J values are plotted in a J - Δa diagram and a regression curve based on a power law is drawn, which is referred to as the J-R curve. The J-R curve is shown schematically for a ductile material in Figure 2.6. With increasing crack length, the J-integral required for further crack extension also increases. In the case of unstable fracture, the slope of the J-R curve becomes zero since no further loading of the crack tip is necessary to propagate the crack. The construction line, exclusion line and offset lines are required for the determination of a provisional J_Q parameter, which is defined as the J value at the intersection of the J-R curve with the 0.2mm offset line.

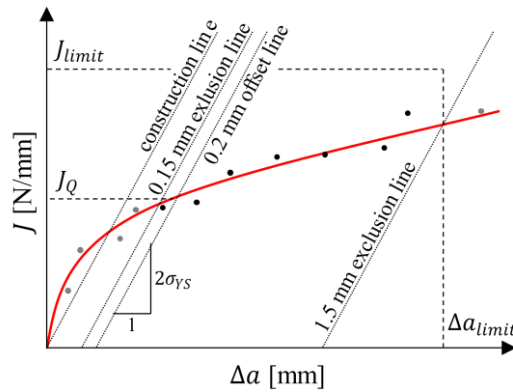


Figure 2.6: J-R curve for determination of fracture toughness of a ductile material adapted from [41]

In the E1820 standard, it is assumed that specimens of a certain size and material have a limited testing capacity regarding J and Δa :

$$J_{\max} = \frac{b_0 \sigma_{YS,eff}}{10} \text{ or } J_{\max} = \frac{B \sigma_{YS,eff}}{10}, \quad (2.22)$$

whichever is smaller, and

$$\Delta a_{\max} = 0.25b_0. \quad (2.23)$$

In Equation (2.22), $\sigma_{Y,\text{eff}}$ denotes the effective yield strength, which is calculated as the average of the 0.2% offset yield strength and the ultimate tensile strength.

Additionally, to ensure high constraint conditions during crack extension, limits are specified on the size and geometry of the specimens used for testing:

$$B > \frac{10J_Q}{\sigma_{Y,\text{eff}}}, b_0 > \frac{10J_Q}{\sigma_{Y,\text{eff}}}. \quad (2.24)$$

If those conditions are met, the provisional J_Q value is replaced with the critical J-integral at the point of crack initiation, J_{Ic} . This value can then be used to calculate the fracture toughness K_{Jc} of the material using Equation (2.14). In the case that the conditions in Equation (2.24) are not met, which is to be expected when testing miniaturized specimens, J_Q cannot be replaced and an invalid value for the fracture toughness, K_Q , is calculated [41].

2.3 Fracture mechanisms

Fracture of metallic materials can be classified into different categories based on the macroscopic behavior, microscopic mechanisms of material separation or type of loading, such as overload, fatigue or creep. According to the amount of plastic deformation present in a structure at fracture, a distinction between brittle fracture, where little to no plastic deformation is present, and ductile fracture, where the structure shows a significant amount of plastic deformation associated with fracture, can be made. This classification is only valid on the macroscopic level, as fracture may be brittle on the microscopic scale, but the entire structure may show significant plastic deformation before fracture. Therefore, a distinction is usually made based on the micro-mechanisms of fracture that take place in the plastic zone ahead of crack tip and lead to crack extension [46].

On the fracture surfaces, distinct microscopic features are observable by means of SEM that can be used to determine the micro-mechanisms responsible for fracture. Ferritic steels, such as RPV steels, usually experience brittle fracture at low temperatures, which is associated with the micro-mechanism of cleavage fracture. Above the DBTT, ferritic steels fracture by ductile tearing, where the nucleation, growth and coalescence of micro-voids is the mechanism responsible for crack extension. Within the lower part of DBT region, both cleavage fracture and ductile tearing are present simultaneously. This is referred to as quasi-cleavage, where cleavage facets visible on a fracture surface combine with regions of micro-void coalescence that can often be identified as tear ridges along the grain boundaries.

By studying the fracture surfaces of fracture mechanics specimens and characterizing the micro-mechanisms responsible for fracture, a better understanding of the material behavior and differences between small and large geometries can be gained [46].

2.3.1 Cleavage fracture

Microscopic cleavage fracture is characterized by material separation through direct rupture of the atomic planes. As this mechanism does not involve plastic deformation, cleavage fracture is also referred to as brittle fracture. It is caused mainly by normal stresses perpendicular to the crack plane [46]. Factors promoting cleavage fracture are low temperatures due to the limited amount of active slip systems,

and high constraint conditions that restrict the material's ability to reduce high stresses through plastic deformation [29].

When the crack path passes along grain boundaries, the micro-mechanism is referred to as intergranular cleavage. On the other hand, transgranular cleavage is observed when the crack passes directly through individual grains, cutting them into two parts. The crack paths of intergranular and transgranular cleavage are shown schematically in Figure 2.7 (a). On the fracture surfaces of ferritic steels that experienced brittle fracture, transgranular cleavage is the most common feature.

In Figure 2.7 (b), a SEM micrograph of multiple transgranular cleavage facets and an intergranular facet on the fracture surface of a RPV steel tested within the DBT region is shown. The transgranular cleavage facets are easily recognizable by sets of fine steps called “river lines” that are created by the passing of the fracture through the individual grains. Within each grain, cleavage planes with different orientations are located. To keep the continuity of the propagating plane, rotation of the cleavage planes is necessary. As this rotation cannot be done abruptly, it is done in consecutive steps that make up the river pattern [46]. It is possible to follow the river pattern “upstream”, in the direction where the branches of the river merge into one stream, to identify the crack growth direction through the grain. The crack path can be traced back to the point where fracture was initiated by following the river pattern across multiple grains. In this way, the fracture initiation sites can be identified.

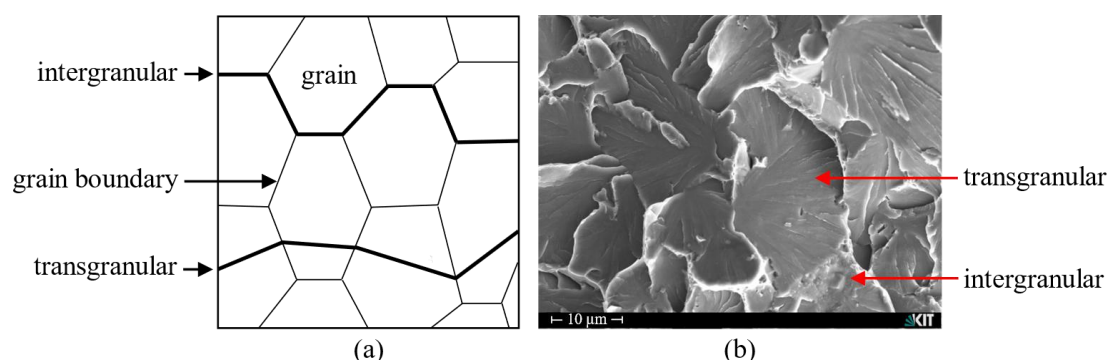


Figure 2.7: Classification of cleavage fracture according to the crack path (a) adapted from [46] and SEM micrograph showing transgranular and intergranular cleavage facets in SA-508 Cl.3 (b)

In some cases, cleavage fracture is initiated by the fracture of brittle inclusions such as sulfides, carbides, or oxides within the surrounding steel matrix. The fractured particles act as stress concentrators and, in the sense of weakest-link statistics, as critical defects limiting the fracture toughness of the material. Cleavage initiation from particles is recognizable by the river pattern pointing from all directions to a clearly defined location on a cleavage facet or grain boundary. If the fractured inclusion at the center of the river pattern is sufficiently large, its chemical composition can be analyzed by means of energy-dispersive X-ray (EDX) spectroscopy.

Cleavage fracture can also be initiated from grain boundaries or within regions of intergranular fracture. In those cases, the river pattern does not point to a singular location, but can be observed to loop around the initiation site without a clear indication of the exact point of fracture initiation.

2.3.2 Ductile tearing

Ductile tearing is a stable fracture mode, meaning that material separation occurs slowly and is accompanied by large plastic deformations. During ductile tearing, crack growth takes place in three consecu-

tive steps: Void nucleation, growth and coalescence. Nucleation of voids is usually initiated at inclusions or second-phase particles. Thereby, material separation is achieved by decohesion of the inclusion or particle and the surrounding matrix. The voids grow by plastic deformation until adjacent voids are large enough to merge into an internal cavity. In Figure 2.8, a SEM micrograph of a cavity formed by coalescence of multiple voids, surrounded by cleavage facets, is shown. The particles that caused void nucleation are clearly visible in the center of the respective voids. Between the cavity and the surrounding cleavage facets, clusters of smaller voids can be seen. The shape and size of the micro-voids are directly related to the shape, size and distribution of the nucleating particles, the ductility of the material and the load application mode [46].

Within the lower part of the DBT region, a limited amount of ductile tearing usually precedes cleavage fracture. The extent of ductile crack growth strongly depends on the material's ability to plastically deform and is consequently dependent on temperature. With increasing temperature, the amount of stable crack extension before initiation of cleavage fracture increases until at a certain temperature, enough constraint is lost through plastic deformation that the conditions for cleavage fracture are no longer met. Above this temperature, ductile tearing is the only fracture mechanism present.

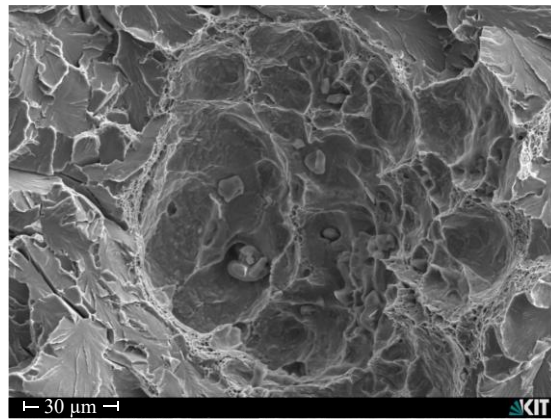


Figure 2.8: Cavity formed by coalescence of multiple voids surrounded by cleavage facets in SA-508 Cl.3

2.4 Cohesive zone model

To simulate the fracture process within the framework of the finite-element-method, it is necessary to introduce a material damage model. Several numerical approaches exist to model crack propagation and predict the fracture toughness of ferritic steels. In general, micro-mechanical and phenomenological damage models are distinguished. The micro-mechanical models are based on local fracture criteria established most often from tests on volume elements [47]. Their parameters characterize the micro-structure of the material and therefore have physical relevance. The most used micro-mechanical damage models include Rousselier and Gurson-type models for ductile damage and the Ritchie-Knott-Rice (RKR) and Beremin models for the prediction of cleavage fracture. In the following, a brief description of these models is given.

Gurson type models, such as the Gurson-Tvergaard-Needleman (GTN) model [18–20], are based on metal plasticity and use Gurson's flow function [21] and a damage parameter to model ductile fracture. The specific void volume fraction is used as the damage parameter, which describes the loss of stiffness resulting from void growth and coalescence in front of the crack tip. Rousselier's original ductile damage model, proposed in 1987 [48], is based on a thermodynamics framework and considers finite strain,

isotropic hardening and cavity growth [49]. It uses a plastic flow potential similar to Gurson's model and a damage variable that describes the porosity of the material. The model can be applied to simulate ductile fracture of uncracked and cracked structures [50]. A disadvantage of both porous metal plasticity models is their strong mesh dependence [51], resulting from the parameters of the models being directly related to the size of the elements in the ligament. Therefore, these models are considered to be inflexible and require a high level of experience to use correctly [52]. They further require several parameters to be calibrated, increasing complexity.

A cleavage fracture criterion that describes the onset of cleavage fracture in terms of a critical stress being sustained over a characteristic distance in front of the crack tip was introduced by Ritchie et al. in 1973 [53] and is known as the RKR model. Ritchie et al. assumed that the measured toughness of a brittle material is not determined by the highest stress at any point, but rather by the volume over which stress is applied [54]. In the original model, the characteristic distance and the critical stress are further assumed to be constant across the temperature range of the DBT region. Therefore, the temperature dependence of the fracture toughness is entirely determined by the temperature dependence of the plastic properties of the material. In the lower shelf region, where the temperature dependence of the yield strength is large, the fracture toughness can be predicted successfully by the RKR model. On the other hand, the variation of the yield strength with temperature is comparably low in the DBT region, leading to a significant underestimation of fracture toughness. Consequently, the model has mainly been used to predict the fracture toughness of steels in the lower shelf region [55]. Yang et al. (2003) [56] introduced a local critical stress to improve the capability of the RKR model to predict the median fracture toughness of RPV steels in the DBT region. They calibrated the characteristic distance by measuring the distance of cleavage initiation sites on the fracture surfaces of fracture mechanics specimens at multiple temperatures. Applying this modified RKR model, it was shown that good predictions of the fracture toughness Master Curve of ferritic steels can be achieved. However, due to the deterministic nature of the RKR model, no predictions of the scatter of fracture toughness in the DBT model can be made.

The Beremin model, introduced in 1983 [22], is derived from the "local approach" to fracture and is commonly used to describe the fracture behavior of ferritic steels in the DBT region. It is based on Weibull statistics and the micro-mechanisms of brittle fracture. It introduces the Weibull stress as a probabilistic parameter that follows a two-parameter Weibull distribution. The Weibull stress is assumed to be the crack driving force, which means that cleavage fracture occurs at a critical value of the Weibull stress corresponding to a given failure probability. Implementing the Beremin model into the framework of the finite-element-method, it is possible to predict fracture toughness by defining conditions leading to material failure [47]. For parameter identification, the model relies on measurements obtained from tensile and fracture mechanics tests [57]. Several modifications of the Beremin model exist, for example to add a strain- or temperature-dependence to the Weibull stress. One disadvantage of the original Beremin model is that, since no material damage is simulated, it can only be used to predict the probability of cleavage fracture initiation. Consequently, it cannot be used to simulate ductile crack extension prior to unstable fracture. However, it can be used in conjunction with a ductile fracture model such as the GTN model, considerably improving predictions [58].

In phenomenological models, which apply the methods of continuum mechanics on a global scale, the evolution of a damage parameter is used as a failure criterion. A frequently and successfully applied phenomenological damage model is the cohesive zone model (CZM). In this model, damage is only considered within a cohesive zone that is connected to the bulk of the material. Failure of the cohesive elements leads to separation of the adjacent continuum elements. This means that crack propagation can

usually only be simulated along pre-defined paths. To simulate an arbitrary crack path, cohesive elements would have to be embedded between all continuum elements around the crack tip, which requires considerable computational resources. However, for the simulation of fracture mechanics tests, a straight crack path is a reasonable assumption.

In terms of its applicability, the CZM has several advantages over the micro-mechanical damage models described above. An important advantage is the mesh-independence of the CZM parameters [59]. This means that, as long as mesh convergence is achieved, changes in element size do not produce different results. In addition, the CZM in its simplest form only requires the identification of two parameters and can be applied to simulate both brittle and ductile fracture behavior on a macroscopic scale. It is noted that, since no microscopic flaws are modeled within the cohesive zone that can act as fracture initiators, the model is not capable of simulating the mechanisms of cleavage fracture observed in physical specimens. To predict unstable fracture of a specimen or structure, a suitable macroscopic failure criterion must be introduced. The CZM can further be used to simulate both uncracked and cracked structures and can theoretically be applied to any solid material. The CZM can be modified to include the dependence of the model parameters on strain-rate, stress triaxiality or hydrogen concentration, among others [60].

In the past, the CZM has been used extensively to simulate ductile and brittle fracture of various materials [12,61–63]. In most cases, either purely ductile or purely brittle fracture was investigated. A so-called unified CZM was proposed by Liu et al. (2013) [64] that can be used for the simulation of both brittle and ductile fracture based on a ductility parameter that characterizes the properties of the cohesive elements. They defined the ductility parameter to be the ratio between the materials yield strength and the tensile strength, meaning that the value of the parameter is 1 for linear elastic materials and between 0 and 1 for ductile materials. While the versatility of the model is an advantage, it cannot be used to predict the fracture toughness scatter of ferritic steels in the DBT region due to its deterministic nature.

Another unified CZM approach for the simulation of RPV steels in the DBT region based on temperature and failure probability dependent cohesive zone parameters was developed by Chakraborty & Biner (2014) [58]. Their procedure requires three calibration points for the cohesive zone parameters, with one on the upper shelf for ductile fracture and two on the lower shelf for cumulative failure probabilities of 5% and 95%. The cumulative failure probabilities are obtained from a three-parameter Weibull distribution (Equation (2.16)). In their study, Chakraborty & Biner evaluated the CZM parameters from experimentally obtained fracture toughness data, but it is noted that the parameters could also be determined from micro-mechanistic simulations of ductile and brittle fracture by considering the underlying microstructures and only using the flow curves. A functional relationship is derived between the CZM parameters and the calibrated values to allow the complete evaluation of the Master Curve within the DBT region. Chakraborty & Biner report numerical fracture toughness values that are comparable to experimental results using CT specimens with 25 mm thickness and single-edge-notched-bend (SENB) specimens. While this unified approach does consider the statistical nature of cleavage fracture by introducing failure probability dependent cohesive zone parameters, the model itself is still deterministic as no stochastic properties are implemented into the cohesive zone. To introduce an uncertainty into the numerically obtained fracture toughness values, spatially varying properties of the CZM must be taken into account.

Due to the advantages of the CZM over the micromechanics-based approaches, especially regarding the applicability for both brittle and ductile fracture behavior, the CZM is used in this work to simulate CT

specimens of different sizes over a wide range of temperatures between the lower shelf and the upper shelf of fracture toughness transition. A few studies on the application of spatially distributed cohesive zone parameters, which have been conducted in the past to simulate the statistical fracture behavior of different materials, are presented in Section 2.4.3.2.

2.4.1 Principle

The CZM has its origin in the strip-yield model proposed by Dugdale (1960) [65], who tried to solve the problem of the stress singularity at the crack tip. The idea of Dugdale's model is shown schematically in Figure 2.9 (a). He introduced a cohesive force in front of the crack tip that prevents the crack from extending and is equal to the yield strength of the material σ_{YS} . Dugdale used the model to analytically characterize the plastic deformation near the crack tip. Its application as a damage model within the FEM occurred substantially later [66].

CZMs in their present form date back to the work of Barenblatt (1962) [67], who replaced the yield strength in Dugdale's model with a cohesive law to model decohesion of atomic bonds [68]. In Figure 2.9 (b), Barenblatt's model is shown schematically. Both models have in common that the area behind the crack tip is traction-free. While in Barenblatt's model the cohesive traction is expressed as a function of the distance from the crack tip, in modern cohesive models the tractions are defined as functions of the separation of the cohesive surfaces. The constitutive law that describes this relationship is called the traction-separation-law (TSL).

Over the last few decades, numerous TSLs have been developed to model ductile and brittle fracture of various materials. Most work on the development of the CZM for the application to metallic materials can be attributed to Needleman (1987) [69] and Tvergaard and Hutchinson (1992, 1994) [70,71] [66].

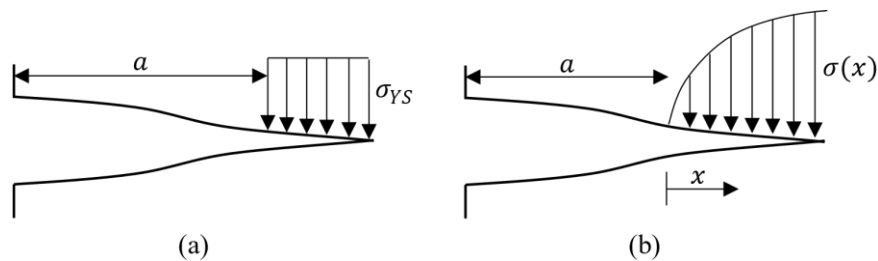


Figure 2.9: Dugdale's model using a constant cohesive traction equal to the materials yield strength (a) and Barenblatt's model using a cohesive traction that depends on the distance from the crack tip (b) adapted from [68]

The basic idea of the CZM for the modeling of ductile fracture is shown in Figure 2.10. The real ductile tearing process (a), consisting of void nucleation, growth and coalescence is modeled by a TSL, simulating material separation directly at the crack tip (b). The cohesive elements, which are placed between the two initially parallel surfaces of the continuum in the ligament, work against the separation of the crack planes until a critical separation is reached. Reaching the critical separation, the cohesive elements “break” and cause the crack to extend. Thereby, damage is limited to the cohesive zone, meaning that no damage must be modeled for the surrounding continuum elements.

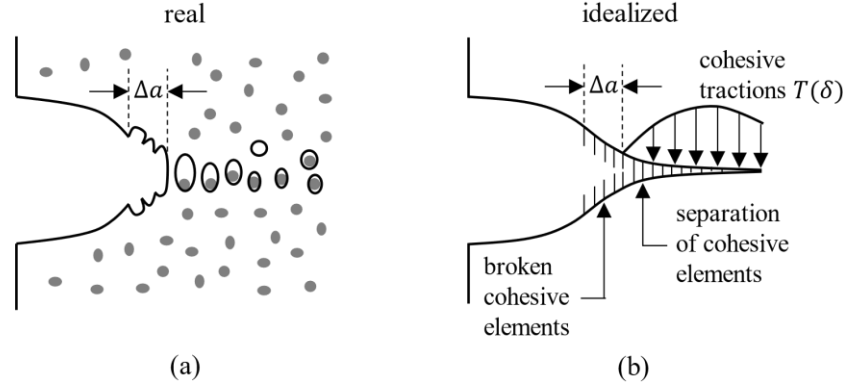


Figure 2.10: Representation of the real ductile fracture process (a) by the CZM (b) adapted from [66]

2.4.2 Traction-separation-laws

The choice of the appropriate TSL for the simulation of a specific fracture mode is one of the key concerns for the application of the CZM. Several TSL shapes are suited for ductile fracture and many authors have successfully used cohesive laws with different TSL shapes for the simulation of the exact same ductile tearing problems. Since the CZM is a phenomenological model and does not simulate the micro-mechanical fracture processes observed in real materials, the TSL can be freely chosen [66]. Although the exact choice of the TSL has a significant impact on the behavior of individual cohesive elements, it was shown by Tvergaard and Hutchinson (1994) [70] that the effect on the macroscopic fracture behavior can be relatively weak when simulating ductile tearing. In the case of quasi-brittle fracture, it is stated by de Borst (2002) [72] that the shape of the TSL plays a much bigger role and is sometimes more important than the value of the cohesive strength.

All TSLs have in common that they can be described by three parameters, of which two are independent:

- Cohesive strength σ_c : Maximum resistance against separation that can be applied by a cohesive element before damage is initiated in the form of stiffness degradation.
- Critical separation δ_c : Displacement of the cohesive surfaces relative to the initial displacement where the cohesive stress reaches zero and the cohesive element fails.
- Cohesive energy Γ_c : Area under the TSL curve and total strain energy absorbed by a cohesive element at the point of failure.

Since only two cohesive zone parameters are independent, the third parameter can be calculated as a function of the other two depending on the shape of the TSL. Besides the cohesive strength, which can be determined from experiments, the cohesive energy is often used as the second parameter due to its physical meaning. The cohesive energy is equal to the J-integral at crack initiation [60].

In Figure 2.11, several TSL shapes are shown that are commonly used to simulate fracture of various materials. The triangular shape (a) is used to simulate unstable fracture modes and was first introduced by Hillerborg et al. (1976) [73] to simulate fracture in concrete. They used an infinite initial stiffness of the TSL, meaning that all inelastic deformation is assumed to be material separation [68]. Thereby, the cohesive surfaces only separate once the cohesive strength is reached. To avoid numerical difficulties, a bilinear TSL with a finite, albeit very high, initial stiffness is often used instead of an infinite initial stiffness.

The exponential (Figure 2.11 (b)) and polynomial (Figure 2.11 (c)) TSL shapes were first used by Needleman in 1987 and 1990 [69,74] to simulate fracture in ductile metals. These TSLs are characterized by a finite initial stiffness and a smooth shape. Tvergaard and Hutchinson (1992) [71] introduced a more versatile TSL with a trapezoidal shape (Figure 2.11 (d)) to simulate ductile tearing. The TSL is similar to the triangular TSL but with a region of constant cohesive stress that is equal to the cohesive strength. Using two additional shape parameters, δ_1 and δ_2 , the initial stiffness, the range of the region of constant cohesive stress and the unloading slope can be defined. The trapezoidal TSL is an extension of the triangular TSL, which is obtained when the same value is chosen for the two shape parameters. Therefore, the same equations can be used to define the respective sections of the TSLs:

$$\sigma = \begin{cases} \sigma_c \frac{\delta}{\delta_1 \delta_c} & \text{for } \delta < \delta_1 \delta_c, \\ \sigma_c & \text{for } \delta_1 \delta_c \leq \delta \leq \delta_2 \delta_c, \\ \sigma_c \left(\frac{\delta_c - \delta}{\delta_c - \delta_2 \delta_c} \right) & \text{for } \delta_2 \delta_c < \delta \leq \delta_c. \end{cases} \quad (2.25)$$

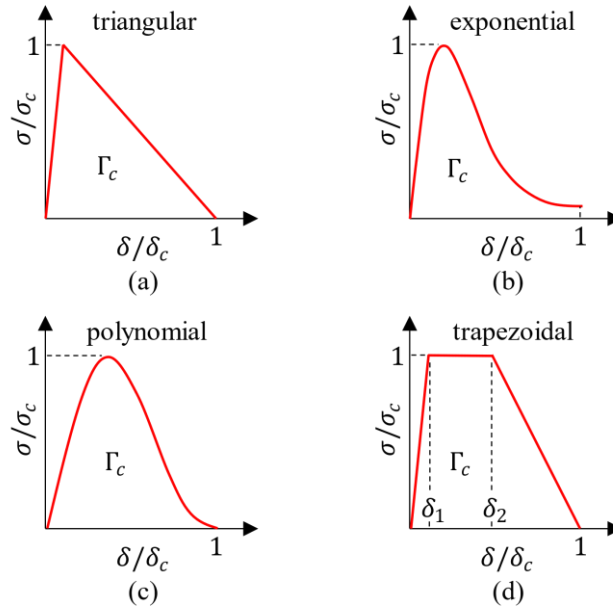


Figure 2.11: Traction-separation-laws commonly used to simulate fracture of different materials [69,71,73,74]

Integration of the TSL yields the cohesive energy:

$$\Gamma_c = \int_0^{\delta_c} \sigma d\delta = \frac{1}{2} \sigma_c \delta_c (1 - \delta_1 + \delta_2). \quad (2.26)$$

The TSL by Tvergaard and Hutchinson is used in this work due to its high versatility for simulating both brittle and ductile fracture processes. The cohesive strength can be calibrated by testing notched round bar specimens and determining the maximum axial stress at the point of fracture [66]. The cohesive energy can then be used as a fitting parameter and the critical separation follows from Equation (4.1). Regarding the shape parameters δ_1 and δ_2 , Scheider (2006) [60] suggests to choose δ_1 as small as possible without introducing convergence problems, whereas δ_2 should be chosen to obtain a moderate slope of the softening region of the TSL.

2.4.3 Modifications to the standard CZM

The CZM in its basic form with constant parameters of the TSL, as presented in the previous section, can be used to simulate ductile and brittle fracture of various materials. Limitations on the applicability of the model exist when different geometries are studied using a single set of cohesive parameters or if the dependence of the fracture behavior on specific field quantities or microstructural features must be considered. For instance, the fracture behavior may depend on the applied strain rate or the distribution of critical defects in front of the crack tip. In such cases, the standard CZM must be modified to include the dependence of the cohesive zone parameters on the respective field quantity or to take into account the spatial variation of fracture-mechanical properties. Previous studies by various authors on the triaxiality dependence of the CZM parameters and the application of spatially distributed parameters to simulate probabilistic fracture behavior are presented below.

2.4.3.1 Triaxiality dependence

Several authors have used triaxiality-dependent cohesive zone parameters to solve the transferability problem and account for the constraint effect observed in ductile fracture. In 2000, Siegmund & Brocks [75] calibrated a triaxiality-dependent CZM by studying material failure on unit cells separated from an actual crack problem. Thereby, they showed that the cohesive strength increases significantly with triaxiality up to a triaxiality of two. At higher triaxialities, the dependence is far less pronounced as the cohesive strength shows saturation behavior. It was further observed that the cohesive energy decreases with triaxiality and shows the same saturation behavior at high triaxialities. Siegmund & Brocks applied the model to simulate ductile fracture in a middle tension (MT) and a CT specimen and compared the J-R curves with results obtained from GTN simulations. They report a good agreement between the models for both the global fracture behavior as well as for local quantities at the crack tip. It was further shown that the inclusion of triaxiality dependence of the cohesive parameters has no influence on the mesh convergence of the FE model. It was concluded that the triaxiality-dependent CZM is promising for the modeling of ductile fracture as it combines the most attractive features of the physically motivated GTN model and the phenomenological CZM.

In a review on phenomenological fracture criteria, Brocks (2005) [76] stated that, while cohesive strength and cohesive energy were found to be triaxiality-dependent, this dependence may be neglected in numerical predictions of the J-R curve when only one specimen geometry is considered. The weak triaxiality dependence of the cohesive energy is assumed to be due to the global plastic strain energy being much greater than the separation energy in the process zone. Li & Yuan (2016) [77] simulated side-grooved CT specimens and also found that the cohesive strength seems more sensitive to the triaxiality than the cohesive energy. They further showed that a linear triaxiality dependence of the cohesive zone parameters significantly improves three-dimensional crack growth predictions over simulations using constant parameters.

Scheider & Brocks (2006) [78] report that by applying a triaxiality-dependent CZM to simulate ductile fracture, the dependence of the fracture behavior on the TSL shape can be reduced, meaning that the same TSL can be used for different geometries and constraint conditions. They further recommended that, when using a constant model, the determination of the cohesive zone parameters should be performed with specimens that have a constraint similar to the structure under consideration. In 2011, Scheider et al. [79] performed ductile fracture simulations on a notched round bar, a middle tension (MT) and a CT geometry made of an aluminum alloy using a triaxiality-dependent CZM. They reported

that the model is able to predict the failure of all simulated structures well, which is not the case for a CZM with constant parameters.

In a study by Chen et al. (2005) [80], a 10 mm thick CT specimen geometry of RPV steel was simulated using constant cohesive zone parameters that were determined by fitting the simulated crack extensions to experimental data. It was found that the experimentally obtained crack front shapes cannot be predicted by the simulations as the simulated crack front shapes show a strong tunneling effect. A better fit between the simulated and experimental crack growth was achieved by reducing both cohesive zone parameters near the side-surface of the specimen, showing their triaxiality dependence. It is further reported that decreasing the cohesive strength results in a decrease of the triaxiality level in front of the crack tip, while decreasing the cohesive energy leads to an increasing triaxiality. Thereby, it was shown that the cohesive zone parameters are not only dependent on triaxiality, but that the triaxiality is also dependent on the cohesive zone parameters.

While several studies exist on the application of triaxiality-dependent cohesive zone parameters for the simulation of ductile fracture, few authors have used a triaxiality-dependent cohesive zone model to simulate unstable fracture. As explained in Section 2.1.4, the constraint of a structure is characterized by the amount of plastic deformation around the crack tip. It is therefore assumed that there is no triaxiality dependence of the cohesive zone parameters for structures that do not show macroscopic plastic deformation before fracture. Mahler & Aktaa (2016) [12] confirmed this assumption by simulating the fracture process in KLST (from the German “Kleinstprobe” meaning “small specimen”) and standard-sized bend specimens of T91 steel both on the upper shelf and the lower shelf using a triaxiality-dependent cohesive strength and a constant cohesive energy. They successfully predicted fracture toughness values in both regimes and conclude that triaxiality dependence of the cohesive strength must be considered if plastic deformation is visible in the global force-displacement curve. It was further shown that a constant cohesive strength yields better results if unstable fracture occurs in the elastic regime. Consequently, for ferritic steels in the DBT region, where both macroscopic plastic deformation and cleavage fracture occur simultaneously, it is necessary to introduce a triaxiality-dependent CZM to simulate different geometries.

In conclusion, the triaxiality dependence of the cohesive strength must be considered for the transferability of the CZM to different geometries if macroscopic plastic deformation is present. As shown by Brocks (2005) [76], the triaxiality dependence of the cohesive energy can be assumed to be negligible due to the plastic strain energy being much larger than the separation energy. In this work, the approach by Mahler & Aktaa is adopted and a triaxiality-dependent cohesive strength with a constant cohesive energy is used for the simulation of fracture mechanics tests in the DBT region and on the upper shelf.

2.4.3.2 Random spatial distribution of CZM parameters

To simulate statistical effects in the fracture behavior of different materials and structures by means of the CZM, some authors have applied spatially distributed cohesive zone parameters. Thereby, a random or stochastic distribution of two or more sets of CZM parameters within the cohesive zone is assumed, resulting in a variation of the fracture parameters that can be compared to the statistical distribution of experimentally obtained values.

Schicker (2005) [81] simulated the statistical failure behavior of quasi-brittle materials assuming a statistical distribution of the local rupture strength as a function of the microstructure. The numerical investigations were performed using both the so-called “chain-of-bundles” model and FE-models based on cohesive elements with a random spatial distribution of the cohesive strength. It was shown that both

the individual and statistical failure behavior can be better predicted by the FE-model. In another study on the effect of microstructural randomness on the fracture of composite laminates, Khokhar et al. (2009) [82] introduced the fracture energy of cohesive elements as a random variable based on Weibull's failure probability distribution (Equation (2.16)). They emphasized the need to account for the microstructural randomness of these laminates as predictions based on uniform failure properties could significantly overestimate the critical value of crack lengths.

The deformation and fracture behavior of components made of fully lamellar TiAl alloy was simulated by Kabir (2008) [83], focusing on the variability of local material properties and their influences on translamellar fracture. Thereby, a stochastic CZM was introduced to capture the scatter of the macroscopic fracture behavior of chevron notched bend specimens based on the distribution of the fracture parameters of individual lamellar colonies. Based on the numerical results, it is concluded that the proposed approach can predict the stochastic nature of crack initiation and propagation as observed in experiments. It is further stated that global specimen failure with stable or unstable crack growth can be explained in terms of local material property variation.

Based on the presented studies, it is concluded that the introduction of a CZM with random spatial distribution of the model parameters can be a viable approach to simulate the statistical nature of fracture in different materials. To the author's knowledge, a probabilistic CZM has so far not been applied to simulate the fracture behavior of ferritic steels within the DBT region. Therefore, an approach to identify spatially distributed parameters for mesoscale modeling of the cohesive zone in an RPV steel is presented in this work.

2.4.4 Implementation

The cohesive elements are implemented into the FE software ABAQUS as a user-defined-element (UEL) subroutine. Originally developed by Scheider in 2006 [60], the Fortran code for the UEL subroutine was modified to incorporate the TSL by Tvergaard and Hutchinson. The UEL subroutine can be used for 2D, axisymmetric and 3D analyses and allows for the definition of dependencies of the cohesive zone parameters on additional field variables such as stress triaxiality, strain rate and hydrogen concentration.

For the sake of clarity, only the 2D case is considered in the following. In addition, since only Mode I loading is relevant for the investigations in this work, the other modes are not discussed here. In Figure 2.12 (a), it is shown how the cohesive elements are embedded as a zero-thickness layer between two layers of continuum elements that make up the bulk of the material. Since the cohesive elements have no thickness, they do not represent an interface made up of a separate material "gluing" the continuum elements together, but rather a process zone where material degradation is localized [84]. Although the cohesive elements have one dimension less than the adjacent continuum elements, they still have an upper and a lower surface that are separated under load. Therefore, each cohesive element has the same number of nodes as the surrounding continuum elements in a structured mesh. In Scheider's UEL subroutine, a linear 3D cohesive element has four integration points.

Normal separation of the surfaces of the cohesive elements, which results from externally applied Mode I loading, is shown in Figure 2.12 (b). The cohesive elements resist the external load by applying a normal stress σ_N in the opposite direction. From the difference of the displacements of the adjacent continuum elements in loading direction, the normal separation is calculated:

$$\delta_N = u_2^{(+)} - u_2^{(-)}. \quad (2.27)$$

In the equation, $u_2^{(+)}$ denotes the displacement of the upper cohesive surface in loading direction and $u_2^{(-)}$ is the displacement of the lower cohesive surface.

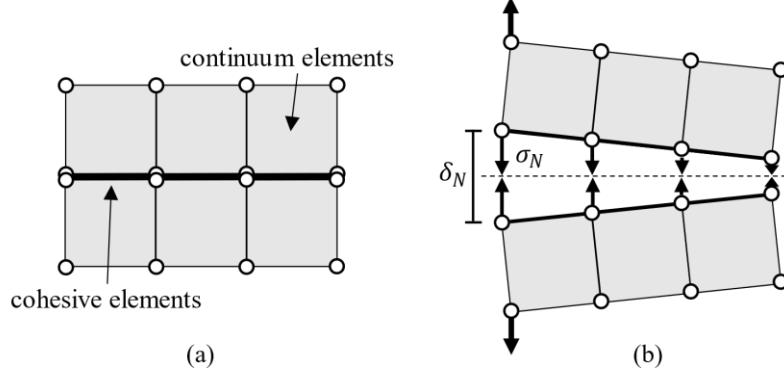


Figure 2.12: Cohesive elements embedded between continuum elements (a) and normal separation of cohesive elements following external Mode I loading (b) [85]

To reduce simulation time and memory usage, it is often useful to reduce the size of the model by introducing symmetry conditions. As the simulation of cracked structures requires a fine discretization to resolve the high stress and strain gradients, the exploitation of model symmetries is particularly important. Fracture mechanics specimens for Mode I testing are symmetric in the thickness and loading directions. Therefore, the model size can be reduced to a quarter specimen geometry. In the FE model of a fracture mechanics specimen, the cohesive elements are usually placed in the crack plane along the ligament, starting at the crack tip.

When dealing with cohesive elements that are placed along a symmetry plane, special considerations must be made regarding their deformations. If the displacement of the lower cohesive surface $u_2^{(-)}$ is constrained, the cohesive element undergoes unsymmetric deformation upon loading. The resulting mixed-mode opening is shown in Figure 2.13 (a). To achieve pure Mode I opening of the cohesive elements, the displacements of the lower cohesive surface nodes must be coupled to the displacements of the upper nodes in loading direction and crack growth direction according to Figure 2.13 (b). This is realized in ABAQUS by applying so-called “constraint equations” to each individual node pair. Establishing nodal constraints introduces additional residual forces, which must be accounted for in the UEL subroutine by adjusting the cohesive strength to one half of the calibrated value [84].

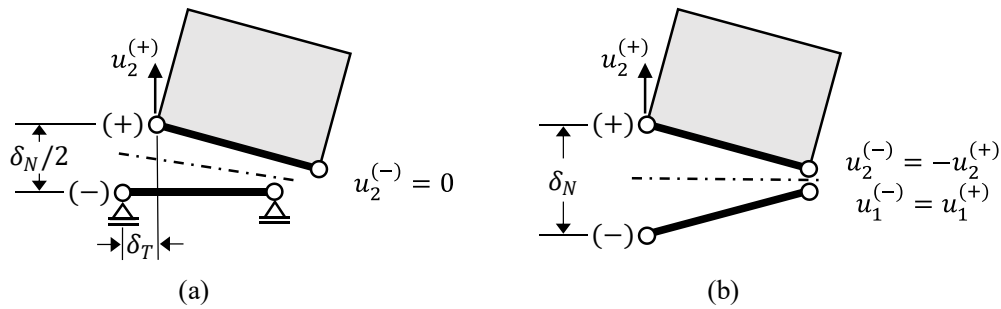


Figure 2.13: Lower cohesive surface constrained by boundary condition (a) and lower cohesive surface constrained by coupled node displacements (b) [84]

Tabular data of cohesive strength, critical separation and triaxiality are passed to the UEL subroutine to account for the triaxiality dependence of the cohesive zone parameters. Thereby, the cohesive strength values are related to a reference cohesive strength and the critical separations are likewise related to a reference value at a certain triaxiality. Linear interpolation is performed between the respective tabular entries and for triaxialities below or above the defined values, the minimum or maximum entries are taken.

3 Approach

In Chapter 1, the objectives of this work were outlined and some of the methods to be used to obtain the required experimental and numerical data were mentioned. One primary objective is the numerical prediction of fracture toughness of standard-sized CT specimens from small specimen test results. To assess constraint differences between miniaturized and standard-sized specimens, the mean fracture-mechanical behavior of the geometries shall be compared. For this purpose, a deterministic cohesive zone model (CZM) is developed within the framework of the finite-element-method. Thereby, as explained in Section 2.4.3.1, the triaxiality dependence of the cohesive strength is considered and a constant cohesive energy is used. The approach to identify the required model parameters from small specimen test results is described in Section 3.1.

The other main objective of this work is the development of a probabilistic cohesive zone approach based on a random spatial distribution of the model parameters in front of the crack tip. With the developed approach, the statistical fracture behavior of an RPV steel within the ductile-to-brittle transition (DBT) region is predicted. As explained in Section 2.4.3.2, spatially distributed cohesive zone parameters have been used in the past to simulate the stochastic fracture behavior of different materials, but have not yet been applied to ferritic steels in the DBT region. Since the approach to determine the individual cohesive zone parameters remains the same, the probabilistic CZM may be regarded as an extension of the deterministic model. For the development of the probabilistic model, which is described in Section 3.2, additional fractographic investigations are required to determine the spatial distribution of the model parameters within the cohesive zone.

3.1 Deterministic model

The deterministic CZM is used to simulate standard-sized CT specimens based on parameters obtained from small specimen tests and to evaluate the constraint differences between miniaturized and standard-sized geometries. To identify the material parameters required for the FE-simulations, the experimental-numerical approach developed by Mahler & Aktaa (2014) [11] is applied. In Figure 3.1, an overview of the methodology from tensile testing to the prediction of fracture toughness on standard-sized geometries is given. The parameter identification on small specimens involves tensile testing of smooth round bar (SRB) specimens and notched round bar (NRB) specimens as well as fracture mechanics testing using MCT specimens. The method can be applied at any temperature on the lower or upper shelf or within the DBT region.

In a first step, SRB specimens are tested to determine the plastic flow curves to be used as material input data for the FE-simulations. For the calibration of the cohesive strength, NRB specimens are tested until failure. Simultaneously, FE-simulations are carried out on the NRB geometry to determine the stress field in the vicinity of the notch at the experimentally determined fracture strain for each tested specimen. Following Cornec et al. (2003) [66], the cohesive strength is equal to the maximum axial stress in the center of the notch at the point of experimental fracture. It was further shown by Mahler & Aktaa (2014) [11] that the cohesive strength is dependent on the radius of the machined notch and thus on the stress state at the notch. Therefore, testing and simulation of NRB specimens with varying notch radii is required for the evaluation of the triaxiality dependence of the cohesive strength.

The cohesive strength at low triaxialities may be determined from SRB specimens, which can be viewed as notched specimens with an infinite notch radius.

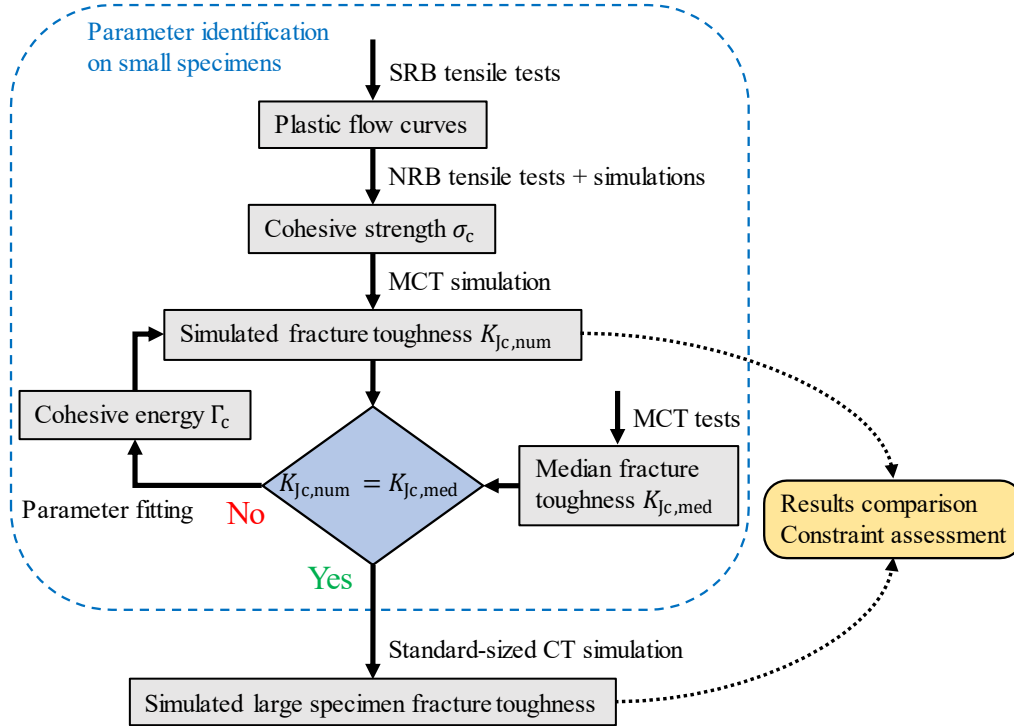


Figure 3.1: Overview of the development of the deterministic CZM and its application within this work [86]

After calibrating the cohesive strength, the cohesive energy is used as a fitting parameter to fit the fracture toughness obtained from MCT simulations to the median fracture toughness at the respective temperature determined by MCT testing following ASTM E1921. The tensile and fracture mechanics tests are described in detail in Chapter 4, while the parameter identification by means of FE-simulation is described in Chapter 5.

Since the triaxiality dependence of the cohesive strength is considered in the model, the parameters identified from small specimen tests may be used to simulate standard-sized fracture mechanics specimens. In this work, standard-sized CT specimens are simulated to be able to compare the resulting fracture toughness values and stress-strain fields around the crack front to the results from the MCT simulations. From those comparisons, constraint differences between small and large specimens are assessed. The simulations of standard-sized CT are described and discussed in Chapter 6.

3.2 Probabilistic model

As the name suggests, the deterministic model cannot be used to predict the statistical scatter of fracture toughness observed in ferritic steels within the DBT region. Furthermore, it is not feasible for use in the nuclear energy industry because the cohesive zone parameters must be calibrated individually for each test temperature within the DBT region, resulting in a large number of required specimens. The probabilistic CZM is developed to mitigate both disadvantages of the deterministic approach. By introducing randomly distributed cohesive zone parameters that, in addition to a functional relationship between the ductile fracture ratio and temperature, require only one calibration on the upper shelf and one calibra-

tion on the lower shelf, statistically distributed fracture toughness values can be predicted across the transition region.

An overview of the development of the probabilistic model and its application within this work is given in Figure 3.2. For the identification of the CZM parameters on the lower and upper shelf, the method used for the deterministic model, as described in Section 3.1, is applied. In case of the upper shelf calibration, instead of fitting the simulated fracture toughness to the median fracture toughness obtained from experiments, the cohesive energy is determined by fitting the simulated force-displacement and J-R curves to the experimental curves. The experimental J-R curve is determined prior to the simulations on small specimens in accordance with the ASTM E1820 standard.

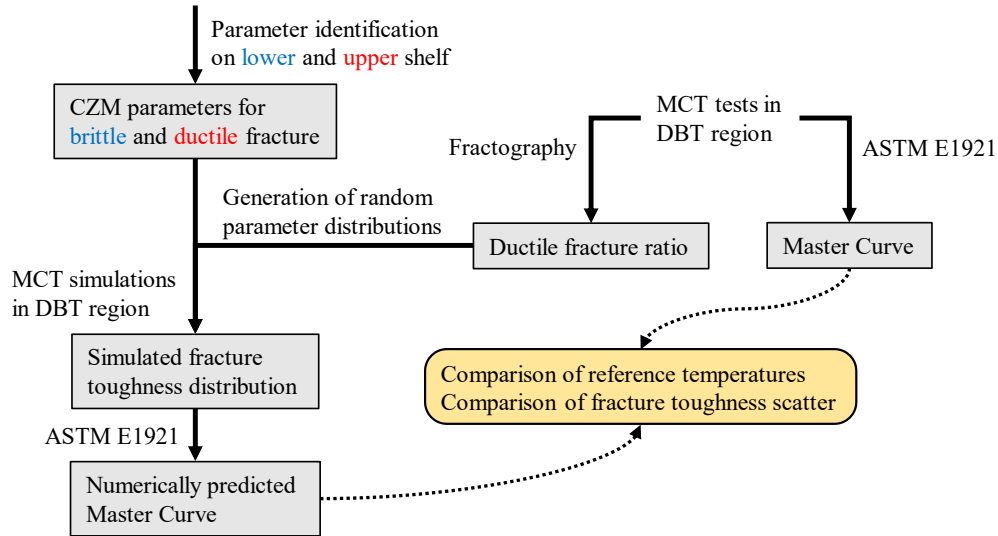


Figure 3.2: Overview of the development and application of the probabilistic CZM (adapted from [99])

For determining the statistical spatial distribution of the CZM parameters within the cohesive zone, fractographic analyses of MCT specimens tested within the transition region are required. Besides transgranular cleavage facets, the fracture surfaces show a seemingly random distribution of regions of micro-void coalescence that can be quantified by means of SEM analysis. A micrograph of the fracture surface of an MCT specimen made of SA-508 Cl.3 RPV steel, which was tested at -45°C and failed by cleavage fracture, is shown in Figure 3.3. In the micrograph, the ductile fracture patches are clearly visible between the surrounding transgranular cleavage facets. A detailed quantitative analysis of the fracture surfaces of MCT specimens tested within the DBT region is performed in Section 4.4.2. The result of the analysis is an estimate of the ductile fracture area based on the total area of the fracture surface of each specimen. The ratio of ductile fracture is then used to randomly distribute the calibrated CZM parameters for brittle and ductile fracture to the cohesive elements within the cohesive zone. For instance, if 10% of the fracture surface shows micro-void coalescence, 10% of the cohesive elements are assigned ductile properties, while 90% are assigned brittle properties. In this way, a random parameter distribution can be generated for each MCT simulation.

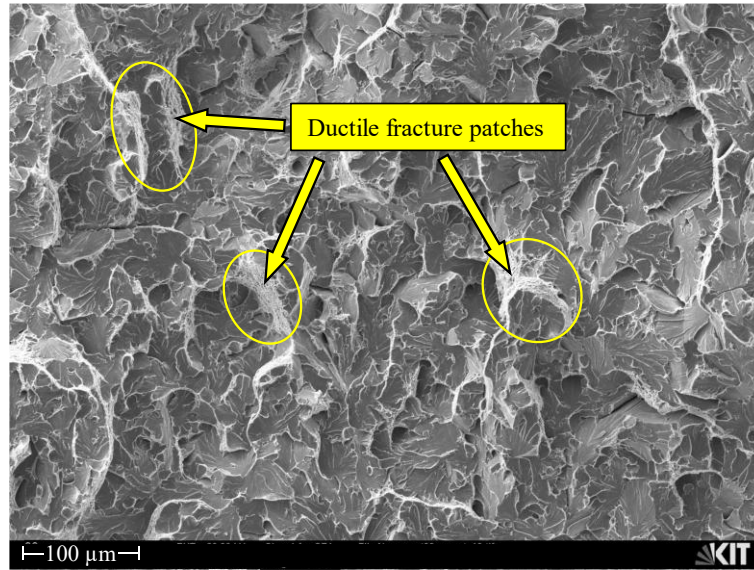


Figure 3.3: Spatial distribution of ductile fracture patches on the fracture surfaces of an MCT specimen that failed by cleavage in the DBT region

Multiple simulations are performed for each temperature to obtain a statistical distribution of fracture toughness. To predict the reference temperature of the material and thereby the Master Curve, each simulation result is treated as a real test according to ASTM E1921, including the consideration of validity limits and data censoring in the case of excessive plastic deformation before fracture.

For validation purposes, the number of simulations performed for each temperature will be equivalent to the number of specimens tested for the experimental Master Curve determination. This allows the precise comparison of the numerically and experimentally obtained reference temperatures and the extent of fracture toughness scatter at each temperature. In the first iteration of the probabilistic model, the ductile fracture regions are assumed to have the same size. In the next step, a variable size of the ductile fracture regions based on the analysis of a number of fracture surfaces is considered for model generation. The application of the probabilistic CZM and its modifications to predict the statistical fracture behavior of the RPV steel SA-508 Cl.3 are described in Chapter 7.

4 Experimental testing and fractography

In this chapter, the experimental testing required for the cohesive zone model (CZM) parameter identification in Chapter 5 is described. The material and the experimental setup for the tensile and fracture mechanics tests are presented in Section 4.1 and 4.2.1. Tensile testing (Section 4.2) includes the testing of smooth round bar (SRB) specimens for the determination of plastic flow curves at multiple temperatures and notched round bar (NRB) specimens for the calibration of the cohesive strength. In Section 4.3, the fracture mechanics tests on MCT specimens within the DBT region and on the upper shelf are described. While the tests in the transition region are used to evaluate the fracture toughness Master Curve of the material following ASTM E1921, the tests on the upper shelf are performed to determine the J-R curve according to ASTM 1820. Based on the tests within the DBT region, the viability of small specimen testing for Master Curve evaluation is discussed in view of the number of specimens required. In addition to experimental testing, the fractographic analysis of the MCT specimens tested in the transition region is described in this chapter (Section 4.4). Besides the assessment of the cleavage initiation sites, the quantification of the fracture surfaces for the determination of the ductile fracture ratio is performed. The ductile fracture ratios are required for the probabilistic CZM approach, which was described in Section 3.2 and is applied in Chapter 7.

4.1 Material

For all tests and simulations performed in this work, the low-alloy steel SA-508 Class 3, as designated in ASME Boiler and Pressure Vessel Code (BPVC) Section II, Part A (2019) [87], is used in the unirradiated condition. Applications of the material include RPVs, steam generators and pressurizers. Compared to the SA-508 Cl.1 and Cl.2 grades, SA-508 Cl.3 is characterized by an improved strength and toughness, high weldability and better irradiation resistance [88–90].

The material block used for to the fabrication of the tensile and fracture mechanics specimens was cut from the replacement closure head of the RPV of the José Cabrera power plant in Spain. In Figure A.1 and Figure A.2 in the Appendix, the dimensions and orientations of the closure head forging and the material block are provided. The base metal was fabricated by means of electric furnace processes. It was further vacuum steam degassed, quenched and a fine grain size was produced by controlled aluminum additions. In Table 4.1, the chemical composition of the RPV steel is listed. The weight-percentages of all elements are within the limits imposed by the ASME code [87].

Table 4.1: Chemical composition of the testing material SA-508 Cl.3 (in wt%)

C	Si	P	S	Cr	Mn	Ni	Cu	Mo	Fe
0.19	0.22	0.008	0.001	0.15	1.36	0.93	0.03	0.52	Balance

4.1.1 Microstructure

Kim et al. (2014) [91] investigated the microstructure of SA-508 Cl.3 by means of SEM and reported a tempered upper bainitic microstructure, which is a lath structure within the prior-austenite grain. They further reported the distribution of rod-shaped cementite particles along the bainitic ferrite lath bounda-

ries, as well as spherical-type cementite and fine MC-type carbides dispersed inside the laths. Im et al. (2001) [92] studied the effects of carbide precipitation on the mechanical properties of low carbon bainitic steels and concluded that the rod-shaped and spherical-type particles in the inter-lath region are considered as major detrimental micro-structural features of these alloys. Optical micrographs of the material used in this work are shown in Figure 4.1 (a) and (b). To reveal the fine-grained tempered bainitic microstructure, the sample was polished and etched with nitric acid. In a previous study by the Centre for Energy, Environmental and Technological Research (CIEMAT) in Spain, the prior-austenite grain size of the material was determined to be 7 to 8 μm [93].

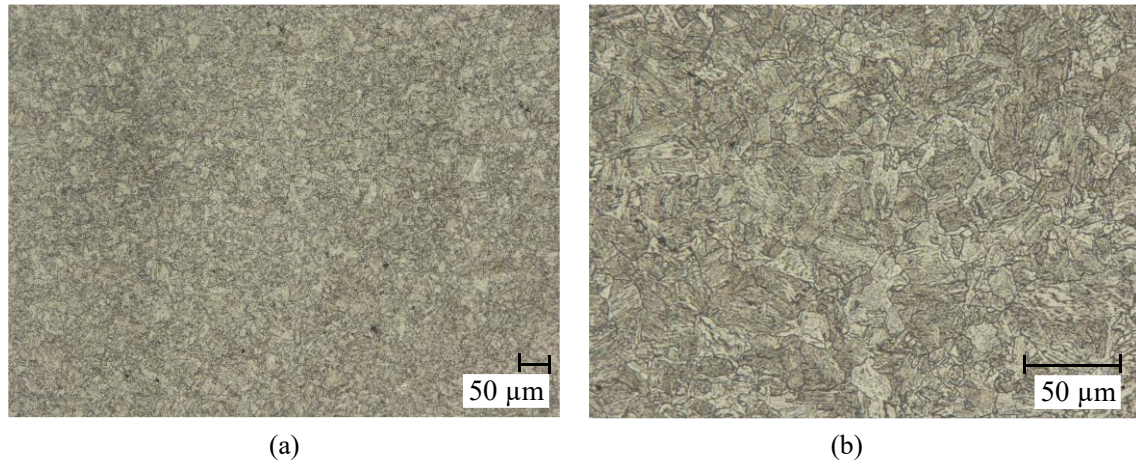


Figure 4.1: Optical micrographs of the material SA-508 Cl.3 (R-L orientation, mag. 300x (a) and 1000x (b))

4.1.2 Mechanical properties

Prior to this work, the mechanical properties of the RPV closure head forging were investigated by CIEMAT. Material was taken from different locations of the forging and a clear dependence of Charpy impact results on the R-coordinate was observed. However, no clear dependence of the impact energies on the L- and C-coordinates was found. Regarding tensile test results, strength differences were observed in the C-coordinate, but not in the other directions. It is likely that the inhomogeneity of the material is a result of uneven cooling during quenching. To mitigate the effects of this inhomogeneity on the tensile and fracture mechanics tests performed in this work, the L-direction was favored for specimen extraction from the given material block. Thereby, extracting specimens in the R- und C-directions was avoided as much as possible. The specimen cutting plans are shown in Figure A.3 and Figure A.4. First, specimens for the development of the deterministic CZM were fabricated from the block. Later, more material was taken from the block to fabricate specimens for the development of the probabilistic CZM. Differences in the dimensions of the NRB specimens were observed between the first and second fabrications. These differences are discussed in Section 4.2.2.

The elastic modulus E of the material is determined using the equation

$$E = 204 - T/16 \text{ GPa} \quad (T \text{ in } ^\circ\text{C}), \quad (4.1)$$

which is derived in the ASTM E1921 standard by fitting the tabular values for ferritic steels contained in ASME BPVC Section II, Part D [94] in the temperature range $-200^\circ\text{C} \leq T \leq 300^\circ\text{C}$. In Table 4.2, the elastic modulus is listed for the temperatures used for tensile and fracture mechanics testing. Poisson's ratio ν is assumed to be equal to 0.3. The yield strength σ_{YS} , ultimate tensile strength UTS and percentage reduction of area RA are obtained from the tensile tests on SRB specimens described in Section 4.2.3. Thereby, the approximate proportionality limit in the stress-strain curve is taken as the

yield strength, the UTS is the maximum engineering stress, and the specimen size/type dependent percentage area reduction is obtained from

$$RA = \left(1 - \frac{A_f}{A_0}\right) \cdot 100, \quad (4.2)$$

where A_f is the cross-sectional area at fracture and A_0 is the initial cross-sectional area. The dependence of yield strength, UTS and RA on temperature is obtained for each test temperature by curve fitting. It is found that the data sets are best described by exponential fitting functions. In Figure 4.2, the yield strength and UTS test results and the respective fitting curves are shown. The temperature dependence of both properties increases with decreasing temperature, with this behavior being more pronounced for the yield strength. In Table 4.2, the fitted values for each test temperature are listed. The yield strength at room temperature is 431 MPa and increases to 498 MPa at the lowest test temperature of -80°C.

Table 4.2: Mechanical properties of SA-508 Cl.3

Temperature	E [GPa]	σ_{YS} [MPa]	UTS [MPa]	RA [%]
RT	202.75	431	577	70.84
-30°C	205.88	453	618	68.60
-45°C	206.81	463	633	67.92
-60°C	207.75	476	650	67.25
-70°C	208.34	486	663	66.80
-80°C	209.00	498	676	66.36

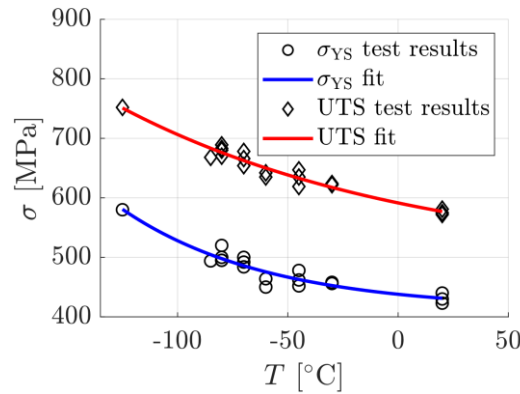


Figure 4.2: Yield strength and UTS results and exponential fit

The reference temperature of the material was determined by CIEMAT using standard-sized CT specimens and is specified as -43°C [95]. It is important to note that this reference temperature was obtained from a different section of the closure head forging than the section from which the block used in this work was taken from. Due to the inhomogeneity of the material, this value cannot be used to validate the reference temperature obtained from small specimens in Section 4.3.5. Nevertheless, the value can be used as an orientation to estimate the optimal test temperatures for the Master Curve evaluation.

4.2 Tensile testing

In this section, the determination of the plastic flow curves from SRB specimens and the tensile testing required for the calibration of the cohesive strength at multiple levels of triaxiality are described. Tensile tests on SRB and NRB specimens were carried out at all temperatures used for fracture mechanics testing between -80°C and RT. To ensure quasi-static loading conditions, all tests were performed under displacement control with a crosshead velocity of 0.002 mm/s , corresponding to a strain rate of $4 \cdot 10^{-4}\text{ 1/s}$.

4.2.1 Experimental setup

All mechanical tests were carried out using a servo-hydraulic universal testing machine from SCHENCK in combination with an MTS control unit. The experimental setup for the tensile tests on SRB and NRB specimens is shown in Figure 4.3. The specimens were form-fitted vertically into fixtures attached to the ends of the piston rods and load was applied by downwards displacement of the lower piston rod. The INSTRON climate chamber surrounding the piston rods is designed for a temperature range between -165°C to 350°C and was used for low-temperature testing. Cooling was carried out by means of liquid nitrogen, which was supplied via a duct from a movable tank. A fan within the climate chamber was used to vaporize and distribute the liquid nitrogen. The temperature in the immediate vicinity of the specimens was measured by thermocouples of type K, with the measured signal from the climate chamber control unit used to switch a valve for controlling the flow of liquid nitrogen. While maintaining the respective test temperatures, small fluctuations of less than 2°C were observed in the climatic chamber. During cooling to the desired test temperature, force control was used to counteract the thermal compression of the piston rods. At the same time, the displacement of the lower crosshead (CHD) was recorded to determine the point at which the heat conduction through the piston rods reached steady state conditions. During testing, the force and CHD were measured by the testing machine.

A camera system outside the climate chamber was used to record the diameter reduction of the specimens during testing, which allowed for the determination of the average true strain and average true stress (see Section 4.2.3). The images were taken by a PIXELINK PL-B782 CMOS-camera with 6.6 megapixels that was triggered once per second by a voltage signal generated by the machine control unit. A long-distance microscope (zoom lens) from the manufacturer INFINITY was attached to the camera to obtain high-resolution images of the necking region of the specimens. Backlighting was used to highlight the contours of the specimens and prevent reflections on the surfaces. Simultaneously, the exposure time of the camera was set as short as possible. The images were stored on a separate computer and processed after testing.

Initially, ice formation on the specimen surfaces during cooling resulted in a significant loss of image quality, making the data unusable for further processing. This problem could be solved by a short blast of gaseous nitrogen from a nitrogen cylinder onto the specimens to blow away the ice prior to testing. The nitrogen cylinder is located outside the climate chamber and is connected to a pipe pointing towards the mounted specimens.

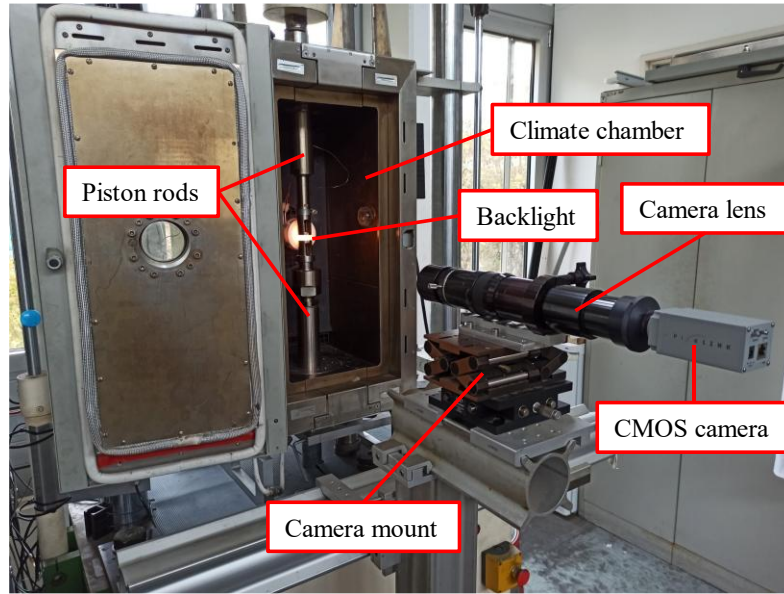


Figure 4.3: Experimental setup including camera system used for tensile testing

4.2.2 Specimens

The main goal of developing small specimen testing techniques (SSTT) is to reduce the amount of (irradiated) material required for the determination of mechanical and fracture-mechanical properties. Therefore, the size of the tensile specimens was chosen to be of the same order of magnitude as the MCT specimens used for the determination of fracture toughness. As shown in Figure A.3, this allows for the retrieval of MCT and tensile specimens from a single material block with relatively little wasted material.

The geometry of the SRB specimens is shown in Figure A.5. Their total length is 27 mm at a diameter of 2 mm and a gauge length of 5 mm. The measured dimensions of all tested SRB specimens are listed in Table A.1 in the Appendix. To allow for easy handling when mounting, the specimens have a shouldered end on each side.

For the tensile tests on NRB specimens, a geometry with a length of 27 mm and a diameter of 2.5 mm was used. The notches were designed to be as narrow as possible to induce a stress state under tensile load that is representative of the stress state in front of the crack tip of a fatigue pre-crack fracture mechanics specimen. The notch root radius r_N was limited to 0.1 mm due to the thickness of the wire used for electrical discharge machining (EDM). The actual representativeness of these U-shaped notches is discussed in Section 5.1.3 by comparing the triaxialities of NRB specimens with the triaxialities reached in front of the crack tip of MCT specimens. In addition to the lower-bound radius of 0.1 mm, NRB specimens with a notch root radius of 0.2 mm were tested to obtain cohesive strength values at lower triaxialities. In both cases, the minimum notch diameter D_N was set to 1.5 mm. The geometries of the NRB specimens are shown in Figure A.6 and Figure A.7, and the measured dimensions of all tested specimens are listed in Table A.2 and Table A.3. In the following, the specimens with a notch root radius of 0.1 mm are referred to as 0.1NRB and the specimens with a notch root radius of 0.2 mm are referred to as 0.2NRB.

As mentioned in Section 4.1.2, the tensile and fracture mechanics specimens were fabricated on two separate occasions. While all SRB and MCT specimens agreed well with their respective specified geometries, a systematic deviation from their specified geometry was observed for the NRB specimens

of the first fabrication. The average notch root radius of the 0.1NRB specimens of the first fabrication is 0.142 mm, which is significantly larger than the specified 0.1 mm. In addition, both the 0.1NRB and 0.2NRB specimens of the first fabrication exhibit flat notches instead of the specified U-shaped notches. The effect of these deviations on the stress state around the notches and thus on the determined cohesive strength values are discussed in Section 5.1.

4.2.3 Smooth round bar tests

The tests on SRB specimens were conducted to determine the plastic flow curves required at each test temperature of the fracture mechanics tests to be used as material input for the FE-simulations. From the force data measured by the testing machine and the images taken by the camera, the average true strain - average true stress curves are obtained at RT, -60 and -80°C. Engineering stress-strain curves are not sufficient since during fracture mechanics testing, the material is loaded beyond the onset of strain localization (necking). The correction method developed by Bridgman (1964) [96] is applied to convert the average true stress into the uniaxial true stress. At the intermediate temperatures -30, -45 and -70°C, the flow curves are obtained inversely by interpolating between the curves determined using the Bridgman correction. To validate the flow curves, the SRB tests were simulated and the numerically determined force-displacement curves are compared to the experimental curves.

4.2.3.1 Direct flow curve determination

For each test temperature between -80°C and RT, multiple SRB specimens were tested until failure. In Figure 4.4, one force-displacement curve is displayed for each temperature that represents the mechanical behavior of the material at that temperature. The force-displacement curves obtained from the remaining SRB tests are shown in Figure A.9. To improve the comparability of the curves, they were shifted on the horizontal axis to align the onset of nonlinear deformation following the linear-elastic regime. The force at yielding, the maximum force and the displacement at fracture increase with decreasing temperature. After reaching the maximum force, the force decreases with increasing displacement until unstable fracture occurs.

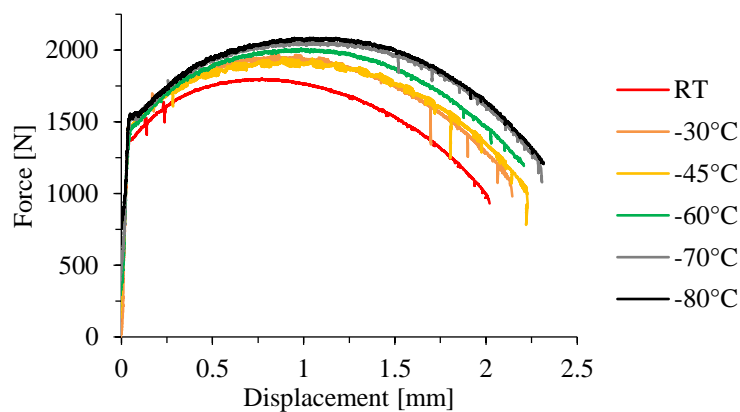


Figure 4.4: Representative force-displacement curves for each test temperature obtained from the tensile tests on SRB specimens

Parallel to the acquisition of force data by the testing machine, images of the specimen contours were taken by the CMOS camera. Selected images of specimen SRB13, which was tested at RT, are shown in Figure 4.5 (a) as examples for the successive loading stages. By using backlighting, the specimen is visible as a black object on a white background, allowing the contours to be traced with high precision.

The points on the engineering stress-strain curve corresponding to the respective images are shown in Figure 4.5 (b). While IMG0001 is the first image taken at the start of the test, IMG0424 shows the specimen contour at the onset of necking. A slight diameter reduction is visible due to the transverse contraction of the specimen during uniform elongation. The contour of the specimen at a point within the unloading regime is shown in IMG0850. Necking as a result of strain localization is clearly visible in the image. The contour at the point of unstable fracture is shown in IMG1075. At this point, the diameter in the neck is greatly reduced as compared to the diameter of the unloaded specimen.

The minimum diameter d_{\min} at each corresponding force value is required to determine the average true stress - average true strain curve for an individual test. To determine the minimum diameter with high accuracy and reduce measurement noise, the raw images from the camera are processed in MATLAB. In a first step, the raw images are transformed into grayscale images where each RGB pixel is assigned a grayscale value between 0 and 255. The grayscale images are then converted into binary images by assigning each pixel with a grayscale value below 255 the binary value 1 (white), while each pixel with a grayscale value of 255 is assigned the value 0 (black).

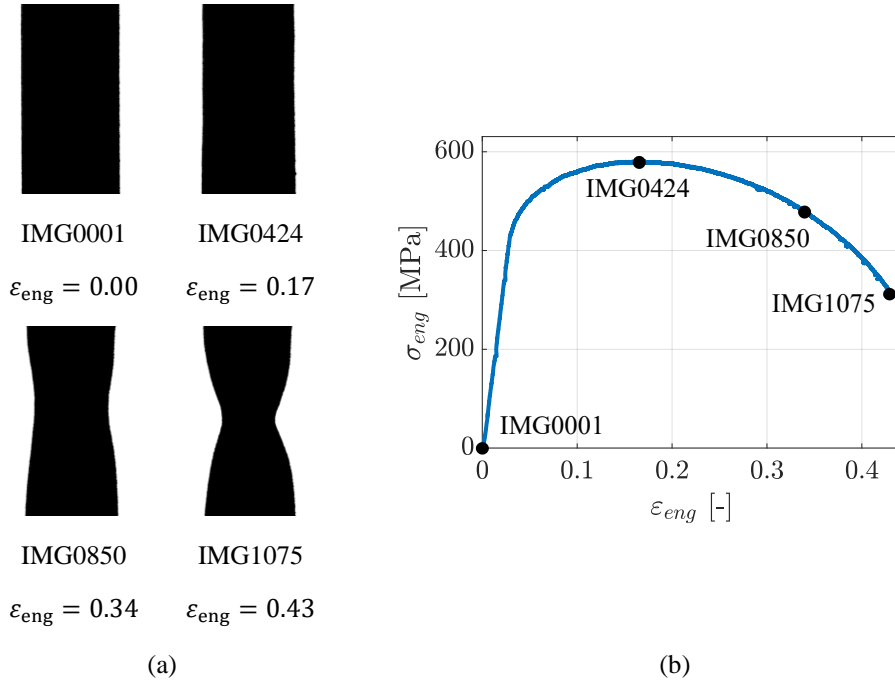


Figure 4.5: Selected images of the contour of specimen SRB13 during testing (a) and corresponding points on the engineering stress - engineering strain curve (b)

To obtain the current diameter along the specimen axis, the number of black pixels in each pixel row is determined and multiplied by the pixel length $L_{\text{pix}} = 3.2 \mu\text{m}$. The diameter curves of specimen SRB13 along its axis are displayed in Figure 4.6 (a) corresponding to their respective contour images in Figure 4.5 (a). From each individual curve, the minimum diameter of the specimen can easily be determined at the corresponding engineering strain. The resulting diameter reduction curve is shown in Figure 4.6 (b). Due to the inherent limitations in the measurement setup's accuracy, a constant minimum diameter is observed during the initial loading phase. Before the onset of necking, the diameter reduction is approximately linear. Afterwards, the diameter reduction is accelerated due to increasing strain localization in the neck. At the point of unstable fracture, the minimum diameter of the specimen is almost halved.

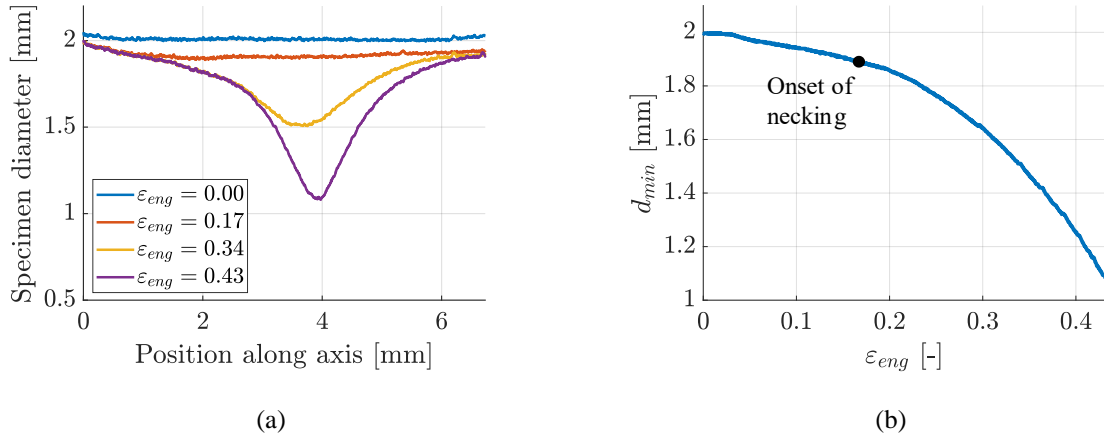


Figure 4.6: Diameter of SRB13 along specimen axis at different load levels (a) and reduction of minimum diameter (b) ((b) adapted from [97])

With the force measured by the testing machine and the minimum diameter curve determined from the images, the average true stress is calculated by

$$\sigma_{t,avg} = \frac{F}{\frac{1}{4}\pi d_{min}^2} \quad (4.3)$$

and the average true strain is calculated by

$$\varepsilon_{t,avg} = 2 \ln \frac{d_0}{d_{min}}, \quad (4.4)$$

where d_0 is the diameter of the specimen prior to testing. To determine the plastic flow curves, which are required as material input for the FE-simulations, the elastic part must first be removed from the average true strain to obtain the plastic part of the average true strain:

$$\varepsilon_{t,pl,avg} = \varepsilon_{t,avg} - \frac{\sigma_{t,avg}}{E}. \quad (4.5)$$

In the next step, the average true stress, which is inherently multiaxial after the onset of necking, is transformed into a uniaxial true stress σ_t by applying the correction method by Bridgman [98]. The method is based on the equation

$$\sigma_t = \frac{\sigma_{t,avg}}{\left(1 + 4 \frac{\rho}{d_{min}}\right) \ln \left(1 + \frac{1}{4} \frac{d_{min}}{\rho}\right)}, \quad (4.6)$$

which takes into account the curvature radius in the neck ρ to calculate the uniaxial true stress. For the determination of the curvature radius in the neck, the first and second derivatives of the specimen radius r with respect to the axial coordinate are required:

$$\rho = \frac{(1 + r'^2)^{3/2}}{r''}. \quad (4.7)$$

The accuracy of the determined curvature radius is severely limited by the resolution of the camera. To improve the quality of the results, the specimen radius is approximated by a fourth order polynomial equation in an axial position range of 225 pixels. In Figure 4.7 (a), the polynomial fit of the radius in the neck on one side of specimen SRB25, which was tested at -80°C , is shown. The noise present in the

image data is removed by the fitting curve and the shape of the neck is well approximated. To calculate the curvature radius, the polynomial equation is differentiated twice at the location of the minimum diameter and Equation (4.7) is applied. This procedure is carried out for both specimen sides visible in the 2D plane of the images, and the average of the respective curvature radii is taken as the effective curvature radius.

The curvature radius of SRB25 is plotted against the engineering strain in Figure 4.7 (b). Prior to necking, the curvature radius obtained from the image processing procedure is measurement noise. Therefore, the Bridgman correction is only applied after the onset of strain localization ($\varepsilon_{eng} = 0.23$ for SRB25). The change in curvature radius beyond the onset of necking is approximated by an exponential fitting equation of the form

$$\rho = C_1 \cdot \exp(C_2 x) + C_3 \cdot \exp(C_4 x), \quad (4.8)$$

where C_1 , C_2 , C_3 and C_4 are fitting parameters and x is the image number. Across all tests, this functional form is found to offer the best representation of the curvature radius evolution.

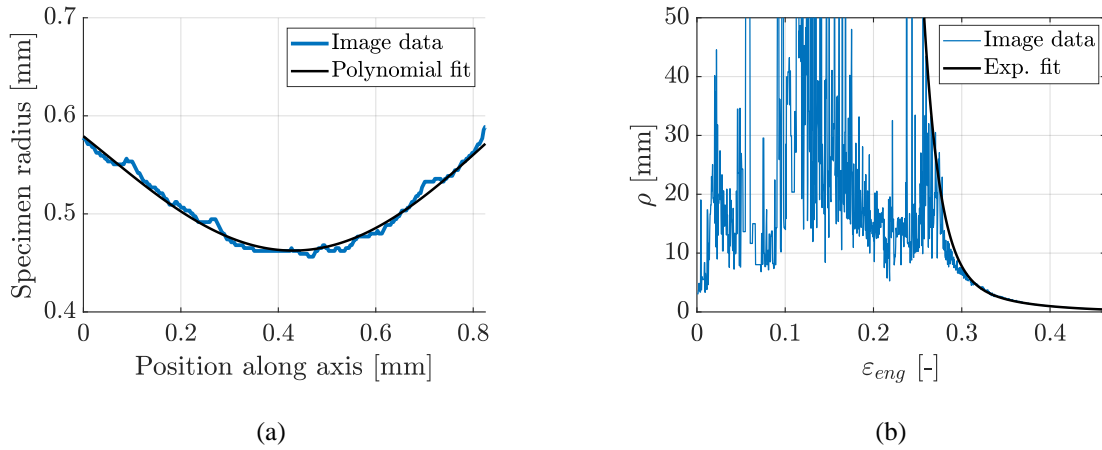


Figure 4.7: Fourth order polynomial fit of the specimen radius in the necking region (a) and exponential fit of the curvature radius against engineering strain (b)

Using the fitted curvature radius and the minimum diameter from the images, the average true stress is transformed into the uniaxial true stress using Equation (4.6). The true stress – true plastic strain curves before and after application of the Bridgman correction are shown in Figure 4.8 for specimen SRB08, which was tested at -80°C . Below an average true plastic strain of about 0.2, there is no difference between the curves. The slopes of both curves reduce from the yield point at $\varepsilon_{t,pl,avg} = 0$ to $\varepsilon_{t,pl,avg} = 0.2$ for the average true stress and to $\varepsilon_{t,pl,avg} = 0.25$ for the uniaxial true stress. Beyond these points, the curves remain approximately linear, with the slope of the uniaxial true stress being lower than the slope of the average true stress. The specimen failed at an average true plastic strain of about 1.2.

A similar behavior is observed for all other SRB specimens used for the direct flow curve determination. The individual uniaxial true stress – true plastic strain curves are shown in Figure A.10. The plastic flow curves used as material input for the simulations are determined as the average of the individual flow curves for each temperature. In Figure 4.9, the final flow curves for RT, -60 and -80°C are shown. As is common for ferritic steels, strain hardening is increased with decreasing temperature. The true plastic strain at fracture is slightly higher for RT as compared to the low temperature curves.

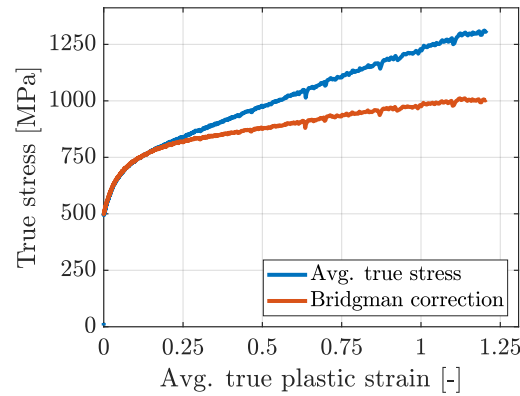


Figure 4.8: Average true stress and Bridgman corrected uniaxial true stress for specimen SRB08 tested at -80°C

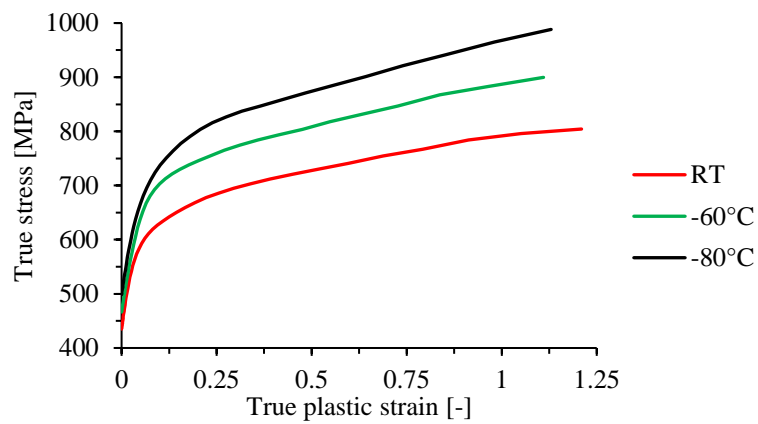


Figure 4.9: Plastic flow curves for RT, -60°C and -80°C obtained from the direct determination method (adapted from [99])

To validate the determined flow curves and the Bridgman correction, the SRB tests were simulated and the average true stress – average true strain curves are compared with the experimental curves in Figure 4.10. The simulated curves agree well with the experimental curves for RT, -60°C and -80°C throughout the entire strain range. The FE-model of the SRB specimen used for the simulations is described in Section 5.1.1.

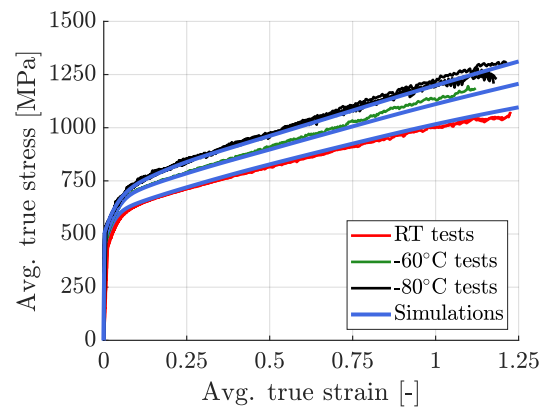


Figure 4.10: Simulated average true stress - average true strain curves at experimental curves at RT, -60°C and -80°C

4.2.3.2 Inverse flow curve determination at intermediate temperatures

At the intermediate temperatures of -30, -45 and -70°C, the direct flow curve determination method is not applicable to the SRB test results. The quality of the images taken during testing is not adequate for the accurate determination of the minimum diameter and the curvature radius due to ice build-up on the specimen surfaces. Instead, the flow curves for these temperatures are determined inversely by fitting simulated force-displacement curves to the experimental curves. To reduce the number of required fitting parameters to a single value, it is assumed that the shapes of the flow curves at the intermediate temperatures are similar to the shapes of the flow curves at RT, -60 and -80°C (Figure 4.9). The intermediate flow curves can then be obtained by interpolating between the already determined flow curves using the interpolation parameter λ . For instance, the interpolated true stress at -70°C is calculated by

$$\sigma_{t,-70} = \sigma_{t,-60} + \lambda(\sigma_{t,-80} - \sigma_{t,-60}), \quad (4.9)$$

meaning that $\lambda = 0$ would lead to the -60°C flow curve and $\lambda = 1$ would lead to the -80°C flow curve. In the same way, the true stresses at -30 and -45°C are obtained by interpolating between the values for RT and -60°C. The fit is considered acceptable if the simulated maximum force is equal to the average maximum force obtained from the tests at a given temperature. The values for λ resulting from the fitting procedure between RT and -60°C are 0.62 for -30°C and 0.86 for -45°C. For -70°C, the value obtained for λ is 0.6.

In Figure 4.11 (a) to (f), the simulated force-displacement curves using the directly determined and the interpolated flow curves are compared to the experimental curves at the respective test temperatures. Machine compliance is accounted for by correcting the measured displacements so that the slope in the elastic regime matches the numerically determined slope. In general, the simulated curves agree well with the experiments. At -60 and -70°C, the force is slightly underestimated by the simulations beyond the point of maximum force. A temporary force of 300 N was applied prior to testing to settle the specimens in the fixtures.

The directly determined and interpolated flow curves are displayed in Figure 4.12 for all test temperatures. With decreasing temperature, the strain hardening capability of the material increases. The true plastic strain at fracture is highest at RT. At the test temperatures between -30 and -80°C, the true plastic strain at fracture remains approximately constant. While the curves for -30, -45 and -60°C are close together, a significant increase in true stress is observed between -60 and -70°C.

To prevent excessive plastic deformation of the finite elements directly at the crack tip that might result in numerical instabilities, all flow curves are extrapolated to a true plastic strain of 5 using a constant slope that is equal to the slope of the individual curves at the point of fracture. In Table A.5, the flow curve data used for the simulations is listed for each test temperature.

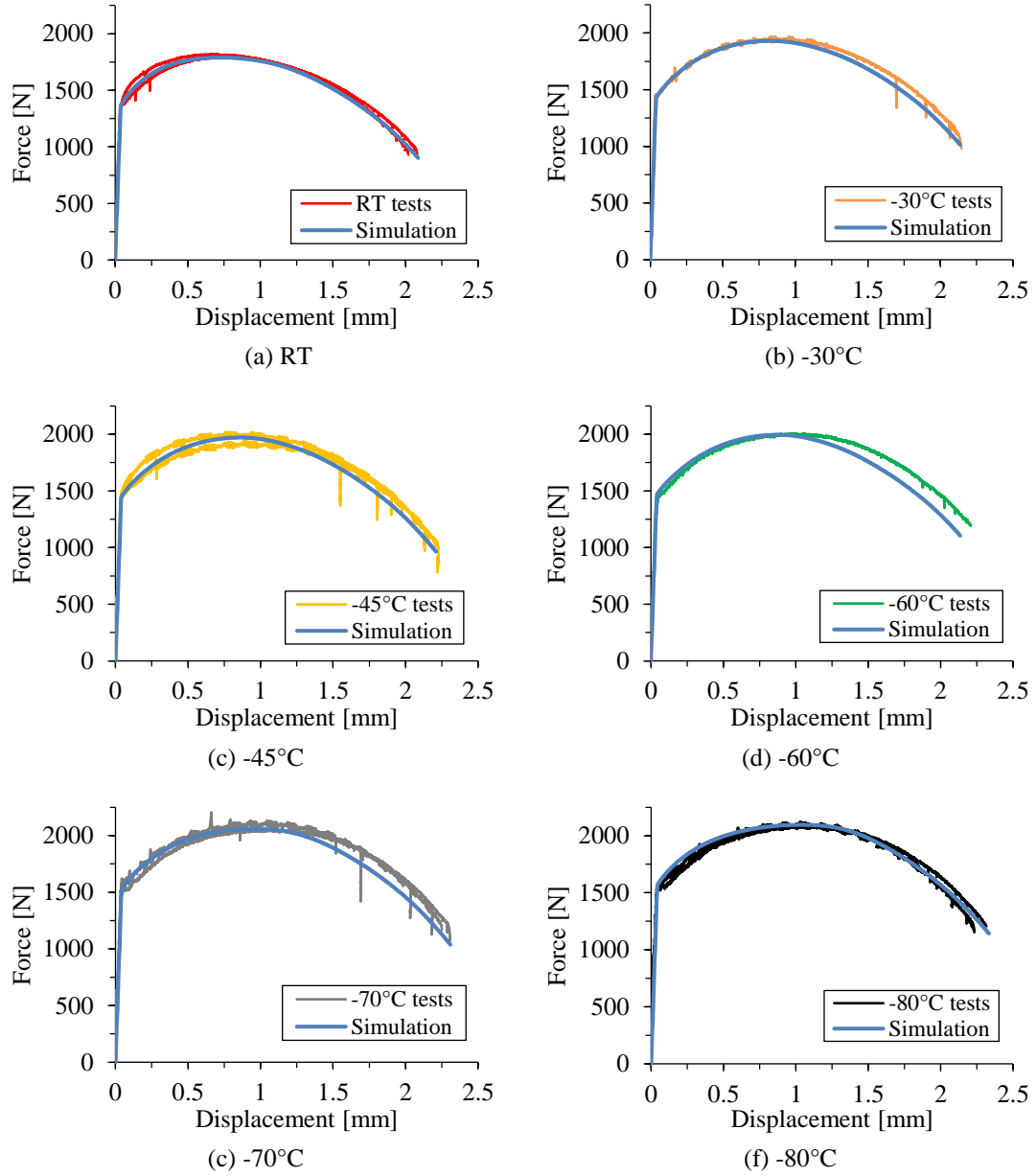


Figure 4.11: Comparison between numerical and experimental SRB force-displacement curves for all test temperatures

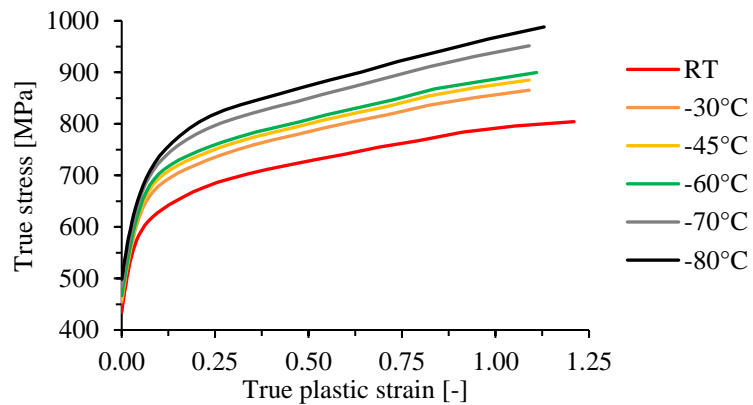


Figure 4.12: Plastic flow curves for all test temperatures between RT and -80°C

4.2.4 Notched round bar tests

The purpose of testing NRB specimens was to calibrate the cohesive strength at multiple levels of triaxiality. By using different notch radii, the stress state in the notch is varied. As with the SRB tests, the force data measured by the testing machine is used in conjunction with the images from the CMOS camera to determine the average true stress – average true strain curves. From these curves, the average true strain at fracture is determined for each test. In Section 5.1, the SRB and NRB tests are simulated, and the cohesive strength values are identified at the experimentally determined fracture points.

Triaxiality-dependent cohesive strength data is required at RT, -60, -70 and -80°C. Multiple 0.1NRB and 0.2NRB specimens were tested at these temperatures using the same experimental setup and test parameters as for the SRB specimens. The force-CHD curves are shown in Figure 4.13 for the 0.1NRB tests (a) and the 0.2NRB tests (b). A large scatter of the mechanical behavior of the specimens is observed at all temperatures. This scatter is not due to material inhomogeneities, but rather to manufacturing-related differences in the geometries and dimensions of the notches. As explained in Section 4.2.2, significant systematic deviations between the notch geometries from two different fabrications of NRB specimens were observed. The specimens with a flat notch from the first fabrication generally show lower force values and a lower CHD at fracture as compared to the specimens with a round notch from the second fabrication.

In Figure 4.14, the first images taken at the start of testing and the last images taken before fracture are shown for specimen 0.1NRB01 (a) from the first fabrication and 0.1NRB11 (b) from the second fabrication. Both specimens were tested at RT. The geometrical differences between the notches are clearly visible. The initial flat notch of specimen 0.1NRB01 is about 40% wider than the round notch of specimen 0.1NRB11. Comparing the images prior to testing and at the fracture point, the widening of the notches in axial direction and the diameter reduction can be seen. While the widening of the notch of specimen 0.1NRB01 is significantly increased as compared to 0.1NRB11, the diameter reduction at the point of fracture is slightly larger for 0.1NRB11.

From the images, the only relevant data for the determination of the average true stress and average true strain is the diameter reduction in the notch. Similar to the SRB tests, the raw images are converted into binary images using MATLAB and the number of pixels with a value of 1 is determined for each pixel row. The number of pixels is then multiplied by the length of a pixel to obtain the diameter. The diameter reduction during testing is determined from the minimum diameter in each successive image.

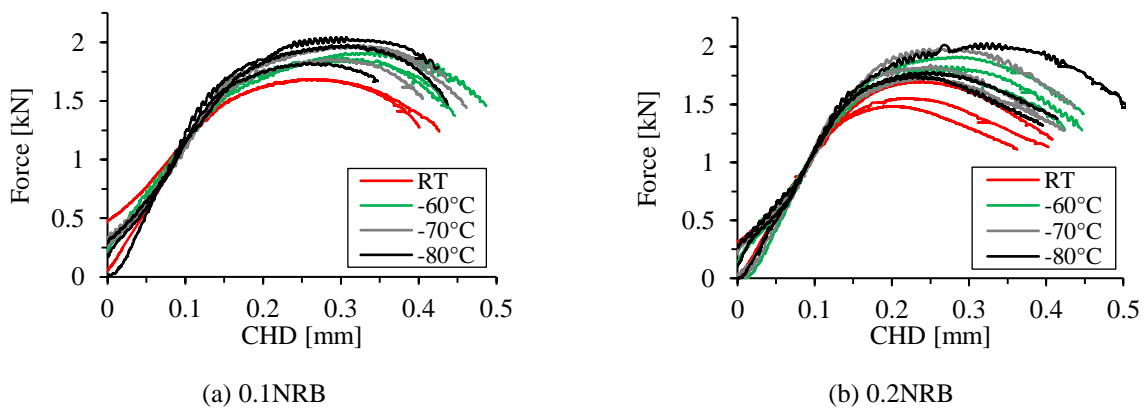


Figure 4.13: Force-CHD curves of the 0.1NRB tests (a) and 0.2NRB tests (b) performed at RT, -60, -70 and -80°C

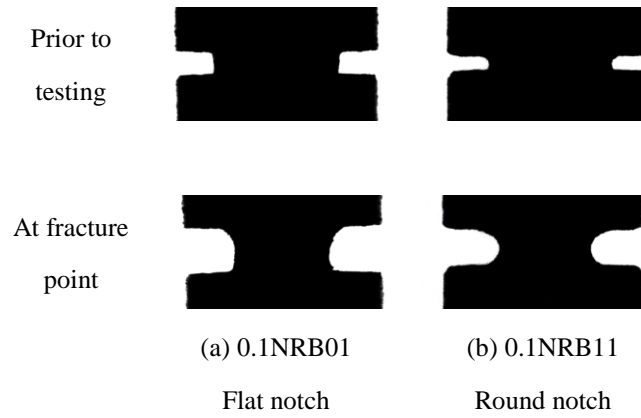
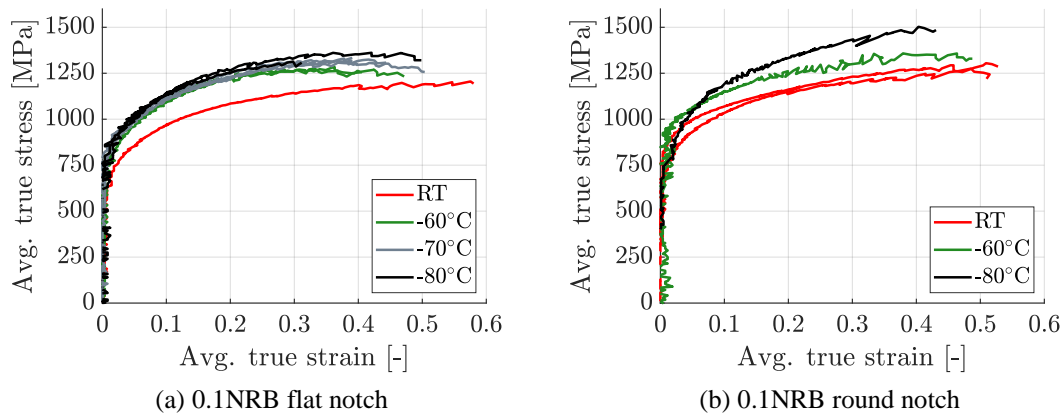


Figure 4.14: Images of the notches of 0.1NRB01 with a flat notch and 0.1NRB11 with a round notch prior to testing and at the point of fracture (both tested at RT)

The average true stresses and average true strains are calculated using Equations (4.3) and (4.4). In Figure 4.15, the resulting curves are shown for the flat-notched (a) and round-notched (b) 0.1NRB specimens and the flat-notched (c) and round-notched (d) 0.2NRB specimens. For a given temperature and notch geometry, the scatter of the curves is relatively low. In some cases, for instance regarding the 0.1NRB flat notch results obtained at -80°C , there is a significant difference between the average true strain values at fracture. The average true strain at fracture is strongly dependent on the geometry and dimensions of the notch. Therefore, the exact geometry of each individual NRB specimen is considered for the numerical identification of the cohesive strength in Section 5.1. In Table A.6,

Table A.7 and Table A.8, the average true stresses and average true strains at fracture are listed for all SRB, 0.1NRB and 0.2NRB specimens.



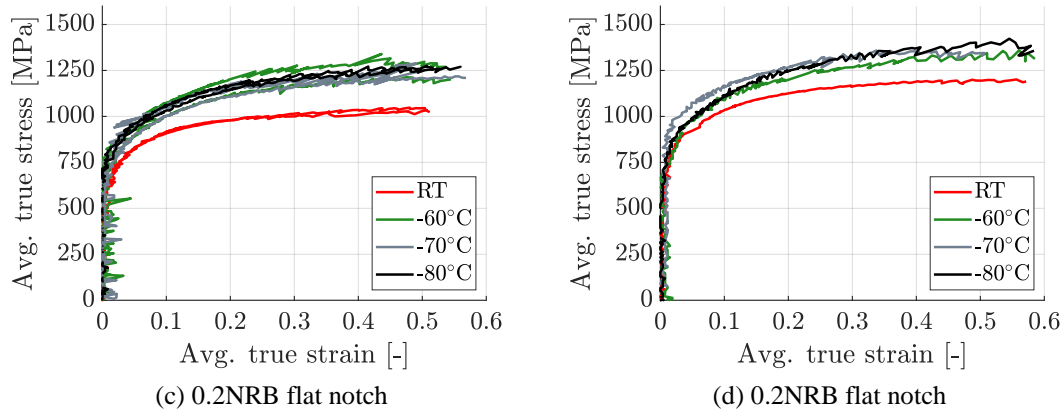


Figure 4.15: Average true stress - average true strain curves for the flat-notched (a) and round-notched (b) 0.1NRB specimens and the flat-notched (c) and round-notched (d) 0.2NRB specimens

4.3 Fracture mechanics testing

Fracture mechanics tests on SA-508 Cl.3 were conducted at RT and at multiple temperatures within the DBT region using a MCT geometry. The tests within the DBT region are required to determine the reference temperature according to ASTM E1921 and subsequently evaluate the fracture toughness Master Curve in Section 4.3.5. The tests performed at RT are used to determine the J-R curve following ASTM E1820 in Section 4.3.6. Additionally, the broken halves of the MCT specimens tested in the DBT region are used in Section 4.4 to characterize the cleavage initiation sites and to perform quantitative fractographic analyses which are required for the probabilistic fracture simulations in Chapter 7.

In Section 5.2, the MCT tests are simulated, and the cohesive energy is calibrated within the DBT region by fitting the simulated fracture toughness to the median fracture toughness obtained from the Master Curve and at RT by fitting the simulated J-R curve to the experimental J-R curve.

4.3.1 Experimental setup

The same universal testing machine by SCHECNK used for the tensile tests was used for fracture mechanics testing. The testing machine was described in Section 4.2.1. Clevises were attached to the piston rods to allow MCT specimens to be mounted via loading pins. The mounting setup for MCT specimens is shown in Figure 4.16. To prevent slight translational deviations of the piston rods from inducing bending moments while loading, the clevises were designed to allow for rotation relative to the loading direction. The displacement of the specimen halves was measured using a clip gauge extensometer that was attached to knife edges located at the front face of the MCT specimens. Thermocouples were attached to the upper clevis to allow for temperature-controlled activation of the liquid nitrogen valve. Contrary to the tensile tests, a camera system was not required for the fracture mechanics tests as the displacement of the specimen halves was measured by the clip gauge extensometer.

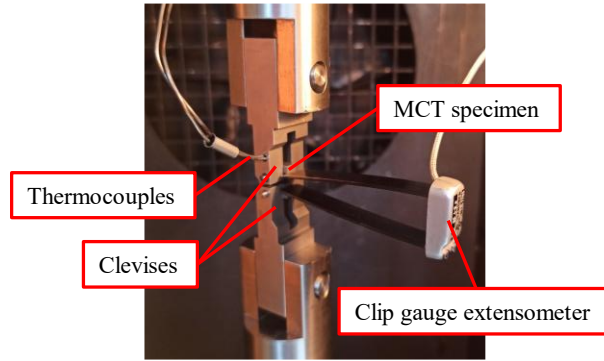


Figure 4.16: MCT specimen mounted into the clevises with clip gauge extensometer and thermocouples attached

4.3.2 Specimens

The miniaturized compact tension (MCT) specimens used in this work for fracture mechanics testing have a thickness of 4 mm (0.16T CT) and comply with the dimensions specified in the ASTM E1921 standard. To be able to mount a conventional clip gauge extensometer onto the specimens, it was necessary to increase the width of the MCT geometry between the pin holes and the front face by 1.5 mm. The effects of this geometric modification on the measured displacements are discussed in Section 4.3.4. In Figure A.8, the specified dimensions of the MCT geometry are shown and in Table A.4, the measured dimensions of the specimens are listed.

The MCT specimen is considered to be a promising geometry for future surveillance programs due to the possibility to machine eight specimens from a single broken Charpy specimen. Additionally, it is believed to be the highest constraint geometry as compared to other eligible geometries such as notched bend bars or circumferentially cracked round bars [6]. High constraint conditions are desirable in order to obtain a high measurement capacity for a limited volume of material.

4.3.3 Fatigue pre-cracking

Following ASTM E1921 and E1820, fracture mechanics specimens are required to be fatigue pre-cracked prior to testing to introduce a sharp initial crack. As the size and shape of the fatigue pre-crack are considered to influence the fracture-mechanical behavior of a specimen significantly, limits are specified on both parameters to qualify individual specimens for fracture toughness evaluation.

The pre-cracking procedure was performed using a CRACKTRONIC resonance testing machine by the manufacturer RUMUL, which is shown in Figure 4.17. Similar to the setup shown in Figure 4.16, the MCT specimens were mounted into clevises and fixed with loading pins. During pre-cracking, the dynamical system was excited harmonically at its natural frequency with a maximum stress intensity factor K_{\max} that was well below the fracture toughness of the material. Limits on K_{\max} are specified in the testing standards to prevent plastic deformation of the material in the vicinity of the crack tip during pre-cracking. According to ASTM E1921, K_{\max} is limited to $25 \text{ MPa}\sqrt{\text{m}}$ at the start of pre-cracking, resulting in a maximum allowable fatigue force P_{\max} of 1080 N for the given MCT geometry. At pre-crack extensions close to the targeted a_0/W ratio of 0.5, K_{\max} is limited $15 \text{ MPa}\sqrt{\text{m}}$, corresponding to a P_{\max} of 556 N. Regarding ASTM E1820, the maximum stress intensity factor at the start of pre-cracking is limited by

$$K_{\max} = \left(\frac{\sigma_{YS,RT}}{\sigma_{YS,test}} \right) (0.063 \cdot \sigma_{YS,RT} \text{ MPa}\sqrt{\text{m}}), \quad (4.10)$$

where $\sigma_{YS,RT}$ and $\sigma_{YS,test}$ are the yield stresses at RT and at the test temperature respectively. In this work, fracture-mechanical tests for the J-R curve determination were only conducted at RT, where a limit of $27.2 \text{ MPa}\sqrt{\text{m}}$ is obtained for K_{\max} . This value is similar to the limit imposed by the E1921 standard.

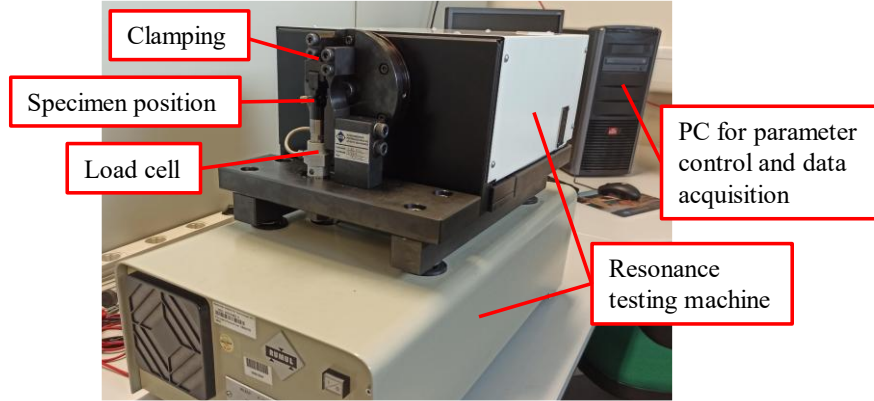


Figure 4.17: Resonance testing machine used for fatigue pre-cracking of MCT specimens

Maintaining a constant force cycle, the maximum stress intensity factor increases with increasing fatigue crack length. To prevent K_{\max} from surpassing the limits specified in the standards, the maximum fatigue force was reduced in two discrete steps. For each pre-cracking step, a fatigue force ratio $R = P_{\min}/P_{\max}$ of 0.1 was used, following the recommendations given in the ASTM standards. The applied maximum fatigue forces and the resulting mean fatigue forces and amplitudes are listed in Table 4.3. In the first step, a maximum fatigue force of 850 N was used, which is lower than the allowed value but was found to be high enough to initiate the fatigue crack. The third and last step was conducted with a maximum force of 550 N, which is close to the specified limit.

During pre-cracking, the natural frequency ω_0 of the dynamical system decreases with increasing crack length. This means that the difference between the natural frequencies before and after pre-cracking, $\Delta\omega_0$, can be used as a measure of the fatigue crack extension. To achieve the targeted pre-crack extension of 1.5 mm, which is required for a a_0/W ratio of 0.5, a total reduction of the natural frequency of 14 Hz was applied. The total reduction of the natural frequency is the sum of the $\Delta\omega_0$ resulting from the individual loading steps, which are listed in Table 4.3.

Table 4.3: Parameters used for the respective loading steps of the fatigue pre-cracking procedure

Step	P_{\max} [N]	P_{mean} [N]	P_{amp} [N]	R [-]	$\Delta\omega_0$ [Hz]	N_{cycles} [-]
1	850	467.5	382.5	0.1	3.5	90-120k
2	650	357.5	292.5	0.1	1.5	50-70k
3	550	302.5	247.5	0.1	9	170-200k

An optical microscope was used to quantify the fatigue pre-crack extension after the fracture mechanics tests were performed. To distinguish between the fatigue pre-cracks and the regions of slow-stable crack growth, the specimens tested at RT were heat-tinted at 300°C for one hour to allow for an oxide layer to form on the fracture surfaces. After testing, the specimens were cooled to cryogenic tempera-

tures in liquid nitrogen and final fracture was induced by impact loading. In Figure 4.18 (a), an optical micrograph taken of MCT10, which was tested at -60°C , is shown with a clear distinction between the machined notch, fatigue pre-crack and brittle fracture surface. Following the ASTM standards, the pre-crack length a_{pc} is measured at nine equidistant points along the thickness direction starting from the tip of the machined notch. The total crack length at each point is determined as the sum of the measured pre-crack length and the distance between the pin holes and the notch tip a_{notch} in crack growth direction. In Figure 4.18 (b), the total crack lengths of all pre-cracked and tested MCT specimens at the individual measurement points are displayed. For most specimens, a symmetrical and reasonably straight pre-crack with a deviation of about 0.4 mm between the longest and shortest crack length was achieved. The blue curves show fatigue pre-cracks that meet the straightness requirement specified in the standards, while the red curves indicate invalid pre-crack shapes that show a significant deviation between the average and the minimum or maximum crack lengths. Test results obtained from specimens with invalid pre-cracks cannot be used for fracture toughness determination. From 27 MCT specimens tested within the DBT region following ASTM E1921, two test results (MCT14 and MCT21) are deemed invalid due to pre-crack asymmetry. Likewise, one test result (MCT23) out of nine tests performed for the determination of the J-R curve according to ASTM E1820 is deemed invalid.

The initial crack length a_0 is determined by calculating the total average of the seven inner crack length measurements and the average of the two outer measurements. In Table A.4, the initial crack lengths are listed for all tested MCT specimens. The average a_0 of all specimens that meet the pre-crack straightness requirement is 3.99 mm, which is very close the targeted value of 4 mm required for $a_0/W = 0.5$. In addition, a standard deviation of 0.066 mm is obtained for the data set, indicating the high precision of the applied pre-cracking procedure.

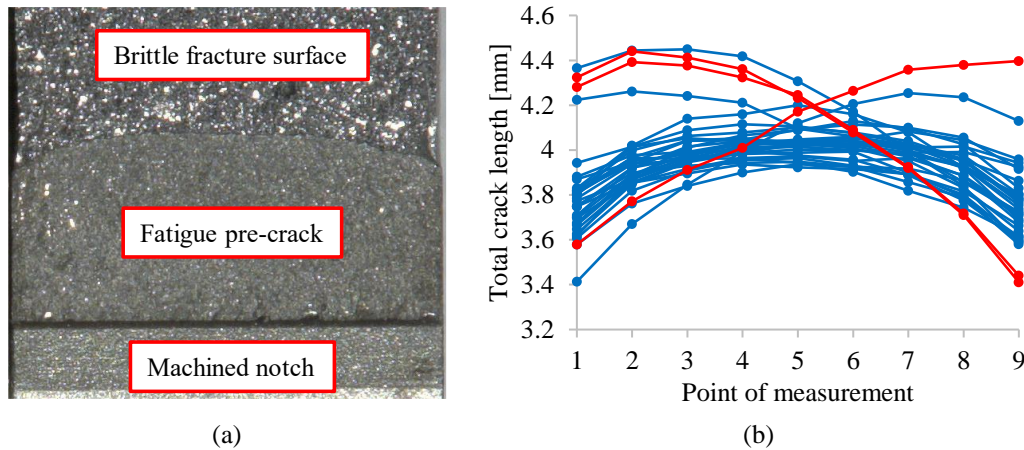


Figure 4.18: Optical micrograph of the fracture surface of MCT10 tested at -60°C (a) and total crack lengths of all pre-cracked MCT specimens at nine equidistant measurement points along the specimen thickness (b)

4.3.4 Front face to load line displacement conversion

In Section 4.3.1, it was explained that due to the small size of the MCT geometry, the clip gauge extensometer was attached to knife-edges positioned at the front face of the specimens. According to the ASTM standards, the displacement at the load line position is required for determining the fracture toughness from tests on CT specimens. Therefore, the measured front face displacement FFD, as shown in Figure 4.19, must be converted into the load line displacement LLD. Following Landes (1980) [100],

the load line displacement can be calculated using a linear interpolation between the front face position and the center of rotation,

$$LLD = FFD \frac{a + Rb}{a + Rb + c}, \quad (4.11)$$

where c is the distance between the pin holes and the front face. The rotation factor R is the distance between the crack tip and the center of rotation divided by b . The center of rotation is the point on the ligament where the loading in the crack plane changes from tension closer to the crack tip to compression in the direction of the specimen backside.

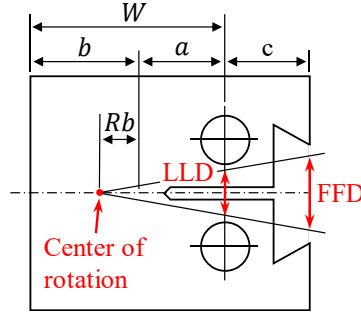


Figure 4.19: Schematic of the modified MCT geometry showing method of linear interpolation for front face to load line displacement conversion

Choosing an adequate value for R is difficult as the rotation factor is not constant during a test. Additionally, the linear interpolation in Equation (4.11) is only an approximation for small rotation angles and becomes less accurate for large rotations. Nonetheless, a constant rotation factor of 0.33 is recommended by Landes, supposedly leading to an error of less than one percent in the value of J for most cases. In ASTM E1921, a constant conversion factor LLD/FFD of 0.73 is specified for the standard CT geometry, corresponding to a rotation factor of 0.352 if $a_0/W = 0.5$ is assumed. With this rotation factor, a conversion factor of 0.607 is obtained for the modified MCT geometry used in this work.

To verify the applicability of the specified conversion factor for the tests within the DBT region, elastoplastic simulations with a stationary crack are carried out using the FE-model described in Section 5.2.1. The material properties for -60°C are used and the cohesive elements are removed from the model since crack growth is not taken into account. Four simulations with varying initial crack lengths a_0 , as listed in Table 4.4, are performed and the resulting front face to load line conversion factors are compared in Figure 4.20 (a) to the values obtained using Equation (4.11). The simulated conversion factors are represented by the solid lines, while the dotted lines show the corresponding analytically determined (constant) factors. For all initial crack lengths, the simulated conversion factors increase monotonically with pin displacement. At low pin displacements the increase is more pronounced as compared to pin displacements close to 0.6 mm. With increasing initial crack length, the influence of the pin displacement on the conversion factor is reduced. The analytically determined conversion factors using $Rb = 0.352 \cdot b$ describe the mean behavior of the simulated curves well and can therefore be viewed as “effective” conversion factors for the respective initial crack lengths.

Table 4.4: Geometric parameters used for the stationary crack simulations and corresponding conversion factors obtained from Equation (4.11)

Simulation	W [mm]	c [mm]	a_0 [mm]	b_0 [mm]	a_0/W [-]	LLD/FFD [-]
1	8	3.5	3.6	4.4	0.45	0.595
2	8	3.5	4.0	4.0	0.50	0.607
3	8	3.5	4.4	3.6	0.55	0.618
4	8	3.5	5.2	2.8	0.65	0.639

By using a constant conversion factor, an error is introduced into the K_J values determined by means of ASTM E1921. In Figure 4.20 (b), the K_J curves from the simulations with varying initial crack lengths are plotted against the pin displacement. While the solid lines show the K_J curves determined using the simulated LLD, the dotted lines are obtained using the simulated FFD multiplied with the respective constant conversion factor. For all initial crack lengths, the dotted lines are slightly below the solid lines. With decreasing crack length, the error introduced by the displacement conversion increases. For $a_0/W = 0.45$, the maximum error at a pin displacement of 0.6 mm is 2.3%.

In some situations, this error may cause a K_{Jc} result to be censored according to ASTM E1921 that would otherwise be uncensored. While this can have an influence on the number of specimens required for the determination of a valid reference temperature, using a constant conversion factor is still considered to be acceptable so as not to increase the complexity of the testing procedure. Furthermore, MCT specimens tested in the DBT region usually fracture at significantly lower displacements than 0.6 mm. At lower displacements, the error introduced by using a constant conversion factor is less pronounced.

For the determination of the J-R curve following ASTM E1820, the influence of crack extension on the conversion factor must be investigated. A crack growth simulation with cohesive elements is performed at RT using the MCT model described in Section 5.2.1 with $a_0/W = 0.5$. For the cohesive strength a value of 1850 MPa is assumed, while a value of 3 N/mm is used for the cohesive energy. The simulation is stopped at a pin displacement of 4 mm, at which a total crack extension Δa of 1.43 mm is obtained. In Figure 4.21 (a), the simulated conversion factor is compared to the constant factor of 0.607, which is used for the tests within the DBT region, and a constant factor of 0.632 resulting from Equation (4.11) with $R = 0.5$. The conversion factor of 0.607 is surpassed by the simulated value at a pin displacement of 0.24 mm. It is clear that this conversion factor is less accurate for ductile tearing tests as compared to tests that are terminated at low displacements by unstable fracture. An overall better representation of the simulated conversion factor is obtained using the constant factor of 0.632.

In Figure 4.21 (b), the crack resistance curves using the LLD and the converted FFD are shown. While the curves are similar at small crack extensions, a relative decrease in the J-integral using the converted FFD is observed with increasing crack growth. At the final crack extension of 1.43 mm, the error in J introduced by using a conversion factor of 0.607 is 8.7%. Using the factor 0.632 reduces this error to 5.0%. While this is still a substantial difference to the J-integral obtained from the LLD, it is considered an acceptable error as the aim of this work is not to determine the material's fracture toughness experimentally as accurately as possible, but to develop a numerical method to predict the experimental J-R curve as closely as possible.

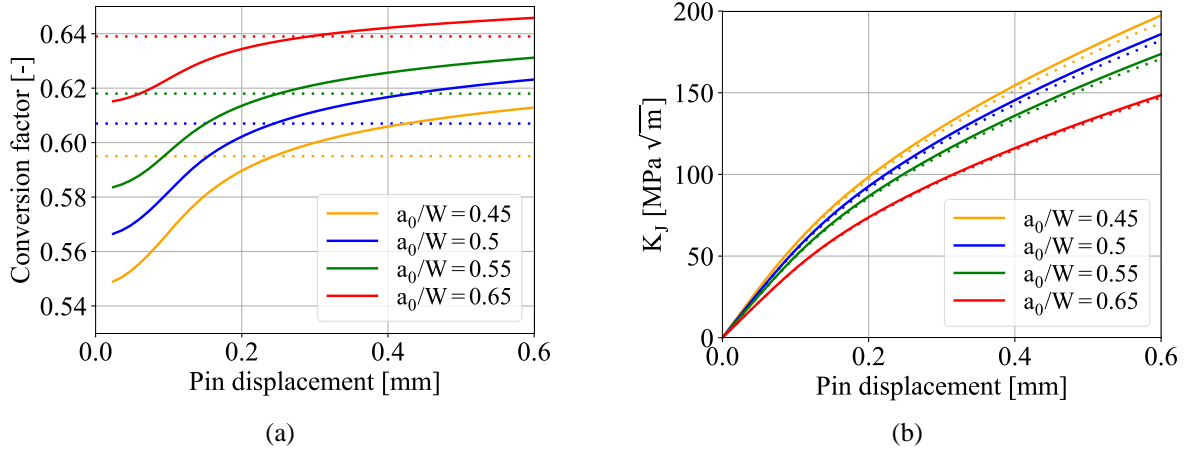


Figure 4.20: Simulated conversion factors (solid lines) and constant conversion factors (dotted lines) for different initial crack lengths (a) and K_I curves obtained using the LLD (solid lines) and the converted FFD (dotted lines) (b)

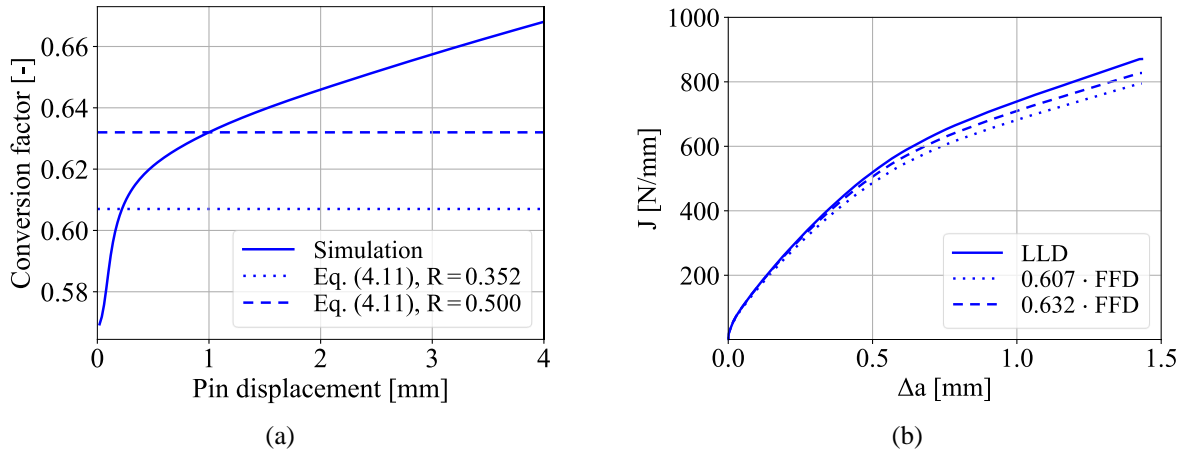


Figure 4.21: Simulated and constant conversion factors under the influence of crack growth (a) and J-R curves obtained using the LLD and the converted FFD (b)

4.3.5 Testing within the DBT region

Fatigue pre-cracked MCT specimens were tested within the DBT to determine the reference temperature T_0 , which is required for the evaluation of the fracture toughness Master Curve following ASTM E1921. The testing standard was described in Section 2.2.1. Additionally, the MCT tests are necessary to obtain samples for the fractographic analyses in Section 4.4. The median fracture toughness values from the Master Curve are used in Chapter 5 to identify the cohesive energy for the low-temperature fracture mechanics simulations, while the results of the quantitative fractographic analyses are used in Chapter 7 for the development of the probabilistic cohesive zone model.

4.3.5.1 Test temperature selection

An important aspect of testing sub-sized specimens for the determination of the reference temperature is the selection of appropriate test temperatures to minimize the volume of material required. Given that tests performed at temperatures close to and above T_0 contribute the most to meeting the data set size criterion in Equation (2.19), the test temperature should be chosen as high as possible without producing an excessive amount of censored K_{Ic} results. This is especially relevant for sub-sized specimens as

due to their inherent low constraint, the $K_{Jc,limit}$ is often surpassed even at temperatures well below T_0 [8]. Consequently, the width of the optimal test temperature range for determining a valid T_0 using as few sub-sized specimens as possible can be as narrow as 20°C. Since the exact reference temperature is generally not known before testing, finding the optimal test temperature range can be challenging. In the standard, it is recommended to select the test temperatures to be close to that at which the $K_{Jc,med}$ value will be $100 \text{ MPa}\sqrt{\text{m}}$.

As mentioned in Section 4.1.2, a value of $T_0 = -43^\circ\text{C}$ was determined for the given RPV steel in a previous study by CIEMAT using large CT specimens. Due to the described material inhomogeneities, this value is not fully representative of the fracture mechanical behavior of the material used in this work. Nonetheless, it was used as an orientation to select the initial test temperature for the MCT tests. The first tests were conducted at -80°C to avoid censoring of K_{Jc} results. After each test, the complete data set was used to calculate the provisional T_{0Q} . Based on the result, the temperature for further testing was selected. As the K_{Jc} values obtained at -80°C were well below the $K_{Jc,limit}$ at that temperature, subsequent tests were performed at -70 , -60 , -45 and -30°C .

4.3.5.2 Fracture toughness determination

In total, 27 MCT tests were performed for the determination of T_0 following ASTM E1921. A cross-head velocity of 0.002 mm/s was used, resulting in an elastic K -rate of $0.44 \text{ MPa}\sqrt{\text{m}}/\text{s}$. As explained in Section 4.3.3, two test results are invalid due to the fatigue pre-cracks of specimens MCT14 and MCT21 not meeting the straightness requirements specified in the standard. Furthermore, none of the three tests performed at -30°C terminated in cleavage fracture, so these tests are also considered invalid. In Figure 4.22, the force-LLD curves obtained from the remaining 22 tests are shown. The LLD is calculated for each test individually using Equation (4.11) with the respective initial crack length a_0 from Table A.4 and a rotation factor of 0.352. As expected, the LLD at fracture decreases on average with decreasing temperature while the force increases. At all temperatures, significant scatter of the LLD at fracture is observed, which is particularly pronounced at -45 and -60°C . This scatter is the result of the inherently statistical nature of cleavage fracture within the DBT region as described in Section 2.3.1. In addition, force scatter is observed at the individual test temperatures, which is assumed to be mostly due to the varying initial crack lengths and pre-crack shapes of the specimens.

The fracture toughness is determined from each force-LLD curve individually. First, the critical J-integral at fracture J_c is obtained by calculating the sum of the elastic and plastic parts of J using Equations (2.10) and (2.13). The value of J_c is then transformed into the corresponding stress intensity factor K_{Jc} by means of Equation (2.14). Following the ASTM standard, weakest-link statistics is applied to estimate the fracture toughness $K_{Jc,1T}$, as obtained from a CT specimen with 25 mm thickness, from the K_{Jc} value. Thereby, the size-correction formula in Equation (2.18) is applied. The J_c , K_{Jc} and $K_{Jc,1T}$ results from all valid MCT tests are listed in Table A.9.

In Table 4.5, the average $K_{Jc,1T}$ and the corresponding standard deviation for each test temperature are shown. With decreasing temperature, a significant reduction of the average fracture toughness is observed. This reduction is less pronounced between -70 and -80°C , indicating that the lower shelf of the transition region is approached in this temperature range. Likewise, the standard deviation of $K_{Jc,1T}$ decreases rapidly from -45 to -70°C . Between 70 and -80°C , a slight increase of the standard deviation is observed, which can be attributed to the small sample size. The reduced scatter below -60°C is a further indication of the lower shelf being approached.

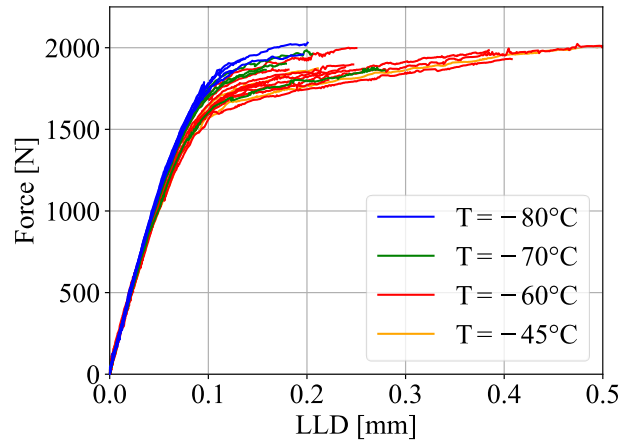


Figure 4.22: Force-LLD curves from the MCT tests used for the determination of T_0

Table 4.5: Average $K_{Jc,1T}$ and corresponding standard deviation obtained from the valid MCT tests for each test temperature

T [°C]	N_{tests} [-]	Avg. $K_{Jc,1T}$ [MPa $\sqrt{\text{m}}$]	Std. dev. of $K_{Jc,1T}$ [MPa $\sqrt{\text{m}}$]
-45	3	101.21	33.83
-60	9	82.17	24.87
-70	4	61.29	7.86
-80	6	55.75	10.17

4.3.5.3 Master Curve evaluation

Before the reference temperature T_0 is calculated and the Master Curve can be established, the K_{Jc} values obtained from the MCT tests must undergo the censoring procedure specified in ASTM E1921 and described in Section 2.2.1. The K_{Jc} results of specimens MCT11 and MCT13 tested at -60°C and MCT28 and MCT30 tested at -45°C surpass their respective $K_{Jc,\text{limit}}$ values (Equation (2.17)) and are therefore replaced by the limit. In Table A.9, the $K_{Jc,\text{limit}}$ values are listed for all specimens. Data censoring due to stable crack growth is not required as no specimen shows ductile crack extension Δa beyond the crack growth limit of 200 μm . The largest Δa was measured for specimen MCT30 with 190 μm . Most specimens failed without a significant amount of stable crack growth prior to cleavage fracture. For those specimens, the exact measurement of Δa was omitted.

Censored test results do not contribute to the data set size criterion in Equation (2.19) and should be avoided to reduce the number of specimens necessary to obtain a valid reference temperature. With the uncensored and censored $K_{Jc,1T}$ results a provisional T_{0Q} is calculated. The provisional value is replaced by the valid T_0 if the data set size criterion is met. A total of 18 uncensored $K_{Jc,1T}$ values are obtained from the MCT tests and their contributions r_i are listed in Table 4.6. The criterion yields a value of 2.42 for the data set size, which is well above the required minimum of 1. Therefore, the data set is considered large enough to determine the reference temperature with sufficient accuracy and T_{0Q} is replaced by T_0 . For the material SA-508 Cl.3, a reference temperature of -31.5°C is obtained with a standard deviation of 6.2°C .

Table 4.6: Contributions of the MCT tests to the data set size criterion in Equation (2.19)

$T - T_0$ [°C]	n_i [-]	r_i [-]
50 to -14	1/6	1
-15 to -35	1/7	7
-36 to -50	1/8	10

Applying Equation (2.20), the median fracture toughness of the material can be calculated from T_0 at any temperature in the lower transition region, resulting in the Master Curve shown in Figure 4.23. In addition to the Master Curve, the uncensored and censored values of $K_{Jc,1T}$, the $K_{Jc,limit}$ and the 5% and 95% tolerance bounds are displayed in the diagram. The tolerance bounds are computed from the corresponding equations in the standard.

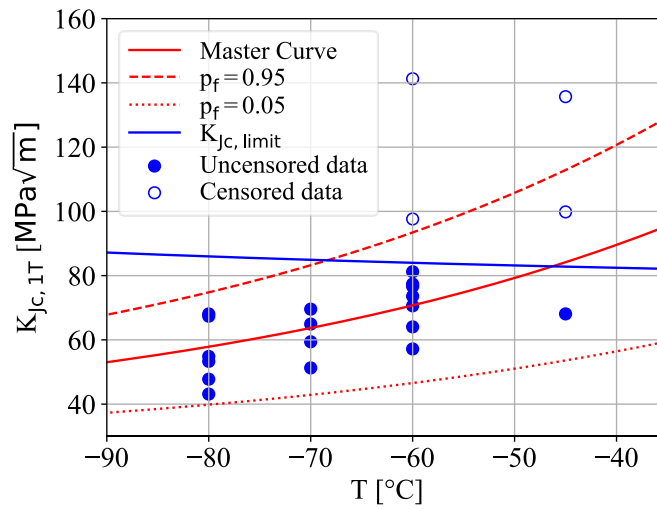


Figure 4.23: Fracture toughness Master Curve for SA-508 Cl.3 established from the uncensored and censored $K_{Jc,1T}$ results obtained from testing MCT specimens between -80 and -45°C

Apart from three $K_{Jc,1T}$ values, all data points are within the specified tolerances. The outliers were obtained at -45 and -60°C and show significantly increased fracture toughness values as compared to the other data points at these temperatures. This scatter towards higher fracture toughness is due to increasing macroscopic plastic deformation, which leads to a loss of constraint at the crack tip, reducing the probability of cleavage initiation.

Following the standard, the data set used for the determination of T_0 can be further analyzed to evaluate the macroscopic inhomogeneity of the material based on the SINTAP method [101]. A screening criterion is specified that decides whether the material is homogeneous or inhomogeneous. If the material violates the screening criterion, further assessment of the inhomogeneity and the determined fracture toughness results is required. The given data set meets the screening criterion and is therefore considered macroscopically homogeneous. For the calculations within the screening procedure, the reader is referred to the ASTM E1921 standard.

The determination of T_0 for SA-508 Cl.3 using MCT specimens was performed within the scope of a round robin exercise between four European research institutes as part of the FRACTESUS project. A detailed description of the round robin is given in [102]. Besides the reference temperature of -30.4°C determined by KIT (the tests at -45°C are not included at this point), the other participants obtained T_0

values of -38.0, -53.3 and -58.2°C. The significant deviations in T_0 are assumed to be due to macroscopic material inhomogeneities, as the material tested by KIT was extracted from a different location of the RPV closure head forging compared to the testing material received by the other participants. These inhomogeneities are believed to be the result of differences in the cooling rate during quenching due to the large thickness of the forging.

Experimental testing of 0.5T and 1T CT specimens from SA-508 Cl.3 steel for the determination of T_0 was performed by CIEMAT within the scope of the SOTERIA project [103]. The specimens were cut from different sections of the closure head forging and a reference temperature of -43.0°C was obtained. This value is 11.5°C below the T_0 of -31.5°C determined on small specimens in this work. Due to the aforementioned material inhomogeneities, the reference temperatures are not directly comparable. However, a comparison can be made between the T_0 obtained from large specimens and the T_0 of all MCT tests performed within the scope of the FRACTESUS round robin, since the MCT specimens were also cut from multiple different sections of the forging. The T_0 of the MCT tests is -45.6°C, which is 2.6°C below the large specimen T_0 . In comparison, Scibetta et al. (2002) [6] found a small specimen bias of 8.5°C below the T_0 obtained from large specimens. By showing that the difference between the reference temperatures is even smaller than the expected bias, a step is made towards verifying the MCT geometry to be used for the evaluation of fracture toughness in the DBT region.

4.3.5.4 Test temperature recommendations

In the Introduction, it was explained that the main goal of this research is to reduce the amount of material required for determining the fracture toughness of RPV steels within the DBT region. To achieve this goal, the primary objective is to develop a numerical model to predict the experimental fracture toughness, thus minimizing the number of tests. While predictive models offer the possibility to reduce material requirements significantly in the future, there is the potential to improve current testing requirements and recommendations by focusing specifically on small specimen testing.

The results of the Master Curve evaluation using MCT specimens show that the test temperature selection has a large impact on the number of specimens required to meet the data set size criterion. As mentioned in Section 4.3.5.1, it is recommended in the standard to select the test temperatures to be close to that at which the median fracture toughness, $K_{Jc,1T,med}$, will be $100 \text{ MPa}\sqrt{\text{m}}$ for the given specimen size. Thereby, the optimal test temperature for the given material and specimen geometry would be about -60°C. The $K_{Jc,1T,limit}$ at this temperature is $125.6 \text{ MPa}\sqrt{\text{m}}$, which is $25.6 \text{ MPa}\sqrt{\text{m}}$ above the median fracture toughness, while the standard deviation of $K_{Jc,1T}$ obtained from the nine tests performed at -60°C is $24.87 \text{ MPa}\sqrt{\text{m}}$. Consequently, it must be assumed that when testing at this recommended temperature, a considerable proportion of the results may require censoring. This is reflected in the fact that two out of the nine K_{Jc} values obtained from the MCT tests at -60°C had to be censored.

While the test temperature recommendation in ASTM E1921 may be suitable for larger specimens, it is suggested here that for the MCT geometry, a temperature should be selected with a $K_{Jc,1T,med}$ closer to $90 \text{ MPa}\sqrt{\text{m}}$. This value corresponds to an optimal test temperature of -70°C for the material and specimens used in this work. At this temperature, the $K_{Jc,1T,limit}$ is about $43 \text{ MPa}\sqrt{\text{m}}$ above the median value, while the standard deviation of $K_{Jc,1T}$ is only $7.86 \text{ MPa}\sqrt{\text{m}}$. Therefore, the number of censored data points is expected to be greatly reduced. The exact value of the optimal test temperature naturally depends on the yield strength of the material, whereby materials with higher yield strength have a greater $K_{Jc,limit}$ and are therefore better suited for testing at higher temperatures.

In general, the $K_{Jc,1T,med}$ is not known prior to testing. It is therefore possible that a significant number of tests must be dedicated to finding the optimal test temperature. The choice is to either start at a high temperature and decrease it for subsequent tests if the K_{Jc} values require censoring, or to start at a low temperature and increase it to obtain fracture toughness values that contribute more to the data set size criterion. The ASTM standard does not give recommendations for the initial test temperature when using miniaturized specimens. It is advisable to start at a low temperature as the fracture toughness scatter is much smaller on the lower shelf compared to the transition region. This means that a K_{Jc} result obtained on the lower shelf is more likely to represent the mean fracture behavior of the material at the selected test temperature. In the transition region, outliers may lead to false estimations of the location of T_0 on the temperature axis. In addition, specimens tested within the transition region may not fail by cleavage fracture if the selected test temperature is too high. In this case, no estimation can be made of the location of T_0 and the specimen is wasted.

4.3.6 Testing on the upper shelf

Fracture mechanics testing on the upper shelf is required for the calibration of the cohesive energy for ductile fracture in Section 5.2.2. The cohesive energy is identified by fitting the simulated force-LLD and J-R curves to the experimental curves, which are determined in this section. Since only the curves are required, it is not necessary to determine an upper shelf fracture toughness value for the material. It can be assumed that any fracture toughness value determined following ASTM E1820 would be invalid due to violating the specimen size requirements specified in the standard. The cohesive elements with ductile fracture properties will be used for the probabilistic CZM approach described in Chapter 3.

4.3.6.1 Force-displacement curves

As with the tests conducted within the DBT region, the pre-cracked MCT specimens were loaded with a K -rate of $0.44 \text{ MPa}\sqrt{\text{m/s}}$, resulting from a crosshead velocity of 0.002 mm/s . All tests were carried out at RT. The basic procedure specified in ASTM E1820 was applied, meaning that multiple specimens were loaded to varying crosshead displacements, unloaded, and broken using liquid nitrogen to induce brittle fracture. To obtain the load line displacements required for the calculation of J , the measured front face displacements are multiplied with a conversion factor of 0.632, resulting from Equation (4.11) with the rotation factor $R = 0.5$.

A total of eight MCT specimens were loaded to crosshead displacements between 1 and 6 mm for the determination of the J-R curve. The targeted displacements for each test are listed in Table A.10. In Figure 4.24, the force-LLD curves obtained from the tests are shown. Beyond the elastic regime, the maximum force is reached at a LLD of about 1 mm. The compliance of the specimens increases with increasing crack length, causing the force to decrease with further loading. A significant scatter of the maximum force values is observed in a range of about 200 N around the average maximum force of 2030 N. This scatter is assumed to be caused by the different initial crack lengths and pre-crack shapes of the specimens.

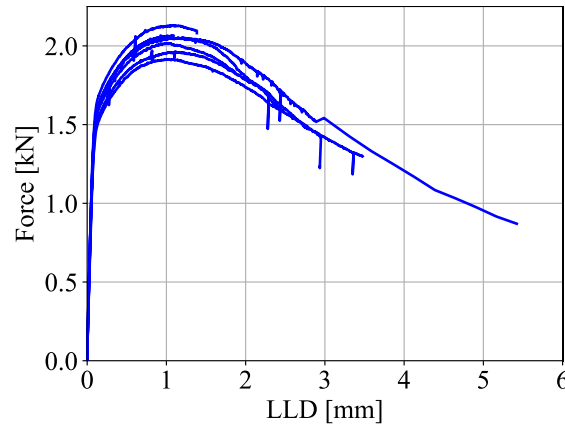


Figure 4.24: Force-LLD curves obtained from the tests on MCT specimens at RT

4.3.6.2 Ductile crack extension

As described in Section 4.3.3, the specimens were heat-tinted after testing and broken using liquid nitrogen. The fatigue pre-crack length and ductile crack extension Δa were measured by means of optical microscopy. The crack extension Δa is defined as the difference between the final physical crack length a_p and the initial crack length a_0 . For measuring a_p , the same procedure is applied as for measuring a_0 , but the nine measurements end at the tip of the ductile crack instead of the tip of the fatigue pre-crack. Additionally, the uniform distance between the measurement points in thickness direction is compressed to account for the thickness reduction of the specimens caused by necking.

In Figure 4.25, the fracture surfaces of four MCT specimens tested at RT with final crosshead displacements between 1 to 6 mm are shown. The dark purple strips in the center of the images are the regions of ductile crack extension. Below are the fatigue pre-cracks in a lighter hue of purple, while the gray, glossy regions above are the final brittle fractures induced by impact loading. The measured values for Δa are listed in Table A.10 for all specimens tested at RT.

With increasing CHD, increased necking is observed at the tips of the ductile cracks, resulting from the plane stress condition at the side surfaces of the specimens. A pronounced tunneling effect is observed in the ductile crack extension, with the crack growing faster in the center of the specimens as compared to the side surfaces. In Figure 4.25 (d), it can be seen that at large displacements, the crack in the center is caught up and even surpassed at the side surfaces. The tunneling of the crack front can also be explained by the constraint effect, as in the center of the specimens, plastic deformation is constrained by the surrounding material and more strain energy is available for crack propagation.

In ASTM E1820, straightness requirements are specified not only for the fatigue pre-crack but also for the front of the ductile crack in order to obtain valid test results. Side-grooving is a commonly applied measure to increase the constraint at the side surfaces and therefore improve the straightness of the ductile crack. The addition of side grooves was not considered for the MCT specimens tested at RT since the objective of these tests is not to obtain valid fracture toughness data, but to identify the cohesive energy for ductile fracture.

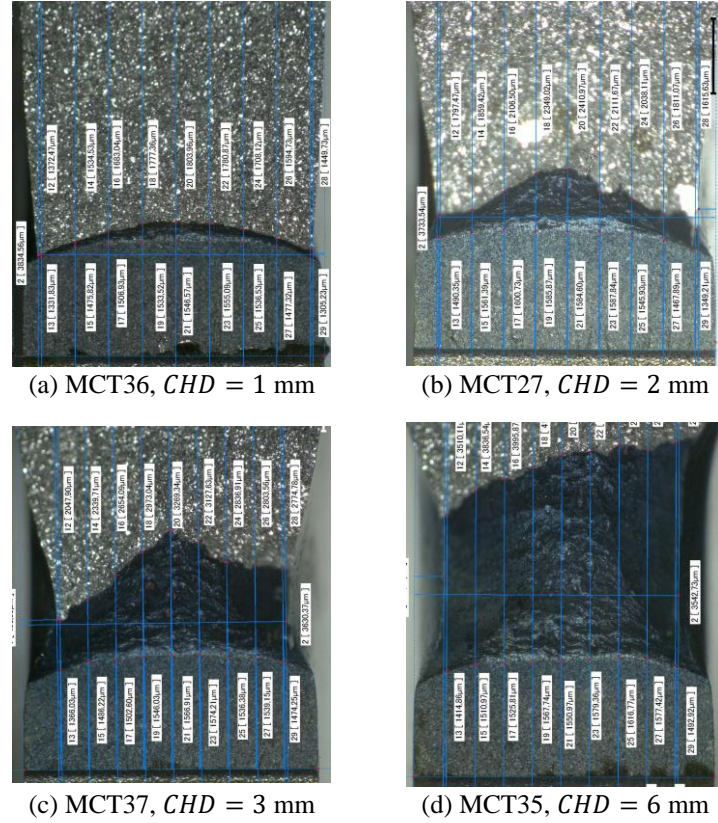


Figure 4.25: Fracture surfaces of four MCT specimens tested at RT with final crosshead displacements between 1 and 6 mm

4.3.6.3 J-R curve determination

In addition to the force-LLD curves, the experimental J-R curve is required for a complete characterization of the macroscopic fracture mechanical behavior of the material at RT. The calibration of the cohesive energy in Section 5.2.2 is performed by fitting both the numerical force-LLD and J-R curves to the experimental results. As with the tests performed within the DBT region, the J-integral is calculated for each test using the respective force and displacement data. By means of Equations (2.10) and (2.13), the elastic and plastic parts of the J-integral are determined, which are then added together to obtain J . According to ASTM E1820, crack propagation must be taken into account by applying a correction factor to the plastic part of J depending on the ductile crack length. The correction factors and corrected J values obtained from the MCT tests at RT are listed in Table A.10.

In Figure 4.26, the crack growth corrected J values are displayed against Δa . As expected, the J-integral increases with increasing crack length, with a maximum J of 996 N/mm measured at a ductile crack extension of 2.64 mm. The data points are fitted with a power law function of the form

$$J = C_1 \Delta a^{C_2}, \quad (4.12)$$

where $C_1 = 631.6 \text{ N/mm}^2$ and $C_2 = 0.487$ are the fitting parameters obtained using the method of least squares. In addition to the J-R curve, the maximum J-integral capacity $J_{\max} = 201.6 \text{ N/mm}$ and the maximum crack extension capacity $\Delta a_{\max} = 1 \text{ mm}$, as determined by Equations (2.22) and (2.23) for the MCT geometry, are shown in Figure 4.26. All data points obtained from the MCT tests surpass the J-integral capacity of the geometry, which is not surprising since the standard is not designed for testing miniaturized specimens with low constraint. The calculation of a provisional fracture toughness value K_Q is not performed here, as it is not required for the identification of the cohesive energy.

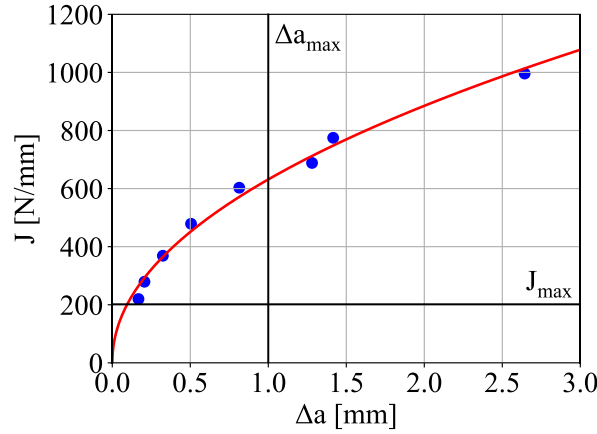


Figure 4.26: J-R curve for SA-508 Cl.3 at RT obtained by testing MCT specimens

4.4 SEM fractography

Fractographic studies are carried out on the broken halves of the MCT specimens tested within the DBT region to gain additional insight into the fracture processes in front of the crack tip. SEM is suitable for this purpose as it allows for a clear distinction between individual cleavage facets and regions of ductile crack propagation on the fracture surfaces. By tracing the river patterns visible on the cleavage facets, the initiation sites of unstable fracture are localized and characterized in Section 4.4.1. The locations of the cleavage initiation sites are related to the mechanical fields obtained from FE-simulations to assess the conditions for unstable fracture. In addition, energy-dispersive X-ray (EDX) analysis is applied to identify initiating particles, such as carbide or sulfide inclusions.

In Section 4.4.2, the fracture surfaces are analyzed quantitatively regarding the respective ratios of cleavage facets and regions of ductile fracture. The ratio of the ductile fracture area is correlated with the test temperature and the fracture toughness values obtained from the MCT tests. This quantitative analysis of the fracture surfaces is required for the development of the probabilistic CZM in Chapter 7, as the number of ductile and brittle cohesive elements within the cohesive zone will be based on the ratio between the ductile fracture area and the total fracture area.

All micrographs were taken by means of a ZEISS EVO10 SEM with a tungsten filament using both the secondary and backscattered electron detectors and an acceleration voltage of 20 kV. The samples were subjected to ultrasonic cleaning in isopropanol for two minutes to remove dust and loose particles from the fracture surfaces.

4.4.1 Cleavage initiation sites

Identification of the cleavage initiation sites is possible when the main fracture mode is transgranular cleavage, which is the case for all MCT specimens tested at -45°C and below. The approach by Chekhonin et al. (2023) [104] is applied to locate the initiation sites in Section 4.4.1.1 and to characterize them based on the types of initiators in Section 4.4.1.3. Once an initiation site is found, high-magnification micrographs are taken to reveal possible initiating particles. If a particle is suspected to be present at the center of an initiation site, EDX point measurements are carried out to identify the

composition of the particle. The initiation site locations are related to the numerical stress and triaxiality fields in the vicinity of the crack front in Section 4.4.1.2 to assess the constraint conditions at fracture.

4.4.1.1 Initiation site locations

In Figure 4.27, the procedure for locating the cleavage initiation sites is shown for specimen MCT08, which was tested at -70°C . In an overview image of the fracture surface at low magnification (a), the so-called “chevron markings”, which spread out from a distinctive area close to the crack front, can be clearly seen. The markings are revealed by differences in height and generally become weaker as the initiation site is approached.

In the next step, the magnification is progressively increased towards the initiation site (b) and the river lines visible on the individual cleavage facets are traced back until they converge at a single point or appear to circle around a grain boundary. In case of specimen MCT08, the river lines converge towards a single point. The same procedure is then performed for the other specimen half, as the mirrored image taken of the initiation site sometimes shows features that are not visible on the first fracture surface.

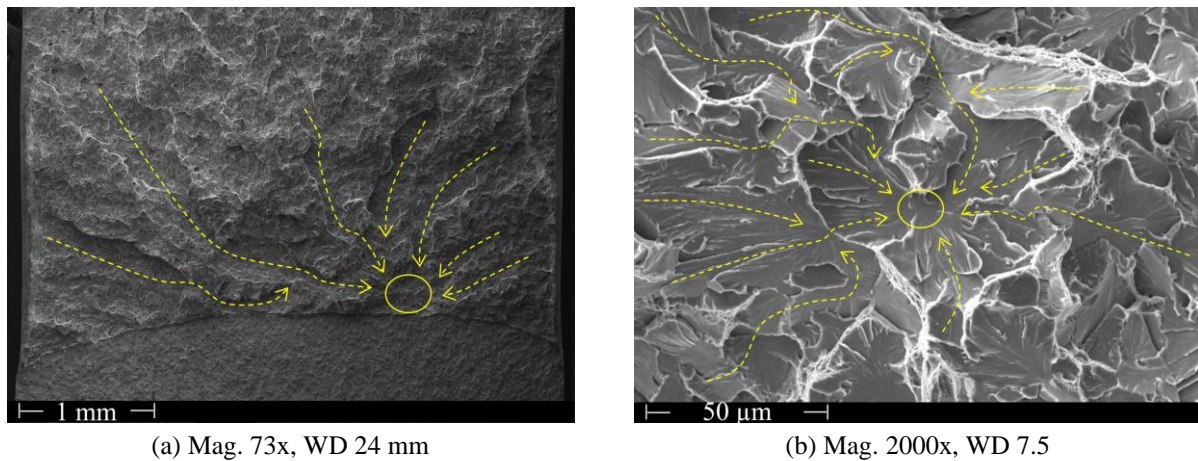


Figure 4.27: Procedure for locating the cleavage initiation site on the fracture surface of specimen MCT08 tested at -70°C

The approach described is generally unproblematic for specimens that were tested well below T_0 and failed at low values of K_{IC} , because their fracture surfaces consist almost exclusively of transgranular cleavage facets. The fracture surfaces of specimens tested closer to T_0 show a mixture of cleavage facets and regions of micro-void coalescence (quasi-cleavage) that cause the local crack growth direction to vary significantly. As a result, there are often several candidates for initiation sites in close proximity to each other, making it difficult to identify the main initiator. Therefore, the initiation sites could not be located for specimens MCT09, MCT11 and MCT12 tested at -60°C . As an example, a micrograph of the expected location of the initiation site of specimen MCT12 is shown in Figure 4.28. Tracing the river lines visible on the cleavage facets it is observed that, while most of them point towards a specific region, they do not converge towards a particular point or grain boundary that can be determined to be the initiator.

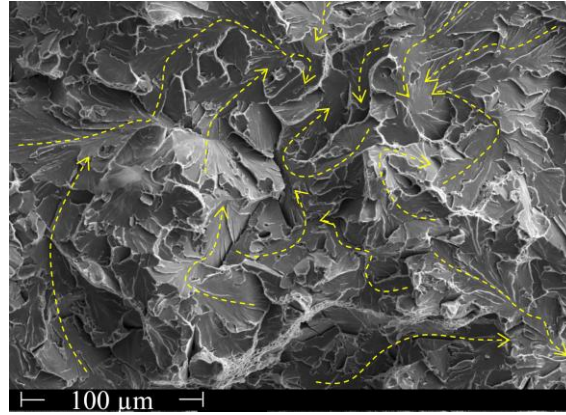


Figure 4.28: Expected location of the initiation site of specimen MCT12 with river lines not pointing towards a particular point or grain boundary

In Figure 4.29 (a), the locations of all cleavage initiation sites found on the fracture surfaces are shown. The initiation sites are located less than 1 mm from the center of the 4 mm thick specimens. Within this range, the distance from the mid thickness shows considerable scatter, which appears to be uncorrelated to the testing temperature. The measurements agree with a study performed by Wallin et al. (2016) [105], who also analyzed the initiation site locations on the fracture surfaces of MCT specimens of the same material tested within the DBT region. All initiation sites being located near the mid thickness is assumed to be due to the reduced constraint at the side surfaces. To show that cleavage initiation occurs under high constraint conditions, numerical simulations are required to assess the stress and triaxiality fields in the crack plane.

The distance from the crack front is determined by measuring the distance from the local tip of the ductile crack extension to the initiation site in crack growth direction. The median distance of the initiation sites from the crack front is 66.2 μm . Most initiation sites are located around this distance with measurements ranging from 27 to 83 μm . There are four outliers showing significantly greater distances from the crack front of up to 221 μm . As with the distance from the mid thickness, the distance from the crack front appears to be uncorrelated to the testing temperature, but the scatter is more pronounced at -60 and -45°C. The same observation was made for the $K_{Jc,1T}$ results from the MCT tests in Section 4.3.5.2.

In Figure 4.29 (b), the distance of the initiation sites from the crack front is related to the fracture toughness test results. A positive correlation with $R = 0.72$ is found by means of linear regression, meaning that on average, the distance to the crack front increases with increasing $K_{Jc,1T}$. It is observed that the correlation is strong for $K_{Jc,1T}$ results below 75 $\text{MPa}\sqrt{\text{m}}$, but weakens beyond this value. The exact locations of the initiation sites and the corresponding fracture toughness values are listed in Table A.11. In Section 4.4.1.2, the stress and triaxiality levels close to the crack front are determined numerically to assess the loading and constraint conditions at the initiation sites.

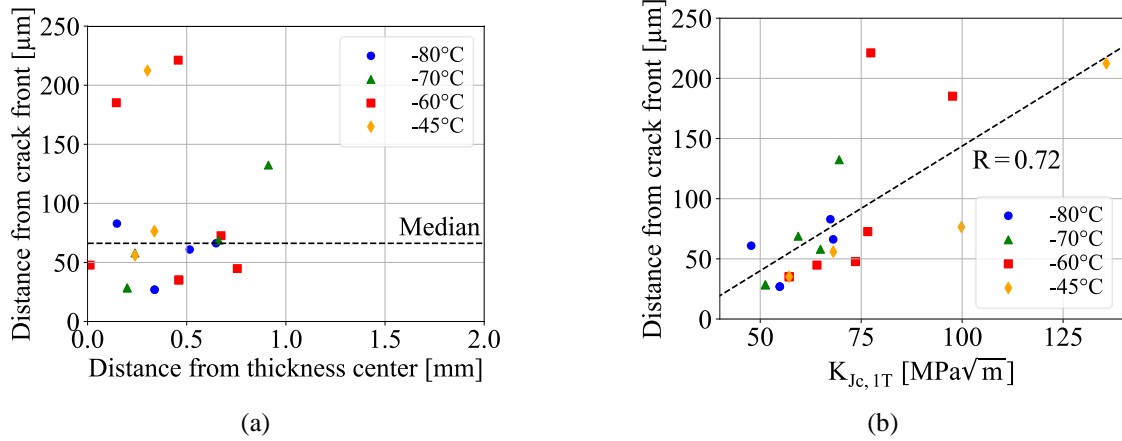


Figure 4.29: Locations of the cleavage initiation sites on the fracture surfaces (a) and correlation between $K_{Jc,1T}$ and the distance from the crack front (b)

4.4.1.2 Stress and triaxiality fields near the crack front

Following Ritchie et al. (1973) [53], the condition for cleavage fracture is that the local maximum principal stress ahead of a stress concentrator exceeds a critical value over a characteristic distance. This critical fracture stress is assumed to be insensitive to temperature. By relating the initiation site locations in Figure 4.29 (a) to the numerical stress fields in the crack plane at fracture load, the fracture stress can be determined for each test.

First, the development of the maximum principal stress σ_1 and triaxiality h along the ligament and in thickness direction is investigated. For the simulations, the FE-model described in Section 5.2.1 is used without cohesive elements, as none of the MCT specimens tested at -45°C and below experienced significant ductile crack extension. Figure 4.30 (a) shows the evolution of σ_1 near the crack front in the center of the specimen at -60°C . In the diagram, x denotes the distance from the crack front in the direction of the specimen backside. The maximum σ_1 increases up to an LLD of about 0.4 mm and decreases slightly at larger displacements. Additionally, with increasing displacement, the peak of σ_1 is being shifted away from the crack front and the stress is distributed more evenly, resulting in a flattening of the curve. Apart from slightly different σ_1 values, the curves for -45 , -70 and -80°C are similar. As the maximum principal stress is assumed to be the driving factor for cleavage fracture, the distance of an initiation site from the crack front should correspond to the location of the peak of the maximum principal stress at fracture load. This was confirmed in Section 4.4.1.1, with Figure 4.29 (b) showing that the distance of the initiation sites from the crack front increases with increasing fracture toughness.

The triaxiality near the crack front, as shown in Figure 4.30 (b), decreases considerably with increasing displacement due to the inelastic deformation of the material. At the same time, the triaxiality peak is shifted away from the crack front similar to σ_1 . High constraint conditions promoting brittle fracture are assumed to be present when h is above a value of 2 [106]. At an LLD of 0.6 mm, the triaxiality peak barely reaches this value, indicating substantial constraint loss in front of the crack. This loss of constraint in combination with the reduction of the maximum principal stress at large displacements reduces the likelihood of cleavage initiation with increasing plastic deformation. Hence, none of the MCT tests performed at -30°C , where plastic deformation is expected to be most pronounced, terminated by cleavage fracture.

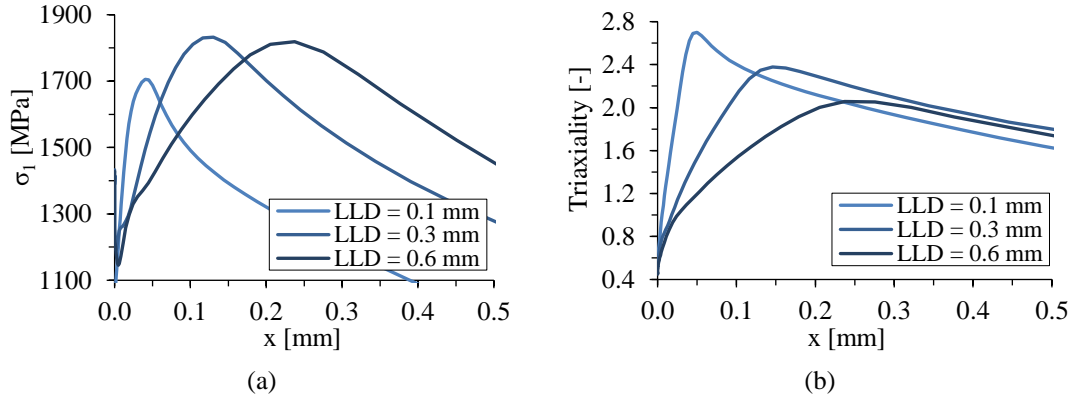


Figure 4.30: Development of the maximum principal stress (a) and triaxiality (b) along the ligament in the center of the specimen with increasing LLD at -60°C

The evolution of σ_1 (a) and h (b) along the thickness direction z starting from the center of the specimen is shown in Figure 4.31 for -60°C. In both cases, the maxima are located in the center and reduce towards the side surface. At an LLD of 0.1 mm, σ_1 is nearly constant up to a distance of 1 mm from the center, followed by a sharp decrease towards the side surface. With increasing displacement, the maximum principal stress increases in the center and reduces at the side surface, while the triaxiality reduces uniformly along the thickness direction. At small displacements, the triaxiality is above a value of 2 along almost the entire crack front, indicating high constraint conditions. The width of this area shrinks to about 0.5 mm at a displacement of 0.6 mm, again showing the considerable constraint loss of the MCT geometry under high load. This is reflected in the cleavage initiation sites being located close to the mid thickness of the specimens, as shown in Figure 4.29 (a).

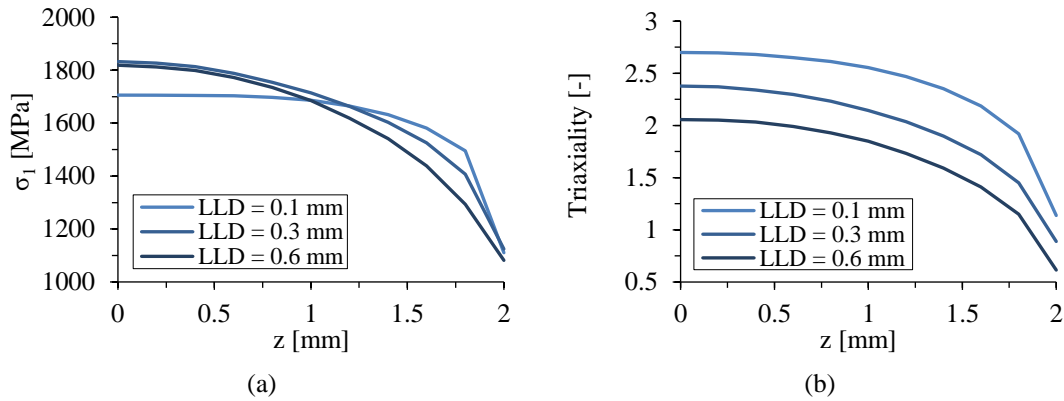


Figure 4.31: Development of the maximum principal stress (a) and triaxiality (b) along the thickness direction with increasing LLD at -60°C

The numerical investigations show that, while the MCT specimen can be regarded as a high constraint geometry at small displacements, constraint is lost with increasing load. This is assumed to be due to the onset of macroscopic plastic deformation. To ensure that the $K_{Jc,1T}$ results from MCT specimens are comparable to the values obtained from different specimen types and sizes, the fracture behavior should be sufficiently similar. This means that the cleavage initiation sites should be located within the high constraint region. The maximum principal stress and triaxiality values at the locations of the initiation sites at the respective fracture loads are listed in Table A.11. With the exception of MCT01 and MCT20, brittle fracture initiation occurred within the area where the triaxiality is greater than 2. In total, the triaxialities at the initiation sites range from 1.7 to 2.54. Additionally, most of the initiation

sites are located within 35 μm of the points on the ligament where the maxima of σ_1 and h are observed, confirming that cleavage initiation is strongly correlated to conditions of high stress and high triaxiality. From these results, it can be concluded that the fracture behavior of the MCT specimens is in accordance with theoretical expectations. MCT specimens should behave similar to larger CT geometries as long as excessive plastic deformation is avoided. This supports the recommendation in Section 4.3.5.4 to use a lower test temperature for miniaturized specimens as compared to the test temperature recommended in the ASTM E1921 standard.

4.4.1.3 Types of initiators

Brittle fracture initiation in bainitic steels was observed or is commonly presumed to happen at fractured precipitates, inclusions or grain boundaries [32,104,107,108]. Following the river pattern visible on the cleavage facets to its origin, two different characteristic appearances of initiation sites can be distinguished. The river lines either converge towards a single point from multiple directions, or they point towards a grain boundary from the direction of one facet, while the river lines of the surrounding facets appear to loop around the grain boundary.

In the first case, which is shown in Figure 4.32 (a, b), cleavage fracture was initiated at particle inclusions. From the fractured or de-bonded particles, which usually are too small to be seen on SEM micrographs, the crack extends in all directions simultaneously. The river lines pointing towards the initiation site generally become weaker as the initiation site is approached. Examples of grain boundary initiation are shown in Figure 4.32 (c, d). As the name suggests, micro-crack propagation is started along the length of a grain boundary, meaning that no exact point of initiation can be identified. The river lines on the surrounding cleavage facets represent a closed loop around this grain boundary, which usually appears as a topographic step. It is assumed that a micro-crack originating from a grain boundary will eventually find its way back to the initiation site. Since the crack plane changes with each grain, this will lead to the appearance of a step at the initial grain boundary [104].

The type of initiator was identified for 16 specimens, with nine initiation sites (56%) showing the characteristics of particle initiation and seven initiation sites (44%) being located at grain boundaries. The initiation sites of the remaining MCT specimens could not be characterized due to insufficient quality of the fracture surfaces or ambiguity of the river patterns. Chekhonin et al. (2023) [104] performed an extensive fractographic study on 41 broken MCT specimens of unirradiated A508 Cl.3 type RPV base metal steel. They found that 32% of the initiators were Mo-rich carbides, while 23% were Al-rich inclusions and 38% were grain boundary initiators. The increased proportion of grain boundary initiators found in the present work is likely due to the small sample size. In the following, the results of EDX spot measurements at the suspected locations of initiating particles are presented.

The working principle of EDX is that characteristic X-rays generated by the interaction of the specimen material with the primary electron beam are collected by an X-ray detector. The energy and intensity distribution of the signal is measured and analyzed to identify elements and their respective concentrations within the interaction volume of the electron beam. The interaction volume is determined by the acceleration voltage of the SEM and the density of the sample material [109]. For the given material and an acceleration voltage of 20 kV, the lateral spread of the electron beam is about 1.2 μm and it reaches a depth of 1.1 μm . This means that the spatial resolution for the EDX analysis is about 1 μm .

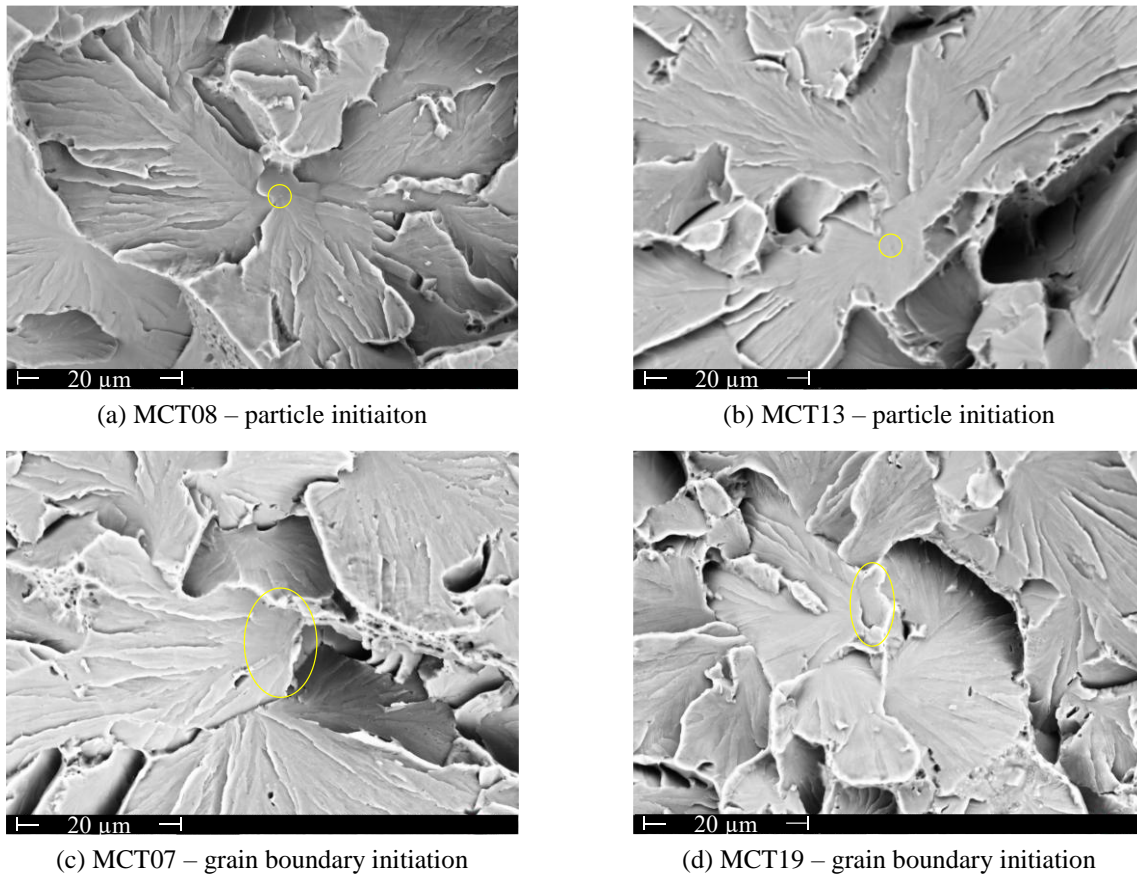


Figure 4.32: SEM micrographs (mag. 5000x) showing cleavage fracture initiation at particles (a, b) and at grain boundaries (c, d)

Several EDX spot measurements were carried out on both fracture surfaces of all MCT specimens showing particle initiation. First, one measurement of the matrix material close to each initiation site was taken as a reference. The reference spectrum of one fracture surface of specimen MCT08 is shown in Figure 4.33. Besides Fe, which naturally makes up most of the chemical composition of the steel, peaks can be identified for C, Si, S and Mn. In addition, trace amounts of Al, P, Cr, Ni and Mo are found. The spectrum is similar to the reference measurements taken from the other specimens.

Subsequent measurements were taken at the suspected locations of the initiating particles with about 1 μm distance between the individual spots. Except for specimen MCT08, no increased concentration of the non-metals C, N, O and S or any metals commonly found in inclusions, such as Al, Mn, Mo and Cr is found at any initiation site.

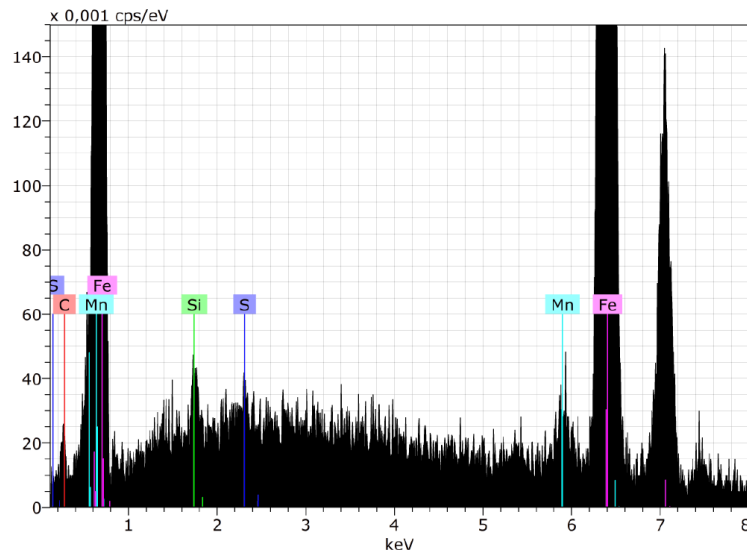


Figure 4.33: EDX reference spectrum of the steel matrix

In Figure 4.34, a spectrum of MCT08 at the initiation site is shown. Compared to the reference spectrum, increased concentrations of S and Mn are found, indicating the presence of an MnS inclusion. Figure 4.35 shows the position of the spot measurement at the particle and the reference measurement of the matrix. The inclusion is positioned at the point where the river lines of multiple cleavage facets converge. The concentrations of S and Mn at the initiation site are 1.01 and 5.07 wt.% respectively, while the reference measurement yields concentrations of 0.16 and 0.86 wt.%. Despite the considerable increase, the concentrations of the inclusion elements at the initiation site are very low compared to Fe. This means that the inclusion is significantly smaller than the interaction volume of the electron beam. An exact determination of the size of the inclusion is therefore not possible by means of EDX analysis. From the micrograph alone, it is difficult to identify the shape of the particle. The size can only be approximated to be less than 0.5 μm .

On the other fracture surface of the specimen MCT08, a similar concentration of S and Mn is found at the location of the initiation site. From this it can be concluded that micro-crack nucleation occurred by brittle fracture of the particle.

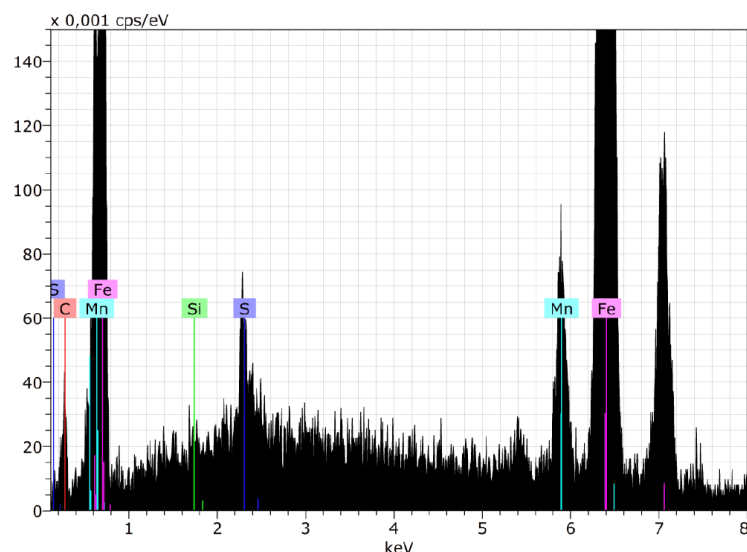


Figure 4.34: EDX spectrum of the initiating particle found on the fracture surface of MCT08

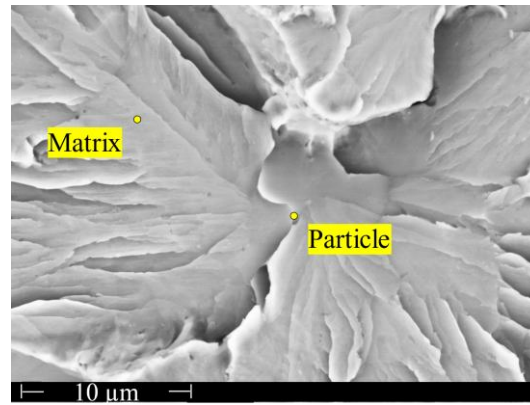


Figure 4.35: Location of the initiating particle on the fracture surface of MCT08

It is rarely possible to find the exact location of an initiating particle based on SEM micrographs, as they are usually very small in modern grades of RPV steels and often cannot be distinguished from the surrounding material. Finding the inclusions by means of EDX spot measurements is so time consuming that it is impractical for multiple specimens. For the purpose of this research, it is considered to be enough to find one initiating particle to show that inclusions can indeed be responsible for micro-crack nucleation and, eventually, unstable fracture of the structure. This again indicates that the fracture behavior of the MCT specimens is according to theoretical expectations, further strengthening the confidence in this geometry.

4.4.2 Quantitative analysis of the fracture surfaces

At the temperatures present in the lower transition region, the primary slip systems in BCC metals are not active and therefore, most grains in the vicinity of the crack front exhibit brittle behavior under load [110]. It is assumed that some grains are oriented favorably for the few active slip systems to allow dislocations to move, causing plastic deformation and eventually void nucleation, growth and coalescence. Hence, as explained in Section 3.2, the fracture surfaces of the MCT specimens that failed by cleavage fracture within the DBT region show a mixture of trans- and intergranular cleavage facets and regions of micro-void coalescence that appear to be randomly distributed.

A quantitative fractographic analysis of all MCT specimens tested for the evaluation of T_0 is performed to determine the ratio of ductile fracture with respect to the testing temperature and $K_{Jc,1T}$. The temperature-dependent ductile fracture ratio (DFR), which is the approximate ratio between the ductile fracture area and the total area of the fracture surface, is used in Chapter 7 for the mesoscale modeling of the cohesive zone. The method to determine the DFR of an individual specimen is shown in Figure 4.36. A total of 15 SEM micrographs are taken in a 3x5 pattern in front of the fatigue pre-crack, covering a length of 1.35 mm in crack growth direction and 3 mm in thickness direction. Within each micrograph, the fracture mode is determined at 16 equidistant locations, resulting in a total of 240 data points per fracture surface.

The fracture mode can be either trans- or intergranular cleavage, micro-void coalescence or secondary cracking. In some cases, parts of the fracture surface are covered in an oxide layer or dirt particles, or the surface itself was damaged in the process of inducing final fracture. Data points located in these regions do not contribute to the determination of the DFR. In Figure 4.37, an SEM micrograph of a fracture surface close to the fatigue pre-crack is shown, which is representative for the fracture surfaces of all MCT specimens tested within the transition region. The fracture surfaces consist mostly of trans-

granular cleavage facets. Regions of micro-void coalescence of varying size and shape, intergranular cleavage facets and secondary cracks are distributed randomly across the fracture surfaces. An accumulation of these fracture modes within a specific part of the investigated region is not observed.

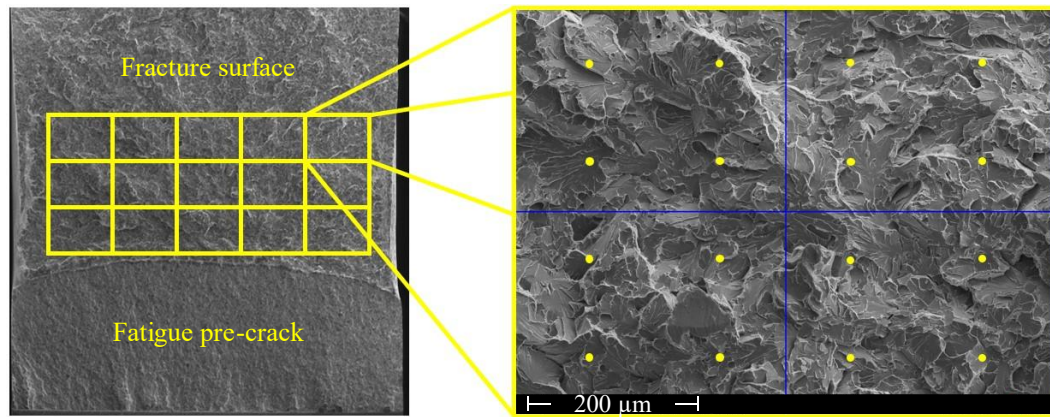


Figure 4.36: Determination of the DFR from 15 SEM micrographs (mag. 500x) arranged in a 3x5 pattern in front of the fatigue pre-crack with 16 equidistant data points per micrograph [99]

The distribution of the data points across the individual fracture modes is shown in Figure 4.38 for specimen MCT12, which was tested at -60°C . Approximately 87% of the data points are located within transgranular cleavage facets, followed by the regions of micro-void coalescence with 7.7%. While secondary cracks are not uncommon, their contribution to the total fracture area is small due to their small size. Grains that fractured along the grain boundaries by intergranular fracture are comparatively rare and make up about 1% of the fracture area on average. The distribution shown in Figure 4.39 is similar for all analyzed MCT specimens, the results of which are listed in Table A.12.

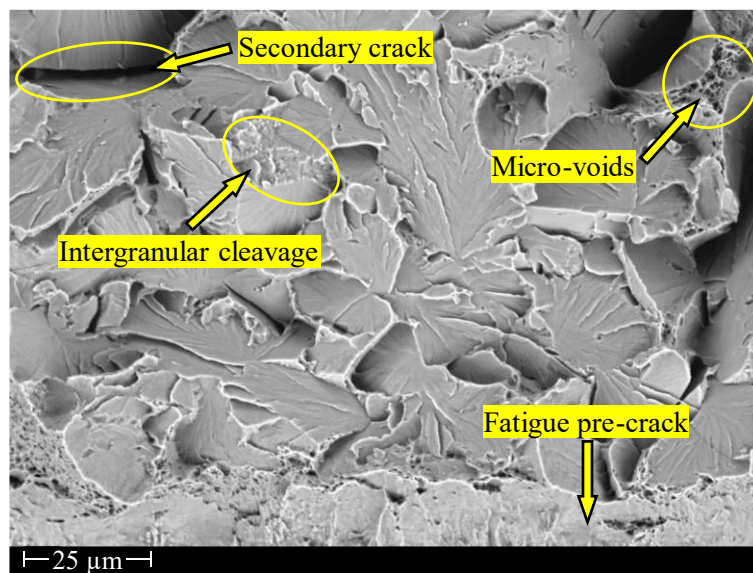


Figure 4.37: SEM micrograph (mag. 2000x) of a fracture surface near the fatigue pre-crack showing the different fracture modes surrounded by cleavage facets (adapted from [99])

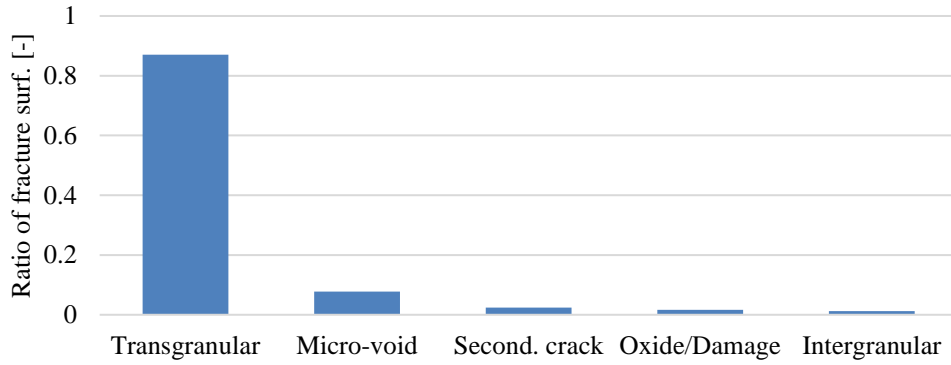


Figure 4.38: Distribution of the individual fracture modes for specimen MCT12 (adapted from [99])

From the total number of data points distributed across the different fracture modes, the ductile fracture ratio is calculated for each specimen. The resulting DFR values are related to the testing temperature in Figure 4.39 (a). A strong correlation between the DFR and temperature is obtained by means of linear regression with $R^2 = 0.77$. The regression line is well suited to describe the temperature dependence of the DFR following the equation

$$DFR = 0.00173 \cdot (T - T_0) + 0.1199. \quad (4.13)$$

This equation is used in Chapter 7 to control the ratio of cohesive elements with ductile fracture properties for the probabilistic CZM.

While the trend towards higher DFR values with increasing temperature is clear, significant scatter of the individual DFR results is observed at the test temperatures below -45°C . To explain this scatter, the DFR is related to the $K_{Jc,1T}$ results from the MCT tests in Figure 4.39 (b). For -80°C , a strong positive correlation is found with $R^2 = 0.75$, meaning that most of the variability of the DFR can be described by the scatter of $K_{Jc,1T}$. Consequently, the ratio of the ductile fracture area increases on average with the crack driving force. This is also observed for -70°C , although the coefficient of determination for the four data points is only 0.27. For -60 and -45°C , the correlation between the DFR and $K_{Jc,1T}$ is weak, in the latter case even negative, which is assumed to be due to the small sample size of three data points. The weak correlation indicates that the scatter of the DFR cannot be described by the scatter of $K_{Jc,1T}$. To summarize, the trend towards increasing DFR values with increasing $K_{Jc,1T}$ is found to be strong at temperatures well below T_0 and appears to be less pronounced with increasing temperature.

In addition to the ductile fracture ratio, the size and shape of the regions of micro-void coalescence are required to accurately model the fracture surfaces on the mesoscale. In Figure 4.40, a micrograph of the fracture surface of specimen MCT33, which was tested at -45°C , is shown with the ductile fracture regions highlighted in yellow. The size and shape of the ductile fracture regions vary considerably, with most looking like thin, curved rods, while some are more compact. The largest regions extend beyond $200\text{ }\mu\text{m}$ in one direction, while the smallest are only a few micrometers in size. A dependence of the size and shape of the ductile fracture regions on the temperature or fracture toughness is not observed.

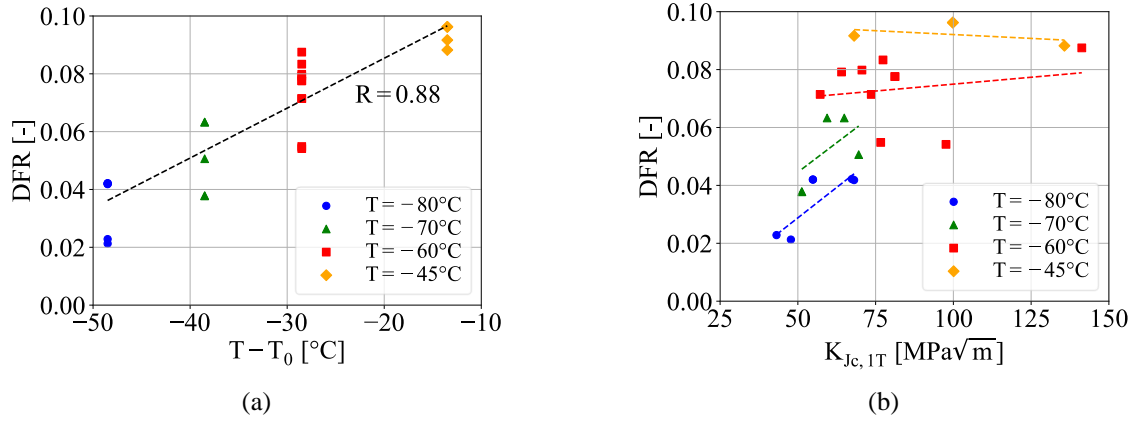


Figure 4.39: Correlation between DFR and test temperature (a) [99] and correlation between DFR and $K_{Jc,1T}$ (b)

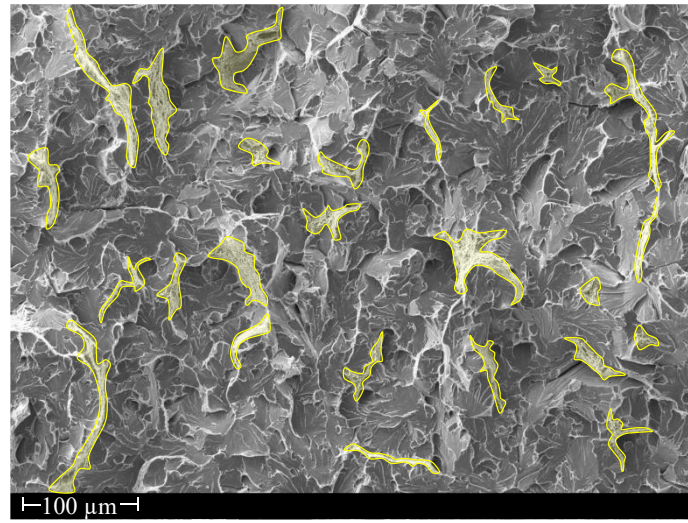


Figure 4.40: SEM micrograph (mag. 500x) showing the ductile fracture regions on the fracture surface of specimen MCT33 tested at 45°C

Within the framework of the FEM, it is not practicable to model the exact shapes of the ductile fracture regions as the element size in the ligament would become exceedingly small. Therefore, the shapes are approximated by rectangles, the average size of which is determined from 100 individual measurements distributed over several fracture surfaces. As a large proportion of the ductile fracture regions are very small, only regions with edge lengths of least 10 μm and a maximum aspect ratio of 10 are taken into account. On average, the long edge of the rectangles is 51.05 μm, while the short edge is 18.27 μm. The average aspect ratio is 3.25, with the long edge pointing more often in thickness direction than in the direction of crack growth. These results are used in Chapter 7 for designing the FE mesh in the vicinity of the crack front, where the cohesive zone is located.

4.5 Summary of the experiments and fractography

In this chapter, the experimental results required for the fracture-mechanical simulations on MCT and standard-sized CT specimens were generated. For all mechanical and fracture-mechanical tests, the RPV steel SA-508 C1.3 in the unirradiated condition was used.

First, the plastic flow curves at RT and multiple temperatures within the transition region were determined by means of SRB specimens. The tensile tests were supported by a camera system to record the contour of the specimens during testing. From the images, the diameter reduction and curvature radius of the neck were determined. The diameter reduction was used to calculate the average true stress and average true strain, while the curvature radius was used to transform the average true stress into the uniaxial true stress by means of the Bridgman correction method. In this way, the flow curves for RT, -60 and -80°C were determined. The flow curves for -30, -45 and -70°C were determined inversely by simulating the tensile tests with interpolated flow curves and fitting the numerical force-displacement curves to the experimental curves.

In addition to testing SRB specimens, NRB specimens with 0.1 mm and 0.2 mm notch root radius were tested to determine the average true strain at the point of unstable fracture. Again, the camera system was utilized to obtain the diameter reduction in the notch root. The tensile tests are simulated in Chapter 5 to determine the cohesive strength as a function of stress triaxiality.

Fracture mechanics tests according to ASTM E1921 were performed on MCT specimens within the DBT region to determine the reference temperature of the material and to evaluate the fracture toughness Master Curve. A valid reference temperature of -31.5°C (-30.4°C without the tests at -45°C) was obtained from a total of 27 MCT tests between -80 and -30°C, of which five were invalid and four were censored due to exceeding the fracture toughness limit imposed by the standard. The evaluation confirmed that while miniaturized specimens can be used to obtain a valid reference temperature, it can be difficult to find the optimal test temperature range in order to use as few specimens as possible. The median fracture toughness values obtained from the Master Curve are used in Chapter 5 to calibrate the cohesive energy at multiple temperatures. The low temperature MCT results are further used in Chapter 7 for validating the probabilistic CZM approach described in Section 3.2. Furthermore, MCT tests were performed at RT to determine the J-R curve following ASTM E1820. The J-R curve is also used in Chapter 5 for the calibration of the cohesive energy at RT.

Extensive fractographic analyses by means of SEM were performed on the broken halves of the MCT specimens tested within the DBT region. The cleavage initiation sites were located on the fracture surfaces and characterized based on the type of initiator. Particle initiation was observed on 56% of the fracture surfaces, while grain boundary initiation was identified on the remaining 44%. Simulations of the stress and triaxiality fields in the vicinity of the crack front were used to show that the initiation sites are located within the region of high constraint, demonstrating that the fracture behavior of the MCT specimens is according to theoretical expectations. Apart from the initiation sites, quantitative fractography was carried out to identify the regions of micro-void coalescence on the fracture surfaces and to determine the ductile fracture ratio as a function of temperature. The ductile fracture ratio is used in Chapter 7 for the development of the probabilistic CZM.

5 Cohesive zone parameter identification

In the previous chapter, the experimental methods and corresponding results required for the development of the deterministic and probabilistic cohesive zone models, as described in Chapter 3, were presented. Tensile tests on smooth round bar specimens were performed to determine the flow curves required for the elasto-plastic FE-simulations in this chapter. In addition, notched round bar specimens were tested to obtain the average true strain at fracture at different levels of triaxiality. The numerical simulations of the tensile tests, which are used to identify the cohesive strength in dependence of the test temperature and the stress triaxiality, are described in Section 5.1. The second cohesive zone parameter, the cohesive energy, is calibrated in Section 5.2 by using it as a fitting parameter to simulate the MCT tests within the DBT region and at RT. Thereby, a criterion for unstable fracture is defined for determining numerical K_{Jc} values.

All numerical simulations in this work are performed using the implicit solver of ABAQUS/Standard 2019. The loading is assumed to be quasi-static, as dynamic effects are assumed to be negligible.

5.1 Simulation of round bar specimen tests

The main purpose of simulating the tensile tests on round bar specimens is to identify the maximum axial stress at the point of experimental fracture, which is assumed to be equal to the cohesive strength at the given test temperature. Thus, the simulations are terminated once the diameter reduction in the neck or in the notch is equal to the diameter reduction at fracture observed experimentally. The numerical force-displacement curves resulting from the SRB simulations were already used in Section 4.2.3.2 for the inverse determination of the flow curves at -30, -45 and -70°C.

5.1.1 FE-models

Since the geometries of the round bar specimens are rotationally symmetric with respect to their longitudinal axis, axisymmetric FE-models can be used to simplify the meshing process and drastically reduce the simulation time. In addition, the geometries are symmetric in the longitudinal direction, which allows for the model size to be halved again. This is achieved by applying appropriate boundary conditions to the symmetry axes.

In Figure 5.1, the FE-model of the SRB specimens is shown. The displacement is introduced at a reference point located on the symmetry axis in y-direction, with the reference point being kinematically coupled to the shoulder of the specimen. The mesh is highly refined close to the symmetry axis pointing in x-direction to be able to resolve the stress and strain gradients in the neck. By introducing a small flaw in the form of a diameter reduction of 0.1 μm , necking is forced to develop at this position. The element length within the highly refined region is 5 μm in both directions. A total of 11431 quadrilateral axisymmetric elements with one integration point (CAX4R) are used, resulting in 35292 degrees of freedom. As the measured dimensions of the tested SRB specimens (Table A.1) do not deviate significantly from specified geometry shown in Figure A.5, this geometry is used for all simulations.

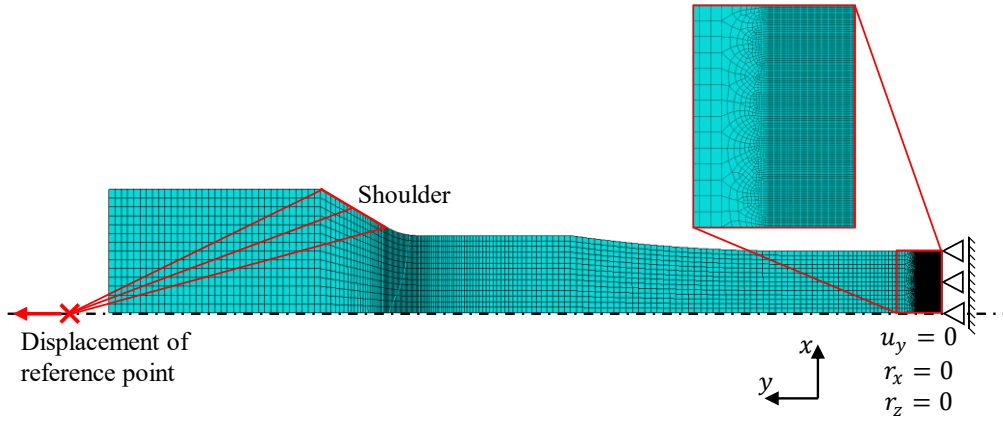


Figure 5.1: Axisymmetric FE-model of the SRB specimen geometry

In terms of the general modeling strategy, the NRB models are similar to the SRB model. Contrary to the SRB specimens, the tested NRB specimens show significant deviations from their specified geometries (Figure A.6 and Figure A.7) with regard to the shape and size of the notches, as explained in Section 4.2.2. Since the mechanical behavior of the specimens is strongly affected by the initial notch geometry, the notch is modeled individually for each simulated test. A distinction is made between flat-notched specimens from the first fabrication and round-notched specimens from the second fabrication.

The model for the 0.1NRB geometry (0.1 mm notch root radius) is shown in Figure 5.2 with close-up views of the mesh in the vicinity of a flat notch and a round notch. As with the SRB model, the mesh is highly refined in the region where high stress and strain gradients are expected. The element length near the notches is 5 μm in both directions. Apart from the geometry of the notch, the model for the 0.2NRB geometry is identical. Depending on notch shape and size, the models consist of approximately 16700 CAX4R elements with a total of 50100 degrees of freedom.

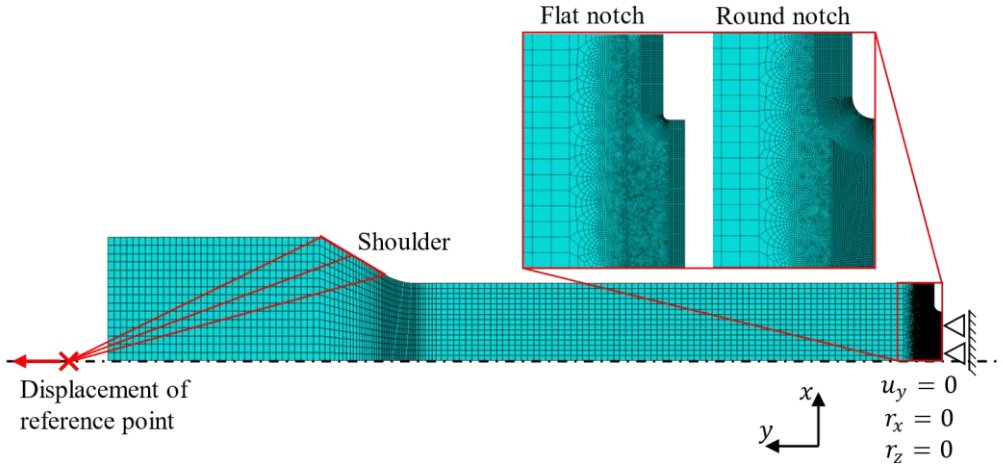


Figure 5.2: Axisymmetric model of the 0.1NRB geometry with close-up views of the mesh in the vicinity of a flat notch and a round notch

5.1.2 Average true stress – average true strain curves

In the following, the numerical average true stress – average true strain curves are compared to the corresponding experimental curves to validate the modeling approach for the tensile test simulations. The numerical average true stresses and average true strains are determined from the reaction forces in y -direction acting on the reference point and the displacement in x -direction of the surface node in the

notch root. The simulated and experimental curves for the SRB geometry were already compared in Section 4.2.3.1 for validating the plastic flow curves, showing good agreement.

Regarding the NRB geometries, it was explained in the previous section that the initial shape of the notch is critical for the mechanical response of the specimens. This effect is shown in Figure 5.3, comparing the numerical average true stress – average true strain curves for specimens 0.1NRB10 (a) and 0.1NRB13 (b) to the experimental curves using both a flat and a round notch geometry. Specimen 0.1NRB10 was produced in the first fabrication, meaning that it has a flat notch, and was tested at -70°C . In contrast, specimen 0.1NRB13 was produced in the second fabrication with a round notch and was tested at RT. Comparing the simulated curves, it can be deduced that the round notch geometry generally yields higher average true stress values as compared to the flat notch geometry. This is according to the true stresses calculated from the experimental force and diameter reduction data. The curves further show that, if the appropriate notch geometry is used for the model, the simulated average true stress – average true strain curves agree well with the experimental curves.

Similar results are obtained for the remaining 0.1NRB and 0.2NRB specimens tested in Chapter 4. The mechanical behavior of the specimens can be simulated with high accuracy by modeling the notch shape individually for each specimen. In the next step, the numerical simulations are evaluated at the respective points of experimental fracture to determine the maximum axial stresses and triaxialities for the triaxiality-dependent cohesive strength.

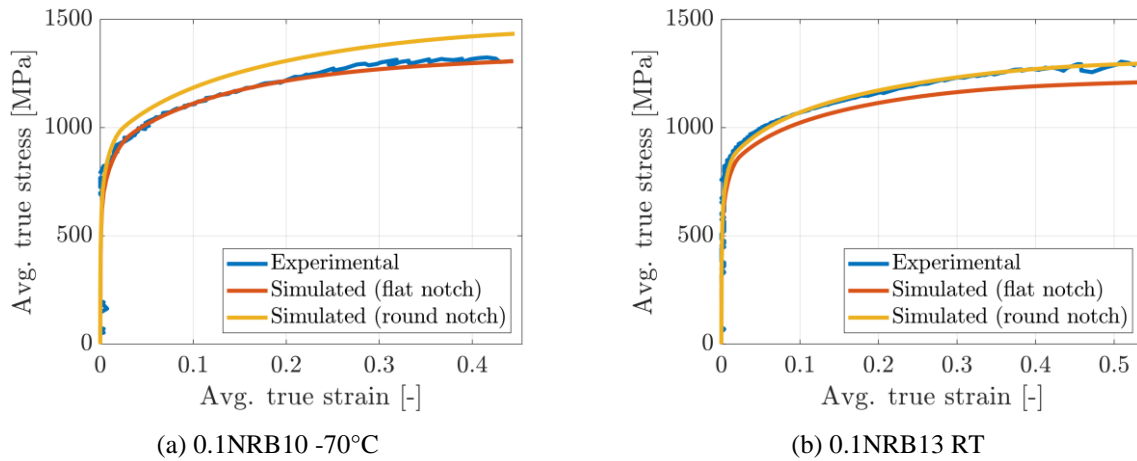


Figure 5.3: Numerical average true stress – average true strain curves using both a flat and a round notch geometry and corresponding experimental curves for specimens 0.1NRB10 and 0.1NRB13

5.1.3 Triaxiality-dependent cohesive strength

Following Cornec et al. (2003) [66], the cohesive strength σ_c is equal to the maximum axial stress at the point of fracture. By testing different geometries of tensile specimens, σ_c is identified at multiple levels of triaxiality h . With decreasing notch root radius, the stress state within a specimen becomes increasingly multiaxial. This means that the highest values of σ_c and h are expected to result from the 0.1NRB tests, while the SRB tests are expected to yield the lowest values.

In Figure 5.4, the axial stresses σ_{ax} (normal stresses in y -direction) and the triaxialities of specimens SRB09, 0.1NRB12 and 0.2NRB12 are shown at the respective points of experimental fracture. Each contour plot displays a quarter of a specimen's necking region, with the symmetry axes in x - and y -direction extending from the point of peak stress or triaxiality. The specimens were tested at -60°C . In

all cases, the maxima of σ_{ax} and h are reached in the center of the specimens at the location of the minimum diameter. This is observed for all simulated tensile specimens. As expected, the overall levels of stress and triaxiality are lowest for the SRB specimen, reaching a maximum axial stress $\sigma_{ax,max}$ of 1459 MPa and a maximum triaxiality h_{max} of 0.93. Significantly higher values are obtained from the 0.2NRB geometry with $\sigma_{ax,max} = 1823$ MPa and $h_{max} = 1.63$. The highest stresses and triaxialities are obtained from the 0.1NRB geometry with $\sigma_{ax,max} = 1947$ MPa and $h_{max} = 1.93$, which is a smaller increase as compared to the difference between the SRB and the 0.2NRB results. The individual maximum axial stress values and corresponding maximum triaxialities from all tensile test simulations are listed in Table A.13 and used as support points for interpolating the triaxiality-dependent cohesive strength at each test temperature.

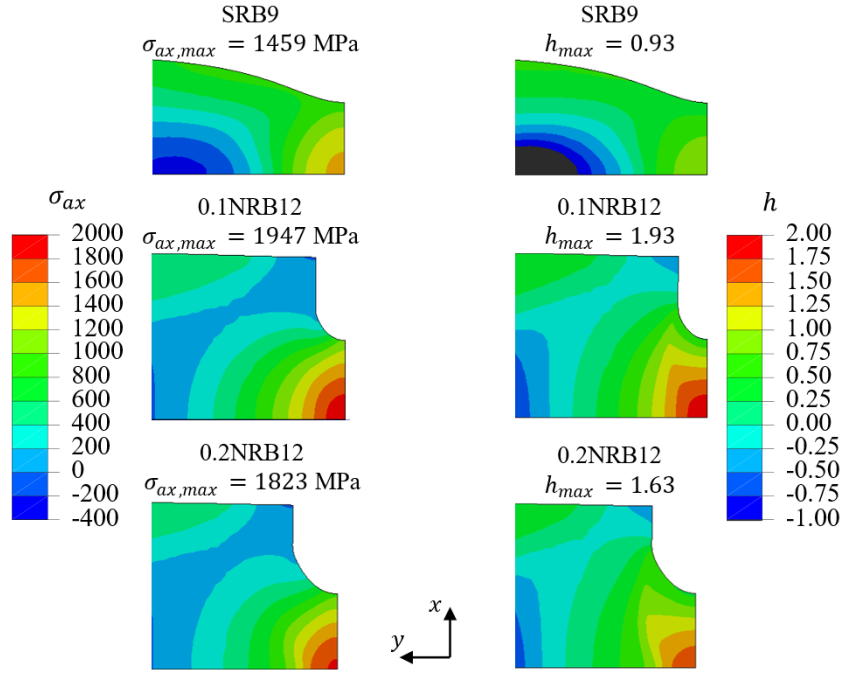


Figure 5.4: Axial stress and triaxiality at -60°C in the necking region of specimen SRB9 and near the notches of specimens 0.1NRB12 and 0.2NRB12 at the respective fracture points (adapted from [99])

In Figure 5.5, the triaxiality-dependence of the cohesive strength is shown for RT, -60, -70 and -80°C. The cohesive strength increases linearly with triaxiality and decreases with increasing temperature. Linear interpolation is performed at each temperature to determine a functional relationship between σ_c and the h in the form

$$\sigma_c(h, T) = C_1(T)h + C_2(T). \quad (5.1)$$

Here, C_1 and C_2 are temperature-dependent fitting parameters, the values of which are listed for the respective test temperatures in Table 5.1. It is observed that the slopes of the interpolation lines increase between RT and -60°C, while remaining constant between -60 and -80°C. This means that, while the overall cohesive strength increases with decreasing temperature, the triaxiality dependence of σ_c does not show qualitative differences at low temperatures. It can be assumed that this observation is partly due to the relatively narrow low temperature range studied in this work.

It was shown in Section 4.4.1.2 that the triaxiality in the vicinity of the crack front of an MCT specimen reaches values up to 2.8, which is significantly higher than the maximum triaxiality reached in the center of the NRB specimens. To increase the triaxiality range of the cohesive strength calibration,

NRB specimens with smaller notch root radii than 0.1 mm would have to be tested. This was not carried out in this work due to manufacturing restrictions regarding the minimum diameter of the erosion wire. Based on the quality of the results of the MCT simulations in the next section, the possibility to extrapolate the given triaxiality dependence of σ_c towards higher triaxialities is considered. It is also investigated whether the MCT test results can be predicted using a constant σ_c .

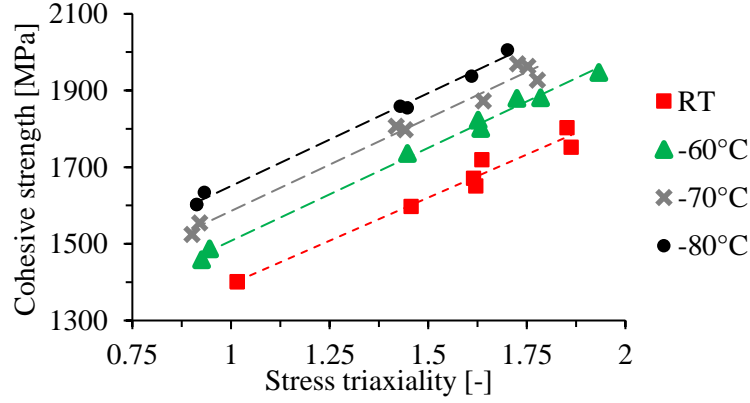


Figure 5.5: Linear interpolation of the triaxiality-dependent cohesive strength for RT, -60, -70 and -80°C (adapted from [99])

Table 5.1: Fitting parameters for the linear interpolation of the cohesive strength following Equation (5.1)

T [°C]	C_1 [MPa]	C_2 [MPa]
RT	449.9	945.8
-60	485.0	1022.7
-70	483.9	1101.7
-80	484.8	1165.9

5.2 Simulation of the MCT tests

In this section, the triaxiality-dependent cohesive strength is used to simulate the MCT tests performed in Section 4.3. The cohesive energy is used to fit the numerical K_{Jc} values to the experimental results obtained within the DBT region and to fit the numerical force-displacement and J-R curves to the experimental curves at RT. Based on the numerical results, the capability of the model to accurately simulate the median fracture behavior of the material is discussed and appropriate modifications are applied to improve the predictions.

5.2.1 FE-models of the MCT geometry

The MCT specimen is modeled as a 3D geometry and, as with the axisymmetric models of the tensile specimens, geometric symmetries are exploited to improve efficiency. A CT specimen is symmetric with respect to the crack plane (xz -plane) and the center plane with normal pointing in thickness direction (xy -plane). Applying appropriate boundary conditions, the geometry is reduced to a quarter model, which is shown in Figure 5.6. The left image shows the mesh for the simulation of unstable fracture at low temperatures, while the mesh in the right image is used for the simulation of stable crack propaga-

tion at RT. Loading is introduced by means of the wedge-shaped pins shown in brown, which are assumed to be rigid. An initial crack length a_0 of 4 mm is assumed, leading to $a_0/W = 0.5$.

The main difference between the models is the length of the cohesive zone. Located in the crack plane starting from the initial crack front at $x = 0$, the cohesive zone is a strip of zero-thickness cohesive elements. The nodes on the upper surface of the cohesive elements are connected to the corresponding nodes of the surrounding continuum elements, while the nodes on the lower surface are constrained by symmetry boundary conditions. These boundary conditions are introduced by means of the “constraint equations” feature of ABAQUS explained in Section 2.4.4. Between the cohesive zone and the specimen backside a conventional symmetry condition in y -direction, as shown in Figure 5.6, is used. The low temperature MCT tests discussed in Section 4.3.5 terminated without a significant amount of stable crack propagation prior to unstable fracture. To reduce the simulation time, the length of the cohesive zone in x -direction is set to 0.1 mm for the low temperature model. For the RT simulations, however, a significantly increased length of the cohesive zone is required to be able to simulate the J-R curve determined experimentally in Section 4.3.6. Therefore, the length of the cohesive zone is set to 2 mm for the RT model.

The low temperature model consists of 22300 linear hexahedral continuum elements with eight integration points, resulting in 133800 degrees of freedom. Additionally, 680 cohesive elements are used. The mesh is highly refined near the cohesive zone, with the continuum elements directly at the crack plane having a length of 1.5 μm in both the x - and y -directions. This small element length is required to capture the large stress and strain gradients in the vicinity of the crack tip and small increments of crack extension prior to unstable fracture. Ten elements are used in thickness direction, which are tapered towards the specimen side surface to accurately simulate necking at the crack tip.

The meshing strategy for the RT model is similar to the low temperature model. A total of 101130 continuum elements with 606780 degrees of freedom and 9240 cohesive elements is used. Due to the significantly increased cohesive zone length and the associated increase in simulation time, the minimum element length in x -direction is set to 3 μm at the initial crack front and increased to 6 μm towards the end of the cohesive zone. Since the total crack extension is considerably larger in the RT simulations, the smaller element length employed for the low-temperature model is not necessary. In y -direction, the minimum element length is 3 μm and ten elements with a taper towards the side surface are used in thickness direction.

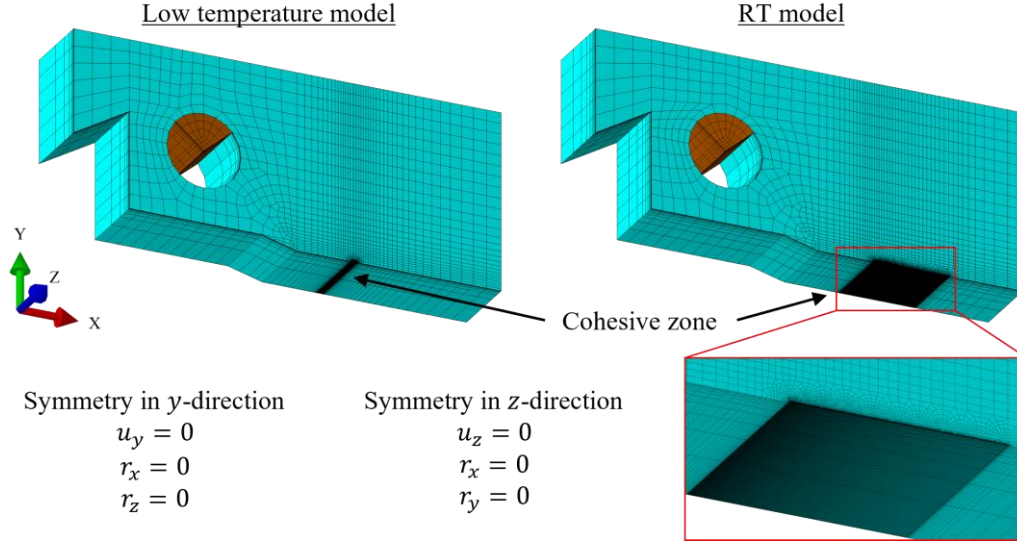


Figure 5.6: Quarter models of the MCT specimen for the crack growth simulations at low temperature and RT (adapted from [99])

Apart from the cohesive strength identified in Section 5.1.3 and the cohesive energy that is calibrated in the next section, the shape of the traction-separation-law (TSL) is a factor impacting the mechanical behavior of the cohesive elements. As explained in Section 2.4.2, a triangular shape with a high initial stiffness is suited for simulating unstable fracture, while a trapezoidal shape is better for stable crack propagation. In Figure 5.7 (a), the triangular shape used for the low temperature simulations is shown, while the trapezoidal shape shown in Figure 5.7 (b) is used for the simulations at RT. To ensure a high initial stiffness, the cohesive strength is reached at 0.1% of the critical separation δ_c for the triangular TSL ($\delta_1 = \delta_2 = 0.001$). In case of the trapezoidal TSL, the shape parameters are set to $\delta_1 = 0.01$ and $\delta_2 = 0.3$, meaning that the cohesive strength is reached at 1% of δ_c and unloading is initiated at 30% of δ_c .

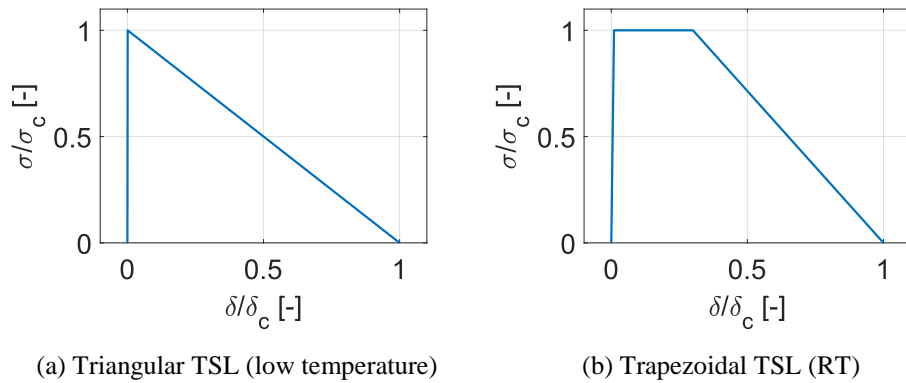


Figure 5.7: Triangular TSL used for the simulation of unstable fracture at low temperatures (a) and trapezoidal TSL for the simulation of stable crack propagation at RT (b) (adapted from [99])

5.2.2 Cohesive energy

Crack growth simulations are performed at -80, -70, -60°C and RT using the respective flow curves determined in Section 4.2.3 and the triaxiality-dependent cohesive strength identified in Section 5.1.3.

The cohesive energy Γ_c is identified by means of the trial-and-error method, meaning that the value of Γ_c is changed after each simulation to fit the numerical results to the experimental data.

For the low temperature simulations, the fit is considered acceptable if the simulated K_{Ic} is within $0.5 \text{ MPa}\sqrt{\text{m}}$ of the median fracture toughness obtained from the Master Curve at the respective test temperature (see Section 4.3.5.3). With this deterministic model it is not possible to simulate the fracture toughness scatter observed experimentally, since no brittle fracture initiators are modeled within the cohesive zone. The probabilistic CZM approach explained in Section 3.2 is used in Chapter 7 to predict the fracture toughness scatter within the DBT region. In addition to using the triaxiality-dependent cohesive strength, it is investigated whether unstable fracture can be predicted using a constant σ_c .

Regarding the stable crack growth simulations at RT, the aim is to predict the experimental force-displacement curves and the J-R curve determined in Section 4.3.6 as accurately as possible. Again, the trial-and-error method is used to identify Γ_c and modifications to the triaxiality dependence of σ_c are carried out to improve the predictions.

5.2.2.1 Criterion for the onset of unstable fracture

Fracture mechanics tests within the lower transition region are usually terminated by cleavage initiation and the fracture point can easily be determined by a sudden reduction of force registered by the load cell. The mechanisms of cleavage fracture are not simulated by the model, so that brittle fracture in the sense of a complete failure of the specimen in a very short time frame, starting from a distinct initiation site, cannot be predicted. An alternative failure criterion is required that is compatible with the deterministic CZM and can be regarded as the beginning of unstable crack extension.

Simulations using the low temperature MCT model with the triaxiality-dependent cohesive strength show that at sufficiently low values of cohesive energy, the incremental crack growth rate

$$\frac{\delta a}{\delta LLD} = \frac{\Delta a_n - \Delta a_{n-1}}{LLD_n - LLD_{n-1}} \quad (5.2)$$

starts to increase rapidly as the crack opening stress σ_y reaches σ_c in front of the crack tip. The total crack extension at the n th increment Δa_n is determined by the total area of all failed cohesive elements divided by half the thickness of the specimen. In Figure 5.8, the crack growth rate is shown against the load line displacement LLD for a simulation at -60°C using a Γ_c of 2 N/mm . The crack starts to grow at an LLD of 0.03 mm and the crack growth rate increases up to an LLD of about 0.2 mm . Beyond this displacement, the crack growth rate remains constant until it starts to increase rapidly at an LLD of 0.3 mm . This increase is assumed to represent the onset of unstable fracture, as a large number of cohesive elements begin to fail at the same time. The origin of this unstable crack propagation is always the crack tip in the mid thickness of the specimen ($z = 0$) since the highest crack opening stress and triaxiality are observed at this location (see Figure 4.31).

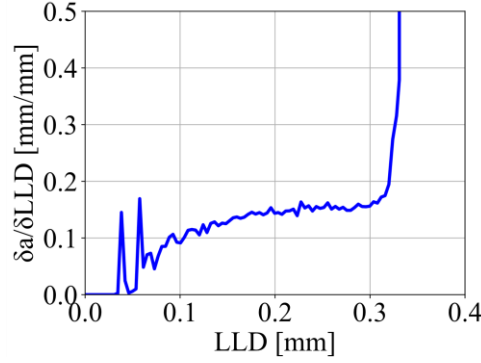


Figure 5.8: Crack growth rate against LLD at -60°C using the triaxiality-dependent cohesive strength and a cohesive energy of 2 N/mm

Crack propagation leads to a reduction of the model stiffness with increasing load and is therefore a highly non-linear process. In addition to the plasticity calculations and geometric non-linearities, the convergence behavior of the simulations is diminished with increasing crack growth rate to the point where the simulation is terminated. A crack growth rate of 0.5 mm/mm is defined as the criterion for the initiation of unstable crack extension and is applied to all simulations within the DBT region.

5.2.2.2 Parameter fitting within the DBT region

First, Γ_c is calibrated using the triaxiality-dependent cohesive strength as identified in Section 5.1.3 for the respective test temperatures. The linear triaxiality dependence is applied between the lowest and the highest triaxiality values obtained from the tensile tests. Below and above these triaxialities, σ_c is assumed to be constant. It was explained in Section 2.4.3.1 that the triaxiality dependence of Γ_c is weak in comparison to that of σ_c . Therefore, the cohesive energy is assumed to be constant for the following simulations.

An increase of Γ_c causes the cohesive elements to require more separation before complete failure, which delays crack propagation. Thereby, increasing Γ_c leads to an increasing value for the numerically predicted fracture toughness $K_{Jc,num}$ and vice versa. By comparing $K_{Jc,num}$ to the median fracture toughness $K_{Jc,MC}$, which is obtained from the Master Curve at the respective test temperature, the numerical result can be fitted iteratively to the experimental value by adjusting Γ_c .

The identified values for Γ_c are listed in Table 5.2 for -80 , -70 and -60°C together with a comparison between $K_{Jc,MC}$ and the corresponding numerical results $K_{Jc,num}$. Using the triaxiality-dependent CZM, the experimental fracture toughness results can be simulated with high accuracy. It is observed that Γ_c decreases with decreasing temperature. This is according to expectations since ductile fracture is a high-energy fracture mode and the amount of micro-void coalescence on the fracture surfaces of the tested MCT specimens reduces with decreasing temperature (Section 4.4.2).

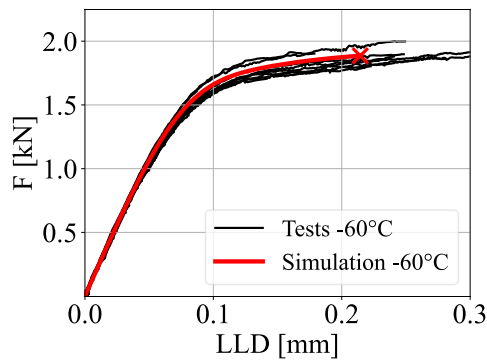
Table 5.2: Identified cohesive energy values for -80, -70 and -60°C using the triaxiality-dependent cohesive strength and comparison between the median fracture toughness from the Master Curve and the numerical results from the MCT simulations

T [°C]	Γ_c [N/mm]	$K_{Jc,MC}$ [MPa \sqrt{m}]	$K_{Jc,num}$ [MPa \sqrt{m}]
-60	1.67	99.40	99.64
-70	1.60	88.40	88.72
-80	1.30	79.30	79.68

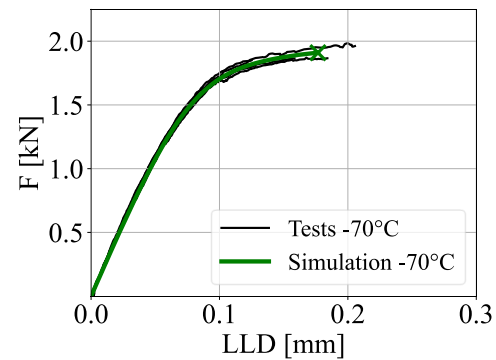
In addition to the fracture toughness results, the numerical force-displacement curves and the simulated stable crack extension prior to unstable fracture are compared to the MCT tests to further validate the calibrated CZM. In Figure 5.9, the numerical and experimental force-LLD curves (a-c) and the numerical J-R curves (d) are shown. The numerical curves end at the point at which the unstable fracture criterion described in the previous section is fulfilled. Good agreement is observed between the simulated force-LLD curves and the average of the experimental curves. While the simulated force at -80°C is slightly below the corresponding experimental average, the fit is considered acceptable. The simulated LLD, force, crack extension and J-integral at the point of unstable fracture are listed in Table A.14.

The numerical J-R curves show that the J-integral at fracture increases with temperature and that the stable crack extension prior to the onset of unstable fracture is very small with 19.8 to 26.7 μm between -80 and -60°C. Except for specimen MCT11, which was tested at -60°C and showed a stable crack extension of 120 μm (Table A.9), no significant ductile crack growth was observed from the MCT tests below -45°C. From the SEM micrographs used for the determination of the cleavage initiation sites in Section 4.4.1, it is estimated that the MCT specimens failed with a stable crack extension between 5 to 50 μm , which is reflected in the numerical results. Furthermore, it is observed both experimentally and numerically that the length of the ductile crack extension increases with increasing temperature. It is concluded that the average fracture-mechanical behavior of the MCT specimens can be accurately predicted by the triaxiality-dependent cohesive strength and a constant cohesive energy within the lower transition region.

At least one SRB specimen and one NRB specimen are required to be tested at a given temperature to obtain the linear triaxiality dependence of σ_c shown in Figure 5.5. Since one of the primary goals of this research is to identify the model parameters using as few specimens as possible, it is investigated in the following whether the macroscopic fracture mechanical behavior of the MCT specimens within the DBT region can also be predicted using a constant value for σ_c . Calibration of a constant σ_c would require only one round bar specimen test if the material is sufficiently homogeneous.



(a) Force-LLD curves -60°C



(b) Force-LLD curves -70°C

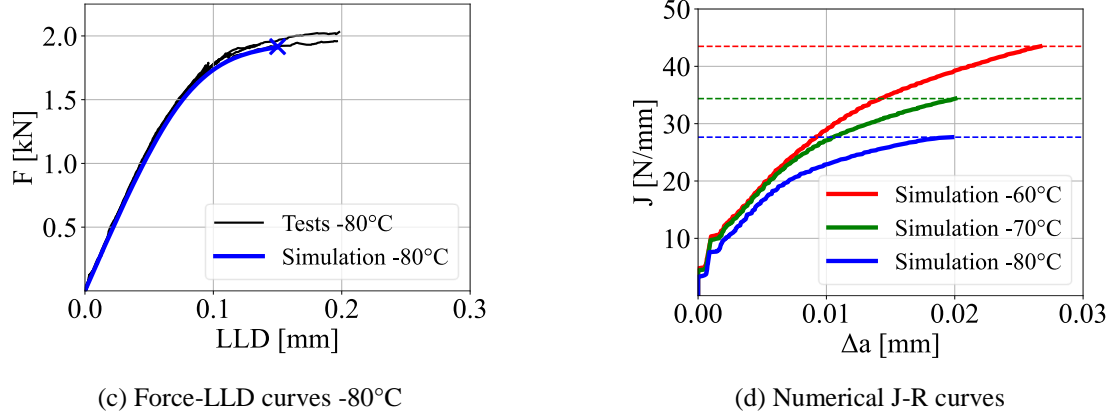


Figure 5.9: Numerical and experimental force-LLD curves (a-c) and numerical J-R curves (d) for the MCT geometry at -80, -70 and -60°C ((a) adapted from [97], (c) adapted from [99])

MCT simulations are performed at -80°C using a constant σ_c of 2005.5 MPa, which is the cohesive strength obtained from the single 0.1NRB test performed at -80°C (see Table A.13). As before, the numerically predicted fracture toughness is compared to the $K_{Jc,MC}$ at -80°C, and Γ_c is adjusted according to the difference between these values to iteratively fit the numerical result to the experimental value. Good agreement is obtained using $\Gamma_c = 0.94$ N/mm, which is lower than the cohesive energy of 1.3 N/mm obtained using the triaxiality-dependent cohesive strength. The lower Γ_c is a consequence of the overall higher level of σ_c , causing the cohesive elements to require more external load for the same separation. A numerical fracture toughness of $80.47 \text{ MPa}\sqrt{\text{m}}$ is obtained with the constant σ_c , while the experimental value is $79.30 \text{ MPa}\sqrt{\text{m}}$. An even better match could be achieved using a slightly lower value for Γ_c . The force-LLD curve is equivalent to the curve shown in Figure 5.9 (c) and the ductile crack extension prior to unstable fracture is $17 \text{ }\mu\text{m}$, which is close to the value of $20 \text{ }\mu\text{m}$ obtained with the triaxiality-dependent cohesive strength. Thereby, it is confirmed that the macroscopic fracture mechanical behavior of the MCT specimens can be successfully simulated using both a triaxiality-dependent and a constant cohesive strength. Based on the literature review in Section 2.4.3.1 it is expected that, for the prediction of fracture toughness from standard-sized CT geometries in Chapter 6, the triaxiality-dependent model will yield better results. The reason is that constraint differences between the miniaturized and the standard-sized geometries are taken into account by the triaxiality-dependent CZM, while the model with constant σ_c is only calibrated for the MCT geometry. However, if only the MCT geometry is of interest, the constant σ_c is sufficient for the simulation of unstable fracture and the number of tensile tests required for the parameter identification can be reduced.

It is further investigated whether the fracture behavior of the MCT specimens in the transition region can be simulated using a triaxiality-dependent cohesive strength that is extrapolated beyond the maximum triaxiality obtained from tensile testing. For this, simulations at -60°C with multiple values for Γ_c between 0.5 and 2 N/mm are performed using the linear triaxiality dependence of σ_c up to $h = 3$. This value is higher than the maximum triaxiality of 2.8 reached in front of the crack tip of MCT specimens. With this model, it is not possible to obtain a result for $K_{Jc,num}$ as the unstable fracture criterion is not met regardless of the value of Γ_c . Strong blunting of the crack tip is observed, followed by slow-stable crack extension with a constant crack growth rate. As mentioned previously, unstable fracture is initiated once the crack opening stress in front of the crack tip reaches the cohesive strength in the mid thickness of the specimen. Due to the high level of triaxiality in this region, σ_c is increased beyond the

maximum crack opening stress reached during loading, resulting in the absence of unstable crack initiation.

It is concluded that, while both the constant and triaxiality-dependent cohesive strength in combination with a constant cohesive energy can be used to simulate the macroscopic fracture behavior of the MCT specimens in the transition region, the triaxiality dependence must be limited to relatively low triaxialities in order to allow the crack opening stress to surpass the cohesive strength, thus facilitating unstable crack growth. In the following, the same investigations are performed for the simulation of ductile crack extension at RT.

5.2.2.3 Parameter fitting on the upper shelf

The MCT simulations at RT are performed to identify Γ_c for ductile crack growth, which is required for the probabilistic CZM approach in Chapter 7. The same method as for the low temperature simulations is applied, fitting the numerical results to the experimental curves from the MCT tests at RT (Section 4.3.6) by adjusting the cohesive energy. Linear triaxiality dependence of σ_c is considered according to the calibration in Section 5.1.3. This means that initially, σ_c is not extrapolated beyond the triaxialities determined from the tensile test simulations. The cohesive strength is assumed to be constant outside of the interpolation range ($h = 1.02 \dots 1.86$ for RT).

In Figure 5.10, the experimental force-LLD curves (a) and the J-R curve (b) are compared to the simulated curves using a Γ_c of 2.25 N/mm. Both the force-LLD curves and the J-R curves show good agreement up to a displacement of about 1.9 mm and a stable crack extension of 0.54 mm. At this point, unstable fracture is predicted according to the unstable fracture criterion defined in Section 5.2.2.1. The maximum σ_c of 1783 MPa is reached by the crack opening stress close to the crack tip in the mid thickness of the specimen ($z = 0$), causing rapid separation of the cohesive elements prior to the simulation terminating.

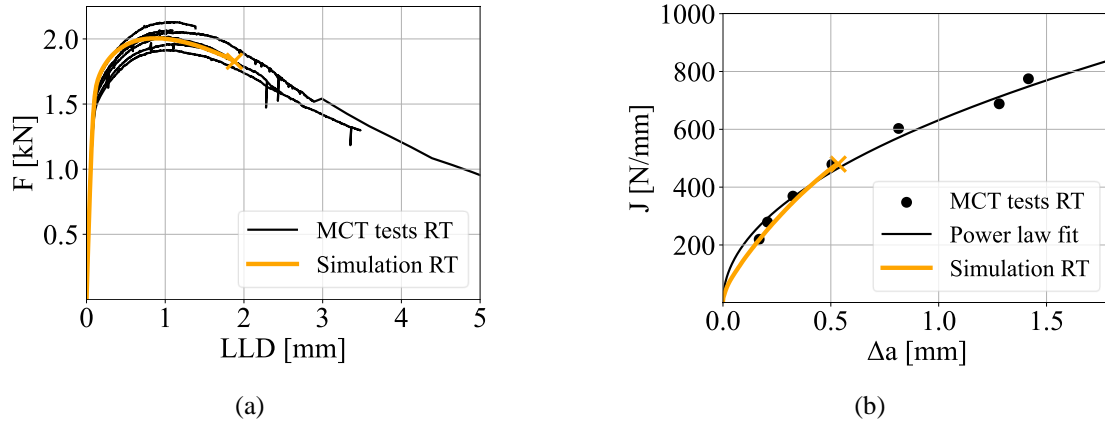


Figure 5.10: Experimental and simulated force-LLD curves (a) and J-R curves (b) at RT using the interpolated triaxiality-dependent σ_c and Γ_c of 2.25 N/mm

As discussed in Section 4.4.1.2, the triaxiality in front of the crack tip of an MCT specimen reaches values of up to 2.8, which is considerably higher than the maximum triaxiality at fracture determined from the tensile test simulations. It can be assumed that by increasing σ_c at high triaxialities, the simulation will not terminate in unstable crack growth due to the higher fracture resistance. For the next simulation, the linear triaxiality dependence of σ_c is extrapolated to $h = 3$, resulting in a maximum cohesive strength of 2295 MPa.

The simulated crack growth rates $\delta a/\delta LLD$ with and without extrapolation of σ_c are compared in Figure 5.11. The curves are similar up to the point where unstable fracture is predicted by the model without extrapolated σ_c . Beyond this point, the extrapolated model predicts a stable increase of the crack growth rate, which is limited to a value of 0.6 mm/mm at a displacement of 2.75 mm. The crack growth rate decreases with further displacement until the simulation is completed at an LLD of 4 mm. This confirms that unstable crack extension can be prevented by increasing the σ_c beyond the maximum triaxiality obtained from the tensile test simulations.

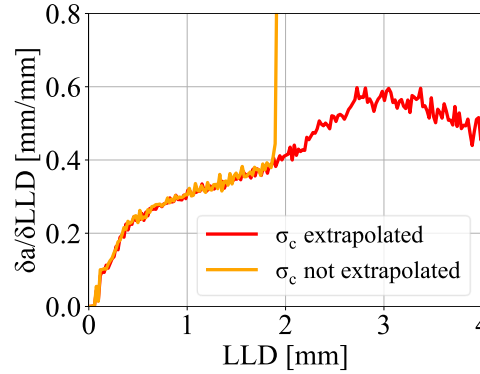


Figure 5.11: Simulated crack growth rates with and without cohesive strength extrapolation

In Figure 5.12, the simulated force-LLD (a) and J-R (b) curves, which are obtained using the extrapolated σ_c , are compared to the experimental curves. The average force from the tests is well predicted by the simulation up to a displacement of 2.5 mm. Above this displacement, the experimental force is slightly underestimated by the numerical curve. A maximum force of 2006 N is obtained numerically, while the average maximum force from the tests is 2025 N. The experimental J-R curve, which was determined by means of a power law fit of the individual MCT test results at RT (Section 4.3.6.3), is predicted with high accuracy. At the final LLD of 4 mm, a stable crack extension of 1.7 mm at a J-integral of 813 N/mm is obtained numerically. Overall, the agreement between the curves is satisfactory for the purpose of developing the probabilistic CZM.

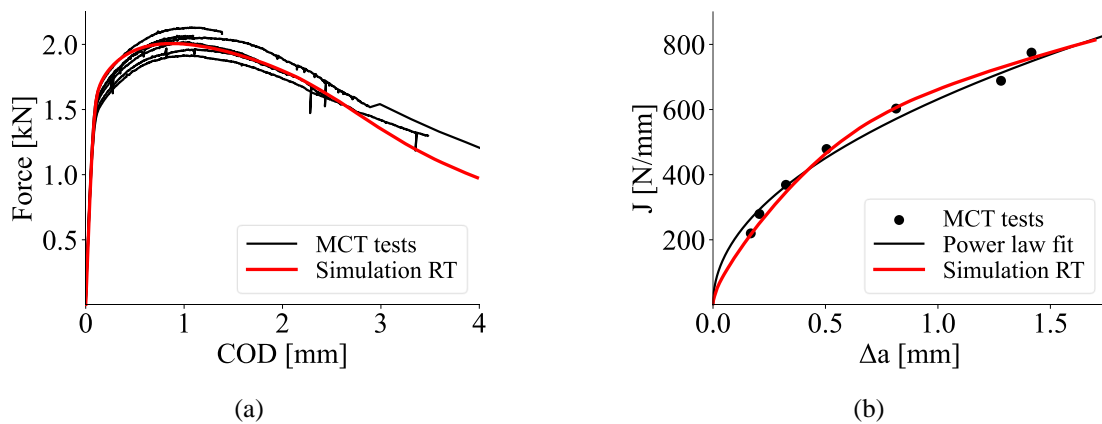


Figure 5.12: Experimental and simulated force-LLD curves (a) and J-R curves (b) at RT using the extrapolated triaxiality-dependent σ_c and Γ_c of 2.25 N/mm (adapted from [99])

The macroscopic results show that, with the applied calibration method, it is necessary for the simulation of stable crack growth to define the triaxiality dependence of the cohesive strength throughout the entire range of triaxialities observed in front of the crack tip. In addition to the force-LLD and J-R

curves, the evolution of the shape of the crack front predicted by the simulation can be compared to the experimental results for further validation of the cohesive parameters.

In Figure 5.13, optical micrographs of the regions of ductile crack extension at multiple levels of cross-head displacement are compared to the numerically predicted regions of stable crack growth at equivalent load levels. In the micrographs, stable crack extension is represented by the dark purple strips between the fatigue pre-cracks and the glossy gray surfaces of the manually induced brittle fracture. The blue regions in the bottom images show the areas of failed cohesive elements and therefore represent the simulated ductile crack extension. Additionally, the red regions show the remainder of the cohesive zone that has not yet failed.

Comparing the shape of the ductile crack front at the respective load levels, it is observed that, while the average crack extension is similar, the tunneling effect visible in the micrographs is not accurately predicted by the simulation. Although both the experimental and the numerical fracture surfaces show that the maximum crack extension is obtained at the mid thickness of the specimens, the difference between the crack extension at the mid thickness and at the side surfaces is more pronounced on the experimental fracture surfaces. The simulated crack extension is nearly constant along the thickness direction and only reduces near the side surfaces, while the micrographs show a steady reduction of the ductile crack length from the mid thickness to the side surfaces.

A considerable difference between physical MCT specimens and the model is introduced by assuming a perfectly straight pre-crack front. The fatigue pre-cracks of the specimens tested at RT were shown to be curved to varying degrees. Following Camas et al. (2012) [111], the crack front curvature has a strong influence on the stress state along the thickness direction, decreasing the dominance of the plane strain state with decreasing crack front radius. Thereby, the distance of the plane strain region from the side surfaces is increased. This effect can be expected to cause decelerated crack extension near the side surfaces due to the reduced constraint. The influence of the pre-crack shape is reflected in the experimental and numerical crack front shapes in Figure 5.13.

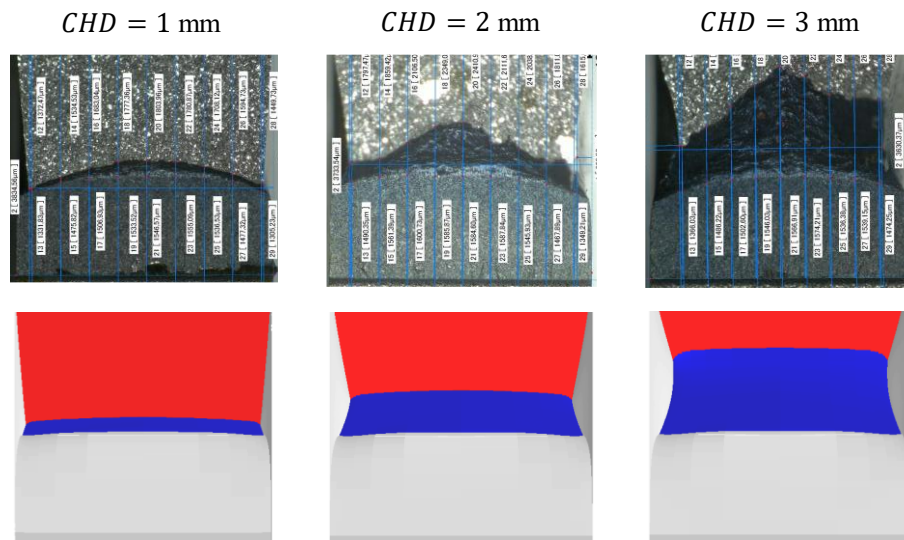


Figure 5.13: Evolution of the shape of the crack front from the MCT tests at RT (top) and corresponding numerical predictions (bottom)

Even though the exact crack growth behavior of the MCT specimens could not be replicated by the simulation, it was shown that the results of the deterministic triaxiality-dependent CZM are according to

theoretical expectations. In addition, the average fracture-mechanical behavior of the material at RT, as represented by the numerical force-LLD and J-R curves, could be predicted with high accuracy.

It is noted that the calibrated Γ_c of 2.25 N/mm is considerably lower than the cohesive energies used for the simulation of ductile crack growth in other structural steels for nuclear applications. Mahler & Aktaa (2021) [112] used a Γ_c of 11 N/mm to simulate ductile crack extension of Eurofer97-2 steel in KLST and 0.5T CT specimens at RT and Mahler (2016) [86] used a Γ_c of 10 N/mm to simulate tests on KLST and standard-sized SENB specimens of T91 steel at RT. Comparing the crack growth resistance of the materials, they obtained a J-integral of 614 N/mm at a crack extension of 0.5 mm for Eurofer97-2 and a value of 497 N/mm for T91 using KLST specimens, while a J-integral of 451 N/mm is obtained from the MCT tests on SA-508 Cl.3 performed in this work. Although the J-integral of SA-508 Cl.3 is 27% lower than the value for Eurofer97-2 and 9% lower than T91, these differences alone do not justify the significantly lower cohesive energy determined for SA-508 Cl.3.

Another aspect that might be responsible for the deviation in the calibrated values of Γ_c is the numerical modeling. The simulations should be as similar as possible to ensure that the results are comparable. As with the MCT simulations carried out in this work, the FE solver ABAQUS/Standard in conjunction with the cohesive element implementation by Scheider (2006) [60] was used by Mahler to perform fracture-mechanical simulations. To improve the comparability of the results, the meshing strategy applied by Mahler for simulating T91 tests on KLST specimens is adopted, and the cohesive energy is calibrated once more for SA-508 Cl.3 using the MCT test results obtained in Section 4.3.5. For the MCT simulations described in this chapter, an increasing element length of 3 to 6 μm in crack growth direction, starting from the initial crack tip, was used. In crack opening direction, an element length of 3 μm was applied in the vicinity of the cohesive zone. In comparison, an increasing element length starting from 5 μm at the initial crack front to 25 μm at the end of the cohesive zone and an element length of 9 μm in crack opening direction was used by Mahler. In addition, 10 elements in thickness direction were employed in this work, as opposed to 5 elements used by Mahler.

Applying Mahler's discretization to the MCT model described in Section 5.1.1, the cohesive energy is calibrated, resulting in a value of 6 N/mm. This result is considerably closer to the value of 10 N/mm for T91 as compared to the original value of 2.25 N/mm for SA-508 Cl.3. A comparison between the numerical force-displacement and J-R curves using the respective meshing strategies is shown in Figure 5.14. It can be seen that the fracture-mechanical behavior of the material is described well by both simulations and the curves are nearly identical.

A mesh dependence of the numerical results is indicated by the significant increase in Γ_c from 2.25 N/mm to 6 N/mm. In his dissertation, an extensive convergence study was performed by Mahler [86] and mesh convergence was confirmed. Since shorter element lengths in all spatial directions are used in this work, the applied discretization can also be expected to yield converged results. The numerical cause of the deviation in the calibrated cohesive energies is not further investigated in this work. It was shown that, using Mahler's discretization, the cohesive energy of SA-508 Cl.3 is comparable to the Γ_c he obtained for Eurofer97-2 and T91. This result is a verification of the applied parameter identification methodology.

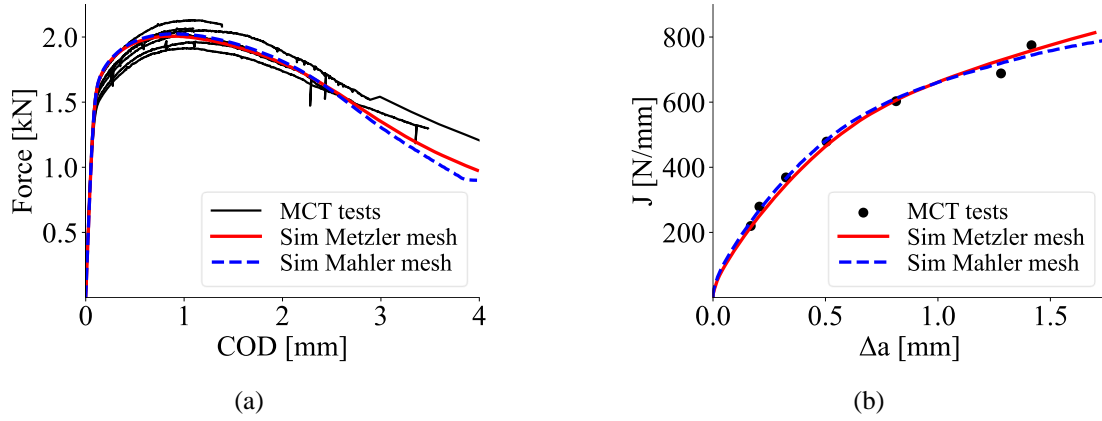


Figure 5.14: Experimental and simulated force-LLD curves (a) and J-R curves (b) at RT using the discretization described in this chapter with $\Gamma_c = 2.25$ N/mm and Mahler's discretization with $\Gamma_c = 6$ N/mm

5.2.3 Summary of the cohesive zone parameter identification

The objective of this chapter was to calibrate the cohesive strength σ_c and cohesive energy Γ_c for the simulation of fracture-mechanical tests within the DBT region and at RT for the development of the probabilistic CZM approach in Chapter 7. For the calibration of σ_c , which is assumed to be equal to the maximum axial stress at fracture, the tensile tests performed in Chapter 4 were simulated. By using different geometries of round bar specimens, σ_c was identified at different levels of triaxiality, whereby a linear relationship was found at all test temperatures. Due to manufacturing constraints limiting the minimum notch root radius of the NRB specimens, this relationship is limited to a triaxiality range of approximately 0.9 to 1.8, while the triaxiality in front of the crack tip of MCT specimens reaches values of up to 2.8.

MCT simulations at -60, -70 and -80°C were performed to identify Γ_c using a triangular TSL with the aforementioned cohesive strength calibration. An unstable fracture criterion based on the simulated crack growth rate was introduced to obtain numerical fracture toughness predictions. On the basis of these predictions, Γ_c was adjusted iteratively to fit the numerical results to the respective median fracture toughness values from the Master Curve. Good agreement between the numerical and experimental fracture toughness results, as well as the force-LLD curves, was achieved for cohesive energies between 1.3 and 1.67 N/mm, increasing with temperature.

It was further investigated whether the fracture behavior of the MCT specimens in the transition region can be simulated using both a constant σ_c and the linearly triaxiality-dependent σ_c extrapolated to a triaxiality of 3. While satisfactory results were achieved at -80°C using a constant σ_c of 2005.5 MPa and $\Gamma_c = 0.87$ N/mm, unstable fracture could not be simulated with the extrapolated σ_c regardless of the choice of Γ_c . It was found that unstable fracture is initiated by the crack opening stress reaching σ_c in front of the crack tip. This condition is not met when using the extrapolated σ_c , as the cohesive strength is too high at the high level of triaxiality present in front of the crack tip. It was concluded that the fracture behavior of the MCT specimens in the transition region can be predicted using both the constant and the triaxiality-dependent σ_c as long as the maximum σ_c is sufficiently small to facilitate unstable fracture initiation.

In addition to the MCT simulations within the DBT region, simulations were performed at RT to calibrate Γ_c for ductile crack growth. As with the low temperature simulations, the numerical force-LLD and J-R curves were fitted to the experimental results by adjusting Γ_c . It was shown that, using the

triaxiality-dependent σ_c without extrapolation, unstable fracture is predicted by the model as σ_c is reached by the crack opening stress in front of the crack tip. The initiation of unstable fracture could be prevented by using an extrapolated σ_c . Thereby, good agreement between the numerical and experimental results is obtained with $\Gamma_c = 2.25$ N/mm.

Apart from the macroscopic fracture-mechanical behavior, it was found that the tunneling of the ductile crack front observed on the fracture surfaces of the MCT specimens tested at RT cannot be replicated by the simulation. This is considered to be due to the fact that a straight initial crack front is used in the FE model, whereas fatigue pre-cracks in physical specimens show considerable curvature, altering the stress state in the vicinity of the crack front.

The triaxiality-dependent CZM is used in the next chapter to simulate unstable fracture of standardized CT specimens within the DBT region. Thereby, the loss of constraint observed in MCT specimens is assessed by comparing the mechanical fields in front of the crack tip with the large geometries.

6 Simulation of standard-sized CT specimens

Simulations of standard-sized CT specimens are performed within the DBT region to investigate whether the triaxiality-dependent CZM can be used for geometries other than the MCT, and to evaluate differences in the mechanical and fracture-mechanical behavior of different sizes of CT specimens. This is an important objective for validating the MCT geometry for fracture-mechanics testing within the transition region. The FE-models of a 0.5T CT geometry with 12.5 mm thickness and a 1T CT geometry with 25 mm thickness are described in Section 6.1. In Section 6.2, the simulated force-displacement curves, the predicted stable crack extension prior to unstable fracture and the predicted fracture toughness values from the standard-sized models are compared to the MCT simulations carried out in Chapter 5. Additionally, the mechanical fields in the vicinity of the crack front are compared between the geometries to assess their influence on the numerically predicted fracture behavior. In Section 6.3, the influence of the crack tip constraint on the numerical fracture toughness results is discussed.

6.1 FE-models of the standard-sized CT geometries

The FE-models of the standard-sized specimens represent geometrically upscaled versions of the MCT model described in Section 5.2.1. This means that all model parameters apart from the dimensions and number of elements are identical. In Figure 6.1, the quarter model of the 1T CT specimen is shown with the stiff loading pin. As with the MCT model, the element length in the cohesive zone is set to $1.5\text{ }\mu\text{m}$ in crack growth direction, but instead of 10 elements in thickness direction, 14 elements are used for the standard-sized models. This is to prevent the aspect ratio of the elements in the mid thickness of the specimens to become too large, causing numerical problems. The 0.5T CT model consists of 32700 elements with 196300 degrees of freedom, while the 1T CT model consists of 35000 elements with 210000 degrees of freedom. Both models also consist of 966 cohesive elements located in a strip of 0.1 mm length in front of the initial crack tip.

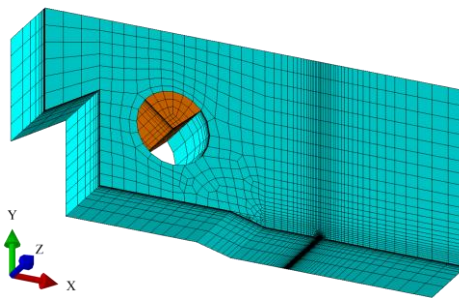


Figure 6.1: Quarter model of the 1T CT specimen with the stiff loading pin shown in brown

6.2 Numerical results

Elasto-plastic simulations with the standard-sized CT models are performed at -60 , -70 and -80°C using the respective flow curves determined in Section 4.2.3. Crack growth is simulated by means of the CZM using a triangular TSL with the triaxiality-dependent cohesive strength and constant cohesive energy calibrated in the previous chapter. To facilitate the initiation of unstable fracture, the cohesive

strength is not extrapolated beyond the maximum triaxialities obtained from the tensile test simulations. As with the MCT simulations, the unstable fracture criterion based on the numerical crack growth rate is employed to be able to predict numerical fracture toughness values.

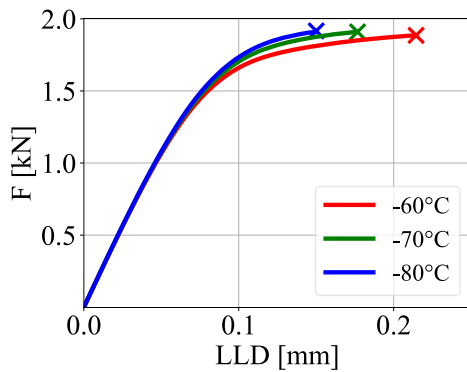
6.2.1 Force-displacement and J-R curves

In Figure 6.2, the simulated force-LLD and J-R curves from the MCT model (a, b), the 0.5T CT model (c, d) and the 1T CT model (e, f) are shown. All simulations terminate shortly after meeting the unstable fracture criterion. The initiation of unstable fracture predicted by the models is reflected in the flattening of the J-R curves near the maximum stable crack extension.

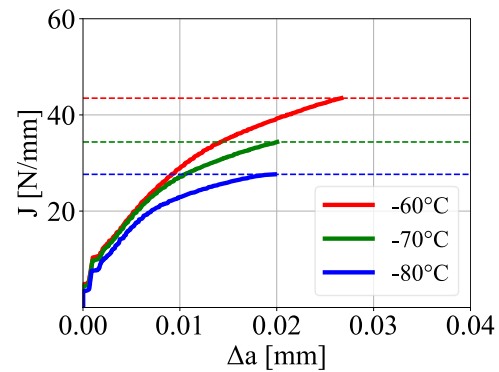
The force-LLD curves from the MCT simulations were already described in Section 5.2. Inelastic behavior prior to unstable fracture is shown by the 0.5T CT curves at all temperatures, albeit with a significantly smaller fraction of macroscopic plastic deformation as compared to the MCT results. In comparison, the force-LLD curves obtained from the 1T CT simulations show even less inelastic behavior, with the -80°C curve ending almost within the linear-elastic regime. The force-displacement curves indicate differences in the constraint of macroscopic plastic deformation between the geometries. These constraint differences are studied in detail in Section 6.2.2 by comparing the size of the plastic zone around the crack front relative to the specimen size.

The numerical J-R curves obtained from the three models are similar at the individual temperatures. In all cases, the largest stable crack extension before unstable fracture is predicted at -60°C , while the crack extensions at -70 and -80°C are almost identical. Overall, the crack extensions predicted by the 0.5T and 1T CT models are slightly larger than the MCT predictions. The largest J-integral values at fracture are obtained from the 1T CT geometry, followed by the 0.5T CT and finally the MCT model. The simulated LLD, force, crack extension and J-integral at fracture are listed for each model and temperature in Table A.14.

In the next section, the constraint differences between the geometries are studied based on the mechanical fields in the vicinity of the crack front, including the crack opening stress, triaxiality and equivalent plastic strain. Assessment of the constraint loss in MCT specimens is important for validating the geometry for use in future surveillance programs. This is done by showing under which conditions the mechanical and fracture-mechanical behavior of MCT specimens is similar to that of standard-sized specimens.



(a) MCT model



(b) MCT model

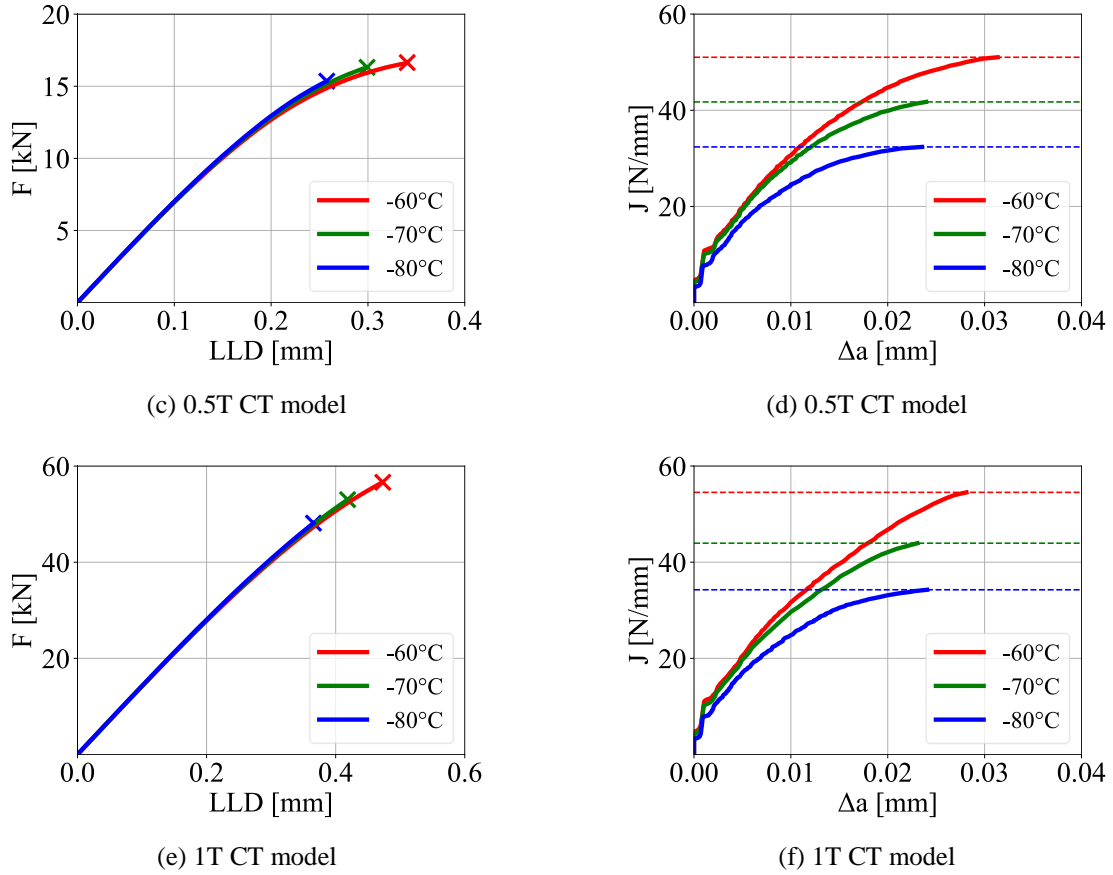


Figure 6.2: Simulated force-LLD and J-R curves from the MCT model (a, b), the 0.5T CT model (c, d) and the 1T CT model (e, f) at -60, -70 and -80°C

6.2.2 Mechanical fields in front of the crack tip

Apart from the statistical size effect, the constraint level near the crack front is considered to influence the results obtained from fracture-mechanical testing. Loss of constraint is assumed to lead to a reduction of the overall stress level in front of the crack tip, causing a reduction in J_{el} . On the other hand, the increased plastic deformation will lead to an increase in J_{pl} , which in turn leads to an increase in K_{Jc} . The force-displacement curves in Figure 6.2 showed that both the 0.5T and 1T CT models predict little macroscopic plastic deformation prior to unstable fracture, particularly at -80°C. It may therefore be assumed that both geometries fail under similarly high constraint conditions. Constraint loss of the MCT geometry is indicated by an increased macroscopic plastic deformation prior to unstable crack growth. By analyzing and comparing the mechanical fields in front of the crack tip, the constraint differences between the CT geometries are further assessed.

The field quantities describing the mechanical behavior of the geometries in front of the crack tip are the crack opening stress σ_y as the driver of crack growth and unstable fracture, the triaxiality h as a constraint parameter describing the stress state and the equivalent plastic strain $\varepsilon_{p,eq}$, which is used in conjunction with the triaxiality to describe loss of constraint with increasing load and temperature. The accumulated equivalent plastic strain

$$\varepsilon_{p,acc,eq} = \int_0^{\tilde{t}} \dot{\varepsilon}_{p,eq} dt \quad (6.1)$$

is a scalar measure of the inelastic deformation of the material, with the equivalent plastic strain rate $\dot{\varepsilon}_{p,eq}$ for von Mises plasticity defined by

$$\dot{\varepsilon}_{p,eq} = \sqrt{\frac{2}{3} \dot{\varepsilon}_p : \dot{\varepsilon}_p}, \quad (6.2)$$

where $\dot{\varepsilon}_p$ denotes the plastic strain rate tensor. In the case of monotonic proportional loading, the equivalent plastic strain is equal to $\varepsilon_{p,acc,eq}$. To determine the mechanical fields, simulations with the MCT, 0.5T and 1T CT models were carried out applying the cohesive zone parameters calibrated in Section 5.2.2. Size-adjustment of the cohesive energy was not considered for this study.

In the following diagrams, x denotes the distance from the initial crack tip in crack growth direction and z/B is the distance from the mid thickness towards the side surface normalized by the initial thickness of the respective geometry. The field quantities in the mid thickness and along the thickness direction are obtained from the simulations at -60 and -80°C . The x -position of each z/B_x -curve is the position of the maximum of the respective field quantity along the mid thickness.

First, the field quantities are compared for a moderate crack tip load of $K_I = 35 \text{ MPa}\sqrt{\text{m}}$. In Figure 6.3, the crack opening stresses are shown at the positions and temperatures mentioned above. All models predict similar curves at both temperatures. The highest values of σ_y are obtained from the MCT simulation with 1756 MPa at -60°C and 1856 MPa at -80° , while the 1T CT model yields the lowest values with 1743 and 1843 MPa. For all geometries, the maximum σ_y is reached in the mid thickness at a distance of about 10 to 12 μm from the initial crack tip.

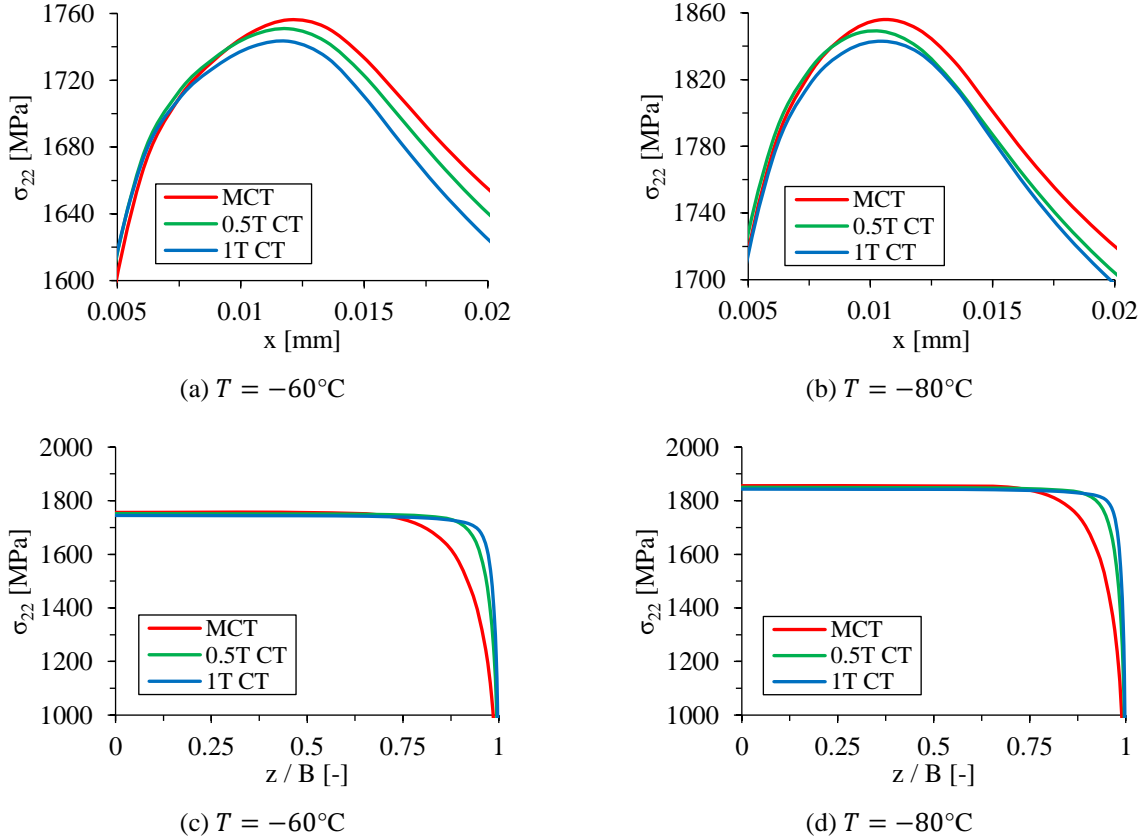


Figure 6.3: Crack opening stress in the mid thickness (a, b) and along the thickness direction at the x -position of the maximum σ_y (c, d) for $K_I = 35 \text{ MPa}\sqrt{\text{m}}$

The crack opening stress remains approximately constant over most of the thickness for all geometries. At 75% of the distance from the mid thickness towards side surface, the σ_y of the MCT begins to decrease rapidly towards the side surface. With the 0.5T and 1T CT geometries, this reduction only begins at 90 and 95% of the distance respectively.

Regarding the triaxiality, which is shown in Figure 6.4, the standard-sized models predict similar maximum values with 2.90 at -60°C and 2.85 at -80°C , while the maxima predicted by the MCT model are slightly lower with 2.88 and 2.83. The locations of the triaxiality maxima are offset from the peaks of the crack opening stress by about $2\text{ }\mu\text{m}$ in crack growth direction. As with the crack opening stress, all geometries show a region of constant h starting from the mid thickness, followed by a strong decrease near the side surface. For the MCT, the reduction starts at about half the thickness, while for the 0.5T and 1T CT the decrease begins at 85 and 90% of the thickness respectively. Similar minimum triaxialities between 0.6 to 0.7 are observed at the side surfaces for all geometries at both temperatures.

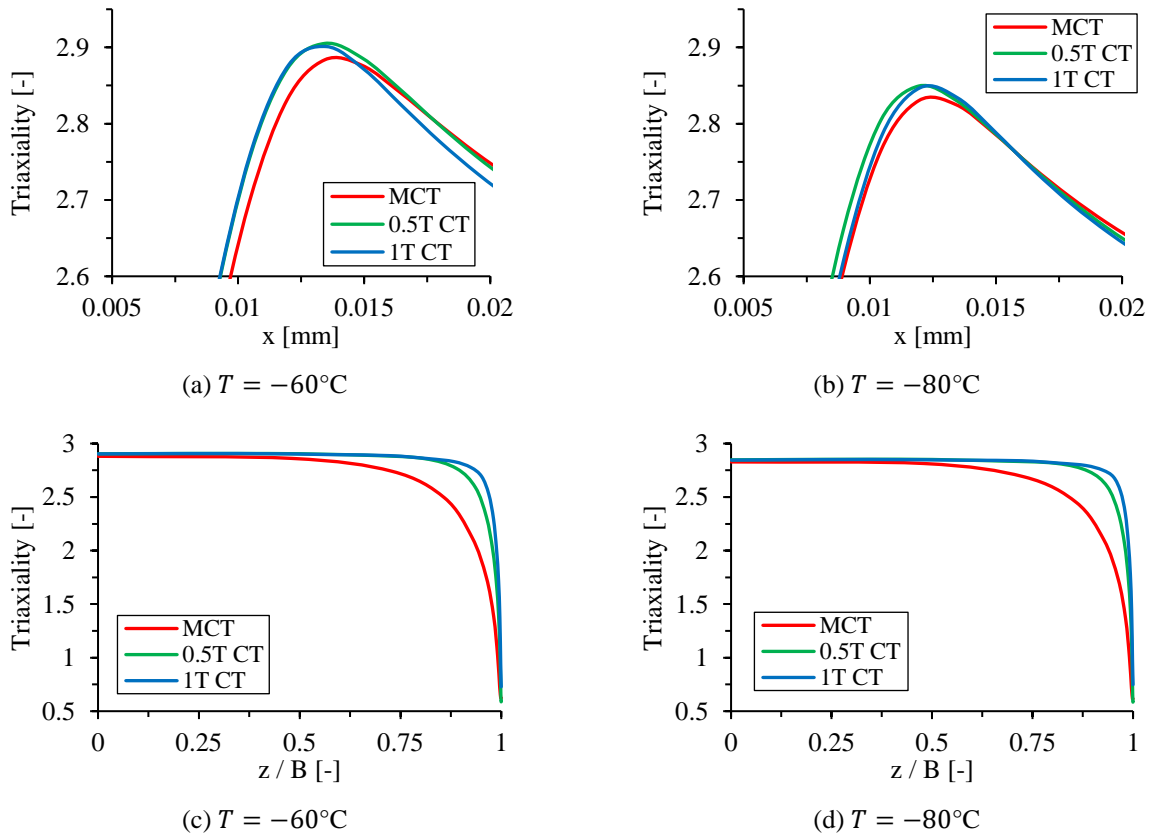


Figure 6.4: Triaxiality in the mid thickness (a, b) and along the thickness direction at the x -position of the maximum h (c, d) for $K_I = 35\text{ MPa}\sqrt{\text{m}}$

The equivalent plastic strain is shown in Figure 6.5. In the mid thickness, the highest $\varepsilon_{p,eq}$ is obtained for the MCT, followed by the 0.5T and 1T CT geometries. An overall increase of $\varepsilon_{p,eq}$ from -80 to -60°C is observed. At -60°C , the plastic zone size along the ligament is $457\text{ }\mu\text{m}$ for the MCT, $344\text{ }\mu\text{m}$ for the 0.5T CT and $270\text{ }\mu\text{m}$ for the 1T CT. At -80°C , the plastic zone sizes reduce to 391 , 287 and $247\text{ }\mu\text{m}$. Thereby, a relative decrease of the plastic zone size by 14% is observed for the MCT, while a decrease of 17% is found for the 0.5T CT and 9% for the 1T CT.

All $\varepsilon_{p,eq}$ curves along the thickness direction decrease with increasing distance from the mid thickness. While the curves from the large specimen simulations are similar, the MCT shows lower $\varepsilon_{p,eq}$ above 85% of the distance towards the side surface and higher $\varepsilon_{p,eq}$ closer to the mid thickness.

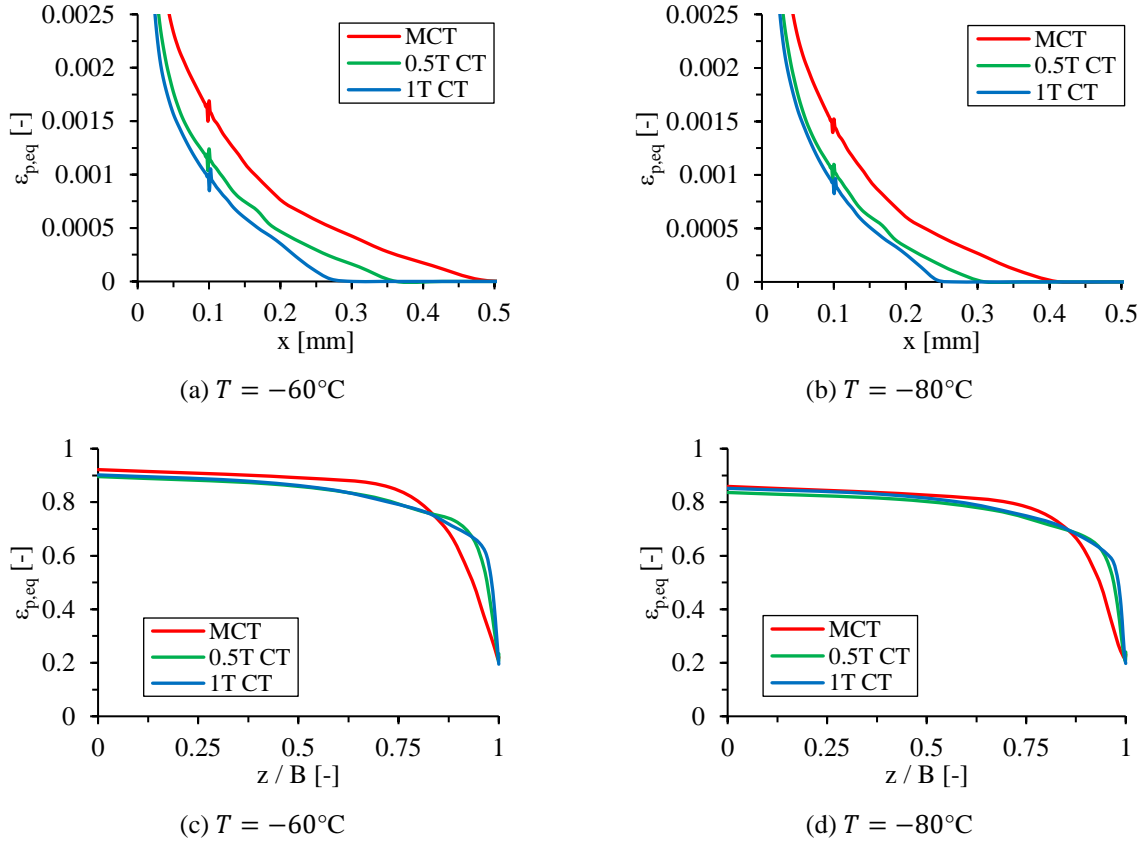


Figure 6.5: Equivalent plastic strain in the mid thickness (a, b) and along the thickness direction at the x -position of the maximum $\varepsilon_{p,eq}$ (c, d) for $K_I = 35 \text{ MPa}\sqrt{\text{m}}$

From the numerical results at $K_I = 35 \text{ MPa}\sqrt{\text{m}}$, it is concluded that the mechanical behavior of the geometries is comparable at this moderate load level at both -60 and -80°C . Similar levels of maximum crack opening stress and maximum triaxiality are observed throughout most of the normalized thickness starting from the mid thickness. However, the MCT differs from the other geometries by its behavior near the side surfaces. Both the crack opening stress and triaxiality are significantly reduced above 75% of the distance from the mid thickness, showing that some constraint is lost already at this load level. Additionally, an increased plastic zone size is observed for the MCT, which is particularly noticeable at -60°C . This confirms that plastic deformation is less constrained in the MCT compared to the standard-sized geometries. However, the MCT can still be regarded as a high constraint geometry at this load level.

In the next step, K_I is increased to $70 \text{ MPa}\sqrt{\text{m}}$, and the resulting mechanical field quantities are compared again. The crack opening stress curves are shown in Figure 6.6. At -60°C , the maximum σ_y from the MCT simulation is 1789 MPa , while the 0.5T and 1T CT models yield 1775 and 1765 MPa respectively. With the increased loading, the difference between the MCT and the 1T CT maxima is increased from 13 MPa to 26 MPa . In contrast, it is found that the difference in the maximum σ_y is decreased at -80°C . At this temperature, the MCT simulation yields a maximum σ_y of 1871 MPa , while 1872 MPa is

obtained from the 0.5T and 1864 MPa from the 1T CT simulation. Here, the difference between the maxima from the MCT and the 1T CT simulations is only 7 MPa.

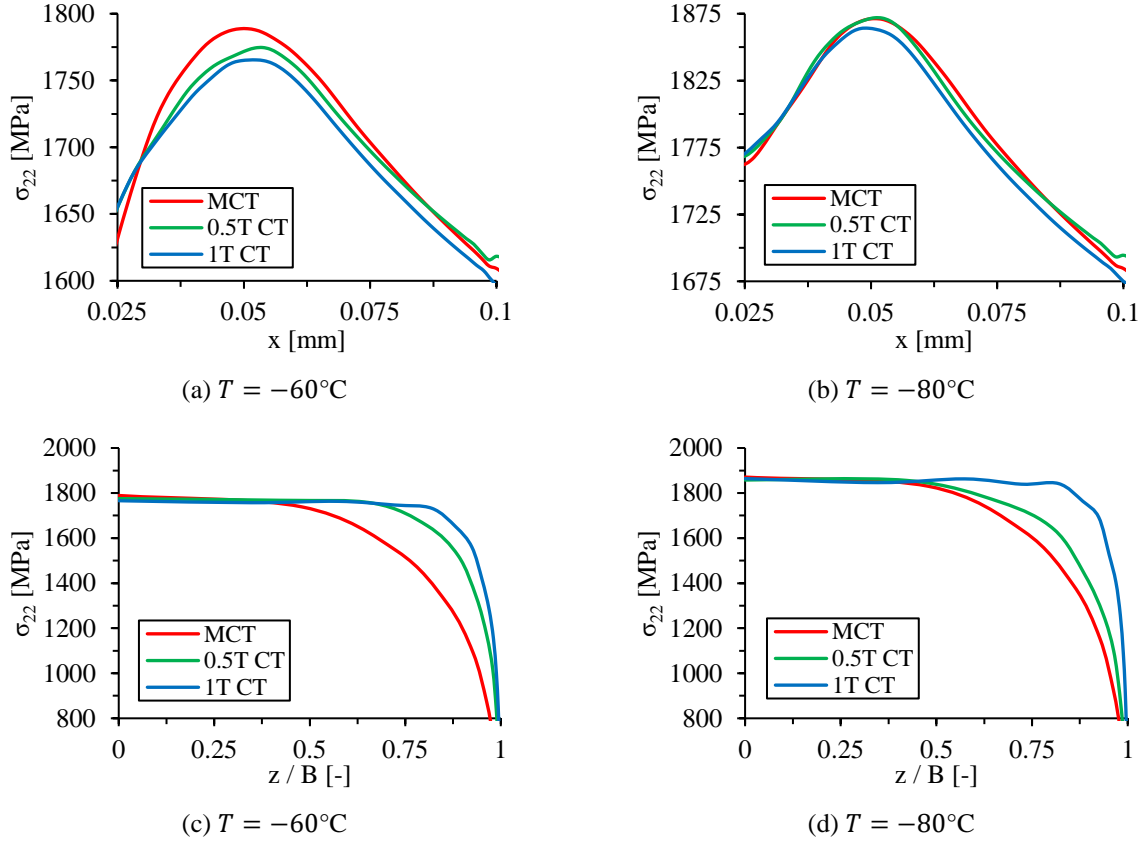


Figure 6.6: Crack opening stress in the mid thickness (a, b) and along the thickness direction at the x -position of the maximum σ_y (c, d) for $K_I = 70 \text{ MPa}\sqrt{\text{m}}$

The curves along the thickness direction show that the region of constant σ_y is reduced for all geometries compared to $K_I = 35 \text{ MPa}\sqrt{\text{m}}$. At -60°C , the crack opening stress of the MCT begins to decrease already at 45% of the distance from the mid thickness to the side surface compared to 75% at the lower crack tip load. For the 0.5T CT, the region of constant σ_y is reduced from 90 to 70% of the distance from the mid thickness. The smallest decrease is observed for the 1T CT geometry from 95 to 80%.

In Figure 6.7, the triaxiality curves are shown for $K_I = 70 \text{ MPa}\sqrt{\text{m}}$. With the increased loading, a reduction of the maximum h in front of the crack tip from 2.88 to 2.70 is observed for the MCT at -60°C . At the same time, the maximum triaxiality values from the standard-sized geometries reduce only slightly from 2.90 to 2.88. At -80°C , the maximum h from the MCT is reduced from 2.83 to 2.69, which is a smaller reduction compared to -60°C . Again, a minor reduction from 2.85 to 2.82 is observed for the standard-sized geometries.

The standard-sized geometries are shown to maintain a high level of triaxiality over a large part of the normalized thickness at both temperatures. With the 0.5T CT, the region of constant h extends to half the thickness, while at $K_I = 35 \text{ MPa}\sqrt{\text{m}}$ it was 85% of the thickness. In case of the 1T CT, the region of constant h is reduced from 90 to 75% of the thickness with increased crack tip load. The curves of the MCT show that at $K_I = 70 \text{ MPa}\sqrt{\text{m}}$, the region of constant triaxiality has vanished entirely with a

reduced h along the entire thickness. A monotonous decrease in h is observed starting from the mid thickness, while at $K_I = 35 \text{ MPa}\sqrt{\text{m}}$ the region of constant h covered half the thickness.

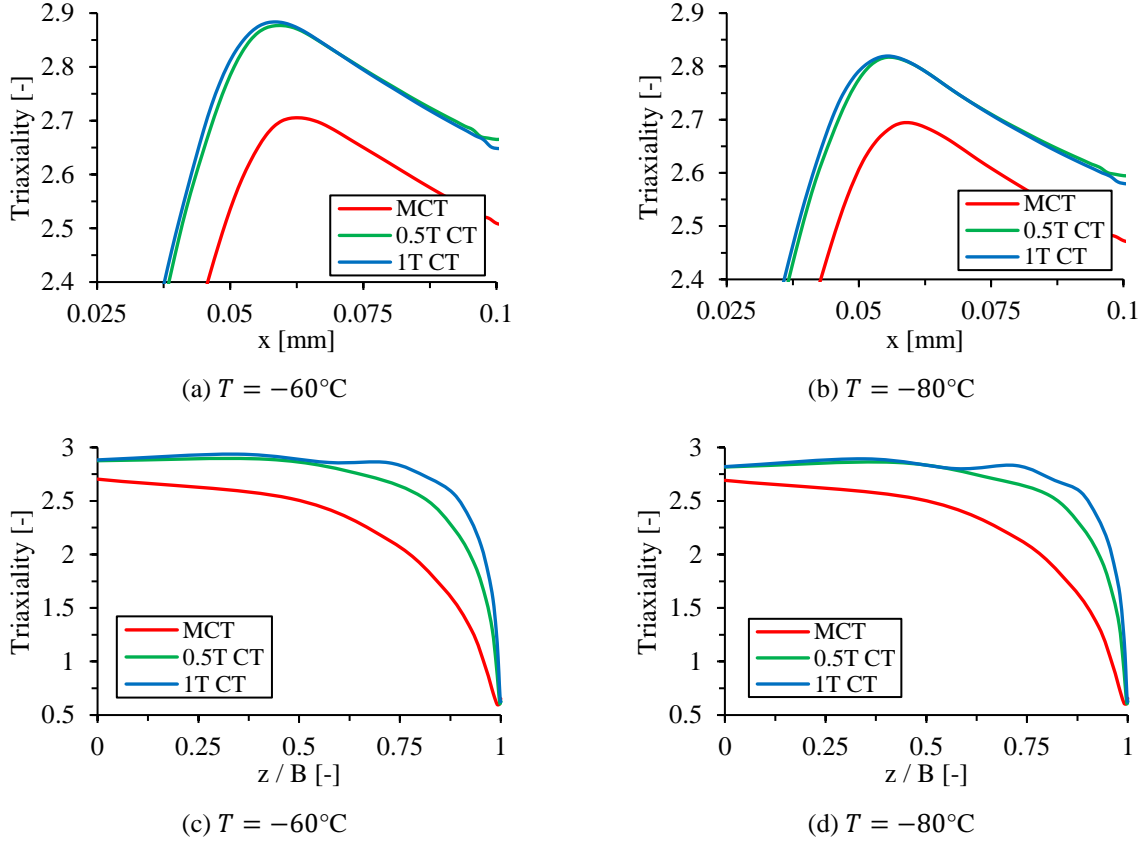


Figure 6.7: Triaxiality in the mid thickness (a, b) and along the thickness direction at the x -position of the maximum h (c, d) for $K_I = 70 \text{ MPa}\sqrt{\text{m}}$

Regarding the equivalent plastic strain in Figure 6.8, a significant increase is observed for the MCT compared to the standard-sized geometries in the mid thickness. The equivalent plastic strain from the MCT simulation is about 2.4-times larger than the $\varepsilon_{p,eq}$ from the 1T CT model at a distance of 0.1 mm from the initial crack tip at both temperatures. At $K_I = 35 \text{ MPa}\sqrt{\text{m}}$, the $\varepsilon_{p,eq}$ of the MCT was only 1.6-times larger than the 1T CT value at the same distance from the crack tip. The equivalent plastic strain of the 0.5T CT is comparable to the 1T CT in crack growth direction.

Similar curves are obtained in thickness direction for all geometries. As with the results at $K_I = 35 \text{ MPa}\sqrt{\text{m}}$, the equivalent plastic strain of the MCT is slightly higher than the $\varepsilon_{p,eq}$ of the standard-sized geometries near the mid thickness but lower close to the side surface.

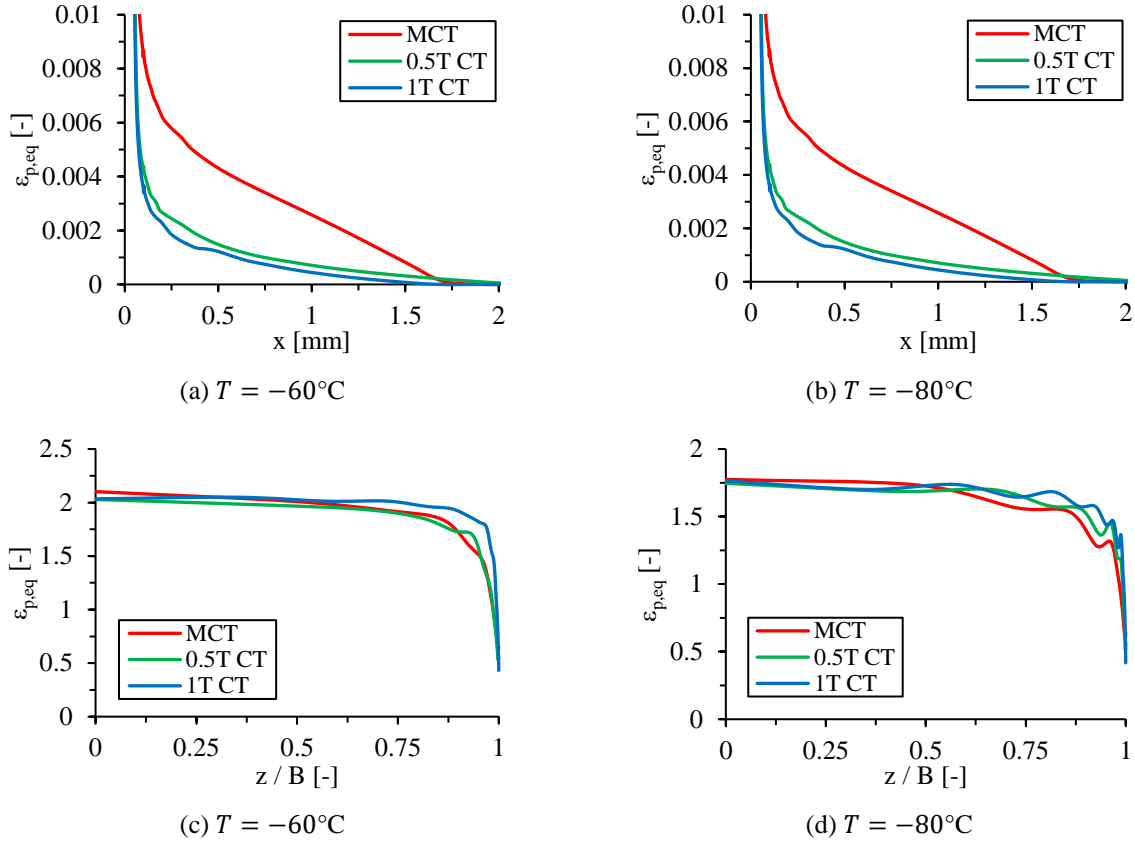


Figure 6.8: Equivalent plastic strain in the mid thickness (a, b) and along the thickness direction at the x -position of the maximum $\varepsilon_{p,eq}$ (c, d) for $K_I = 70 \text{ MPa}\sqrt{\text{m}}$

Compared to the results at $K_I = 35 \text{ MPa}\sqrt{\text{m}}$, a greater overall difference of the mechanical field quantities between the MCT and the standard-sized geometries is observed at $K_I = 70 \text{ MPa}\sqrt{\text{m}}$. The evolution of the triaxiality in front of the crack tip shows that at high crack tip loading, the constraint level of the MCT specimen decreases throughout the entire thickness. Simultaneously, the constraint level of the standard-sized geometries is maintained throughout most of the thickness and only reduces near the side surfaces. That being said, the decrease in triaxiality of the MCT in the mid thickness is small with 0.18 at -60°C and 0.14 at -80°C . Additionally, the crack opening stress was shown to remain comparable to the standard-sized geometries throughout half the thickness. Regarding the inelastic behavior, a significant increase of the equivalent plastic strain was observed for the MCT in crack growth direction compared to the large geometries. In the following, the plastic zone sizes are compared for $K_I = 70 \text{ MPa}\sqrt{\text{m}}$ to further assess the extent of macroscopic plastic deformation.

In Figure 6.9, the plastic zones ($\varepsilon_{p,eq} > 10^{-4}$) are shown in red on the MCT, 0.5T and 1T CT geometries at -60°C . While the plastic zones of both the 0.5T and 1T CT are limited to a region around the crack tip, the size relative to the specimen dimensions is significantly larger for the 0.5T CT compared to the 1T CT geometry. Additional plastic deformation is observed at the backside and the pin holes of the 0.5T CT due to compressive stresses. Regarding the crack plane, it is found for both the 0.5T and the 1T CT that the plastic zone is more pronounced close to the side surfaces than in the mid thickness. This shows that, at the given crack tip load, plastic deformation is constrained in the mid thickness due to the plain strain condition.

Contrary to the standard-sized geometries, large-scale plastic deformation that extends from the initial crack tip to the specimen backside is observed for the MCT geometry. At the side surfaces, the crack tip plastic zone is merged with the region of plastic deformation resulting from the compressive stresses at the specimen backside. Halfway along the ligament, where the rotation point of the specimen halves is located, a boundary of elastic deformation remains between the plastically deformed regions. The view onto the crack plane shows that the crack tip plastic zone extends almost as far in the mid thickness as near the side surfaces, indicating loss of constraint. The plastic zones at -80°C are not shown here, but correspond to those at -60°C .

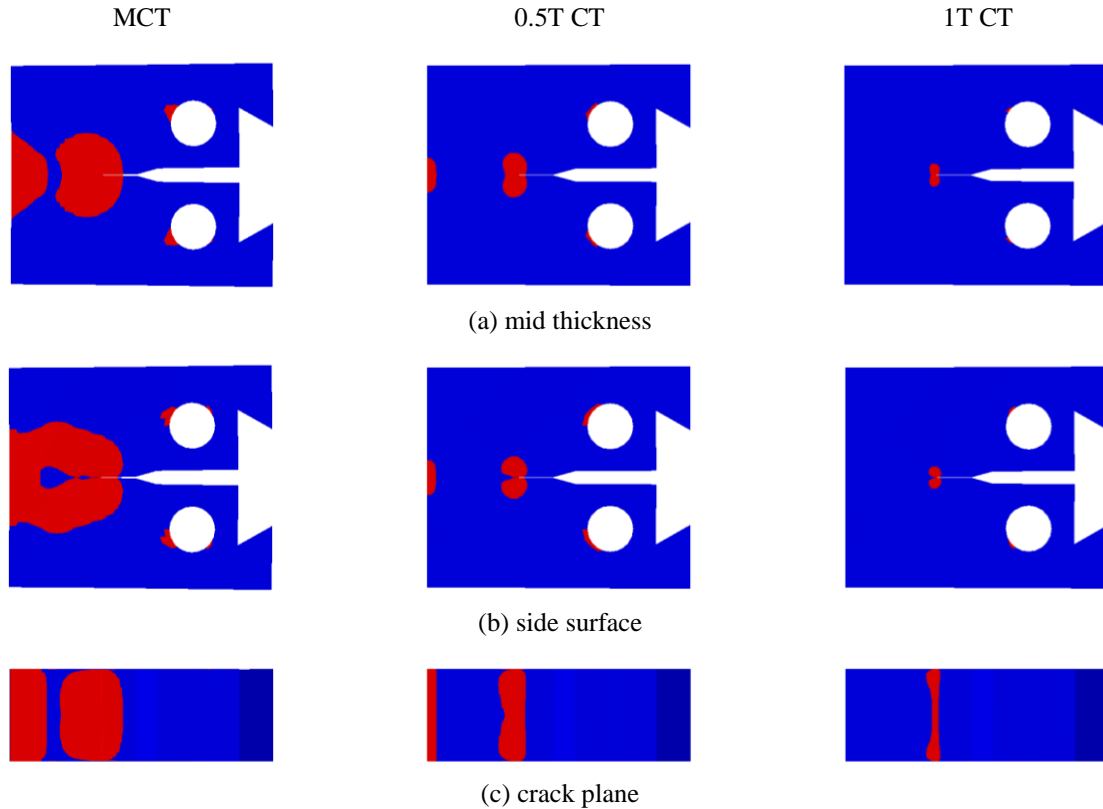


Figure 6.9: Simulated plastic zone sizes of the MCT, 0.5T and 1T CT models for $K_I = 70 \text{ MPa}\sqrt{\text{m}}$ at -60°C

The extent of the plastic zone ahead of the crack tip can be estimated using Irwin's stress relaxation model [113], which, for an elastic-perfectly plastic material, yields

$$R_p = \frac{1}{\pi} \left(\frac{K_I}{\sigma_{YS}^*} \right)^2. \quad (6.3)$$

In this equation, σ_{YS}^* is equal to the yield strength of the material for plane stress and equal to $\frac{1}{1-2\nu} \sigma_{YS}$ for plane strain. The calculated plastic zone sizes for plane stress and plane strain using Irwin's model are plotted against K_I at -60°C in Figure 6.10. The curves are compared to the simulated lengths of the plastic regions starting from the crack tip in the mid thickness of the MCT, 0.5T and 1T CT geometries. At crack tip loads below $20 \text{ MPa}\sqrt{\text{m}}$, the simulated plastic zone sizes of the respective geometries are approximately equal to the calculated R_p for plane strain. This is further confirmation that the MCT can be viewed as a high constraint geometry at low load levels. At crack tip loads beyond $20 \text{ MPa}\sqrt{\text{m}}$, all simulated curves begin to deviate from Irwin's plane strain estimation towards larger plastic zone sizes. This deviation, while similar for the 0.5T and 1T CT geometries, is pronounced in the case of the MCT.

At $40 \text{ MPa}\sqrt{\text{m}}$, the plastic zone of the MCT is almost double the size of the 1T CT plastic zone. It is clear that the plane strain condition is lost at lower K_I in case of the MCT as compared to the standard-sized geometries. While the growth of the plastic zone continues to accelerate for the large geometries beyond $40 \text{ MPa}\sqrt{\text{m}}$, a deceleration is observed for the MCT. This is due to the plastic zone no longer being small compared to the dimensions of the MCT and the crack tip stress field being influenced by the compressive stresses around the specimen backside. At a K_I of $40 \text{ MPa}\sqrt{\text{m}}$, the size of the plastic zone in the mid thickness is 21% of the initial crack length for the MCT, while being 4% and 2% for the 0.5T and 1T CT respectively.

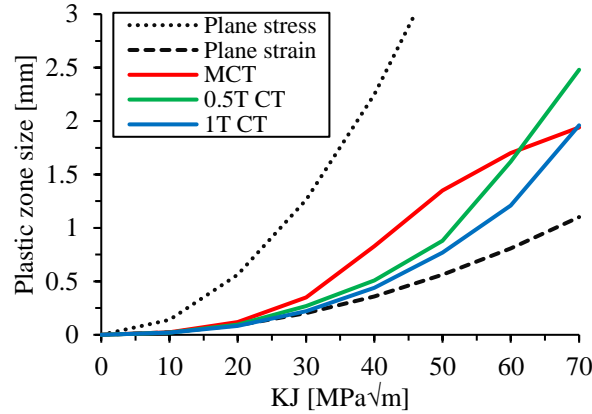


Figure 6.10: Simulated mid thickness plastic zone sizes along the ligament for the MCT, 0.5T and 1T CT geometries at -60°C compared to the analytical plastic zone sizes for plane stress and plane strain

Based on the evaluation of the mechanical fields in front of the crack tip and the plastic zone sizes, it is concluded that, contrary to the large geometries, the MCT experiences constraint loss on a global scale under high crack tip loading. The primary factors for this assessment are a decrease in triaxiality throughout the entire thickness and large scale yielding from the crack front to the specimen backside at high crack tip loads. It is found that this constraint loss is comparable at -60 and -80°C . As the triaxiality in the mid thickness is reduced only slightly, it is presumed that a relatively high level of constraint is maintained within the region experiencing the maximum crack opening stress. It is to be expected that the differences between the geometries in their mechanical behavior will become more pronounced as the loading is increased further.

6.2.3 Fracture toughness

In Table 6.1, the numerical fracture toughness results $K_{Jc,num}$ from the simulations and the corresponding median fracture toughness values $K_{Jc,MC}$ from the Master Curve, which was determined experimentally in Section 4.3.5, are listed. The $K_{Jc,MC}$ values are size-adjusted from the 1T CT geometry to the respective smaller geometries by means of Equation (2.18). As before, the $K_{Jc,num}$ values are determined at the point where the unstable fracture criterion (Equation (2.19)) is met. The predicted fracture toughness values are similar at the respective temperatures. However, an increase with specimen size is observed at all temperatures. With an average increase of $8.0 \text{ MPa}\sqrt{\text{m}}$, the difference is greater between the MCT and 0.5T CT compared to the 0.5T and 1T CT with an average increase of $2.9 \text{ MPa}\sqrt{\text{m}}$.

The results of the MCT simulations are consistent with their corresponding $K_{Jc,MC}$ values, as the cohesive energy was calibrated for this geometry. In contrast, the $K_{Jc,num}$ results from the 0.5T and 1T CT

models are significantly larger than their corresponding Master Curve values. Since no fracture-initiating particles are modeled in front of the crack tip, weakest-link statistics and the related size effect are not accounted for by the CZM. Of course, it would be possible to calibrate the cohesive energy separately for the 0.5T and 1T CT geometries to fit their numerical results to the corresponding $K_{Jc,MC}$ values. However, this would require additional tests on standard-sized specimens and the goal of this study is to predict the fracture toughness using miniaturized specimens only.

Table 6.1: Numerical fracture toughness $K_{Jc,num}$ and median fracture toughness from the experimental Master Curve $K_{Jc,MC}$ (size-adjusted for MCT and 0.5T CT)

Geometry	T [°C]	$K_{Jc,num}$ [MPa \sqrt{m}]	$K_{Jc,MC}$ [MPa \sqrt{m}]
MCT	-60	99.6	99.4
	-70	88.7	88.4
	-80	79.7	79.3
0.5T CT	-60	107.9	79.7
	-70	97.8	71.5
	-80	86.2	64.6
1T CT	-60	111.6	70.2
	-70	100.3	63.3
	-80	88.7	57.5

6.3 Influence of constraint on the numerical fracture toughness

In Section 6.2.2, it was confirmed that the MCT geometry is subject to loss of constraint on a global scale with increasing crack tip load. An overall decrease of the crack opening stress and triaxiality was observed along the thickness direction, starting from the side surfaces. This means that in a physical MCT specimen, the area susceptible to cleavage initiation decreases with increasing load. As a consequence, the median size-corrected fracture toughness obtained from small specimen tests is expected to be larger than the fracture toughness obtained from standard-sized specimens. This was confirmed in an experimental study conducted by Scibetta et al. in 2002 [6], who compared the reference temperatures obtained from MCT and standard-sized CT specimens. They found that on average, the T_0 determined from MCT tests is 8.5°C lower than the reference temperature obtained from standard-sized specimens. Regarding the deterministic CZM, it was explained in Section 5.2.2 that the condition for the initiation of unstable crack growth is the crack opening stress reaching the cohesive strength in front of the crack tip. It was shown by the simulations that the highest σ_y is present in the mid thickness. Therefore, unstable crack growth in the simulations is always initiated at this location and, as a consequence, the numerical fracture toughness results are not influenced by the loss of constraint near the side surfaces.

In Table 6.1, it was shown that the $K_{Jc,num}$ values from the 0.5T and 1T CT simulations are slightly larger than the results from the MCT simulations. This can be explained by the loss of constraint in the mid thickness of the MCT geometry at high crack tip loads. The decreased triaxiality results in a reduction of the cohesive strength in the vicinity of the crack tip (see Section 5.1.3), which in turn facilitates unstable crack initiation in the MCT. Additionally, the cohesive energy was calibrated by fitting the numerical fracture toughness results from the MCT simulations to the median fracture toughness values

from the Master Curve, which were size-adjusted to the MCT geometry. This means that the constraint loss in the mid thickness of the MCT is included in the calibrated Γ_c . In other words, the calibrated Γ_c is too high for the large geometries as they do not experience constraint loss in the mid thickness. Consequently, the $K_{Jc,num}$ results from the standard-sized models are overestimated. In order to obtain lower $K_{Jc,num}$ values from the large geometries, a triaxiality-dependent cohesive energy would have to be used in addition to the triaxiality-dependent cohesive strength. However, developing a method to calibrate a triaxiality-dependent cohesive energy is beyond the scope of this work.

To conclude, the fracture toughness bias between MCT and standard-sized CT geometries observed by Scibetta et al. could not be predicted by the deterministic CZM as the numerical fracture toughness is not influenced by the loss of constraint near the side surfaces. To accurately simulate the constraint effect, it would be necessary to introduce statistically distributed microstructural features across the cohesive zone that can act as unstable fracture initiators. Thereby, a dependence of the numerical fracture toughness results on the reduced crack opening stress and triaxiality near the side surfaces could be established. In addition, the $K_{Jc,num}$ results were shown to increase with increasing triaxiality in the mid thickness, leading to overestimated values from the standard-sized models. To improve the predictions, it is suggested to use a triaxiality-dependent cohesive energy.

6.4 Summary of the standard-sized CT simulations

The triaxiality-dependent cohesive zone parameters for unstable crack growth identified in Chapter 5 were used to simulate a 0.5T and a 1T CT geometry within the DBT region. Thereby, the objective was to predict fracture toughness values for the standard-sized geometries and compare them to the MCT results. In addition, the crack opening stresses, triaxialities and equivalent plastic strains in front of the crack tip were studied in detail to evaluate constraint differences between the geometries.

The investigation of the mechanical field quantities showed that, at moderate crack tip load, the mechanical behavior of the MCT is similar to that of the large geometries. However, differences between the geometries regarding the plastic zone size were observed, indicating that inelastic deformation is less constrained in the MCT. In addition, a reduced triaxiality near the side surfaces was obtained for the MCT. Significant differences between the MCT and the standard-sized geometries were found for all mechanical field quantities at a crack tip load of $70 \text{ MPa}\sqrt{\text{m}}$. The MCT simulations show a decrease in triaxiality along the thickness direction starting from the mid thickness and large scale yielding between the crack front and the backside, confirming that constraint is lost on a global scale. However, a high crack opening stress and a high level of triaxiality are maintained in the mid thickness, showing that the mechanical behavior in this region remains similar to the large geometries.

It was found that the numerical fracture toughness values from the standard-sized models are slightly increased compared to the MCT results. The $K_{Jc,num}$ results were shown to increase with increasing triaxiality in the mid thickness due to the triaxiality-independence of the cohesive energy. It was further concluded that the constraint effect observed in experiments cannot be simulated by the deterministic CZM since the numerical fracture toughness results remain unaffected by the loss of constraint near the side surfaces.

In the next chapter, the probabilistic CZM is described, which is aimed at simulating the statistical nature of the fracture behavior of ferritic steels within the DBT region. Statistically distributed fracture

toughness values are predicted to determine the reference temperature numerically and the result is compared to the experimental T_0 from the MCT tests in Chapter 4.

7 Probabilistic CZM approach

The motivation for the probabilistic CZM approach is to improve the predictive capabilities of the deterministic CZM in terms of fracture toughness by modeling the cohesive zone on the mesoscale. Thereby, regions of lower and higher fracture resistance are introduced that may act as initiators or inhibitors of unstable fracture. By randomly generating the layout of the cohesive zone for each simulation based on the quantitative fractographic results from Section 4.4.2, the statistical nature of the fracture behavior of ferritic steels within the transition region is reproduced. An introduction to the development and applications of the probabilistic CZM was given in Section 3.2.

The modeling of the cohesive zone on the mesoscale based on quantitative fractographic results is described in Section 7.1. In Section 7.2, multiple MCT simulations with randomly generated cohesive zones are carried out within the DBT region. It is first shown how the ductile and brittle cohesive elements in front of the crack tip interact and the numerical mechanism leading to unstable crack extension is explained. The Master Curve approach is applied to the numerical fracture toughness results in Section 7.3 to obtain a reference temperature prediction, which is then compared to the experimental result from the MCT tests performed in Chapter 4. The capability of the probabilistic CZM to predict the experimentally observed fracture toughness scatter within the DBT region is studied in detail. Additionally, the material volume required by the probabilistic CZM approach is evaluated and compared to the material requirement of the experimental Master Curve approach.

7.1 Mesoscale modeling of the cohesive zone

Cohesive elements with either brittle or ductile fracture properties are distributed throughout the cohesive zone based on the ductile fracture ratio DFR determined by means of quantitative fractography. It was shown in Section 5.2 that the fracture behavior of the MCT specimens at RT can only be accurately simulated using a triaxiality-dependent cohesive strength, while the unstable fracture behavior within the transition region could be simulated using both a triaxiality-dependent and a constant cohesive strength. The UEL subroutine by Scheider, which is used for incorporating cohesive elements into the FE-model (see Section 2.4.4), is not designed to handle multiple definitions of triaxiality dependence for separate sets of cohesive zone parameters. This means that, without significant modifications to the subroutine, triaxiality dependence could only be modeled for either the brittle or ductile cohesive elements. Therefore, a constant σ_c of 2005.5 MPa and Γ_c of 0.94 N/mm, as identified in Section 5.2.2.2 at -80°C, are used in conjunction with a triangular TSL for the brittle cohesive elements. For the ductile cohesive elements, the trapezoidal TSL with the triaxiality-dependent σ_c calibrated in Section 5.1.3 and Γ_c of 2.25 N/mm calibrated in Section 5.2.2.3 is used. The first shape parameter δ_1 is set to 0.001 to match the brittle TSL and the second shape parameter δ_2 is kept at 0.3.

In Figure 7.1, the TSLs used for the brittle and ductile cohesive elements are shown. The trapezoidal TSL used for the ductile elements is plotted for multiple levels of triaxiality. While the cohesive strength increases with triaxiality, the critical separation decreases since the cohesive energy remains constant. Above a triaxiality of 2.36, the brittle cohesive strength is surpassed by that of the ductile cohesive elements. In addition, due to the greater cohesive energy at RT, the critical separation of the ductile elements is larger at all triaxialities. Consequently, the ductile elements exhibit an increased

resistance to separation and fracture at high triaxialities compared to the brittle elements. At low triaxialities, the ductile elements show a lower resistance to initial separation. The interaction between the brittle and ductile elements near the crack front is investigated in the next section.

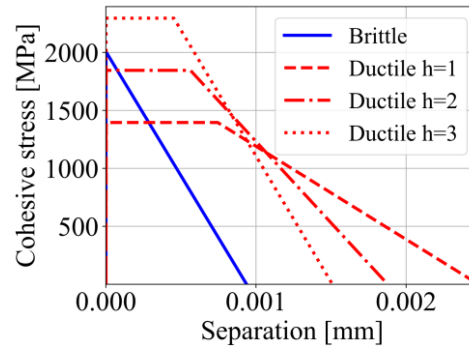


Figure 7.1: TSLs for the brittle and ductile cohesive elements

The quantitative analysis of the fracture surfaces of the MCT specimens in Section 4.4.2 showed that the average size of the ductile fracture regions is about 50 μm in thickness direction and 18 μm in crack growth direction, independent of temperature. For the initial simulations with the probabilistic model, the cohesive elements are grouped into clusters that are of the same size as the average size of the experimental ductile fracture regions. To achieve this, the element length in thickness direction is set to 50 μm , resulting in a total of 40 elements between the mid thickness and the side surface. The element length in crack growth direction is kept at 1.5 μm , meaning that a single cluster consists of 12 elements. Additionally, the length of the cohesive zone is set to 288 μm , so that 12 clusters fit into the cohesive zone in crack growth direction. This results in a total of 480 element clusters with 18x50 μm size across the cohesive zone.

In the next step, a specified number of clusters are randomly assigned ductile cohesive properties based on the DFR. For instance, at -60°C a DFR of 0.0706 is obtained from Equation (4.13), meaning that 7.1% of clusters are assigned ductile properties. The remaining clusters are assigned brittle properties. A new spatial distribution of ductile and brittle clusters is generated for each simulation. In Figure 7.2, examples of probabilistic cohesive zones are shown for -80°C (a) and -45°C (b) with the ductile element clusters shown in red and the brittle clusters shown in blue. As before, the x -coordinate denotes the distance from the initial crack front in direction of the specimen backside, while the z -coordinate indicates the distance from the mid thickness of the specimen to the side surface. It is clear that at -45°C , due to the increased DFR, considerably more ductile clusters are generated compared to -80°C . In some locations, the ductile clusters are connected to form larger clusters. These are expected to have a greater influence on the fracture behavior of the specimen than small clusters. The cohesive zones shown in the figure represent the simplest method to distribute the cohesive zone parameters. A more sophisticated method is introduced in Section 7.3.1 to improve the capability of the model to accurately predict the statistical distribution of fracture toughness within the transition region.

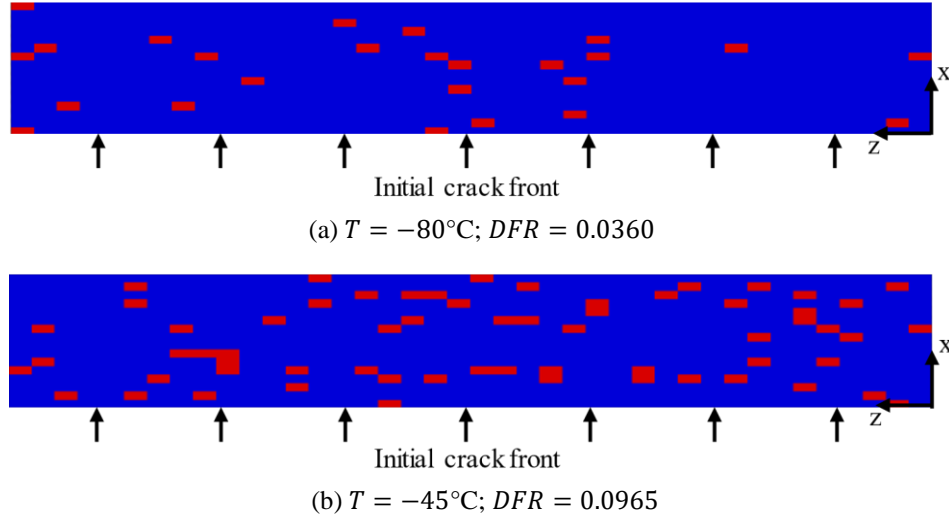


Figure 7.2: Probabilistic cohesive zones for -80°C (a) and -45°C (b) with $18 \times 50 \mu\text{m}$ element cluster size [99]

7.2 Probabilistic MCT simulations

Simulations are performed within the DBT region at -45 , -60 , -70 and -80°C . These temperatures are equivalent to the temperatures used for the experimental Master Curve evaluation in Section 4.3.5. For each temperature, the corresponding flow curve and DFR are used, while the CZM parameters for ductile and brittle fracture remain the same. The DFR values for the respective temperatures obtained from Equation (4.13) are listed in Table 7.1.

First, a single simulation is regarded to study the behavior and interaction of the ductile and brittle cohesive elements in front of the crack tip. The mechanism of unstable crack extension observed in the simulations is described in detail. Subsequently, the influence of the location of the ductile cohesive element clusters on the resulting numerical fracture toughness is investigated based on multiple simulations.

Table 7.1: DFRs at the temperatures used for the MCT simulations

$T [^{\circ}\text{C}]$	$DFR [-]$
-45	0.0965
-60	0.0706
-70	0.0533
-80	0.0360

7.2.1 Initiation of unstable crack growth

In the following, a simulation at -60°C with a randomly generated cohesive zone is regarded. A section of the cohesive zone with a length of $108 \mu\text{m}$ in x -direction starting from the initial crack front is shown in Figure 7.3 (a). The simulation terminated shortly after reaching the unstable fracture criterion defined in Section 5.2.2.1 due to the rapid failure of a number cohesive elements in front of the crack tip. The location of the initiation of unstable crack growth is marked by the orange ellipse. It is noticeable that this area is not located in the mid thickness of the specimen, as was the case in all previous simulations with the deterministic CZM, but between several ductile clusters close to the mid thickness. In Figure

7.3 (b), the normal separation of the cohesive elements at the onset of unstable crack growth is shown, with the gray area representing the elements that have already exceeded the critical separation of the brittle elements $\delta_{c,br} = 0.94 \mu\text{m}$. An increased separation is observed in the initiation region. Furthermore, the largest crack opening stress of 1927 MPa and a triaxiality of approximately 2 are obtained in this area, as shown in Figure 7.3 (c) and (d). At this triaxiality level, the cohesive strength of the ductile elements is around 1850 MPa, which is considerably lower than the σ_c of the brittle elements, which is 2005.5 MPa.

It is evident that the fracture behavior of the brittle elements is influenced by the surrounding ductile elements, since the brittle elements fail even though their σ_c has not yet been reached by the crack opening stress. The interaction observed between the ductile and brittle elements is explained in the following.

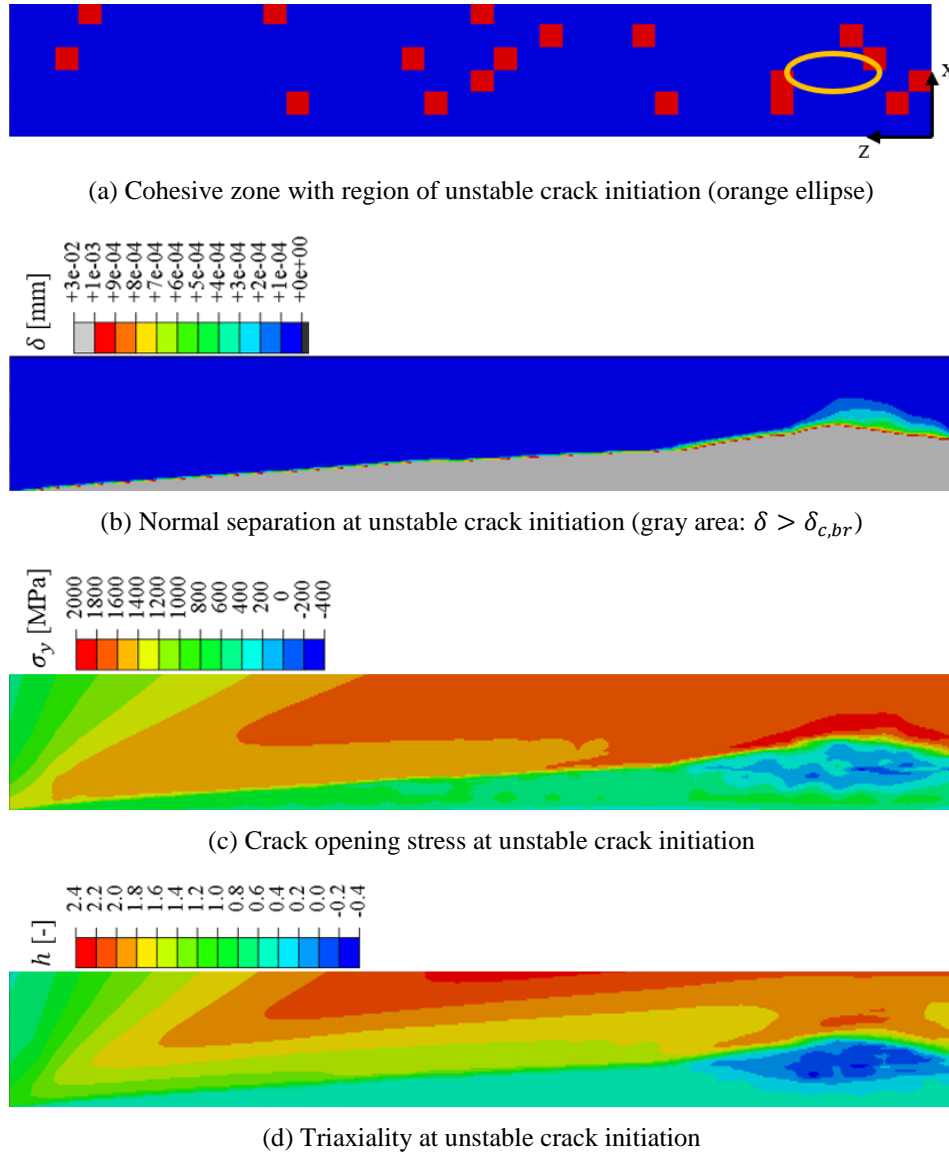


Figure 7.3: Section of the cohesive zone starting from the initial crack tip showing the distribution of ductile and brittle elements (a) and the normal separation (b), crack opening stress (c) and triaxiality (d) at the point of unstable crack initiation

In Figure 7.4, the cohesive stress (a) and separation (b) of a ductile cohesive element and an adjacent brittle element located within the initiation region are displayed against the crack opening displacement

COD. A steep drop in cohesive stress is observed for both elements shortly before the simulation is terminated, indicating rapid fracture. Separation of the ductile element is initiated prior to the separation of the brittle element. Since the separation between the elements must be continuous, the brittle element is forced to separate prematurely due to the ductile element separating.

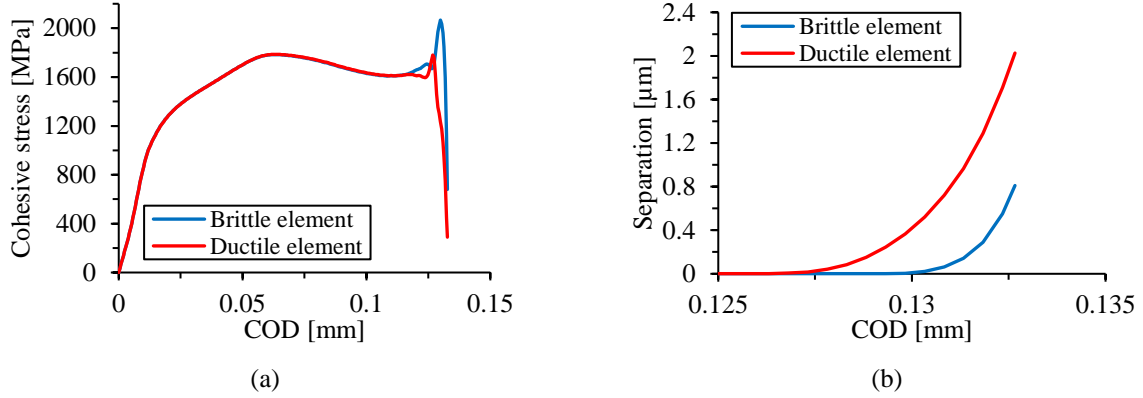


Figure 7.4: Cohesive stress (a) and separation (b) of a ductile cohesive element and an adjacent brittle element in the initiation region against COD

Upon initial separation of the ductile element, a considerable reduction of the triaxiality is observed, which is shown in Figure 7.5 (a). This is followed by a proportional reduction of the cohesive stress due to the linear triaxiality dependence of the ductile cohesive strength. Thereby, the resistance against further separation of the ductile element is drastically lowered compared to the brittle element up to a separation of 0.5 μm, as shown in Figure 7.5 (b). The accelerated separation of the ductile elements surrounding the initiation region is assumed to lead to the fracture of the adjacent brittle elements due to continuity.

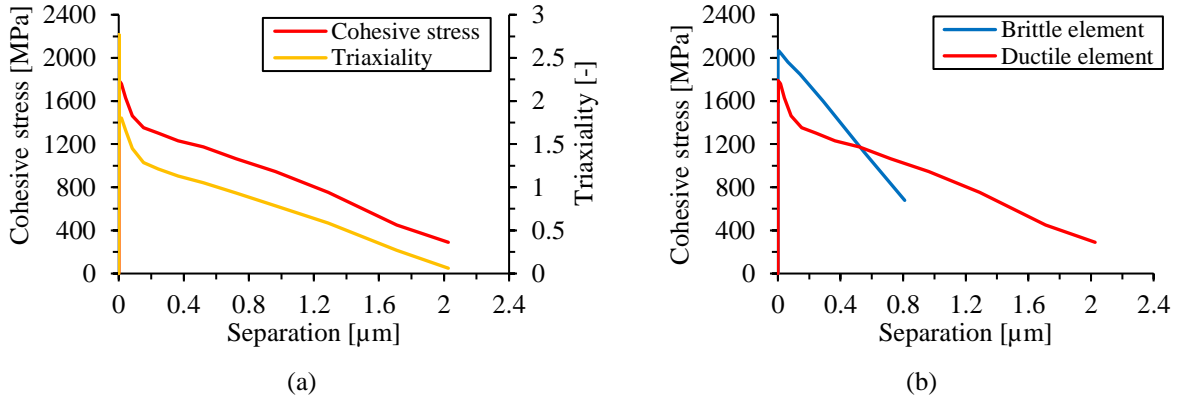


Figure 7.5: Cohesive stress and triaxiality of the ductile element against separation (a) and cohesive stress against separation for both the ductile and brittle element (b)

To verify the observed influence of the ductile elements on the fracture behavior of the brittle elements, a simulation was performed where the ductile elements around the initiation region were replaced by brittle elements. It is found that separation of the brittle elements located at the same position as before, but surrounded by other brittle elements, begins at a significantly higher COD than in the previous simulation. Based on this finding, it is confirmed that the ductile element clusters may act as “weak links” within the cohesive zone by facilitating separation and fracture of the adjacent brittle elements.

It was shown in Section 7.1 that the fracture resistance of the ductile elements is higher than that of the brittle elements due to their 2.4 times higher cohesive energy. The introduction of ductile elements into the cohesive zone consequently increases the total fracture resistance of the model from an energetic point of view. However, in this work, the criterion for failure of a simulated specimen is not complete fracture, but an accelerated crack growth rate exceeding a pre-defined limit, which is used as an indicator for local crack instability.

A number of simulations with randomly distributed ductile and brittle cohesive element clusters were carried out and it is found that unstable crack growth is always initiated within a region where brittle elements are surrounded by ductile clusters. This further strengthens the assumption that the interaction between the ductile and brittle elements is responsible for the rapidly increasing crack growth rate. Of course, the numerical process of fracture described above cannot directly be compared to the mechanisms of cleavage fracture observed experimentally within the transition region. Nonetheless, it can be exploited to obtain statistically distributed numerical fracture toughness values that may depend on the location, shape and size of the ductile element clusters within the cohesive zone.

7.2.2 Influence of ductile cluster location on fracture toughness

In Figure 7.6, a randomly generated cohesive zone at -60°C is shown where the number of ductile clusters near the mid thickness ($z = 0$ mm) is comparatively low. A simulation with this cohesive zone is performed (PCZ18_-60_2) and the region of unstable crack initiation is identified in the middle of the group of ductile clusters highlighted by the orange ellipse. The coordinates of this location and the numerical fracture toughness value $K_{Jc,num}$ predicted by the simulation are listed in Table 7.2 and compared to the simulation discussed in the previous section (PCZ18_-60_1). PCZ18_-60_1 yields a considerably lower $K_{Jc,num}$ than PCZ18_-60_2, which suggests that $K_{Jc,num}$ depends on the distance of the initiation region from the mid thickness and from the initial crack front.



Figure 7.6: Randomly generated cohesive zone of simulation PCZ18_-60_2 with a low number of ductile element clusters near the mid thickness; initiation marked by ellipse

Table 7.2: Location of initiation region and $K_{Jc,num}$ for simulations PCZ18_-60_1 and PCZ18_-60_2

Simulation	x [μm]	z [μm]	$K_{Jc,num}$ [$\text{MPa}\sqrt{\text{m}}$]
PCZ18_-60_1	55.7	205	108.1
PCZ18_-60_2	74.3	675	137.1

To investigate further, eight more simulations were carried out at -60°C and the respective $K_{Jc,num}$ results are plotted in Figure 7.7 against the x -coordinates (a) and z -coordinates (b) of the unstable fracture initiation regions. On average, the simulated initiation regions are located at $z = 379$ μm . This is in good agreement with the average distance of the experimental initiation sites to the mid thickness, which is 414 μm (see Section 4.4.1.1). As with the experimental initiation sites, all of the numerical initiation regions are located within 1 mm from the mid thickness.

Linear regression is performed on both data sets shown in Figure 7.7 and a weak correlation between $K_{Jc,num}$ and the z -coordinate is found with a coefficient of determination of $R^2 = 0.21$. Simultaneously, $K_{Jc,num}$ appears to be almost completely uncorrelated to the x -coordinate of the initiation regions with $R^2 = 0.04$.

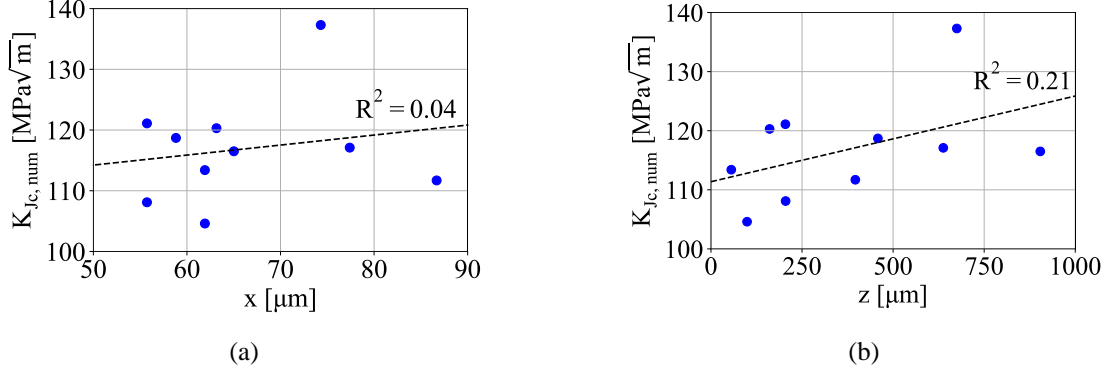


Figure 7.7: Correlation of $K_{Jc,num}$ and x - (a) and z -coordinates (b) of ductile fracture regions predicted by ten probabilistic simulations at -60°C

The precondition of this study was that all simulation parameters apart from the spatial distribution of the ductile clusters are constant, so that the influence of the location of the clusters on the predicted fracture toughness values can be studied isolated from other factors. It was shown that the dependence of $K_{Jc,num}$ on the location of the initiation regions relative to the initial crack front and mid thickness is weak, which means that the differences in $K_{Jc,num}$ must be either due to the position of the ductile clusters relative to each other, their size or both. The simulations show that unstable crack growth is initiated earlier if several ductile clusters in the highly stressed region are located in close proximity to each other, forming a larger cluster. Additionally, lower fracture toughness values are obtained whenever a region of brittle elements is surrounded by several ductile clusters. Consequently, the initiation of unstable crack growth is less influenced by the distribution of the ductile clusters on a global scale, but more on the relative position of a few ductile clusters within the highly stressed region and their size.

7.3 Numerical Master Curve prediction

In this section, the $K_{Jc,num}$ values obtained from a set of probabilistic simulations between -45 and -80°C are used to predict a numerical reference temperature based on ASTM E1921 and subsequently compare the resulting Master Curve to the experimental result from the MCT tests performed in Section 4.3.5. As before, a constant size of $18 \times 50 \mu\text{m}$ is used for the ductile and brittle cohesive element clusters distributed throughout the cohesive zone. Each simulated fracture toughness result is treated like a physical test, including data censoring if the $K_{Jc,limit}$ is exceeded at the respective temperature due to excessive plastic deformation. Size correction of the numerical results is performed to obtain $K_{Jc,1T,num}$. To be able to predict a reference temperature that is comparable to the experimental T_0 , the same number of simulations are carried out at each temperature as the number of MCT tests that were performed within the DBT region.

A numerical reference temperature $T_{0,num}$ of -32.3°C is predicted, which is in good agreement with the experimental T_0 of -31.5°C . The individual $K_{Jc,num}$ and $K_{Jc,1T,num}$ results are listed in Table A.15. All

predicted $K_{Jc,num}$ values at -45°C and two values at -60°C exceed the respective $K_{Jc,limit}$ and are therefore censored. In Figure 7.8, the experimental Master Curve (a) is compared to the numerical result (b). As with the experimental fracture toughness results, the numerical values increase on average with increasing temperature. A large increase is observed from -70 to -60°C , while the increases from -80 to -70°C and from -60 to -45°C are comparably small. This is assumed to be due to the strong decrease of the strain hardening capability of the material from -70 to -60°C , which was determined in Section 4.2.3 and shown in Figure 4.12.

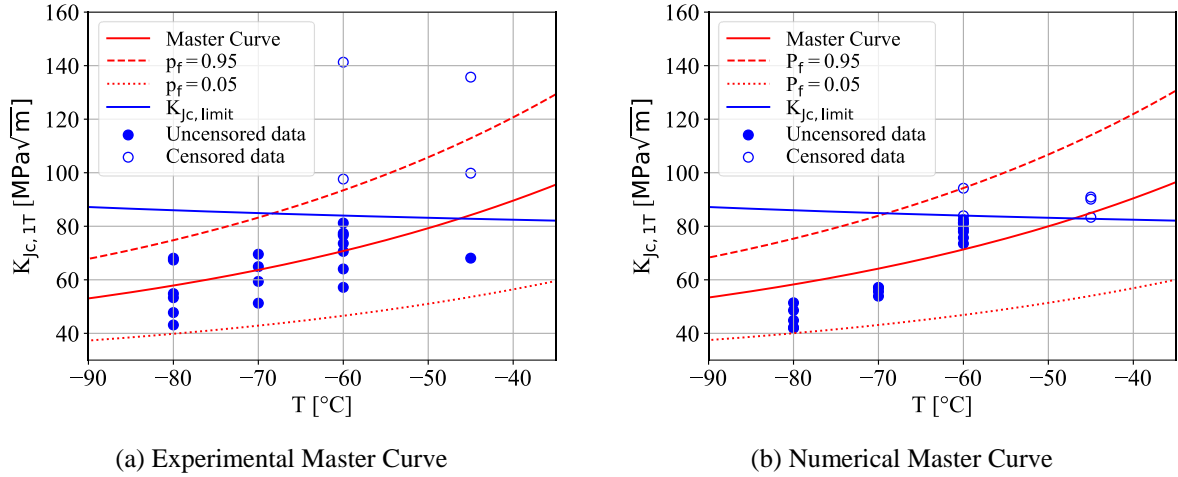


Figure 7.8: Comparison between the experimental Master Curve (a) and the numerically predicted Master Curve using a constant cluster size of $18 \times 50 \mu\text{m}$ (b) (adapted from [99])

Furthermore, it is clear that the scatter of the numerical fracture toughness values is significantly lower than the experimentally observed scatter at all temperatures. The experimental and numerical average and median fracture toughness values and corresponding standard deviations $\sigma_{K_{Jc,1T}}$ are compared in Table 7.3. Apart from -60°C , the simulations yield lower average and median values than the experiments. Due to the two outliers at -60°C exceeding the 95% tolerance bound, the experimental median fracture toughness is significantly lower than the average value. No outliers are observed in the simulations, resulting in similar median and average values. The standard deviations are compared in the last column. As expected, the experimental standard deviations are considerably higher at all temperatures. This is particularly pronounced at -45°C , where the experimental $\sigma_{K_{Jc,1T}}$ is more than eight times the numerical value.

As explained in the previous section, the numerical scatter is exclusively a result of the spatial distribution and size of the ductile cohesive element clusters within the highly stressed region of the cohesive zone. It appears that the statistical effect of this random distribution on $K_{Jc,num}$ is not strong enough to fully describe the experimentally observed scatter. In the case of real experiments, a number of uncertainties contribute to the fracture toughness scatter. These include the dimensions of the individual specimens, the length and asymmetry of the fatigue pre-crack, the loading conditions and, most importantly, the location and size of brittle cleavage-initiating particles in the vicinity of the crack front. These uncertainties are not considered in the simulations but are expected to significantly affect the fracture toughness result of an individual test. The introduction of additional statistically distributed input parameters would drastically increase the complexity of the FE-model and is therefore not considered in this work.

In summary, it was shown that the reference temperature predicted by the probabilistic CZM with constant size of the ductile and brittle cohesive element clusters is in good agreement with the experimental value. It was further found that the statistical effect introduced by the random spatial distribution of the ductile clusters within the cohesive zone is not strong enough to match the experimental scatter. In the next section, variable cluster sizes are introduced to the model to obtain a better representation of the fracture surfaces observed by means of SEM.

Table 7.3: Average and median experimental and numerical fracture toughness values and corresponding standard deviations at each temperature [99]

	T [°C]	$K_{Jc,1T,avg}$ [MPa√m]	$K_{Jc,1T,med}$ [MPa√m]	$\sigma_{K_{Jc,1T}}$ [MPa√m]
Exp.	-45	101.21	99.93	27.62
Num.		88.12	90.11	3.40
Exp.	-60	82.17	76.64	23.45
Num.		81.04	81.06	5.60
Exp.	-70	61.29	62.16	6.81
Num.		55.92	56.35	1.33
Exp.	-80	55.75	54.08	9.28
Num.		45.80	44.85	3.69

7.3.1 Variable size of the ductile cohesive element clusters

For the basic investigations carried out in the previous sections, the probabilistic cohesive zone was designed to be as simple as possible by using element clusters of a constant size. However, the quantitative fractographic analysis in Section 4.4.2 showed that the size and shape of the ductile fracture regions across an individual fracture surface vary considerably. Furthermore, it was established in Section 7.2.2 that the numerical fracture toughness results depend on the size of the ductile element clusters. It is therefore investigated whether the use of clusters of different sizes can increase the scatter of the numerical fracture toughness results.

Four cluster sizes are considered, which are listed in Table 7.4. As before, the length of the clusters in thickness direction is kept at 50 μm , while the length in crack growth direction is doubled for each size, starting at 9 μm . To determine the number of ductile cohesive elements for each size, the surface areas of 100 randomly selected ductile fracture regions from the SEM micrographs were measured. The individual measurements are assigned to the appropriate segments listed in the table. The combined area of the ductile fracture regions in each segment is used to determine the segment's fraction of the total ductile fracture area. Based on these fractions, the number ductile cohesive elements available for each cluster size is determined. For instance, the clusters of 9x50 μm size are assigned 23.2% of the total number of ductile cohesive elements since 23.2% of the total ductile fracture area consists of fracture regions with an area below 675 μm^2 .

Table 7.4: Cohesive element cluster sizes and corresponding ductile fracture area segments with fractions of the total ductile fracture area

Cluster size [μm]	Cluster area [μm ²]	Ductile fracture area segment [μm ²]	Avg. area of ductile fracture regions [μm ²]	Fraction of total ductile fracture area [%]
9x50	450	<675	424.8	23.2
18x50	900	675-1350	949.8	29.9
36x50	1800	1350-2700	1854.9	21.4
72x50	3600	>2700	3464.3	25.5

In Figure 7.9, a cohesive zone with variable cluster size is shown for -60°C. According to the fractions defined in Table 7.4, a relatively even distribution of cluster sizes is obtained. In some locations, adjacent clusters are merged to form larger clusters. Based on the observations from the previous simulations, it is expected that the locations of the large clusters will have a noticeable influence on the resulting $K_{Jc,num}$ values.

As in the previous section, simulations are performed to determine $T_{0,num}$, with the number of simulations at each temperature corresponding to the number of tests performed for the experimental Master Curve evaluation. The numerical reference temperature obtained from the simulations with variable cluster size is -35.1°C, which is about 3°C below the $T_{0,num}$ predicted by the simulations with constant cluster size. This difference is due to an increased number of censored $K_{Jc,num}$ values at -60°C coming from the simulations with variable cluster size, which can be considered coincidental.

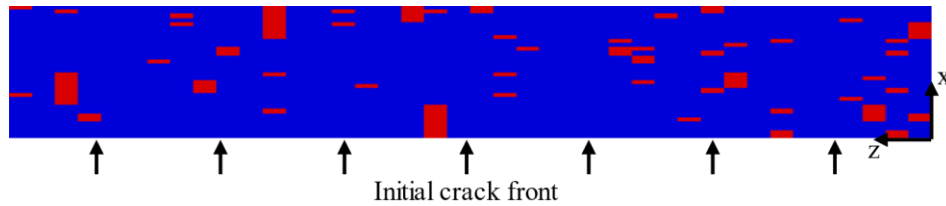


Figure 7.9: Cohesive zone with variable size of the element clusters at -60°C

In Figure 7.10, the predicted Master Curve using cohesive element clusters of constant size (a) is compared to the curve determined using clusters of variable size (b). While the fracture toughness scatter is increased at -70°C, it is reduced at -80°C, -60 and -45°C. As most data points are available at -60°C, the average and median $K_{Jc,1T,num}$ values and corresponding standard deviations are compared in Table 7.5 for this temperature. While the average and median values are similar, the standard deviation is slightly lower in the case of the simulation with variable cluster size. It is concluded that there is a systematic decrease of numerical fracture toughness scatter when using clusters of variable size as opposed to clusters of constant size. The large proportion of small clusters results in a more even distribution of ductile elements throughout the cohesive zone and a homogenization of the fracture-mechanical properties, which means that outliers are less likely to occur. Therefore, to increase the numerical fracture toughness scatter, cluster sizes should be skewed towards larger clusters.

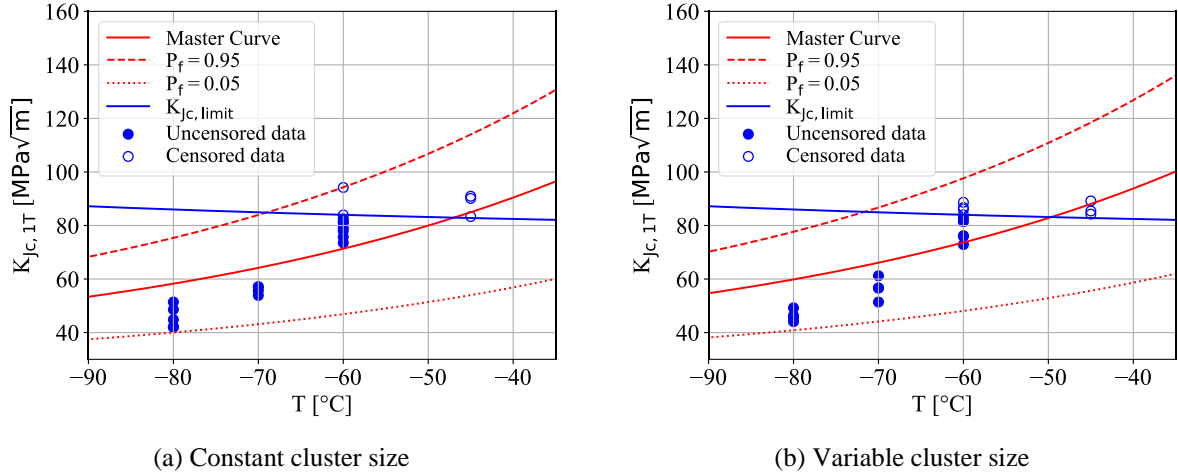


Figure 7.10: Master Curve predicted using cohesive element clusters of constant size (a) and Master Curve determined using variable cluster size (b)

Table 7.5: Average and median numerical fracture toughness values and corresponding standard deviations at -60°C using cohesive element clusters of constant and variable size

	$K_{Jc,1T,avg}$ [MPa√m]	$K_{Jc,1T,med}$ [MPa√m]	$\sigma_{K_{Jc,1T}}$ [MPa√m]
Constant cluster size	81.04	81.06	5.60
Variable cluster size	81.63	82.74	5.17

7.3.2 Statistical distribution of the numerical fracture toughness

It was observed in the previous sections that the scatter of the numerical fracture toughness values is considerably lower than the experimental scatter. In the following, a statistical analysis of 50 $K_{Jc,1T,num}$ results at -60°C , which were obtained by means of the probabilistic CZM with variable cluster size, is performed to determine the probability distribution that best describes the numerical data set. The numerical distribution is then compared to the distribution of the MCT tests performed at -60°C and the distribution assumed in the ASTM E1921 standard. Based on a large number of fracture-mechanical tests on ferritic steels, it is specified in the standard that the scatter follows a three-parameter Weibull distribution with a Weibull modulus of $m = 4$ and a threshold parameter of $K_{min} = 20 \text{ MPa}\sqrt{\text{m}}$.

A histogram of the 50 $K_{Jc,1T,num}$ results at -60°C is shown in Figure 7.11. The values are scattered between 73 to 99 $\text{MPa}\sqrt{\text{m}}$ and the highest relative frequency is obtained at 81 $\text{MPa}\sqrt{\text{m}}$ with 16% of the total data set. An increased relative frequency is observed between 76 and 83 $\text{MPa}\sqrt{\text{m}}$, while $K_{Jc,1T,num}$ values above 91 $\text{MPa}\sqrt{\text{m}}$ are only reached by a few outliers. Several common probability density functions (PDFs) were used to describe the distribution of the data set, and the χ^2 statistic was applied to test how the individual PDFs match the observed scatter. The test is only passed by the three-parameter Weibull distribution with its PDF given by

$$f(K_{Jc,1T,num}) = \frac{m}{K_0} \left(\frac{K_{Jc,1T,num} - K_{min}}{K_0} \right)^{m-1} \exp \left(- \left(\frac{K_{Jc,1T,num} - K_{min}}{K_0} \right)^m \right). \quad (7.1)$$

The parameters of the PDF, namely the Weibull modulus m , scale parameter K_0 and threshold parameter K_{min} , are obtained by fitting and the resulting curve is plotted in the histogram, showing that the numerical fracture toughness scatter is well described.

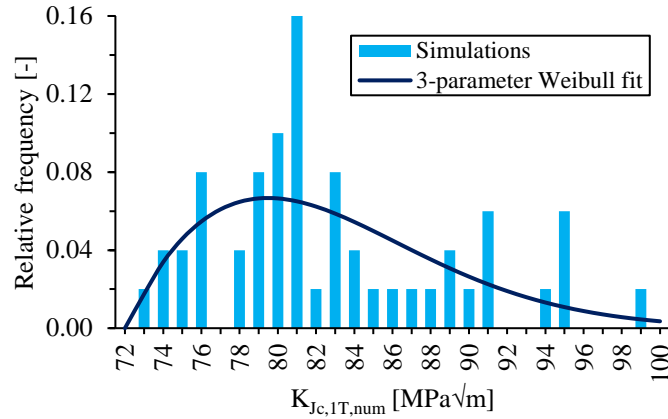


Figure 7.11: Histogram of 50 $K_{Jc,1T,num}$ results at -60°C and corresponding three-parameter Weibull PDF with fully fitted parameters [99]

In Table 7.6, the parameters of the numerical distribution are compared to the experimental distribution of the nine MCT tests performed at -60°C and the distribution assumed in the ASTM standard. The parameters of the numerical and experimental distributions deviate strongly from their corresponding ASTM values. The Weibull moduli and scale parameters are significantly lower, while the threshold parameters are higher. In the standard, a threshold parameter of $K_{min} = 20 \text{ MPa}\sqrt{\text{m}}$ is specified for all temperatures. Based on the experimental $K_{Jc,1T}$ results determined in Section 4.3.5, it is to be expected that at -60°C , MCT specimens of the given material will not fail at this load level. Therefore, it can be assumed that the standard underestimates the lower limit of the fracture toughness scatter at temperatures close to T_0 . Regarding the experimental distribution, the Weibull modulus is similar to the numerical value, while the other parameters are midway between the numerical and the ASTM values. It is noted that the experimental distribution may not accurately represent the statistical fracture-mechanical behavior of the material due to the small data set size of nine K_{Jc} results.

Table 7.6: Parameters of the numerical and experimental three-parameter Weibull distributions and the distribution assumed in the ASTM E1921 standard at -60°C [99]

Distribution	m [-]	K_0 [$\text{MPa}\sqrt{\text{m}}$]	K_{min} [$\text{MPa}\sqrt{\text{m}}$]
Numerical	1.7	11.8	72.4
Experimental	1.6	37.3	49.0
ASTM E1921	4.0	75.5	20.0

The differences between the three-parameter Weibull distributions are highlighted by their cumulative failure probability curves, which are shown in Figure 7.12. Compared to both the experimental and the ASTM distribution, the simulated fracture toughness scatter is significantly reduced. Specifically, at high cumulative failure probabilities, a large deviation is observed between the numerical and the experimental distribution due to the outliers present in the experimental data set. The fracture toughness corresponding to a cumulative failure probability of 90% is $92 \text{ MPa}\sqrt{\text{m}}$ for the simulated distribution, while a value of $113 \text{ MPa}\sqrt{\text{m}}$ is obtained for the experimental distribution. Regarding a 50% cumulative failure probability, both the numerical and the experimental distribution are shifted towards lower fracture toughness values compared to the distribution assumed in the standard. A median $K_{Jc,1T,num}$ of $82 \text{ MPa}\sqrt{\text{m}}$ is predicted by the simulations, while the median $K_{Jc,1T}$ from the MCT tests is $79 \text{ MPa}\sqrt{\text{m}}$.

Meanwhile, a median $K_{Jc,1T}$ of $89 \text{ MPa}\sqrt{\text{m}}$ is obtained from the ASTM distribution. This confirms that the average fracture-mechanical behavior of the material is well described by the probabilistic model.

In an attempt to improve the numerical cumulative failure probability curve to better match the experimental curve, the threshold parameter of the numerical distribution is set to the experimental value of $K_{\min} = 49 \text{ MPa}\sqrt{\text{m}}$. The Weibull modulus and scale parameter are again fitted using the 50 $K_{Jc,1T,\text{num}}$ values from the probabilistic simulations, leading to $m = 5.5$ and $K_0 = 85.6 \text{ MPa}\sqrt{\text{m}}$. The resulting cumulative failure probability curve is represented by the dashed green line in Figure 7.12. Compared to the original numerical distribution, the curve as a whole is slightly closer to both the experimental and the ASTM curve. The fracture toughness scatter is increased at cumulative failure probabilities below 0.2 due to the reduction of the threshold parameter. The difference between the curves is minimal at higher cumulative failure probabilities, but a slight reduction in scatter can be observed above 0.9. Overall, the effect of reducing the threshold parameter on the fracture toughness distribution is relatively small.

As explained before, the probabilistic CZM in its current form cannot be expected to match the scatter obtained in experiments since no fracture initiating particles are present in the cohesive zone. So far, the numerically predicted scatter is exclusively due to the random spatial distribution of the ductile cohesive element clusters. By introducing a randomly located “weakest link” to the cohesive zone, consisting of a few elements with very low cohesive energy, it should be possible to further increase the fracture toughness scatter predicted by the model. Additional statistically distributed model parameters, such as the initial crack length and crack shape, can also be expected to yield a wider range of $K_{Jc,1T,\text{num}}$ results. These advanced modeling strategies are beyond the scope of this work.

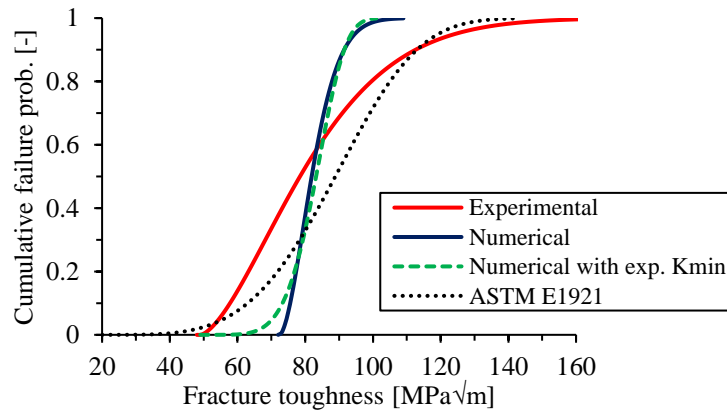


Figure 7.12: Cumulative failure probabilities determined experimentally by means of ASTM E1921 and numerically for -60°C (adapted from [99])

7.3.3 Material requirement

The motivation for developing the probabilistic CZM approach is the high material requirement for the experimental determination of the Master Curve according to ASTM E1921. As stated in the Introduction, the availability of irradiated material for fracture mechanics testing is severely limited. Therefore, the probabilistic CZM aims to predict the reference temperature with less material than is required for a purely experimental determination.

For the experimental determination of T_0 , a minimum of six uncensored K_{Jc} results are required using the multi-temperature method. In practice, this is only possible if an approximate reference temperature

is known before testing, which is usually not the case. If no approximation is available, several specimens are required to find the appropriate test temperature range, which is particularly difficult when testing miniaturized specimens (see Section 4.3.5.4). Even when testing in the optimal temperature range, it is likely that several K_{Jc} results from small specimens require censoring due to their inherently low $K_{Jc,limit}$. Furthermore, it is possible that some specimens within a testing program do not meet the fatigue pre-crack straightness requirement or other dimensional requirements of the standard, invalidating the corresponding K_{Jc} results. Consequently, it is usually necessary to perform significantly more tests than the minimum number specified in the standard.

Within the framework of the FRACTESUS project, a round robin exercise was performed to investigate the differences between the T_0 results obtained by four European institutes using MCT specimens of SA-508 Cl.3 RPV steel, including the low-temperature MCT tests performed in this work. The individual Master Curve evaluations following ASTM E1921 were analyzed by Naziris et al. (2023) [102], revealing that of a total of 71 tests, 64 K_{Jc} results were valid, of which 55 (77% of total) required no censoring. The average contribution of each uncensored test result to the data set size criterion defined in Equation (2.19) was 0.132. This means that, based on this data set, a minimum of eight uncensored test results and 11 total MCT tests are required for the experimental determination of the reference temperature. It is noted that within this round robin, an approximate T_0 was given prior to testing as an orientation for selecting the initial test temperature. Without this knowledge, it can be assumed that at least three additional tests may be required for finding the optimal test temperature range. Consequently, a total of 14 MCT specimens should be considered as the minimum for determining T_0 experimentally.

Regarding the probabilistic CZM approach, smooth and notched round bar specimens (SRB, NRB) are required in addition to MCT specimens to determine the plastic flow curves and to calibrate the cohesive strength. In Table 7.7, the minimum required number of specimens for calibrating the probabilistic CZM at three temperatures within the DBT region is listed for each specimen type. It is assumed here that the material is homogeneous. The plastic flow curves are required at each temperature of interest within the transition region and at RT, while the calibration of the CZM parameters is only necessary at the temperature closest to the lower shelf and at RT. As it was shown in Section 5.2.2.2 that the fracture behavior at low temperatures can be simulated using a constant cohesive strength, only a single 0.1NRB specimen is required to be tested near the lower shelf. At RT, the SRB specimen tested for generating the flow curve can be used in addition to a 0.1NRB test to determine the linear triaxiality dependence of σ_c . Close to the lower shelf, three MCT specimens are required to obtain a statistically meaningful value for the cohesive energy. An additional MCT test is required at RT to determine the J-R curve based on the resistance curve method specified in ASTM E1820. If the basic procedure is followed, more MCT tests are necessary for this purpose. The J-R curve is required for the calibration of the upper shelf cohesive energy. Lastly, in addition to the three MCT tests close to the lower shelf, at least three more MCT specimens should be tested at an intermediate temperature within the DBT region to determine the temperature dependence of the ductile fracture ratio (DFR). The DFR is used to determine the number of randomly distributed ductile cohesive elements across the cohesive zone. In total, at least seven MCT tests are required for the calibration of both Γ_c and the DFR.

Given that the round bar specimen geometries require approximately 13% less material volume than a standard MCT geometry, it can be assumed that the minimum volume required for calibrating the probabilistic CZM at three temperatures within the DBT region is equivalent to 12 MCT specimens. Therefore, the material volume needed is slightly lower than that required for the experimental determi-

nation of T_0 . If flow curve data within the transition region and/or the J-R curve at RT is known beforehand, the material requirement for the probabilistic CZM can be reduced further. Likewise, it can be reduced if less than three temperatures within the DBT region are considered for the calibration of the model. However, the material requirement may also increase considerably if the material properties of the steel are inhomogeneous, which is also the case for the experimental determination of T_0 .

It is noted that the minimum required number of specimens in Table 7.7 is based on the best-case scenario where all calibrations are performed without the use of spare specimens. This assessment may be considered too optimistic since in practice, some spare specimens are always needed. However, this is the case for all mechanical testing methods and is therefore also valid for the experimental Master Curve evaluation following ASTM E1921.

Table 7.7: Minimum required number of specimens for calibrating the probabilistic CZM at three temperatures within the DBT region [99]

Specimen type	N_{tests} [-]	Determination purpose
SRB	4	- Flow curves (DBT region and RT) - Cohesive strength (RT)
0.1NRB	2	- Cohesive strength (lower shelf and RT)
MCT	7	- Cohesive energy (lower shelf and RT) - Ductile fracture ratio (DBT region)

7.4 Summary of the probabilistic CZM approach

The experimental and numerical groundwork performed in Chapters 4 and 5 was used to develop the probabilistic CZM approach, which is based on a random spatial distribution of cohesive elements with either ductile or brittle properties throughout the cohesive zone. A detailed analysis of the mechanical behavior of a ductile element connected to a brittle element showed that unstable crack initiation of the brittle elements is facilitated by the separation of surrounding ductile elements. The accelerated separation of the ductile elements was found to be accompanied by a reduction in cohesive strength, which in turn is caused by a decreasing triaxiality. Furthermore, it was observed that the numerical fracture toughness results are influenced by the size and relative distance of the ductile element clusters. However, only a weak dependence of the $K_{\text{Ic,num}}$ values on the position of the initiation regions relative to the initial crack front and mid thickness was found.

In the next step, the probabilistic CZM was used to determine a numerical reference temperature for the material, which was shown to be in good agreement with the experimental T_0 determined in Section 4.3.5. The scatter of the numerical fracture toughness results was found to be significantly reduced compared to the experimentally observed scatter. In an attempt to increase the numerical scatter, ductile cohesive element clusters of variable size were introduced, which were shown to have the opposite effect by further decreasing the scatter. This effect was attributed to the large proportion of small ductile clusters homogenizing the fracture-mechanical properties throughout the cohesive zone. In addition, a statistical characterization of the fracture toughness results from 50 simulations with variable cluster size was performed to quantify the differences between the numerically predicted scatter, the scatter of the nine MCT test results at -60°C and the scatter assumed in the Master Curve approach according to ASTM E1921. As with the experimental results, the numerical fracture toughness values were found to

follow a three-parameter Weibull distribution. A significant deviation of the fitted parameters of the numerical distribution compared to the distribution assumed in the standard was obtained. The agreement with the experimental distribution, however, was shown to be better. A comparison of the cumulative failure probabilities confirmed that, while the average fracture-mechanical behavior of the material is well described by the model, additional uncertainties are required to be modeled in order to increase the numerical fracture toughness scatter.

Lastly, the material volume required for the experimental determination of T_0 using MCT specimens was compared to the minimum material requirement for a numerical T_0 determination with the probabilistic CZM approach. It was concluded that, assuming a homogeneous material, the average amount of material required is slightly lower for the numerical approach.

8 Discussion

Several research goals for this PhD program were specified in the Introduction. On the experimental side, the main objective was to generate material parameters to be used for the development of the numerical crack growth simulations with the cohesive zone model. Another aim of the MCT tests within the transition region was to demonstrate the use of miniaturized specimens for determining the reference temperature following the ASTM E1921 standard. Thereby, it was investigated whether the fracture-mechanical behavior of the MCT geometry is comparable to that of standard-sized CT geometries in order to verify the geometry for use in future surveillance programs.

The numerical objectives include the continued development of the cohesive zone parameter identification method introduced by Mahler & Aktaa (2014) [11] and application of the calibrated parameters to the simulation of standard-sized CT geometries. Here, the aim was to predict the fracture toughness obtained from large geometries and to characterize the loss of constraint observed in sub-sized specimens by comparing the mechanical fields in front of the crack tip to those determined with the standard-sized models. The main focus of the numerical activities, however, was the development of a probabilistic CZM approach for predicting statistically distributed fracture toughness values within the DBT region and use of the predicted values for determining a numerical reference temperature based on ASTM E1921. Besides an accurate prediction of the reference temperature, the main concern in developing this approach was to reduce the material volume required for fracture-mechanics characterization of ferritic steels.

In the following, it is discussed whether the experimental and numerical goals set in this work were achieved, how the findings can benefit research projects related to small specimen test technique, and if the developed numerical models are suited for application within the nuclear power industry.

8.1 Viability of the MCT geometry

In the past two decades, a number of authors advocated the MCT specimen as a promising geometry for future surveillance programs [8,9,16,43–45]. A key benefit of the MCT is that eight specimens can be machined from a single broken Charpy specimen [6]. However, when testing according to ASTM E1921, the problem of an inherently narrow test temperature window of small specimens, resulting from loss of constraint at temperatures close to T_0 , remains unresolved [8,9,16].

The experimental results generated in this work confirm the findings of previous research programs and strengthen confidence in the MCT geometry. A valid reference temperature was obtained for the RPV steel SA-508 Cl.3 from 24 MCT specimens, whereby two test results were deemed invalid due to pre-crack asymmetry and four fracture toughness values required censoring for exceeding the plasticity limit specified in the standard. This showed that it is possible to determine the reference temperature from miniaturized specimens without excessively generating censored test results. However, most specimens were tested within a temperature range where the contribution of each test result towards the data set size requirement of the standard is reduced. It was shown that a narrow temperature window exists for the investigated steel, in which the expected proportion of uncensored test results is reasonably low, while simultaneously an increased contribution of each test towards the data set size criterion can be achieved. Therefore, to reduce the number of specimens required, the main concern is to find

this optimal test temperature range. If no approximation of the reference temperature is available prior to testing, this is a process that may itself require a sizable number of tests. Based on the fracture toughness results obtained from the MCT tests, it is recommended to select a test temperature corresponding to a median size-corrected fracture toughness of $90 \text{ MPa}\sqrt{\text{m}}$.

The MCT tests within the transition region confirm that a valid reference temperature can be obtained using a reasonable number of specimens, as long as most tests are performed within the optimal test temperature range. To further verify the MCT geometry, the fracture surfaces of broken specimens were studied to show that the fracture-mechanical behavior of the MCT is similar to that expected from standard-sized specimens. Detailed fractographic analysis was carried out to locate and characterize the cleavage initiation sites and correlate their location to numerical stress and triaxiality fields in front of the crack tip. It was found that most initiation sites are located near the mid thickness of the specimens within the region of high triaxiality. This means that cleavage fracture is initiated under high constraint conditions, which is an essential prerequisite of the Master Curve approach.

The mechanical behavior of the MCT specimens was further assessed by comparing the numerical stress, strain and triaxiality fields in front of the crack tip with those obtained from 0.5T and 1T CT geometries at 30 and 50°C below T_0 . At a crack tip load of $35 \text{ MPa}\sqrt{\text{m}}$, the behavior of the geometries was found to be similar, indicating that the MCT is a high-constraint geometry at moderate displacements. However, an overall decrease in triaxiality and strong increase in plastic strain was observed for the MCT at a crack tip load of $70 \text{ MPa}\sqrt{\text{m}}$, while the mechanical behavior of the 0.5T at 1T geometries remains mostly the same. Still, the MCT was shown to maintain a high level of triaxiality and crack opening stress near the mid thickness. Large scale plastic deformation of the MCT was observed from the initial crack front to the specimen backside, whereas plasticity of the standard-sized geometries is confined to the crack tip region even at this high load level. It is concluded that, while the MCT maintains high constraint conditions within the highly stressed region close to the mid thickness, the area susceptible to cleavage fracture is reduced significantly due to large scale plastic deformation. It is to be expected that the differences between the geometries continue to increase with increasing loading.

Overall, the experimental, fractographic and numerical results generated in this work support the view of the MCT geometry as a viable candidate for future surveillance programs. The mechanical and fracture-mechanical behavior of the geometry at temperatures sufficiently below T_0 was shown to be in line with expectations. The narrow range of optimal test temperatures remains the main deficiency of the geometry. However, this disadvantage is shared by all miniaturized geometries.

8.2 Evaluation of the probabilistic CZM approach

A step towards the complete numerical description of the statistical fracture-mechanical behavior of ferritic steels within the transition region was made by introducing the probabilistic CZM approach. The approach is based on the random spatial distribution of cohesive elements with brittle or ductile fracture properties throughout the cohesive zone based on a ductile fracture ratio (DFR). It was shown that the interaction between the ductile and brittle cohesive elements allows for the determination of statistically distributed numerical fracture toughness values depending on the randomized layout of the cohesive zone. The numerical fracture toughness follows a three-parameter Weibull distribution, which is the same distribution assumed in the ASTM E1921 standard to describe the statistical fracture behavior of ferritic steels within the transition region. From a materials science perspective, however, the fracture

behavior predicted by the probabilistic CZM does not yet accurately represent the mechanisms of cleavage fracture observed in ferritic steels. In ferritic steels, unstable fracture is usually initiated from brittle second-phase particles such as carbides. Without the presence of such initiators in the cohesive zone, the fracture toughness scatter obtained from simulations with the probabilistic CZM is significantly underestimated compared to the experimentally observed scatter. It can be assumed that the introduction of small regions of significantly reduced fracture resistance, which are distributed throughout the cohesive zone, may contribute to an increased scatter of the numerical fracture toughness results. Aside from the prediction of the scatter, the median fracture toughness was found to be similar to the experimental results, demonstrating the capability of the probabilistic CZM approach to predict the reference temperature of the material.

The purpose of most of the experimental and numerical activities performed in this work was to calibrate the parameters necessary for the probabilistic CZM. Therein lies a significant drawback of the approach. The identification of several flow curves, sets of cohesive zone parameters and the ductile fracture ratio (DFR) requires considerable resources, including the testing of multiple types of specimens, detailed quantitative fractographic analysis and complex numerical simulations in 3D. An increased likelihood of inaccuracies and errors is introduced by this complexity. In particular, the quantitative fractographic analysis required for determining the DFR is susceptible to operator bias. This means that a systematic difference in the identified DFR may be introduced depending on the person performing the analysis. This is in addition to the natural statistical variation of the DFR. In comparison to the probabilistic approach, the experimental determination of T_0 is significantly faster and easier to perform. However, the numerical determination of T_0 is not the sole objective of the probabilistic approach. The main goal is to be able to accurately simulate the statistical fracture mechanisms of ferritic steels within the transition region, thus enabling detailed material characterization.

For the nuclear energy industry in particular, an advantage of the probabilistic CZM approach is the possibility of reducing material requirements for the evaluation of the reference temperature of RPV steels in the future. Based on several independent T_0 evaluations of SA-508 Cl.3 RPV steel from MCT specimens within the framework of the FRACTESUS project [102], it was concluded that on average, 14 MCT specimens are required to obtain a valid reference temperature experimentally. Assuming a homogeneous material, it was shown in this thesis that the approximate material volume of 12 MCT specimens is the minimum required for a numerical T_0 determination by means of the probabilistic CZM. This number may be reduced further if flow curve data and/or the J-R curve of the material at RT in the considered condition is available. However, it should be noted that the material requirements stated are based on the best-case scenario in which all tests provide usable results, which may be difficult to achieve given the high complexity of the calibration methods.

To conclude, the probabilistic CZM is considered to be a promising approach for the detailed numerical characterization of the statistical fracture-mechanical behavior of ferritic steels within the transition region. With the first iteration of the model presented in this thesis, the mean fracture behavior of the investigated RPV steel can already be predicted with high accuracy. That being said, the model offers a number of opportunities for improving its predictive capabilities regarding the numerical fracture toughness scatter. Measures for increasing the scatter that have not been applied in this work include the introduction of statistically distributed model parameters, such as the DFR, and the modeling of “weakest links” distributed throughout the cohesive zone. In addition, a variable starting crack length and crack shape can be considered. It is noted that these measures, while certainly effective, would further increase the complexity of the model.

9 Summary and outlook

For the safe long-term operation of nuclear reactors, it is essential to monitor the evolution of the fracture-mechanical behavior of the structural steels used for the reactor pressure vessel (RPV) under the influence of neutron irradiation. The location of the ductile-to-brittle transition (DBT) region is of particular importance due to its safety relevance. Since the availability of irradiated material is severely limited, it is necessary to develop small specimen test techniques for fracture-mechanical testing within the DBT region. In the past decades, the miniaturized compact tension specimen (MCT) has been shown to be a promising geometry for future surveillance programs. However, further demonstration of the viability of the geometry is required due to the effect of loss of constraint observed during testing, and additional efforts are necessary to further reduce the material requirement of established testing standards.

In the present work, an experimental-numerical method introduced by Mahler & Aktaa (2014) [11] was applied and developed further to calibrate a novel probabilistic cohesive zone model (CZM) to be used for fracture-mechanical simulations of MCT specimens within the transition region. The objective was to use the calibrated CZM in conjunction with a finite-element-model of the MCT to demonstrate the numerical prediction of the reference temperature of the RPV steel SA-508 Cl.3 based on the Master Curve methodology. The developed approach was evaluated based on the accuracy of the predicted reference temperature and the material volume required for the identification of the model parameters.

First, plastic flow curves of the material SA-508 Cl.3 were determined at room temperature and multiple temperatures within the transition region between -80 and -30°C to be used as elasto-plastic material model for the simulations. For this, smooth round bar specimens were tested and the diameter reduction during testing was recorded by a camera system to later identify the true stresses and true strains. The same setup was applied to test notched round bar specimens, which were later used to numerically determine the triaxiality dependence of the cohesive strength, which is the first parameter for the CZM.

MCT specimens of the same material were tested within the DBT region to determine a reference temperature of -31.5°C and to evaluate the fracture toughness Master Curve following the ASTM E1921 standard. The individual MCT test results were required for the calibration of the second cohesive zone parameter, which is the cohesive energy. Of a total of 22 valid fracture toughness results, 4 required censoring according the limit specified in the standard. Based on this result, the optimal test temperature for using as few specimens as possible was determined to be located where the median fracture toughness is $90 \text{ MPa}\sqrt{\text{m}}$. Extensive fractographic analysis of the tested MCT specimens was performed to locate and characterize the cleavage initiation sites and correlate their positions to numerically determined stress and triaxiality fields. It was found that most initiation sites are located within the region of high constraint and that 56% of initiation sites show the characteristics of particle initiation, while 44% are positioned at grain boundaries. Furthermore, quantitative fractographic analysis was carried out to identify the temperature dependence of the ductile fracture ratio (DFR), which is defined as the ratio between the total area of the ductile fracture regions visible on the fracture surfaces and the total area of the fracture surfaces. The average DFR, which increases from 3.6% to 9.7% between -80 and -45°C, was required as an input parameter for the probabilistic CZM. In addition to the transition region, MCT specimens were tested at room temperature to determine the J-R curve of the material, which was required to calibrate the cohesive energy on the upper shelf.

The numerical part of the parameter identification procedure included the simulation of the smooth and notched round bar specimen tests to calibrate the triaxiality dependent cohesive strength, whereby a linear triaxiality dependence was obtained for all temperatures. The MCT tests within the transition region and at room temperature were simulated by using the cohesive energy as a fitting parameter. For the low-temperature simulations, a failure criterion was defined to identify the initiation of unstable crack growth based on the crack growth rate. It was shown that the low-temperature tests can be simulated with either a triaxiality dependent or a constant cohesive strength, while the J-R curve at room temperature can only be simulated with a triaxiality dependent cohesive strength.

The calibrated CZM was used to simulate a 0.5T CT and a 1T CT specimen to predict the fracture toughness obtained from large geometries and to evaluate differences between the mechanical and fracture-mechanical behavior of the MCT and the standard-sized geometries. Weakest-link statistics were applied to size-adjust the cohesive energy and a good agreement between the numerical fracture toughness values and the experimental results from the Master Curve was achieved. The mechanical behavior of the MCT was found to be similar to the large geometries at low crack tip loading, however loss of constraint of the MCT was observed at high crack tip loading. Nevertheless, the MCT was shown to maintain a high level of constraint within the highly stressed region close to the mid thickness of the specimen. Large-scale plastic deformation of the MCT was observed while the plastic zone remains confined to the crack tip region for the standard-sized geometries.

For predicting statistically distributed fracture toughness values within the DBT region, the cohesive zone in front of the crack tip was divided into randomly spatially distributed clusters of cohesive elements with ductile fracture properties and clusters with brittle fracture properties. The cohesive zone parameters obtained from the -80°C calibration were used for the brittle elements, while the room temperature calibration was used for the ductile elements. The two parameter sets form the basis of the probabilistic CZM approach. Based on the DFR, which was determined by means of quantitative fractography, the total number of ductile elements across the cohesive zone was determined. Simulations with randomly generated cohesive zones were performed to study the interaction of the ductile and brittle elements. It was found that the ductile elements cause the adjacent brittle elements to separate and fail prematurely, resulting in the unstable crack growth criterion being met at lower fracture toughness values than in simulations with only brittle elements. Furthermore, it was observed that the numerical fracture toughness results are not correlated to the location of the ductile clusters on a global scale, but rather to the size of the clusters and their relative position.

The probabilistic CZM was used to predict a numerical reference temperature using the same number of simulations at each temperature as the number of MCT tests performed within the DBT region for the experimental Master Curve determination. Thereby, the numerical fracture toughness results were treated as physical test results according to the ASTM E1921 standard. The calibrated model was shown to predict a reference temperature of -32.3°C , which is in good agreement with the experimental value of -31.5°C . However, the scatter of the numerical fracture toughness values is significantly reduced compared to the test results. An attempt was made to increase the numerical scatter by introducing ductile element clusters of variable size, which proved to have the opposite effect due to a homogenization of the cohesive parameters throughout the cohesive zone. A statistical analysis of 50 probabilistic simulations at -60°C revealed that the numerical fracture toughness values follow a three-parameter Weibull distribution with a Weibull modulus of 8.9, which is substantially higher than the value of 4 specified in the ASTM standard, indicating the reduced scatter of the numerical results.

Lastly, the amount of material required for the numerical determination of the reference temperature with the probabilistic CZM approach was compared to the material required for an experimental determination. It was found that, in case of a homogeneous material, the probabilistic CZM requires a minimum material volume of 12 MCT specimens in the best-case scenario, while the experimental determination requires 14 MCT specimens on average.

The probabilistic CZM approach has been shown to be an effective method for predicting the median fracture-mechanical behavior of the RPV steel SA-508 Cl.3 within the transition region. It can be assumed that the method is applicable to other ferritic steels, although this was not investigated in this work. Improvements to the predictive capabilities of the model are required to increase the numerical fracture toughness scatter to better match experimental results. The introduction of randomly distributed unstable fracture initiators throughout the cohesive zone is expected to contribute to an increased scatter. As an additional result, it was confirmed that the material requirement for the numerical determination of T_0 is slightly lower than for the experimental determination of the reference temperature following ASTM E1921.

References

- [1] Debarberis, L., Sevini, F. *Integrity of reactor pressure vessels in nuclear power plants: Assessment of irradiation embrittlement effects in reactor pressure vessel steels*. In: Integrity of Reactor Pressure Vessels in NPPs. Internat. Atomic Energy Agency IAEA, Vienna, Austria (2009). ISBN 978-92-0-101709-3.
- [2] Server, W. L. and Brumovsky, M. *International Review of Nuclear Reactor Pressure Vessel Surveillance Programs*. ASTM International, West Conshohocken, PA (2018). DOI 10.1520/STP1603-EB.
- [3] Minnebo, P. *Master curve approach to monitor fracture toughness of reactor pressure vessels in nuclear power plants*. IAEA-TECDOC-1631. Internat. Atomic Energy Agency IAEA, Vienna, Austria (2009). ISBN 978-92-0-111009-1.
- [4] Cicero, S., Lambrecht, M., Swan, H., Arffman, P., Altstadt, E., Petit, T., Obermeier, F., Arroyo, B., Álvarez, J. A., and Lacalle, R. “Fracture mechanics testing of irradiated RPV steels by means of sub-sized specimens: FRACTESUS project.” *Procedia Structural Integrity* Vol. 28 (2020): pp. 61–66. DOI 10.1016/j.prostr.2020.10.008.
- [5] H2020-Euratom FRACTESUS Project: Fracture mechanics testing of irradiated RPV steels by means of sub-sized specimens. URL <https://fractesus-h2020.eu/>. Date of access 18.08.2025.
- [6] Scibetta, M., Lucon, E., and van Walle, E. “Optimum use of broken Charpy specimens from surveillance programs for the application of the master curve approach.” *International Journal of Fracture* Vol. 116 (2002): pp. 231–244. DOI 10.1023/A:1020165900918.
- [7] Lucon, E., Scibetta, M., Chaouadi, R., van Walle, E., and Dean, S. W. “Use of Miniaturized Compact Tension Specimens for Fracture Toughness Measurements in the Upper Shelf Regime.” *Journal of ASTM International* Vol. 3 No. 1 (2006). DOI 10.1520/JAI13235.
- [8] Sánchez, M., Cicero, S., Kirk, M., Altstadt, E., Server, W., and Yamamoto, M. “Using Mini-CT Specimens for the Fracture Characterization of Ferritic Steels within the Ductile to Brittle Transition Range: A Review.” *Metals* Vol. 13 No. 1 (2023): p. 176. DOI 10.3390/met13010176.
- [9] Sokolov, M. A. “Development of Mini-Compact Tension Test Method for Determining Fracture Toughness Master Curves for Reactor Pressure Vessel Steels.” ORNL/TM-2017/275. Oak Ridge National Laboratory (2017).
- [10] ASTM International. “Standard Test Method for Determination of Reference Temperature, To, for Ferritic Steels in the Transition Range.” E1921 - 21. ASTM International, West Conshohocken, PA (2021).
- [11] Mahler, M. and Aktaa, J. “Approach for Determining Fracture Mechanical Properties from Tests on Small Size Specimens at Room Temperature.” *Procedia Materials Science* Vol. 3 (2014): pp. 434–439. DOI 10.1016/j.mspro.2014.06.073.
- [12] Mahler, M. and Aktaa, J. “Prediction of fracture toughness based on experiments with sub-size specimens in the brittle and ductile regimes.” *Journal of Nuclear Materials* Vol. 472 (2016): pp. 178–185. DOI 10.1016/j.jnucmat.2015.08.046.
- [13] Rolfe, S. T. and Barsom, J. M. *Fracture and Fatigue Control in Structures: Applications of Fracture Mechanics*. ASTM International, West Conshohocken, PA (1999). DOI 10.1520/MNL41-3ED-EB.
- [14] Gross, D. and Seelig, T. *Fracture Mechanics*. Springer International Publishing, Cham (2018). DOI 10.1007/978-3-319-71090-7.

- [15] Bhowmik, S., Sahoo, P., Acharyya, S. K., Dhar, S., and Chattopadhyay, J. "Evaluation and effect of loss of constraint on master curve reference temperature of 20MnMoNi55 steel." *Engineering Fracture Mechanics* Vol. 136 (2015): pp. 142–157. DOI 10.1016/j.engfracmech.2015.01.022.
- [16] Lucon, E., Scibetta, M., Chaouadi, R., and van Walle, E. "Fracture Toughness Measurements in the Transition Region Using Sub-Size Precracked Charpy and Cylindrical Bar Specimens." *Small Specimen Test Techniques: 4th Volume*. ASTM International, West Conshohocken, PA (2002). DOI 10.1520/STP1418-EB.
- [17] Nanstad, R. K., Sokolov, M. A., and Lucon, E. "Influence of Specimen Size/Type on the Fracture Toughness of Five Irradiated PRV Materials." *Proceedings of the 15th International Conference on Environmental Degradation of Materials in Nuclear Power Systems - Water Reactors*. Ottawa, Ontario, Canada, August 9-13 2015.
- [18] Tvergaard, V. and Needleman, A. "Analysis of the cup-cone fracture in a round tensile bar." *Acta Metallurgica* Vol. 32 No. 1 (1984): pp. 157–169. DOI 10.1016/0001-6160(84)90213-X.
- [19] Needleman, A. and Tvergaard, V. "An analysis of ductile rupture in notched bars." *Journal of the Mechanics and Physics of Solids* Vol. 32 No. 6 (1984): pp. 461–490. DOI 10.1016/0022-5096(84)90031-0.
- [20] Needleman, A. and Tvergaard, V. "An analysis of ductile rupture modes at a crack tip." *Journal of the Mechanics and Physics of Solids* Vol. 35 No. 2 (1987): pp. 151–183. DOI 10.1016/0022-5096(87)90034-2.
- [21] Gurson, A. L. "Continuum Theory of Ductile Rupture by Void Nucleation and Growth: Part I—Yield Criteria and Flow Rules for Porous Ductile Media." *Journal of Engineering Materials and Technology* Vol. 99 No. 1 (1977): pp. 2–15. DOI 10.1115/1.3443401.
- [22] Beremin, F. M., Pineau, A., Mudry, F., Devaux, J.-C., D'Escatha, Y., and Ledermann, P. "A local criterion for cleavage fracture of a nuclear pressure vessel steel." *Metallurgical Transactions A* Vol. 14 No. 11 (1983): pp. 2277–2287. DOI 10.1007/BF02663302.
- [23] Irwin, G. R. "Analysis of Stresses and Strains Near the End of a Crack Traversing a Plate." *Journal of Applied Mechanics* Vol. 24 No. 3 (1957): pp. 361–364. DOI 10.1115/1.4011547.
- [24] Sun, C. T. and Jin, Z.-H. *Fracture mechanics*. Elsevier (2012). DOI 10.1016/C2009-0-63512-1.
- [25] Griffith, A. A. "The phenomena of rupture and flow in solids." *Philosophical Transactions of the Royal Society A* Vol. 221 (1921): pp. 163–198. DOI 10.1098/rsta.1921.0006.
- [26] Rice, J. R. "A Path Independent Integral and the Approximate Analysis of Strain Concentration by Notches and Cracks." *Journal of Applied Mechanics* Vol. 35 No. 2 (1968): pp. 379–386. DOI 10.1115/1.3601206.
- [27] Perez, N. *Fracture Mechanics*. Springer International Publishing, Cham (2017). DOI 10.1007/978-3-319-24999-5.
- [28] Rice, J. R., Paris, P. C., and Merkle, J. G. "Some Further Results of J-Integral Analysis and Estimates." *Progress in Flaw Growth and Fracture Toughness Testing*. ASTM International, West Conshohocken, PA (1973): pp. 231–245. DOI 10.1520/STP49643S.
- [29] Anderson, T. L. *Fracture mechanics: Fundamentals and applications*. CRC Press, Boca Raton, FL (2017). DOI 10.1201/9781315370293.
- [30] Hsia, K. J. "Brittle-Ductile Transition." *Encyclopedia of tribology*. Springer, Boston, MA (2013): pp. 273–279. DOI 10.1007/978-0-387-92897-5_263.
- [31] Orowan, E. "Fracture and strength of solids." *Reports on Progress in Physics* Vol. 12 No. 1 (1949): pp. 185–232. DOI 10.1088/0034-4885/12/1/309.

-
- [32] Curry, D. A. and Knott, J. F. "Effect of microstructure on cleavage fracture toughness of quenched and tempered steels." *Metal Science* Vol. 13 No. 6 (1979): pp. 341–345. DOI 10.1179/msc.1979.13.6.341.
 - [33] Curry, D. A. "Comparison between two models of cleavage fracture." *Metal Science* Vol. 14 No. 2 (1980): pp. 78–80. DOI 10.1179/030634580790426292.
 - [34] Peirce, F. T. "'The Weakest Link' - Theorems on the Strength of Long and of Composite Specimens." *Journal of the Textile Institute Transactions* Vol. 17 No. 7 (1926): T355-T368. DOI 10.1080/19447027.1926.10599953.
 - [35] Weibull, W. "A Statistical Distribution Function of Wide Applicability." *Journal of Applied Mechanics* Vol. 18 No. 3 (1951): pp. 293–297. DOI 10.1115/1.4010337.
 - [36] Chao, Y. J. and Lam, P.-S. "Constraint Effect in Fracture - What is it?" 12th International Conference on Fracture 2009, ICF-12, Ottawa, Ontario, Canada.
 - [37] Minami, F., Ohata, M., Shimanuki, H., Handa, T., Igi, S., Kurihara, M., Kawabata, T., Yamashita, Y., Tagawa, T., and Hagihara, Y. "Method of constraint loss correction of CTOD fracture toughness for fracture assessment of steel components." *Engineering Fracture Mechanics* Vol. 73 No. 14 (2006): pp. 1996–2020. DOI 10.1016/j.engfracmech.2006.03.013.
 - [38] Nevalainen, M. and Dodds, R. H. "Numerical investigation of 3-D constraint effects on brittle fracture in SE(B) and C(T) specimens." *International Journal of Fracture* Vol. 74 No. 2 (1996): pp. 131–161. DOI 10.1007/BF00036262.
 - [39] Zhou, Z., Tong, Z., Qian, G., and Berto, F. "Specimen size effect on the ductile-brittle transition reference temperature of A508-3 steel." *Theoretical and Applied Fracture Mechanics* Vol. 104 (2019): p. 102370. DOI 10.1016/j.tafmec.2019.102370.
 - [40] ASTM International. "Test Method for Linear-Elastic Plane-Strain Fracture Toughness of Metallic Materials." E399 - 20. ASTM International, West Conshohocken, PA (2020).
 - [41] ASTM International. "Test Method for Measurement of Fracture Toughness." E1820 - 20a. ASTM International, West Conshohocken, PA (2020).
 - [42] Wallin, K. "Statistical Modelling of Fracture in the Ductile-to-Brittle Transition Region." *Defect assessment in components - fundamentals and applications: Proceedings*. Mechan. Eng. Publ, London (1991): pp. 415–445. ISSN 1352-2418.
 - [43] Nanstad, R. K. and Sokolov, M. A. "The Assessment and Validation of Mini-Compact Tension Test Specimen Geometry and Progress in Establishing Technique for Fracture Toughness Master Curves for Reactor Pressure Vessel Steels." ORNL/TM-2016/602. Oak Ridge National Laboratory (2016).
 - [44] Dzugan, J., Konopik, P., and Rund, M. "Fracture Toughness Determination with the Use of Miniaturized Specimens." *Contact and Fracture Mechanics*. InTechOpen (2018). DOI 10.5772/intechopen.73093.
 - [45] Jose, N. M., Chattopadhyay, J., Durgaprasad, P. V., and Kumar, N. N. "Master Curve of 20MnMoNi55 Steel From Miniature CT Specimens." *Procedia Structural Integrity* Vol. 14 (2019): pp. 403–409. DOI 10.1016/j.prostr.2019.05.049.
 - [46] González-Velázquez, J. L. *Fractography and Failure Analysis*. Springer International Publishing, Cham (2018). DOI 10.1007/978-3-319-76651-5.
 - [47] Besson, J., Berdin, C., Bugat, S., Desmorat, R. *Local approach to fracture*. École des Mines, Paris (2004). ISBN 978-2911762550.
 - [48] Rousselier, G. "Ductile fracture models and their potential in local approach of fracture." *Nuclear Engineering and Design* Vol. 105 No. 1 (1987): pp. 97–111. DOI 10.1016/0029-5493(87)90234-2.

- [49] Chaboche, J. L. "Damage Mechanics." *Comprehensive Structural Integrity*. Elsevier (2003): pp. 213–284. DOI 10.1016/b0-08-043749-4/02085-1.
- [50] Rousselier, G. "The Rousselier Model for Porous Metal Plasticity and Ductile Fracture." *Handbook of Materials Behavior Models: Three-Volume Set ; Nonlinear Models and Properties*. Elsevier Science, Burlington (2001): pp. 436–445. DOI 10.1016/B978-012443341-0/50049-1.
- [51] Samal, M. K., Seidenfuss, M., and Roos, E. "A new mesh-independent Rousselier's damage model: Finite element implementation and experimental verification." *International Journal of Mechanical Sciences* Vol. 51 No. 8 (2009): pp. 619–630. DOI 10.1016/j.ijmecsci.2009.06.006.
- [52] Bernauer, G., Brocks, W., Mühlich, U., Steglich, D., and Werwer, M. "Hinweise zur Anwendung des Gurson-Tvergaard-Needleman-Modells." GKSS-Forschungszentrum Geesthacht (1999).
- [53] Ritchie, R. O., Knott, J. F., and Rice, J. R. "On the relationship between critical tensile stress and fracture toughness in mild steel." *Journal of the Mechanics and Physics of Solids* Vol. 21 No. 6 (1973): pp. 395–410. DOI 10.1016/0022-5096(73)90008-2.
- [54] Becker, T. L., Cannon, R. M., and Ritchie, R. O. "A Statistical RKR Fracture Model for the Brittle Fracture of Functionally Graded Materials." *Materials Science Forum* 308-311 (1999): pp. 957–962. DOI 10.4028/WWW.SCIENTIFIC.NET/MSF.308-311.957.
- [55] Roberts, S. G. "Modelling Brittle-Ductile Transitions.", Oxford, UK (1999). DOI 10.13140/2.1.4183.2964.
- [56] Yang, W.-J., Lee, B.-S., Huh, M.-Y., and Hong, J.-H. "Application of the local fracture stress model on the cleavage fracture of the reactor pressure vessel steels in the transition temperature region." *Journal of Nuclear Materials* Vol. 317 2-3 (2003): pp. 234–242. DOI 10.1016/S0022-3115(03)00106-5.
- [57] Andrieu, A., Pineau, A., Besson, J., Ryckelynck, D., and Bouaziz, O. "Beremin model: Methodology and application to the prediction of the Euro toughness data set." *Engineering Fracture Mechanics* Vol. 95 (2012): pp. 102–117. DOI 10.1016/j.engfracmech.2011.10.019.
- [58] Chakraborty, P. and Biner, S. B. "A unified cohesive zone approach to model the ductile to brittle transition of fracture toughness in reactor pressure vessel steels." *Engineering Fracture Mechanics* Vol. 131 (2014): pp. 194–209. DOI 10.1016/j.engfracmech.2014.07.029.
- [59] Siegmund, T. and Brocks, W. "A numerical study on the correlation between the work of separation and the dissipation rate in ductile fracture." *Engineering Fracture Mechanics* Vol. 67 No. 2 (2000): pp. 139–154. DOI 10.1016/S0013-7944(00)00054-0.
- [60] Scheider, I. "The Cohesive Model: Foundations and Implementation.", 2nd ed. GKSS-Forschungszentrum Geesthacht (2006).
- [61] Dixit, S. and Chaudhari, V. "Evaluation of fracture parameters to simulate fracture process zone for SA 516 pressure vessel steel." *Materials Today: Proceedings* Vol. 28 (2020): pp. 721–724. DOI 10.1016/j.matpr.2019.12.286.
- [62] Dixit, S., Chaudhari, V., and Kulkarni, D. M. "Mode-I Fracture Investigations of Pressure Vessel Steels: Experimental and Simulation Study." *Journal of Materials Engineering and Performance* Vol. 29 No. 11 (2020): pp. 7179–7187. DOI 10.1007/s11665-020-05209-7.
- [63] Scheider, I. and Brocks, W. "Simulation of cup–cone fracture using the cohesive model." *Engineering Fracture Mechanics* Vol. 70 No. 14 (2003): pp. 1943–1961. DOI 10.1016/S0013-7944(03)00133-4.
- [64] Liu, J., Li, J., and Liu, L. "Finite Element Analysis for Brittle and Ductile Fracture Using a Unified Cohesive Zone Model." *Advances in Mechanical Engineering* Vol. 5 (2013): p. 924070. DOI 10.1155/2013/924070.

-
- [65] Dugdale, D. S. "Yielding of steel sheets containing slits." *Journal of the Mechanics and Physics of Solids* Vol. 8 No. 2 (1960): pp. 100–104. DOI 10.1016/0022-5096(60)90013-2.
- [66] Cornec, A., Scheider, I., and Schwalbe, K.-H. "On the practical application of the cohesive model." *Engineering Fracture Mechanics* Vol. 70 No. 14 (2003): pp. 1963–1987. DOI 10.1016/S0013-7944(03)00134-6.
- [67] Barenblatt, G. I. "The Mathematical Theory of Equilibrium Cracks in Brittle Fracture." *Advances in Applied Mechanics* Vol. 7. Elsevier (1962): pp. 55–129. DOI 10.1016/S0065-2156(08)70121-2.
- [68] Schwalbe, K.-H., Scheider, I., and Cornec, A. *Guidelines for Applying Cohesive Models to the Damage Behaviour of Engineering Materials and Structures*. Springer Berlin, Heidelberg (2013). DOI 10.1007/978-3-642-29494-5.
- [69] Needleman, A. "A Continuum Model for Void Nucleation by Inclusion Debonding." *Journal of Applied Mechanics* Vol. 54 No. 3 (1987): pp. 525–531. DOI 10.1115/1.3173064.
- [70] Tvergaard, V. and Hutchinson, J. W. "Toughness of an interface along a thin ductile layer joining elastic solids." *Philosophical Magazine A* Vol. 70 No. 4 (1994): pp. 641–656. DOI 10.1080/01418619408242253.
- [71] Tvergaard, V. and Hutchinson, J. W. "The relation between crack growth resistance and fracture process parameters in elastic-plastic solids." *Journal of the Mechanics and Physics of Solids* Vol. 40 No. 6 (1992): pp. 1377–1397. DOI 10.1016/0022-5096(92)90020-3.
- [72] de Borst, R. "Numerical aspects of cohesive-zone models." *Engineering Fracture Mechanics* Vol. 70 No. 14 (2003): pp. 1743–1757. DOI 10.1016/S0013-7944(03)00122-X.
- [73] Hillerborg, A., Mod  r, M., and Petersson, P.-E. "Analysis of crack formation and crack growth in concrete by means of fracture mechanics and finite elements." *Cement and Concrete Research* Vol. 6 No. 6 (1976): pp. 773–781. DOI 10.1016/0008-8846(76)90007-7.
- [74] Needleman, A. "An analysis of decohesion along an imperfect interface." *International Journal of Fracture* Vol. 42 No. 1 (1990): pp. 21–40. DOI 10.1007/BF00018611.
- [75] Siegmund, T. and Brocks, W. "The Role of Cohesive Strength and Separation Energy for Modeling of Ductile Fracture." *Fatigue and fracture mechanics: 30th volume*. ASTM International, West Conshohocken, PA (2000): pp. 139–151. DOI 10.1520/STP13400S.
- [76] Brocks, W. "Cohesive Strength and Separation Energy as Characteristic Parameters of Fracture Toughness and Their Relation to Micromechanics." *SID Structural Integrity and Durability* Vol. 1 (2005): pp. 233–243. ISSN 1551-3750.
- [77] Li, X. and Yuan, H. "Cohesive Zone Modeling for 3D Ductile Crack Propagation." *Applied Mechanics and Materials* Vol. 853 (2016): pp. 132–136. DOI 10.4028/www.scientific.net/AMM.853.132.
- [78] Scheider, I. and Brocks, W. "Effect of Cohesive Law and Triaxiality Dependence of Cohesive Parameters in Ductile Tearing." *Fracture of Nano and Engineering Materials and Structures*. Springer Netherlands, Dordrecht (2006): pp. 965–966. DOI 10.1007/1-4020-4972-2_478.
- [79] Scheider, I., Rajendran, M. and Banerjee, A. "Comparison of different stress-state dependent cohesive zone models applied to thin-walled structures." *Engineering Fracture Mechanics* Vol. 78 No. 3 (2011): pp. 534–543. DOI 10.1016/j.engfracmech.2010.05.003.
- [80] Chen, C. R., Kolednik, O., Heerens, J. and Fischer, F. D. "Three-dimensional modeling of ductile crack growth: Cohesive zone parameters and crack tip triaxiality." *Engineering Fracture Mechanics* Vol. 72 No. 13 (2005): pp. 2072–2094. DOI 10.1016/j.engfracmech.2005.01.008.
- [81] Schicker, J. "Simulation des Bruchverhaltens quasi-spr  der Werkstoffe bei einachsiger Zugbelastung unter Verwendung eines lokalen statistischen Ansatzes und einfacher statistischer Modelle."

- Dissertation. Christian-Albrechts-Universität zu Kiel, Kiel, Germany (2005). URN urn:nbn:de:gbv:8-diss-14650.
- [82] Khokhar, Z. R., Ashcroft, I. A. and Silberschmidt, V. V. “Modelling the Effect of Microstructural Randomness on the Fracture of Composite Laminates with Stochastic Cohesive Zone Elements.” *Key Engineering Materials* Vol. 417-418 (2009): pp. 13–16. DOI 10.4028/www.scientific.net/KEM.417-418.13.
- [83] Kabir, M. R. “Modeling and simulation of deformation and fracture behavior of components made of fully lamellar gamma-TiAl alloy.” Dissertation. GKSS-Forschungszentrum Geesthacht, Geesthacht, Germany. Accepted by Christian-Albrechts-Universität zu Kiel, Kiel, Germany (2008). ISSN 0344-9629.
- [84] Brocks, W., Arafah, D., and Madia, M. “Exploiting Symmetries of FE Models and Application to Cohesive Elements.” Report. Milano / Kiel (2013). URL http://www.tf.uni-kiel.de/matwis/instatmat/departments/brocks/brocks_homepage_en.html. Date of access 07.09.2020. No longer available on 20.08.2025.
- [85] Blauel, J. G. and Schwalbe, K.-H. *Defect assessment in components - fundamentals and applications: Proceedings*. Mechan. Eng. Publ, London (1991). ISBN 978-0852987421.
- [86] Mahler, M. “Entwicklung einer Auswertemethode für bruchmechanische Versuche an kleinen Proben auf der Basis eines Kohäsivzonenmodells.” Dissertation. Karlsruhe Institute of Technology, Karlsruhe, Germany (2016). DOI 10.5445/KSP/1000049846.
- [87] ASME. “Boiler and Pressure Vessel Code - Section II - Part A.” SA-508. American Society of Mechanical Engineers ASME (2019). ISBN 9780791877012.
- [88] Mandal, P., Lalvani, H., Barrow, A., and Adams, J. “Microstructural Evolution of SA508 Grade 3 Steel during Hot Deformation.” *Journal of Materials Engineering and Performance* Vol. 29 No. 2 (2020): pp. 1015–1033. DOI 10.1007/s11665-020-04611-5.
- [89] Zhou, L., Dai, J., Li, Y., Dai, X., Xie, C., Li, L., and Chen, L. “Research Progress of Steels for Nuclear Reactor Pressure Vessels.” *Materials (Basel, Switzerland)* Vol. 15 No. 24 (2022). DOI 10.3390/ma15248761.
- [90] Kim, S., Lee, S., Im, Y.-R., Lee, H.-C., Oh, Y.-J., and Hong, J.-H. “Effects of alloying elements on mechanical and fracture properties of base metals and simulated heat-affected zones of SA 508 steels.” *Metallurgical and Materials Transactions A* Vol. 32 No. 4 (2001): pp. 903–911. DOI 10.1007/s11661-001-0347-8.
- [91] Kim, M.-C., Park, S.-G., Lee, K.-H., and Lee, B.-S. “Comparison on Mechanical Properties of SA508 Gr.3 Cl.1, Cl.2, and Gr.4N Low Alloy Steels for Pressure Vessels.” *Transactions of the Korean Nuclear Society Autumn Meeting*. Pyeongchang, Korea, October 30-31 2014.
- [92] Im, Y.-R., Jun Oh, Y., Lee, B.-J., Hwa Hong, J., and Lee, H.-C. “Effects of carbide precipitation on the strength and Charpy impact properties of low carbon Mn–Ni–Mo bainitic steels.” *Journal of Nuclear Materials* Vol. 297 No. 2 (2001): pp. 138–148. DOI 10.1016/S0022-3115(01)00610-9.
- [93] Hernández, R., Serrano, M., Plaza, D., Munoz, A., Álamo, D., Sauce, D., and Plaza, F. Unpublished work. CIEMAT.
- [94] ASME. “Boiler and Pressure Vessel Code - Section II - Part D.” American Society of Mechanical Engineers ASME (2019). ISBN 9780791877050.
- [95] Brynk, T., Uytendhouwen, I., Arffman, P., Altstadt, E., Kopriva, R., Obermeier, F., and Serrano, M. “FRACTESUS Project: Final Selection of RPV Materials for Unirradiated and Irradiated Round Robins.” *Proceedings of the ASME 2022 Pressure Vessels and Piping Conference - Vol-*

-
- ume 1: *Codes and Standards*. Las Vegas, Nevada, USA, July 17-22 2022. DOI 10.1115/PVP2022-83871.
- [96] Bridgman, P. W. *Studies in Large Plastic Flow and Fracture: With Special Emphasis on the Effects of Hydrostatic Pressure*. Harvard University Press, s.l. (1964). DOI 10.4159/harvard.9780674731349.
- [97] Metzler, T., Gaganidze, E., Aktaa, J. “Numerical prediction of fracture toughness of a reactor pressure vessel steel based on experiments using small specimens.” *Proceedings of the ASME 2023 Pressure Vessels and Piping Conference - Volume 1: Codes & Standards*. Atlanta, Georgia, USA, July 16-21 2023. DOI 10.1115/PVP2023-105918.
- [98] Lawrence, J. D. *A catalog of special plane curves*. Dover Publ Inc., New York (1972). ISBN 978-0486602882.
- [99] Metzler, T., Gaganidze, E., Aktaa, J. “Prediction of fracture toughness of a reactor pressure vessel steel in the ductile-to-brittle transition region based on a probabilistic cohesive zone model approach.” *Journal of Nuclear Materials* Vol. 605 (2025). DOI 10.1016/j.jnucmat.2024.155556.
- [100] Landes, J. D. “J calculation from front face displacement measurement on a compact specimen.” *International Journal of Fracture* Vol. 16 (1980): pp. 183–186. DOI 10.1007/BF00018249.
- [101] Wallin, K. “Inhomogeneity Screening Criterion for the ASTM E1921 T0 Estimate Based on the SINTAP Lower-Tail Methodology.” *Journal of Testing and Evaluation* Vol. 40 No. 6 (2012): p. 104241. DOI 10.1520/JTE104241.
- [102] Naziris, F., Hernandez Pascual, R., Metzler, T., Gaganidze, E., Uytendhouwen, I., and Kolluri, M. “Master Curve Evaluation Using Miniature C(T) Specimens as Part of a Round Robin Program Within the FRACTESUS Project.” *Proceedings of the ASME 2023 Pressure Vessels and Piping Conference - Volume 1: Codes & Standards*. Atlanta, Georgia, USA, July 16-21 2023. DOI 10.1115/PVP2023-107254.
- [103] H2020-Euratom SOTERIA Project: Safe long-term operation of light water reactors based on improved understanding of radiation effects in nuclear structural materials. Deliverable 3.1. URL <http://www.soteria-project.eu/>. Date of access 14.10.2020. No longer available on 20.08.2025.
- [104] Chekhonin, P., Das, A., Bergner, F., and Altstadt, E. “Microstructural characterisation of brittle fracture initiation sites in reactor pressure vessel steels.” *Nuclear Materials and Energy* Vol. 37 (2023): p. 101511. DOI 10.1016/j.nme.2023.101511.
- [105] Wallin, K., Yamamoto, M., and Ehrnstén, U. “Location of Initiation Sites in Fracture Toughness Testing Specimens: The Effect of Size and Side Grooves.” *Proceedings of the ASME Pressure Vessels and Piping Conference - 2016*. Vancouver, British Columbia, Canada, 7/17/2016 - 7/21/2016. DOI 10.1115/PVP2016-63078.
- [106] Soboyejo, W. *Mechanical properties of engineered materials*. CRC Press, Boca Raton (2002). DOI 10.1201/9780203910399.
- [107] Bowen, P., Druce, S. G., and Knott, J. F. “Effects of microstructure on cleavage fracture in pressure vessel steel.” *Acta Metallurgica* Vol. 34 No. 6 (1986): pp. 1121–1131. DOI 10.1016/0001-6160(86)90222-1.
- [108] Lee, S., Kim, S., Hwang, B., Lee, B.S., and Lee, C.G. “Effect of carbide distribution on the fracture toughness in the transition temperature region of an SA 508 steel.” *Acta Materialia* Vol. 50 No. 19 (2002): pp. 4755–4762. DOI 10.1016/S1359-6454(02)00313-0.
- [109] Ul-Hamid, A. *A Beginners' Guide to Scanning Electron Microscopy*. Springer International Publishing, Cham (2018). DOI 10.1007/978-3-319-98482-7.
- [110] Hull, D. and Bacon, D. J. *Introduction to dislocations*. Butterworth Heinemann Elsevier, Amsterdam, Heidelberg (2011). DOI 10.1016/C2009-0-64358-0.

- [111] Camas, D., Garcia-Manrique, J., and Gonzalez-Herrera, A. “Crack front curvature: Influence and effects on the crack tip fields in bi-dimensional specimens.” *International Journal of Fatigue* Vol. 44 (2012): pp. 41–50. DOI 10.1016/j.ijfatigue.2012.05.012.
- [112] Mahler, M., Fessi, S., Aktaa, J. „Simplified approach for ductile fracture mechanics SSTT and its application to Eurofer97.” *Nuclear Materials and Energy* Vol. 26 (2021). DOI 0.1016/j.nme.2020.100799.
- [113] Irwin, G. R. „Plastic zone near a crack and fracture toughness.” *Proceedings of the 7th Sagamore Ordnance Materials Conference*. Syracuse, New York (1960): pp. IV-63.

Appendix

A.1 Material block dimensions and cutting plans

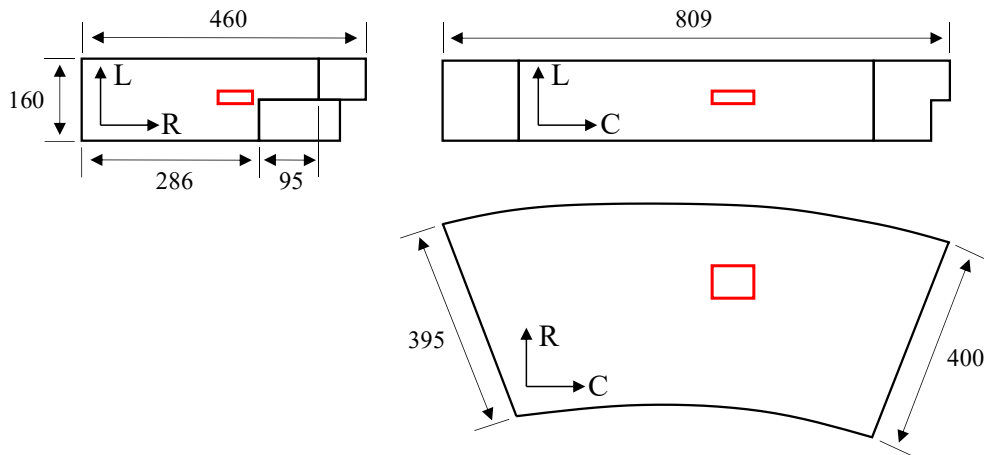


Figure A.1: SA-508 Cl.3 forging dimensions and orientations (dimensions in mm) with location of extracted block in red

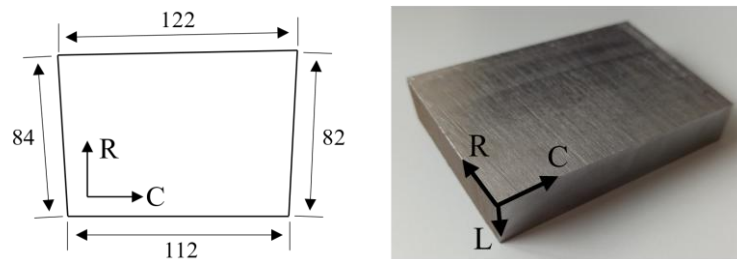


Figure A.2: SA-508 Cl.3 block used for specimen fabrication (dimensions in mm)

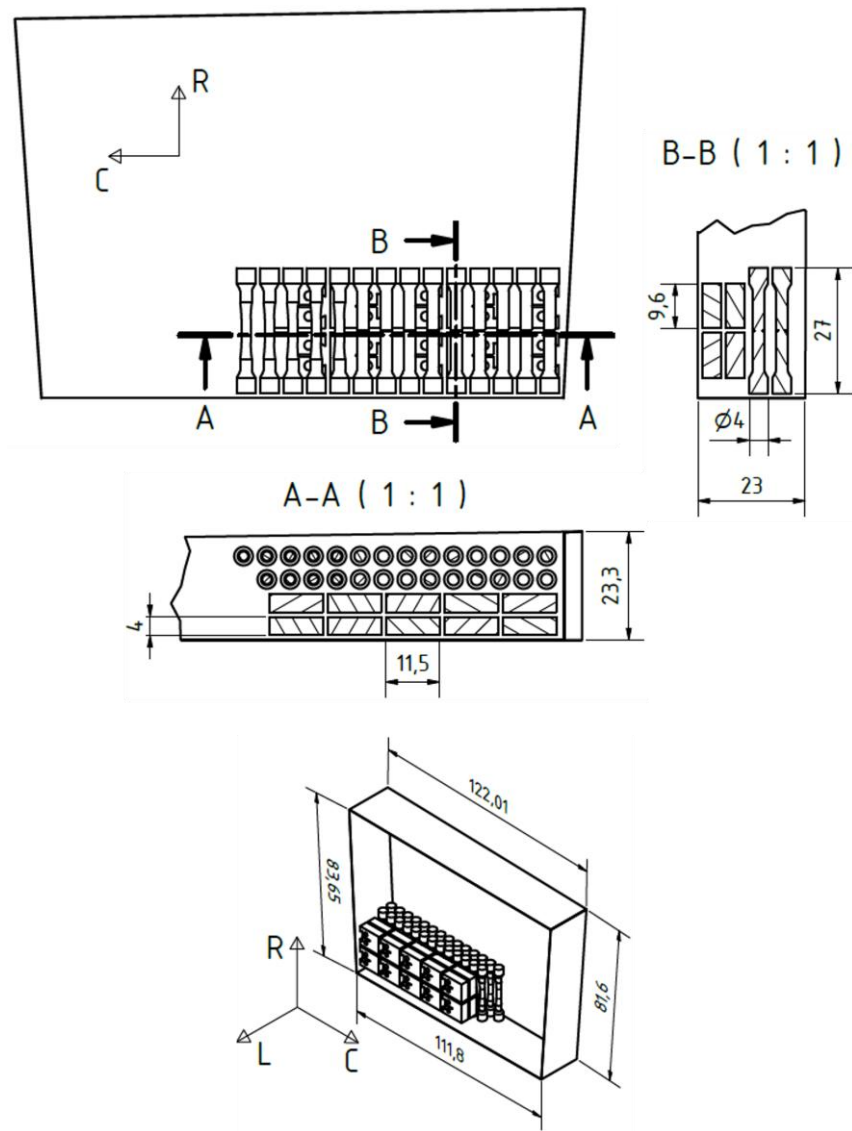


Figure A.3: Cutting plan for the fabrication of the specimens used for the development of the deterministic CZM

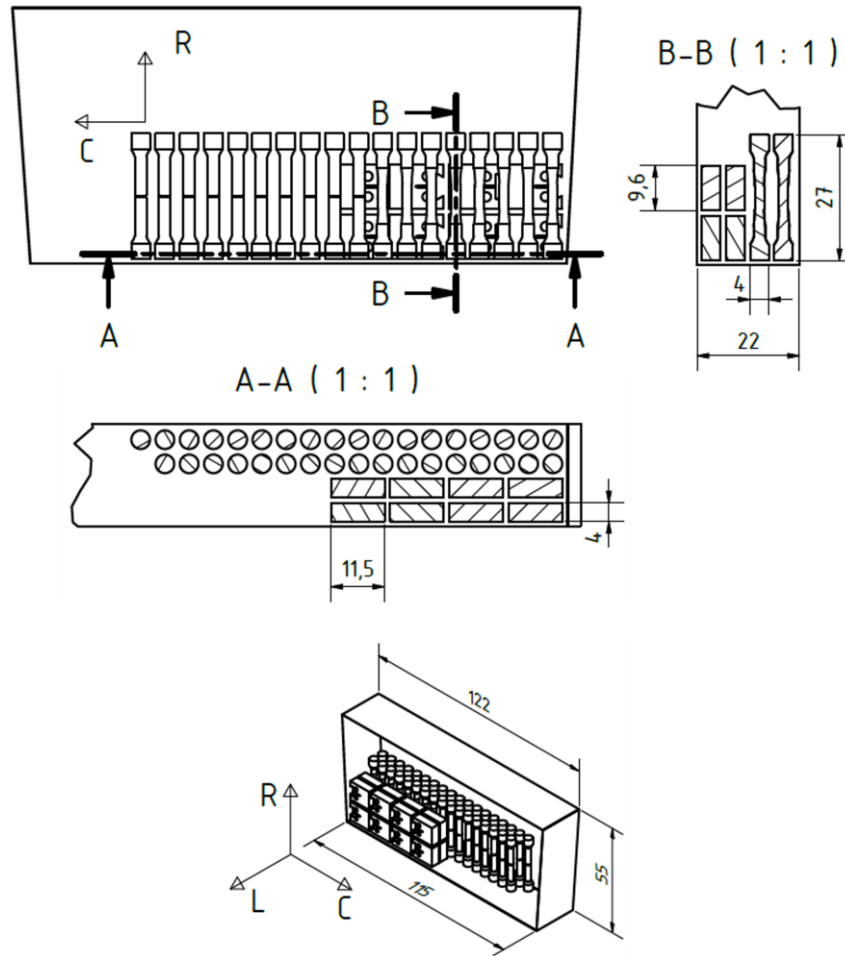


Figure A.4: Cutting plan for the fabrication of the specimens used for the development of the probabilistic CZM

A.2 Specimen geometries and dimensions

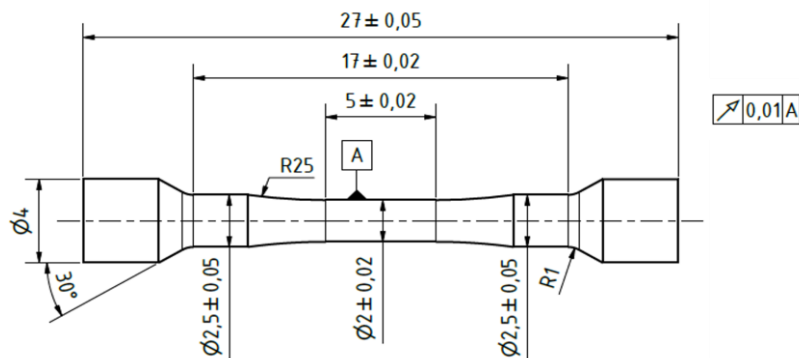


Figure A.5: Smooth round bar specimen geometry

Table A.1: Measured dimensions of the smooth round bar specimens

Specimen	T [°C]	L [mm]	D [mm]
First fabrication			
SRB01	RT	27.055	1.993
SRB02	-85	27.053	2.008

SRB03	-125	27.075	1.994
SRB04	-80	27.071	1.999
SRB05	-60	27.050	2.007
SRB06	-60	27.046	2.000
SRB07	-70	27.091	1.999
SRB08	-80	27.032	1.991
SRB09	-60	27.105	1.995
Second fabrication			
SRB10	-70	26.99	2.000
SRB11	-80	26.98	1.991
SRB12	-60	26.98	1.998
SRB13	RT	26.96	1.997
SRB14	RT	26.98	1.995
SRB15	-70	26.98	1.989
SRB16	-80	26.98	2.000
SRB17	-70	26.96	2.006
SRB18	-30	27.00	2.007
SRB19	RT	26.97	1.997
SRB21	-45	26.94	2.012
SRB22	-45	26.99	1.999
SRB23	-60	26.97	1.992
SRB24	-45	26.94	2.002
SRB25	-80	27.01	1.993
SRB26	-30	26.98	1.996

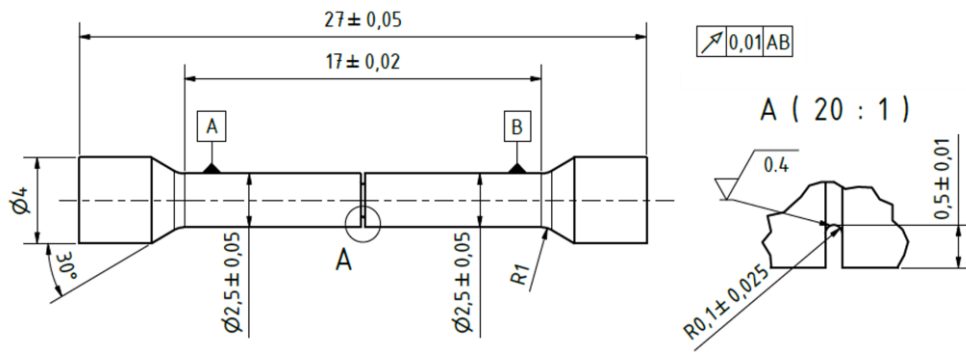


Figure A.6: Notched round bar specimen geometry with 0.1 mm notch root radius

Table A.2: Measured dimensions of the notched round bar specimens with 0.1 mm notch root radius

Specimen	T [°C]	L [mm]	D [mm]	D_N [mm]	r_N [mm]
First fabrication (flat notch)					
0.1NRB01	RT	27.066	2.515	1.520	0.140
0.1NRB02	-60	27.042	2.494	1.525	0.145
0.1NRB04	-60	27.042	2.510	1.521	0.143
0.1NRB05	-70	27.068	2.497	1.566	0.138
0.1NRB06	-80	27.049	2.507	1.543	0.141
0.1NRB07	-70	27.059	2.500	1.557	0.143
0.1NRB08	-80	27.104	2.487	1.493	0.147
0.1NRB09	RT	27.057	2.492	1.550	0.140
0.1NRB10	-70	27.056	2.492	1.526	0.141
Second fabrication (round notch)					
0.1NRB11	RT	27.019	2.497	1.512	0.110
0.1NRB12	-60	27.099	2.514	1.525	0.100
0.1NRB13	RT	27.063	2.504	1.585	0.117
0.1NRB14	-80	27.061	2.499	1.540	0.110

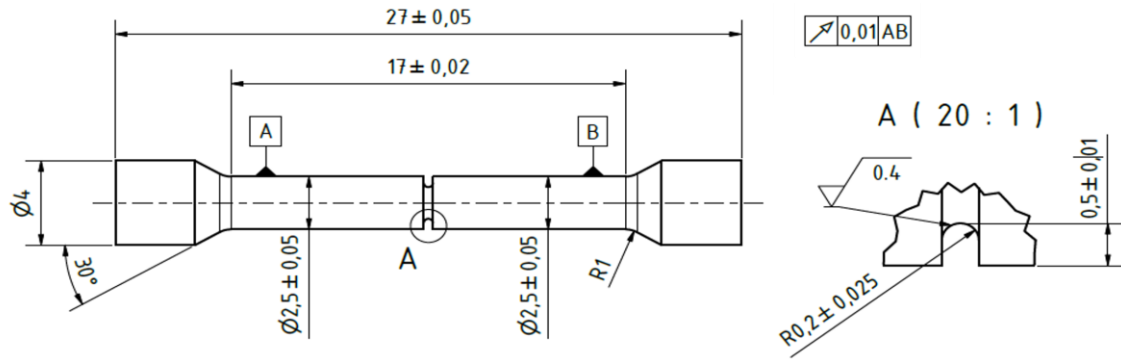


Figure A.7: Notched round bar specimen geometry with 0.2 mm notch root radius

Table A.3: Measured dimensions of the notched round bar specimens with 0.2 mm notch root radius

Specimen	T [°C]	L [mm]	D [mm]	D_N [mm]	r_N [mm]
First fabrication (flat notch)					
0.2NRB01	-60	27.071	2.477	1.563	0.208
0.2NRB02	-70	27.094	2.484	1.547	0.208
0.2NRB03	-80	27.049	2.479	1.529	0.204
0.2NRB04	-80	27.039	2.482	1.524	0.206
0.2NRB05	-60	27.030	2.474	1.560	0.211
0.2NRB06	-70	27.049	2.481	1.550	0.213
0.2NRB07	RT	27.074	2.490	1.514	0.206
0.2NRB08	RT	27.032	2.488	1.550	0.211
Second fabrication (round notch)					
0.2NRB10	RT	27.064	2.500	1.438	0.225
0.2NRB11	RT	27.064	2.518	1.514	0.204
0.2NRB12	-60	27.078	2.494	1.501	0.204
0.2NRB13	-70	27.094	2.478	1.542	0.206
0.2NRB14	-80	27.066	2.514	1.575	0.208

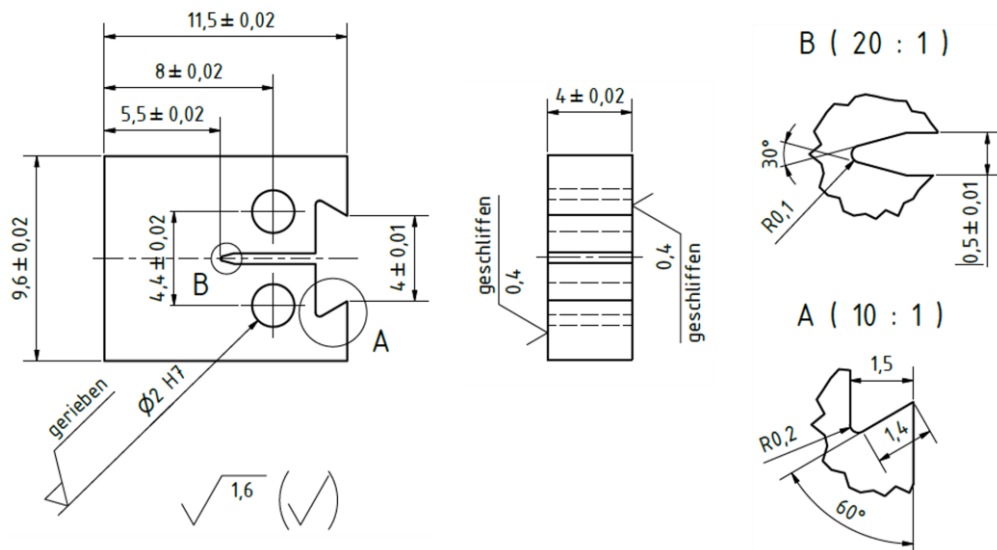


Figure A.8: Miniaturized CT specimen geometry

Table A.4: Measured dimensions of the miniaturized CT specimens

Specimen	T [°C]	W [mm]	B [mm]	H [mm]	c [mm]	a_0 [mm]	a_{notch} [mm]
First fabrication							
MCT01	-80	8.013	3.992	9.600	3.391	3.932	2.585
MCT02	-80	8.002	3.993	9.596	3.452	3.957	2.549
MCT03	-80	8.017	3.989	9.599	3.597	3.890	2.450
MCT04	-80	8.065	3.998	9.598	3.394	4.232	2.526
MCT05	-80	8.036	4.003	9.598	3.525	3.878	2.382
MCT06	-80	8.010	4.002	9.598	3.397	3.899	2.490
MCT07	-70	8.010	3.979	9.598	3.401	3.930	2.513
MCT08	-70	8.017	4.006	9.598	3.501	3.935	2.425
MCT09	-60	8.004	3.995	9.593	3.421	4.036	2.495
MCT10	-60	7.958	4.004	9.597	3.634	3.982	2.300
MCT11	-60	8.010	4.003	9.597	3.382	4.042	2.517
MCT12	-60	7.995	3.996	9.598	3.389	4.046	2.504
MCT13	-60	7.981	4.002	9.597	3.496	4.012	2.428
MCT14	-60	8.022	3.999	9.599	3.394	4.128	2.499
MCT15	-60	8.000	3.997	9.597	3.392	3.987	2.504
MCT16	-60	7.994	4.004	9.599	3.505	3.896	2.405
MCT17	-70	8.024	4.002	9.599	3.409	3.983	2.513
MCT18	-70	7.997	4.006	9.599	3.378	4.000	2.562
MCT19	-60	8.006	3.996	9.599	3.419	3.962	2.539
MCT20	-60	8.010	4.006	9.597	3.523	4.054	2.463
MCT21	-60	7.956	3.991	9.599	3.434	4.116	2.526
Second fabrication							
MCT23	RT	7.959	3.974	9.471	3.458	4.107	2.448
MCT25	RT	7.976	3.975	9.564	3.478	4.086	2.456
MCT26	RT	7.937	3.980	9.550	3.481	3.877	2.446
MCT27	RT	7.965	3.981	9.523	3.480	3.996	2.452
MCT28	-45	7.976	3.982	9.538	2.470	4.056	2.463
MCT29	-30	7.983	3.985	9.602	3.475	4.033	2.462
MCT30	-45	7.979	3.987	9.569	3.483	4.040	2.450
MCT31	-30	7.979	3.988	9.595	3.463	3.918	2.459
MCT32	-30	7.968	3.994	9.556	3.479	4.069	2.450
MCT33	-45	8.036	3.990	9.560	3.530	3.909	2.475
MCT34	RT	7.983	3.986	9.568	3.481	3.958	2.470
MCT35	RT	7.984	3.993	9.605	3.487	4.014	2.466
MCT36	RT	8.017	3.994	9.592	3.494	3.969	2.475
MCT37	RT	7.980	3.993	9.582	3.502	3.973	2.452

A.3 Experimental results

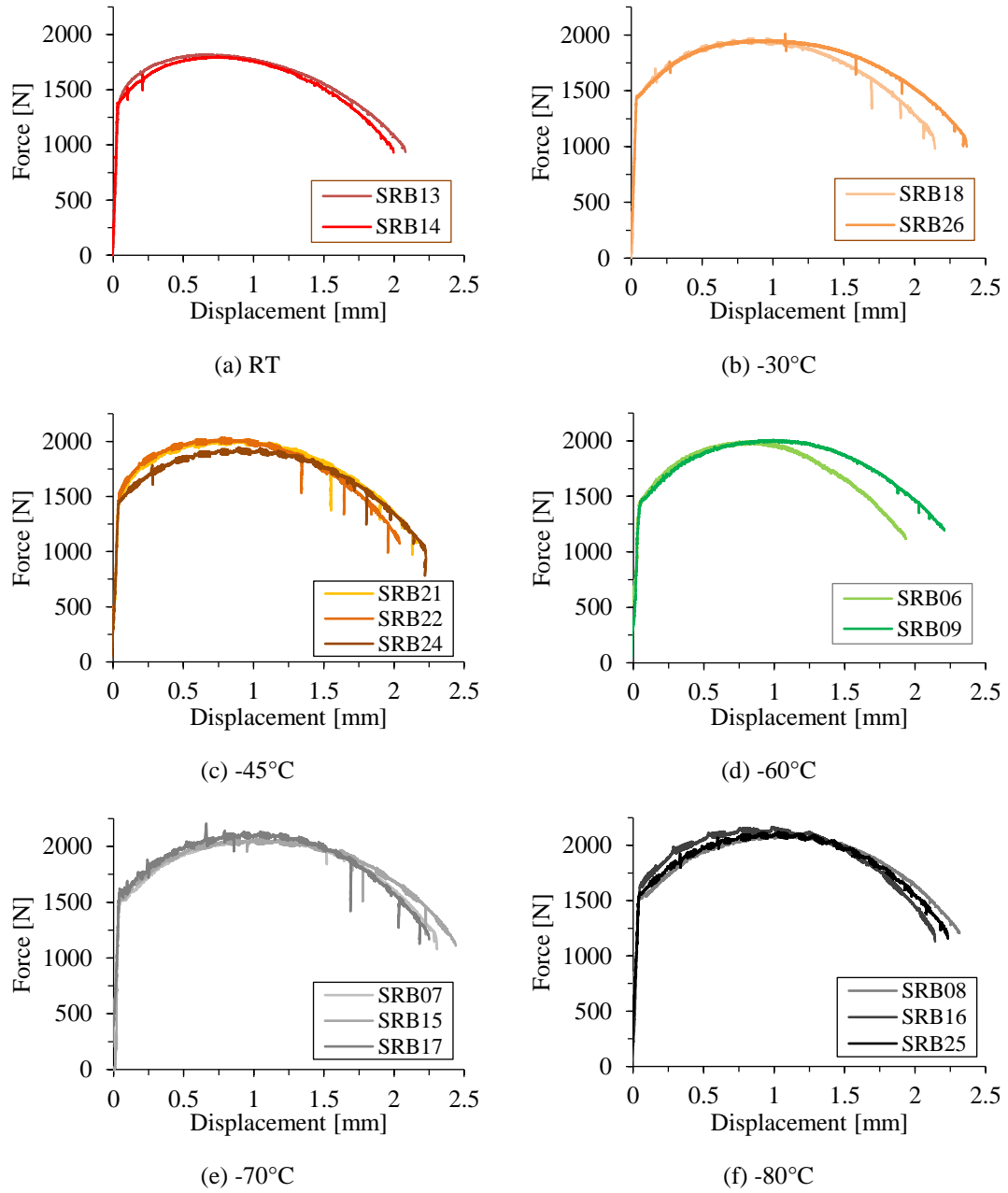


Figure A.9: Force-CHD curves obtained from the SRB tests

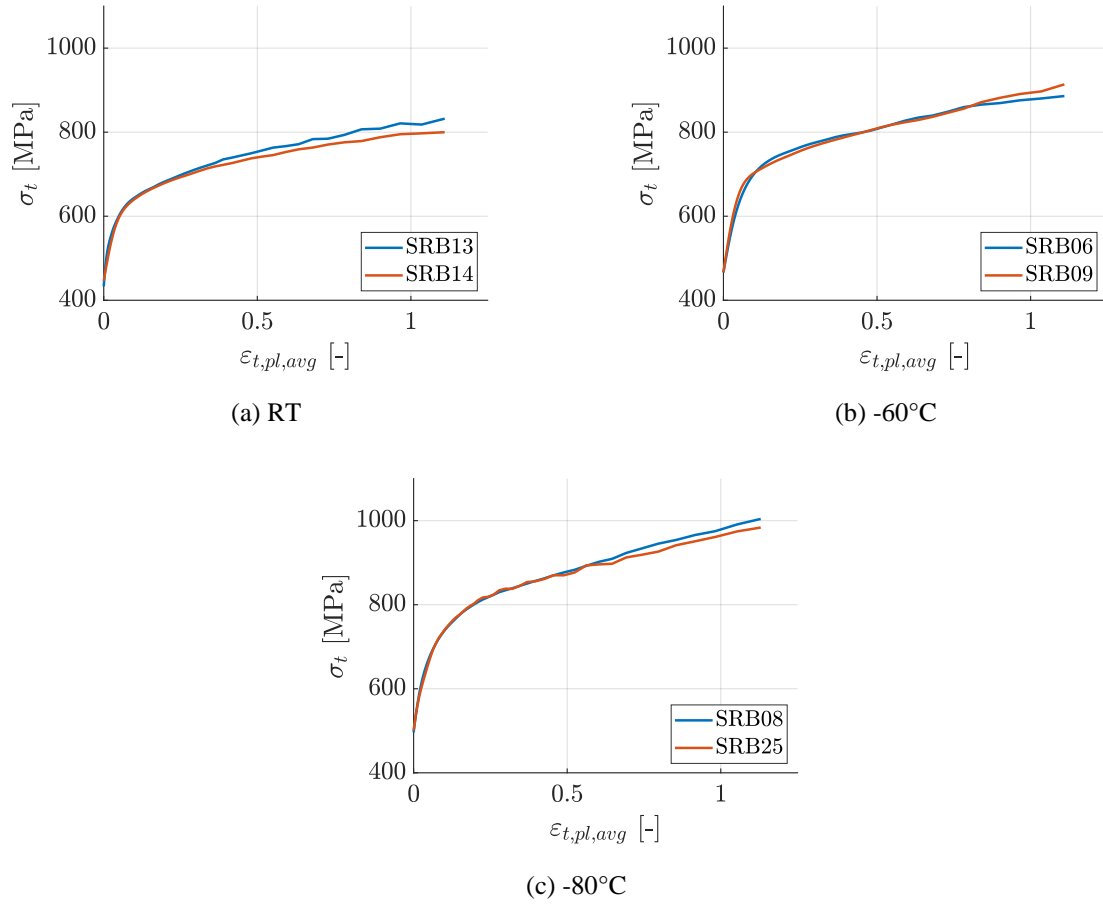


Figure A.10: Uniaxial true stress – true plastic strain curves for all SRB specimens used for the direct flow curve determination

Table A.5: Flow curve data used as material input for the FE-simulations

RT		-30°C		-45°C		-60°C		-70°C		-80°C	
σ_t [MPa]	$\varepsilon_{t,pl}$ [-]	σ_t [MPa]	$\varepsilon_{t,pl}$ [-]	σ_t [MPa]	$\varepsilon_{t,pl}$ [-]	σ_t [MPa]	$\varepsilon_{t,pl}$ [-]	σ_t [MPa]	$\varepsilon_{t,pl}$ [-]	σ_t [MPa]	$\varepsilon_{t,pl}$ [-]
434.9	0.00000	454.3	0.00000	460.0	0.00000	466.4	0.00000	484.4	0.00000	498.4	0.00000
435.9	0.00018	455.1	0.00017	460.8	0.00017	467.1	0.00017	485.2	0.00017	499.2	0.00017
437.0	0.00039	456.0	0.00036	461.6	0.00036	468.0	0.00036	486.1	0.00036	500.2	0.00037
438.2	0.00064	457.1	0.00057	462.7	0.00057	469.0	0.00058	487.1	0.00057	501.2	0.00060
439.7	0.00092	458.3	0.00083	463.8	0.00083	470.1	0.00084	488.3	0.00083	502.5	0.00086
441.3	0.00124	459.7	0.00112	465.2	0.00112	471.4	0.00114	489.7	0.00112	503.9	0.00116
443.2	0.00161	461.3	0.00145	466.7	0.00145	472.9	0.00148	491.3	0.00145	505.6	0.00150
445.4	0.00204	463.1	0.00184	468.5	0.00184	474.7	0.00187	493.1	0.00184	507.4	0.00190
447.9	0.00253	465.3	0.00228	470.5	0.00228	476.6	0.00232	495.2	0.00228	509.6	0.00236
450.8	0.00310	467.7	0.00279	472.9	0.00279	478.9	0.00284	497.6	0.00279	512.1	0.00289
454.1	0.00375	470.5	0.00338	475.6	0.00338	481.6	0.00344	500.4	0.00338	515.0	0.00350
457.9	0.00450	473.7	0.00405	478.7	0.00405	484.6	0.00413	503.6	0.00405	518.3	0.00420
462.2	0.00536	477.4	0.00483	482.3	0.00483	488.1	0.00492	507.3	0.00483	522.0	0.00501
467.1	0.00636	481.6	0.00573	486.4	0.00573	492.0	0.00583	511.4	0.00573	526.3	0.00594
472.6	0.00751	486.4	0.00676	491.0	0.00676	496.6	0.00689	516.2	0.00676	531.2	0.00701
478.8	0.00883	491.9	0.00795	496.4	0.00795	501.8	0.00810	521.7	0.00795	536.8	0.00824
485.8	0.01034	498.1	0.00932	502.5	0.00932	507.8	0.00949	527.9	0.00932	543.1	0.00966
493.5	0.01209	505.2	0.01089	509.4	0.01089	514.6	0.01109	534.9	0.01089	550.3	0.01129
501.9	0.01411	513.0	0.01271	517.2	0.01271	522.3	0.01294	542.8	0.01271	558.2	0.01318
511.0	0.01643	521.9	0.01480	526.0	0.01480	531.0	0.01507	551.6	0.01480	567.1	0.01534
520.8	0.01910	531.6	0.01720	535.8	0.01720	540.8	0.01752	561.4	0.01720	576.9	0.01784
531.1	0.02217	542.4	0.01997	546.7	0.01997	551.8	0.02034	572.2	0.01997	587.6	0.02071

541.7	0.02571	554.0	0.02316	558.6	0.02316	563.9	0.02359	584.0	0.02316	599.1	0.02401
552.5	0.02979	566.5	0.02684	571.6	0.02684	577.1	0.02733	596.7	0.02684	611.5	0.02782
563.3	0.03448	579.7	0.03106	585.5	0.03106	591.3	0.03163	610.3	0.03106	624.5	0.03220
573.8	0.03989	593.5	0.03593	600.1	0.03593	606.3	0.03659	624.5	0.03593	638.2	0.03725
583.9	0.04611	607.4	0.04154	615.1	0.04154	621.9	0.04230	639.2	0.04154	652.2	0.04306
593.5	0.05327	621.3	0.04799	630.2	0.04799	637.6	0.04887	654.1	0.04799	666.6	0.04975
602.4	0.06152	634.8	0.05542	644.9	0.05542	653.0	0.05644	669.1	0.05542	681.3	0.05746
610.9	0.07102	647.5	0.06398	658.9	0.06398	667.6	0.06515	683.8	0.06398	695.9	0.06633
618.9	0.08196	659.1	0.07383	671.7	0.07383	680.9	0.07518	697.8	0.07383	710.4	0.07654
626.7	0.09455	669.6	0.08517	683.2	0.08517	692.7	0.08673	711.1	0.08517	724.4	0.08830
634.5	0.10905	679.1	0.09823	693.4	0.09823	703.2	0.10003	723.5	0.09823	738.0	0.10184
642.4	0.12574	687.8	0.11327	702.6	0.11327	712.6	0.11535	735.2	0.11327	751.2	0.11742
650.6	0.14496	696.1	0.13058	711.3	0.13058	721.4	0.13298	746.6	0.13058	764.3	0.13537
659.3	0.16709	704.3	0.15052	719.7	0.15052	729.9	0.15328	758.0	0.15052	777.5	0.15604
668.3	0.19257	712.5	0.17347	728.0	0.17347	738.2	0.17665	769.4	0.17347	790.9	0.17983
677.5	0.22190	721.0	0.19990	736.4	0.19990	746.5	0.20356	780.5	0.19990	803.9	0.20723
686.2	0.25568	729.8	0.23032	745.2	0.23032	755.4	0.23455	791.2	0.23032	815.8	0.23878
694.7	0.29457	739.3	0.26536	754.7	0.26536	764.9	0.27023	801.6	0.26536	826.9	0.27510
703.4	0.33935	749.1	0.30570	764.3	0.30570	774.4	0.31131	811.5	0.30570	837.1	0.31692
711.9	0.39091	759.1	0.35215	774.0	0.35215	784.0	0.35861	821.1	0.35215	846.8	0.36507
720.6	0.45028	769.0	0.40562	783.6	0.40562	793.3	0.41307	831.8	0.40562	858.2	0.42051
730.4	0.51863	779.2	0.46720	793.8	0.46720	803.9	0.47577	843.4	0.46720	870.8	0.48434
741.2	0.59733	791.6	0.53809	806.9	0.53809	817.8	0.54797	857.6	0.53809	885.5	0.55784
754.7	0.68795	804.6	0.61973	820.4	0.61973	831.3	0.63110	872.5	0.61973	901.0	0.64247
767.2	0.79229	818.2	0.71371	834.5	0.71371	846.7	0.72681	890.3	0.71371	921.1	0.73991
784.3	0.91242	836.2	0.82193	854.5	0.82193	867.7	0.83701	911.0	0.82193	941.5	0.85209
795.8	1.05074	851.3	0.94653	870.1	0.94653	882.8	0.96390	931.3	0.94653	964.8	0.98127
804.3	1.21000	865.4	1.09000	885.1	1.09000	899.7	1.11000	951.6	1.09000	988.2	1.13000
1006.7	5.00000	1248.8	5.00000	1294.4	5.00000	1351.4	5.00000	1504.8	5.00000	1598.4	5.00000

Table A.6: Average true stresses and average true strains at fracture obtained from the SRB tests used for the cohesive strength calibration

Specimen	T [°C]	$\sigma_{t,avg}$ [MPa]	$\varepsilon_{t,avg}$ [-]
First fabrication			
SRB06	-60	1179.6	1.1835
SRB07	-70	1216.3	1.1514
SRB08	-80	1311.9	1.2140
SRB09	-60	1186.0	1.1209
Second fabrication			
SRB13	RT	1066.6	1.2281
SRB14	RT	1053.4	1.2245
SRB16	-80	1229.0	1.1837
SRB17	-70	1179.4	1.1226
SRB25	-80	1207.3	1.1749

Table A.7: Average true stresses and average true strains at fracture obtained from the 0.1NRB tests used for the cohesive strength calibration

Specimen	T [°C]	$\sigma_{t,avg}$ [MPa]	$\varepsilon_{t,avg}$ [-]
First fabrication (flat notch)			
0.1NRB02	-60	1256.1	0.4057
0.1NRB04	-60	1232.5	0.4717
0.1NRB05	-70	1256.5	0.5038
0.1NRB06	-80	1320.8	0.4985
0.1NRB07	-70	1333.7	0.3906
0.1NRB08	-80	1307.2	0.3115

0.1NRB09	RT	1193.9	0.5802
0.1NRB10	-70	1307.6	0.4435
Second fabrication (round notch)			
0.1NRB11	RT	1219.8	0.5247
0.1NRB12	-60	1329.2	0.4875
0.1NRB13	RT	1286.2	0.5276
0.1NRB14	-80	1485.0	0.4407

Table A.8: Average true stresses and average true strains at fracture obtained from the 0.2NRB tests used for the cohesive strength calibration

Specimen	T [°C]	$\sigma_{t,avg}$ [MPa]	$\varepsilon_{t,avg}$ [-]
First fabrication (flat notch)			
0.2NRB01	-60	1201.7	0.5449
0.2NRB02	-70	1209.5	0.5683
0.2NRB03	-80	1265.7	0.5597
0.2NRB04	-80	1263.8	0.5179
0.2NRB05	-60	1269.7	0.5278
0.2NRB06	-70	1253.5	0.5042
0.2NRB07	RT	1031.6	0.5042
0.2NRB08	RT	1023.7	0.5218
Second fabrication (round notch)			
0.2NRB11	RT	1189.9	0.5716
0.2NRB12	-60	1312.8	0.5703
0.2NRB13	-70	1325.7	0.5016
0.2NRB14	-80	1357.4	0.5839

Table A.9: Results of the valid MCT tests within the DBT region following ASTM E1921

Specimen	T [°C]	LLD/FFD [-]	Δa [mm]	J_c [N/mm]	K_{Jc} [MPa \sqrt{m}]	$K_{Jc,1T}$ [MPa \sqrt{m}]	$K_{Jc,limit}$ [MPa \sqrt{m}]	δ [-]
MCT01	-80	0.604	0.00	24.57	75.12	54.84	125.19	1
MCT02	-80	0.605	0.00	39.24	94.93	67.37	124.66	1
MCT03	-80	0.604	0.00	13.95	56.60	43.13	125.78	1
MCT04	-80	0.614	0.00	23.00	72.68	53.32	121.39	1
MCT05	-80	0.603	0.00	40.12	96.00	68.07	126.33	1
MCT06	-80	0.604	0.00	17.77	63.89	47.76	125.61	1
MCT07	-70	0.604	0.00	21.10	69.51	51.27	123.48	1
MCT08	-70	0.605	0.00	42.23	98.34	69.56	123.56	1
MCT09	-60	0.607	0.00	59.76	116.81	81.21	120.35	1
MCT10	-60	0.605	0.00	27.17	78.76	57.17	120.51	1
MCT11	-60	0.607	0.12	196.39	211.74	141.29	120.48	0
MCT12	-60	0.607	0.00	43.83	100.03	70.60	120.07	1
MCT13	-60	0.607	0.00	89.23	142.73	97.63	119.90	0
MCT15	-60	0.606	0.00	53.72	110.74	77.38	121.07	1
MCT16	-60	0.603	0.00	52.55	109.53	76.64	122.38	1
MCT17	-70	0.606	0.00	36.18	91.01	64.92	122.92	1
MCT18	-70	0.606	0.00	29.57	82.28	59.40	122.23	1
MCT19	-60	0.605	0.00	35.22	89.67	64.05	121.53	1
MCT20	-60	0.608	0.00	48.03	104.71	73.60	120.21	1
MCT28	-45	0.608	0.05	94.26	146.36	99.83	117.25	0
MCT30	-45	0.608	0.19	181.51	203.10	135.71	117.53	0
MCT33	-45	0.605	0.00	40.62	96.08	68.09	120.30	1

Table A.10: Results of the MCT tests on the upper shelf following ASTM E1820

Specimen	T [°C]	CHD [mm]	LLD/FFD [-]	Δa [mm]	Corr. fact. [-]	J [N/mm]
MCT23	RT	2.50	0.633	0.81	0.943	219.69
MCT25	RT	3.50	0.633	0.94	0.906	279.22
MCT26	RT	1.50	0.628	1.42	0.978	368.82
MCT27	RT	2.00	0.631	0.32	0.965	478.83
MCT34	RT	1.25	0.630	0.50	0.986	602.95
MCT35	RT	6.00	0.632	0.21	0.840	688.24
MCT36	RT	1.00	0.631	2.64	0.988	774.82
MCT37	RT	3.00	0.631	0.17	0.916	996.11

A.4 Fractography results

Table A.11: Cleavage initiation site locations and numerical maximum principal stress and triaxiality values at the fracture points

Specimen	$T - T_0$ [°C]	$K_{Ic,1T}$ [MPa \sqrt{m}]	LLD [mm]	x [μm]	z [mm]	σ_1 [MPa]	h [-]
MCT01	-48.5	54.84	0.136	26.95	0.338	1710.7	1.71
MCT02	-48.5	67.37	0.196	82.91	0.148	1888.7	2.49
MCT05	-48.5	68.07	0.198	66.21	0.648	1851.4	2.31
MCT06	-48.5	47.76	0.113	60.94	0.515	1726.8	2.54
MCT07	-38.5	51.27	0.125	28.42	0.200	1740.5	2.04
MCT08	-38.5	69.56	0.206	132.40	0.912	1551.1	2.10
MCT10	-28.5	57.17	0.153	35.16	0.460	1712.6	2.02
MCT13	-28.5	97.63	0.384	185.20	0.145	1816.8	2.26
MCT15	-28.5	77.37	0.248	221.20	0.457	1550.3	2.18
MCT16	-28.5	76.63	0.249	72.66	0.673	1750.8	2.10
MCT17	-38.5	64.91	0.184	58.01	0.239	1830.2	2.26
MCT18	-38.5	59.40	0.158	68.85	0.661	1775.2	2.51
MCT19	-28.5	64.05	0.179	44.82	0.755	1715.9	2.06
MCT20	-28.5	73.59	0.241	47.75	0.013	1644.9	1.70

Table A.12: Distribution of the fracture modes on the fracture surfaces of the MCT specimens tested within the DBT region and corresponding ductile fracture ratios

Specimen	$T - T_0$ [°C]	Transgr.	Ductile	2nd. crack	Oxide/Damage	Intergr.	DFR [-]
MCT01	-48.5	226	10	2	2	0	0.0420
MCT02	-48.5	223	10	1	1	3	0.0422
MCT03	-48.5	213	5	1	21	0	0.0228
MCT05	-48.5	226	10	1	1	2	0.0418
MCT06	-48.5	230	5	0	1	0	0.0213
MCT07	-38.5	220	9	5	2	4	0.0378
MCT08	-38.5	219	12	4	3	2	0.0506
MCT09	-28.5	207	18	4	0	3	0.0776
MCT10	-28.5	217	17	2	2	2	0.0714
MCT11	-28.5	210	21	4	0	5	0.0875
MCT12	-28.5	214	19	4	2	1	0.0798
MCT13	-28.5	223	13	2	0	2	0.0542
MCT15	-28.5	220	20	0	0	0	0.0833
MCT16	-28.5	219	13	2	3	3	0.0549
MCT17	-38.5	219	15	0	3	3	0.0633
MCT18	-38.5	222	15	0	3	0	0.0633
MCT19	-28.5	219	19	0	0	1	0.0792

MCT20	-28.5	219	17	2	2	0	0.0714
MCT28	-13.5	216	23	0	0	0	0.0962
MCT30	-13.5	216	21	0	2	1	0.0882
MCT33	-13.5	217	22	0	0	1	0.0917

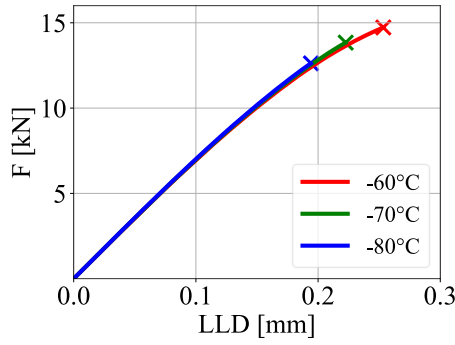
A.5 Numerical results

Table A.13: Cohesive strength and maximum triaxiality at fracture obtained from the SRB and NRB simulations

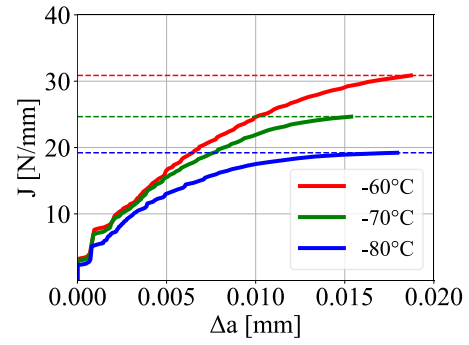
Specimen	T [°C]	σ_c [MPa]	h_{\max} [-]
SRB06	-60	1487	0.947
SRB09	-60	1459	0.926
0.2NRB01	-60	1736	1.4473
0.2NRB05	-60	1801	1.6338
0.2NRB12	-60	1823	1.6273
0.1NRB02	-60	1881	1.7852
0.1NRB04	-60	1880	1.7254
0.1NRB12	-60	1947	1.9334
SRB07	-70	1555	0.921
SRB17	-70	1525	0.902
0.2NRB02	-70	1807	1.4193
0.2NRB06	-70	1798	1.4419
0.2NRB13	-70	1873	1.6403
0.1NRB05	-70	1970	1.7265
0.1NRB07	-70	1927	1.7775
0.1NRB10	-70	1963	1.7529
SRB08	-80	1635	0.932
SRB16	-80	1603	0.914
SRB25	-80	1603	0.914
0.2NRB03	-80	1859	1.4294
0.2NRB04	-80	1855	1.4469
0.2NRB14	-80	1938	1.6101
0.1NRB06	-80	2006	1.7014
SRB13	RT	1402	1.016
SRB14	RT	1402	1.016
0.2NRB07	RT	1598	1.4572
0.2NRB08	RT	1651	1.6209
0.2NRB11	RT	1671	1.615
0.1NRB09	RT	1720	1.6362
0.1NRB11	RT	1803	1.8523
0.1NRB13	RT	1752	1.8629

Table A.14: Load line displacement LLD , force F , crack extension Δa and J determined at the point of unstable fracture from the MCT, 0.5T and 1T CT simulations at -60, -70 and -80°C

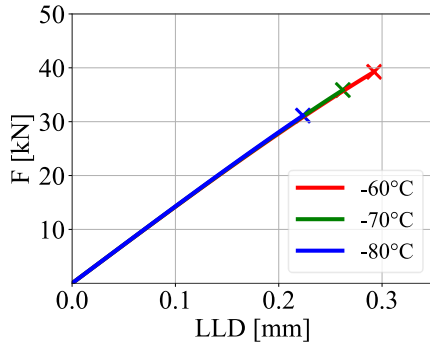
T [°C]	LLD [mm]	F [kN]	Δa [μm]	J [N/mm]
MCT				
-60	0.214	1.89	26.7	43.5
-70	0.177	1.91	20.0	34.4
-80	0.150	1.92	19.8	27.6
0.5T CT				
-60	0.341	16.6	31.3	51.0
-70	0.299	16.3	24.0	41.7
-80	0.257	15.4	23.5	32.4
1T CT				
-60	0.473	56.6	28.1	54.5
-70	0.419	53.0	23.1	44.0
-80	0.366	48.1	24.1	34.3



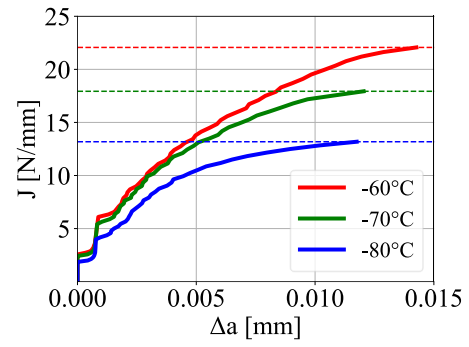
(a) 0.5T CT model



(b) 0.5T CT model



(c) 1T CT model



(d) 1T CT model

Figure A.11: Simulated force-LLD and J-R curves from the 0.5T CT model (a, b) and the 1T CT model (c, d) at -60, -70 and -80°C using the size-adjusted cohesive energy

Table A.15: Numerical fracture toughness results from the probabilistic simulations with a constant cluster size of 18x50 μm

Simulation	T [°C]	$K_{Ic,num}$ [MPa√m]	$K_{Ic,1T,num}$ [MPa√m]
PCZ18_-45_1	-45	132.14	90.92
PCZ18_-45_2	-45	120.15	83.34
PCZ18_-45_3	-45	130.85	90.11
PCZ18_-60_1	-60	117.10	81.41
PCZ18_-60_2	-60	111.66	77.97

PCZ18_-60_3	-60	118.73	82.44
PCZ18_-60_4	-60	104.60	73.51
PCZ18_-60_5	-60	137.33	94.21
PCZ18_-60_6	-60	116.54	81.06
PCZ18_-60_7	-60	113.43	79.09
PCZ18_-60_8	-60	121.07	83.92
PCZ18_-60_9	-60	108.09	75.71
PCZ18_-70_1	-70	76.31	55.61
PCZ18_-70_2	-70	78.64	57.08
PCZ18_-70_3	-70	73.56	53.88
PCZ18_-70_4	-70	78.68	57.12
PCZ18_-70_1	-80	54.71	41.96
PCZ18_-70_2	-80	59.28	44.85
PCZ18_-70_3	-80	69.67	51.42
PCZ18_-70_4	-80	55.10	42.20
PCZ18_-70_5	-80	65.20	48.59

Acknowledgements

This work was completed between September 2020 and February 2025 at the Institute for Applied Materials (IAM) in the Department of Mechanics of Materials and Interfaces (MMI) at Karlsruhe Institute of Technology (KIT).

I would like to extend my sincere gratitude to my supervisor, Prof. Dr.-Ing. Jarir Aktaa, for giving me the opportunity to work on this topic and for his guidance throughout my research. He was always available to talk and helped me find a new perspective whenever I was stuck on a difficult problem. I also thank him for acting as the main referee. My thanks also go to Prof. Dr. Peter Gumbsch for his insightful feedback and for serving as the co-referee.

Within the department, I am particularly thankful to Dr. Ermile Gaganidze for his invaluable guidance, support and encouragement throughout this journey. His mentorship has shaped my growth as a researcher. I am also grateful to Stefan Knaak, Dr.-Ing. Mario Walter and Melina Blem for their technical support with the lab equipment and servo-hydraulic systems. Special thanks go to my office colleague, Dr. Ing. Elvina Gaisina, for the engaging scientific discussions and for sharing her insights into Russian culture. I would also like to thank all the other PhD students and post-doctoral researchers who were at the department during my time there. I greatly enjoyed our conversations during lunch and coffee breaks, and especially the social events we had outside of work.

This research was conducted as part of Work Packages 2, 3, and 4 of the European project FRAC-TESUS, and I would like to thank everyone involved in the project. I am also grateful for the opportunity to attend project meetings in several European countries, which was an invaluable experience.

Last but not least, I want to thank my parents, my brother, and my friends for their support along the way. I could not have made it this far without their encouragement.

List of publications

- **T. Metzler**, E. Gaganidze, J. Aktaa
Application of the Master Curve Approach on SA-508 Cl.3 Reactor Pressure Vessel Steel Using Small Specimens
Presentation at: Nuclear Materials Conference (NuMat) 2022 in Ghent, Belgium
- **T. Metzler**, E. Gaganidze, J. Aktaa
Numerical Prediction of Fracture Toughness of a Reactor Pressure Vessel Steel Based on Experiments Using Small Specimens
Presentation at: ASME Pressure Vessels & Piping Conference (PVP) 2023 in Atlanta, Georgia, USA
- **T. Metzler**, E. Gaganidze, J. Aktaa
Numerical Prediction of Fracture Toughness of a Reactor Pressure Vessel Steel Based on Experiments Using Small Specimens
Proceedings of the ASME Pressure Vessels & Piping Conference (PVP) 2023 in Atlanta, Georgia, USA
- F. Naziris, R. Hernandez, **T. Metzler**, E. Gaganidze, I. Uytendhouwen, M. Kolluri
Master Curve Evaluation Using Miniature C(T) Specimens as Part of a Round Robin Program Within the FRACTESUS Project
Proceedings of the ASME Pressure Vessels & Piping Conference (PVP) 2023 in Atlanta, Georgia, USA
- **T. Metzler**, E. Gaganidze, J. Aktaa
Probabilistic Cohesive Zone Approach to Predict Fracture Toughness in the Ductile-to-Brittle Transition Region
Poster presentation at: 21st International Conference on Fusion Reactor Materials (ICFRM-21) 2023 in Granada, Spain
- **T. Metzler**, E. Gaganidze, J. Aktaa
Prediction of Fracture Toughness of a Reactor Pressure Vessel Steel Within the Ductile-to-Brittle Transition Region Based on a Probabilistic Cohesive Zone Model
Journal of Nuclear Materials Vol. 605 (2024)
- T. Petit, B. A. Baykal, G. Dundulis, R. Erdei, P. Francois, P. Gál, M. Li, **T. Metzler**, F. Péralès, T. Shinko, P. Spätig, P. Ungar, I. Uytendhouwen, P. Vincent
Numerical Investigations on Size Effects and Mini-CT Applications for Master-Curve Determination
Engineering Fracture Mechanics Vol. 325 (2025)